Electrospun PCL Fibres for Oesophageal Tissue Engineering

Anna Johnston

A thesis submitted to the University of Birmingham for the degree of

DOCTOR OF PHILOSOPHY

School of Chemical Engineering

University of Birmingham

March 2024

Acknowledgements

I am deeply grateful to everyone who has supported me throughout my PhD journey.

First and foremost, my sincerest thanks to my supervisor, Anita. Your unwavering support and invaluable advice have been invaluable to my experience. Your expertise, patience and mentorship have been instrumental in helping me navigate the challenging parts of this journey.

To my parents, who have supported me in so many ways during my academic journey, I owe an incredible debt of gratitude. Your endless encouragement and faith in me have made my academic pursuits possible, and I will be forever thankful.

To my sister, Clare, thank you for the love, laughter, and allowing me to vent my seemingly endless frustrations. Thank you for taking care of me when I was too busy to cook, and for reassuring me when I thought I forgot how to use a Haemocytometer.

I would also like to thank everyone at the HTI and the School of Chemical Engineering, thank-you to anyone who has ever given me a word of advice, or kept me company during a late-night lab session. A special thanks to Laura, whose food and pep-talks provided much-needed sustenance and reassurance, and to Lucy, whose friendship during the most stressful times was so valuable.

To all of the friends I found in Birmingham, thank you for the music, the laughter and the boardgames. Your friendships provided the distraction I needed, and helped me maintain some semblance of a work-life balance.

This thesis is not only a result of my hard work, but also a reflection of the support, guidance and inspiration I've received from each of you, and for that I am profoundly grateful.

Abstract

Tissue engineering and regenerative medicine offer promising solutions for the treatment of oesophageal disorders including cancer treatments and Barrett's oesophagus, which often require oesophagectomy followed by replacement of the lost tissue. Due to ongoing donor tissue shortages, there is a need for a tissue engineered solution, yet the development of suitable biomaterial scaffolds remains a critical aspect of this field.

This thesis presents the development of an electrospun polycaprolactone material tailored for oesophageal tissue engineering applications, with the novel step of adding microscale topography to the inherent nanoscale topography of an electrospun material.

The optimisation of the electrospinning process prioritised the reduction of the fibre diameter and enhancement of fibre alignment, key factors known to influence cell migration and tissue organisation. Parameters including applied voltage, solvent system, needle tip-collector distance and collector speed were optimised. The optimisation process determined that a 10 % w/v solution in a 50:50 chloroform: dimethylformamide solvent system using a mandrel collector rotating at 2000 RPM produced highly aligned fibres with small diameters and free from beading.

Tensile testing revealed highly anisotropic mechanical properties of the fibre sheets, with an elastic modulus comparable to porcine oesophageal tissue perpendicular to the fibre direction. The fibre sheets exhibited superior strength parallel to fibre orientation, crucial for implantable materials, while maintaining high elasticity, albeit lower than native tissue, prompting considerations for *in vivo* applications.

In vitro degradation experiments in pH 4 and pH 7 environments were carried out, and various characterisation techniques were used to assess the degradation kinetics over a 12-week period. There was significant degradation at both pH conditions, with a more pronounced and prolonged degradation observed under acidic conditions.

Successful fibronectin functionalisation of the fibres significantly augmented their bioactivity, evidenced by cell viability compared to their non-functionalised counterparts, without affecting fibre diameter or alignment. Moreover, functionalisation increased wettability, potentially increasing bioactivity further.

Various sterilisation and disinfection methods; ethanol, ethylene oxide, UV, and gamma radiation, were assessed for their effects on fibre properties. Ethanol and

ethylene oxide treatments negatively impacted fibre topography. Conversely, UV and gamma radiation showed minimal effects on fibre morphology, suggesting their suitability for sterilisation.

Investigations into fibroblast response suggested that aligned fibres had an elongation effect on fibroblasts, and that the addition of microgrooves could amplify this effect, but that fibre alignment was the main influencing factor.

This work contributes to the development of an electrospun PCL material with promising characteristics for use in oesophageal tissue engineering, offering insights into its optimisation, functionalisation, sterilisation and degradation behaviours.

Contents

List of Figures

List of Tables

Abbreviations

^{60}Co	Cobalt-60
ANG1	Angiopoietin 1
BCA	Bicinchoninic acid
BSA	Bovine serum albumin
$CDCL_3$	Deuterated chloroform
$CHCL_3$	Chloroform
DCM	Dichloromethane
dECM	Decellularised ECM
DiH2O	Deionised water
DMF	Dimethylformamide
DMSO	Dimethyl Sulphoxide
DoE	Design of experiments
DP	Degree of polymerisation
ECM	Extracellular matrix
EDC	N-(3-dimethylaminopropyl)-N'-ethyl carbodiimide hydrochloride
FDA	Food and drug administration
FGF	Fibroblast growth factor
GI	Gastrointestinal
HFIP	Hexafluoro-2-propanol
HSP	Hansen Solubility Parameters
IgG	Immunoglobin G
IMS	Industrial methylated spirits
iPSC	Induced pluripotent stem cell
KCl	Potassium chloride
KH_2PO_4	Potassium phosphate monobasic
MES	2-(N-Morpholino)ethane sulfonic acid hemisodium salt
Na_2HPO_4	Sodium phosphate dibasic
NaCl	Sodium chloride
NHS	*N*-Hydroxy succinimide
NMR	Nuclear magnetic resonance
OGJ	Oesophagogastric junction
OVAT	One variable at a time
PBHV	poly(3-hydroxybutyrate-co-3-hydroxyvalerate)
PCL	Polycaprolactone
PEM	Proton membrane exchange
PET	Polyethylene terephthalate
PFA	Paraformaldehyde
PLGA	poly(lactic-co-glycolic acid)
PLLC	Poly(L-lactide-co-caprolactone)
PTFE	Polytetrafluoroethylene
ROS	Reactive oxygen species
SD	Standard deviation
SE	Standard error of the mean
SEM	Scanning electron microscope

SIS	Small intestinal submucosa
TERM	Tissue engineering and regenerative medicine
TSP	Thrombospondin
UES	Upper oesophageal sphincter
UV	Ultraviolet
VEGF	Vascular endothelial growth factor

1.0 Introduction

1.1 Tissue Engineering

Tissue engineering is an interdisciplinary field that combines principles from engineering, material science and biological sciences in order to develop systems that restore, maintain or improve tissue function[1]. Tissue engineering has garnered significant attention in modern medicine and medical research due to the persistent shortage of organ donations. This shortage leads to lengthy waiting lists for all organ transplants, demonstrated by the 6,959 person waiting list in the UK in March 2023 [2]. The gap between organ availability and the demand for transplants emphasises the critical need for alternative solutions.

In addition to the shortage of donor organs, allotransplants- the transplantation of tissues or organs from another individual- present challenges. Common complications include organ or tissue rejection, requiring the use of immunosuppressant drugs. While these drugs are essential in preventing rejection, they are associated with significant side effects, including *de novo* carcinoma and post-transplant *diabetes mellitus*[3,4].

Autotransplantation, which is where suitable tissue that can functionally replicate the desired tissue is harvested from elsewhere in a patient's body, offers an alternative to allotransplantation that avoids the risk of immune rejection and therefore does not require immunosuppression[5–7]. However, there are issues with this approach; mismatches in the biomechanical properties of the tissues can prevent full functionality from being restored to the area, inadequate vascularisation and innervation can lead to transplant failure, and the procedure of harvesting donor tissue can itself cause further trauma and adverse effects on the donor site[8–11].

A solution employing tissue engineering principles can address many of the challenges associated with standard approaches. Tissue-engineered systems are custom-designed for specific tissues, significantly reducing the likelihood of implant failure, while eliminating the need for immunosuppression, which is a major advantage over traditional transplantation methods.

The “tissue engineering triad” consists of scaffolds, cells, and signalling components. These elements are used in combination or individually to facilitate the regeneration of specific tissues (see **Figure 1.1**) [12,13].

Scaffolds for tissue engineering are composed of biomaterials which are engineered to interact with biological systems for either diagnostic or therapeutic purposes. In tissue engineering, scaffolds made from biomaterials provide a structural support that supports cell attachment, proliferation and differentiation, ultimately aiding in the formation of new tissues[14,15].

The specific properties required of a scaffold can vary significantly between different types of tissues, depending on the functional demands of each tissue type. For example, scaffolds designed for bone regeneration must exhibit high compressive strength and stiffness to withstand forces experienced *in vivo*, while cardiac scaffolds need to be elastic and have high tensile strength to accommodate the contractions of the heart.

Despite these differences, there are certain universal requirements that all scaffolds must meet to be effective. A crucial feature is porosity. Scaffolds must have an interconnected porous structure to allow for the vascularisation. Vascularisation is essential for tissue survival and integration, as it ensures the delivery of oxygen and nutrients to the cells within the scaffold and the removal of waste products. A lack of

sufficient vascularisation can lead to cell death and tissue necrosis, undermining the success of the engineered tissue[16,17].

In addition to porosity, the mechanical properties of scaffolds must be carefully tailored to mimic the ECM of the target tissue. The ECM provides both structural support and biochemical cues that influence cell behaviour *in vivo*. By closely replicating the mechanical properties of a specific tissue's ECM, engineered scaffolds can create a more conducive environment for cell growth and tissue development. This biomimetic approach helps in promoting proper cell alignment, differentiation, and the formation of tissue-specific structures, which are crucial for the functionality of the regenerated tissue[14,18,19].

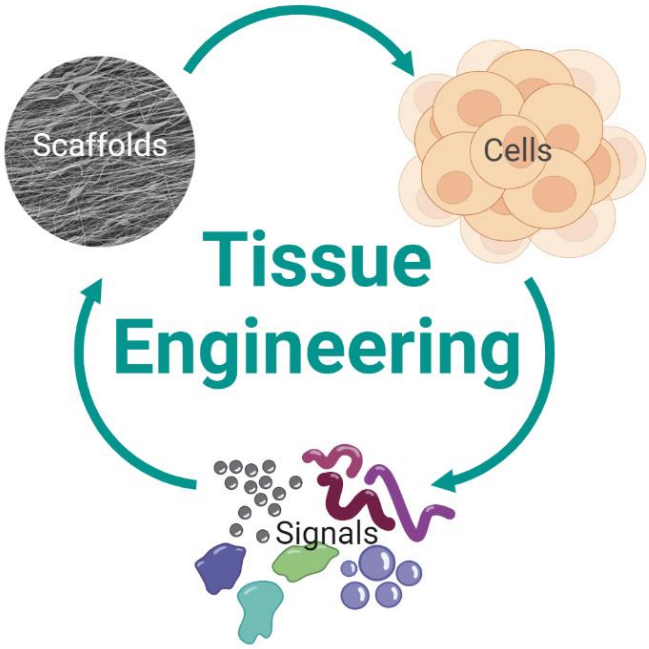

Figure 1.1 The tissue engineering triad. The tissue engineering triad consists of three key components; biomaterial scaffolds, cells and signals. Biomedical scaffolds offer structural support to cells during tissue regeneration, eventually being replaced with new tissue. Signals can take the form of bioactive molecules, such as hormones, peptides and growth factors, or physical cues, including mechanical forces or topographical features. The cellular component can consist of autologous, heterologous or stem cells, which interact with both the scaffold and signalling components to regenerate the desired tissue.

There are various sources of cells that are suitable for use in tissue engineering. Autologous cells, which can be harvested directly from a patient, can be expanded *in vitro* in combination with a biomaterial scaffold or cell signalling element. Although autologous cells avoid the issue of possible adverse immune responses, there is often a limited number of suitable cells available for harvesting, and doing so may result in significant donor-site morbidity. Allogenic donors are other possible sources of cells, but require immunosuppression, similar to traditional transplant methods. Several studies have investigated the use of allogenic cells for tissue engineering, with some promising results. However, the same issues with donor shortages relevant to organ donation are also relevant to allogenic cells. In addition, allogenic cells can induce an immunogenetic response, which may delay or halt tissue regeneration when implanted *in vivo*[20–22].

In response to the challenges associated with donor scarcity and immune rejection, stem cells have emerged as a promising potential cell source for tissue engineering applications. Stem cells are undifferentiated cells that have immense capacity for self-renewal and multipotent differentiation, allowing them to develop into various cell types Stem cells have the added advantage of being able to recruit endothelial lineage cells and coordinate tissue repair responses via increasing macrophage infiltration to a tissue[23].. This versatility makes them ideal candidates for tissue engineering applications.

One significant advantage of using stem cells harvested from the patient (autologous stem cells), is that there is no risk of immune rejection, negating the need for immunosuppression. Allogenic stem cells are taken from donors other than the recipient, offering an alternative to autologous stem cells, albeit with a potential immunogenic effect.

Stem cells can be sourced from several tissue niches, each with unique potential applications. Bone marrow is commonly used as a source of hematopoietic stem cells (HSCs) and mesenchymal stem cells (MSCs), but MSCs can also be harvested from adipose tissue using a much less invasive procedure[24]. MSCs are of particular interest in tissue engineering, as they are multipotent, and can develop into several tissue types including oesophageal tissue[25,26].

However, the use of stem cells is not without challenges. Their capacity for differentiation is largely influenced by their environment, making it challenging to predict their expansion and behaviour once implanted. Their exposure to a broad range of signalling factors *in vivo*, can lead to unexpected or undesired outcomes, such as immunogenicity, or teratoma formation, which has been observed once human embryonic stem cells have been implanted *in vivo*[27,28]. As a result, a major area of research is now focused on developing methods to control the differentiation and behaviour of stems post-implantation, through the use of various chemical and physical signals[18,28].

The signalling component is a crucial element of the tissue engineering triad, and encompasses a wide range of biological, physical and chemical cues that can be used to direct cell behaviour in order to regenerate functional tissue

One approach to incorporating signalling into biomaterial scaffolds involves designing specific topographical features. These features can include patterns in the form of grooves, ridges or pores that provide mechanical cues to cells[12,29–34]. The physical architecture of a scaffold can mimic the natural ECM, encouraging cells to align, which is particularly useful in tissues that have are anisotropic[35–38]. Such mechanical guidance can lead to more organised and functional tissue formation, as cells can

respond to these cues by reorienting their cytoskeleton, expressing focal adhesions, and depositing aligned ECM components[29,32,33,39]. Gene and protein expression has also been shown to be affected by topographical cues, which could be harnessed to mediate ECM deposition and ultimately tissue regeneration[30,33,40–42].

Scaffold surfaces can also be functionalised with various biochemical signals, such as growth factors, cytokines and cell adhesion proteins. This method directly influences cellular activities such as attachment, migration, proliferation and differentiation[16,43,44]. Growth factors, for example, can be incorporated into scaffolds to promote specific lineage differentiation of stem cells or to accelerate tissue healing processes. Pro-angiogenic and vascular growth factors including VEGF and FGF2 incorporated into polymeric biomaterials have been shown to increase cell adhesion, improve regenerated tissue functionality, and have a positive immunomodulatory affect at a wound site, in addition to enhancing angiogenesis, a critical step in the formation of granulation tissue[44–46].

The advent of “smart” biomaterials has further expanded the scope of what can be achieved with biomaterial design by introducing materials that can respond dynamically to environmental changes or external stimuli. These materials can deliver controlled does of growth factor or drugs, release bioactive compounds in response to specific triggers such as pH or temperature, and provide electrical or mechanical stimuli to cells[47–52]. For example, conductive polymers can be used to deliver electrical signals that promote the differentiation of bone, cartilage and cardiac cells, enhancing the functional integration of engineered tissues[47,48].

In many advanced tissue engineering strategies, multiple types of signals are integrated into a single scaffold to create a synergistic effect. For example, a scaffold

may employ mechanical cues from its structure and biochemical signals from surface functionalisation to direct the differentiation and behaviours of MSCs[53–56]. This approach aims to mimic the complex signalling environment of the natural tissue, hopefully improving the functionality and integration of engineered tissue. These integrated systems are particularly promising for applications in complex tissue regeneration, where the coordinated development of multiple cell types and formation of intricate tissue architectures are required.

1.1.1 Biomaterial Scaffold Design

There are many factors that must be considered when designing a biomaterial scaffold in order to ensure it is suitable for a specific function. An ideal scaffold must not only be biocompatible and biodegradable, but also precisely engineered to mimic the ECM of a specific tissue. Its mechanical properties, such as elasticity and strength, are crucial, and influence cell behaviours like adhesion, migration and differentiation, so can play a crucial role in dictating the regeneration process[47,50,51,57]. In addition, these properties are critical, to ensure that the material is able to withstand any forces that a tissue experiences *in vitro*, allowing the scaffold to support the tissue until regeneration is complete. Porosity is also a critical attribute of a scaffold for several reasons; allowing for cell migration in order to populate the scaffold entirely, allowing for transport of nutrients and waste during regeneration, and ensuring that sufficient vascularisation can be achieved in order for regenerated tissue to be functional and sustainable[58–61]. Once a biomaterial scaffold is implanted, it must degrade appropriately. There should be no cytotoxic degradation by-products, and the rate of degradation should be suitable to allow for the gradual transfer of the mechanical load onto the regenerated tissue, while simultaneously maintaining its ECM-like structure.

Tissue engineering and biomaterial scaffolds hold great promise in addressing the challenges currently faced in many current medical approaches to replacement of lost or diseased tissues. By combining principles from engineering, materials science and biology, tissue engineering offers solutions that overcome the limitations of standard medical approaches.

1.2 The Oesophagus

The oesophagus is a muscular tubular organ that transports food and liquids from the mouth to the stomach. The oesophagus extends distally from the pharynx to the stomach, typically measuring 25-28 cm in adults, and can be divided into three distinct sections; the cervical oesophagus, including the upper oesophageal sphincter (UES), the thoracic oesophagus, which includes the oesophagogastric junction (OGJ) and the abdominal oesophagus (see **Figure 1.2**). While typically collapsed, the oesophageal lumen can expand to up to 2 cm to allow passage of a swallowed bolus[62–64].

The oesophageal wall comprises distinct concentric layers; an outer longitudinal muscular propria, a submucosal layer, and an inner mucosal layer lining the lumen (see **Figure 1.3**). Unlike the rest of the gastrointestinal (GI) tract , the oesophagus lacks a serosal layer, and instead has an adventitial layer which is composed of loose connective tissue, which connects the oesophagus to surrounding structures.

The oesophagus mucosa can be further divided into three sublayers; the epithelium, the lamina propria and the muscularis mucosae. The epithelium is the innermost layer and is lined with a non-keratinised stratified squamous epithelium which provides a protective barrier against mechanical damage and pathogens. Beneath the epithelial layer is the lamina propria, which is a connective tissue layer consisting of fibroblasts, myofibroblasts, pericytes, smooth muscle cells and MSCs[65–67]. Mucosal fibroblasts

play a crucial role in maintaining the structural integrity of the tissue ,producing ECM components including collagen and elastin. Finally, the muscularis mucosa is a thin layer of irregularly arranged smooth muscle beneath the lamina propria which extends through the entire GI tract[68]. The muscularis mucosa helps in local movement of the mucosa, aiding in the transport of mucus and contents of the lumen[62,69].

The submucosal layer is a dense connective tissue layer containing larger blood vessels, nerves and glands. These glands secrete mucus, which lubricated the lumen and protects the epithelium from abrasive food particles and gastric contents. The submucosal layer supports the overlaying mucosa and muscularis propria, providing a scaffold for blood and lymphatic vessels which are essential for nutrient delivery and immune responses[70].

The muscularis propria of the oesophagus consists of two distinct layers; an inner circular layer and an outer longitudinal layer, which function together to produce peristaltic contractions. The composition of the muscle in the cervical oesophagus is mainly striated (voluntary), and mainly smooth (involuntary) in the thoracic oesophagus[63,64]. Voluntary swallowing occurs in the cervical section, followed by involuntary peristalsis in the thoracic and abdominal regions actuated by the smooth muscle[71].

Fibroblasts are a pivotal cell type within the lamina propria of the oesophageal mucosa. These cells are responsible for synthesising and remodelling the ECM as well as having a key role in tissue repair and homeostasis[72,73]. Fibroblasts secrete ECM components such as collagen, elastin and proteoglycans which contribute to the mechanical properties of the mucosal layer. This is particularly important in the

oesophagus, where flexibility and resilience are needed to accommodate the passage of food.

Furthermore, these mucosal fibroblasts are involved in wound healing and tissue regeneration. In response to injury, fibroblasts can proliferate and differentiate into myofibroblasts, a more contractile form that aids in wound closure[67,74]. They also produce cytokines and growth factors that regulate immune responses and recruit other cell types needed for tissue repair, such as macrophages[23,75,76].

In the context of tissue engineering, replicating the complex cellular composition and layered structure of the oesophagus is essential for developing functional tissue replacements. Scaffolds must support the growth and function of key cell types, including epithelial cells and mucosal fibroblasts. The inclusion of fibroblasts in engineered constructs can enhance ECM production and remodelling, facilitating the integration and functionality of an implanted scaffold. Additionally, understanding the specific roles of different cell types, such as mucosal fibroblasts in ECM production and wound healing, helps in designing scaffolds that mimic the native tissue environment more closely, improving the outcomes of tissue engineering efforts.

By addressing these cellular and structural considerations we can create biomaterials that not only restore the physical structure of the oesophagus but also support its dynamic biological functions. This approach is crucial for successful tissue regeneration and the long-term success of engineered oesophageal tissues.

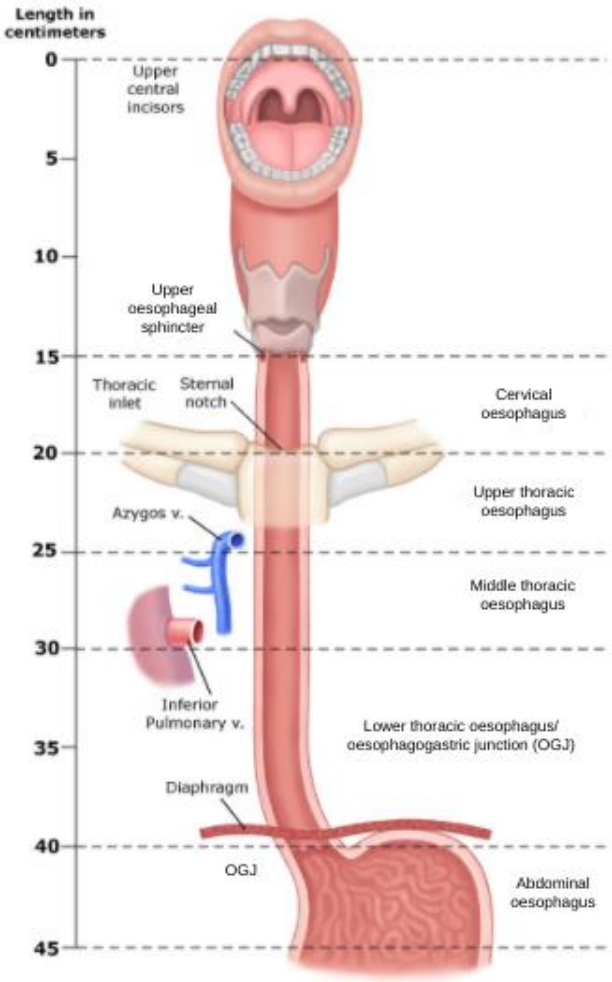

Figure 1.2 Illustration of the human oesophagus[63]

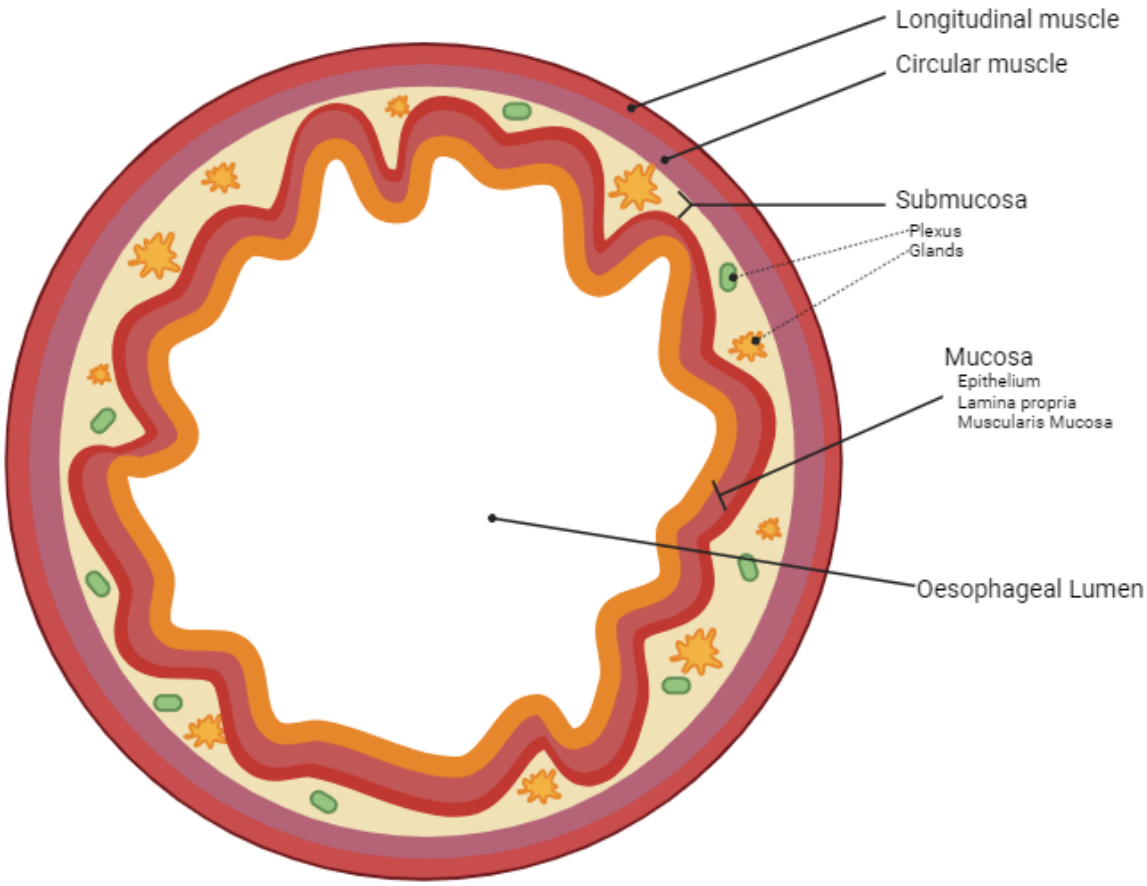

Figure 1.3 Diagram showing the layers of the oesophagus.

Created with BioRender.com

1.2.1 The Need for Oesophageal Repair Strategies

Oesophageal cancer is the eighth most prevalent cancer globally, sixth leading cause of cancer-related deaths, posing significant treatment challenges due to the limited regenerative capacity of oesophageal tissue[77–79]. This lack of regenerative capacity is one factor that leads to a five-year survival rate as low as 12.4 %[80,81]. Poor diet, tobacco use, Barrett's oesophagus and low socioeconomic status have all been linked to a higher risk of certain oesophageal cancers, with global cases rising from 31,000 in 1990 to 473,000 in 2017[82,83]. The standard treatment for oesophageal cancers typically involves oesophagectomy, often with concurrent radiotherapy[78]. Post-oesophagectomy, further surgery is required in order to restore the function of the tissue. Current restorative surgeries are highly invasive and have a major impact on the quality of life of a patient. There are several other conditions which can lead to oesophageal dysfunction which also require surgical repair, such as oesophagitis, refractory chronic strictures, burns, perforations and other injuries.

Oesophageal tissue is non-redundant, if a significant portion of it is lost there is no other mechanism for its function to be performed, and does not have the ability to regenerate, meaning that post oesophagectomy, or if there is significant structural damage to the tissue, surgical repair or replacement must be carried out in order to restore function to the organ. Typically, donor tissue is taken from somewhere along the GI tract. The most commonly used replacement method is gastric conduit, in which the stomach is pulled up and connected to the remaining oesophagus in order to close the gap[84–87]. However, if the stomach is not suitable, the colon or duodenum will be used to harvest donor tissue[88–90]. Additional methods for oesophageal reconstruction include; omental wrapping[89,91], deltopectoral and pectoralis major myocutaneous flaps[92,93].

All methods of oesophagostomy and conduit reconstruction are associated with not-insignificant risks including; anastomotic leakage, pneumonia, arrhythmia, delayed gastric emptying, dysphagia and vomiting[94–97]. The introduction of intestinal flora into the cervical region following duodenal or colonic conduit installation can also lead to severe infection[92]. In addition to the complications and patient morbidity associated with these procedures, the harvesting of donor tissue is, in essence, a second surgical procedure that comes with its own set of risks and potential complications, as well as the loss of tissue affecting function of that area[5,98].

1.2.2 Replacement Materials for the Oesophagus

1.2.2.1 Synthetic Materials

Several synthetic materials have been explored as replacements for lost oesophageal tissue. Polytetrafluoroethylene ((PTFE)-Teflon) patches have been used to replace oesophageal wall in Wistar rats and dogs successfully, but these have not been used in clinical practice[99,100]. Polyethylene terephthalate ((PET)-Dacron) and silicone replacement materials have also been investigated, but similarly have not made it to clinical use due to issues with biocompatibility, high infection rates, anastomotic leakage and strictures[101–103]. While these materials are able to restore structural continuity, they do not exhibit bioactivity, and so do not encourage cellular migration, differentiation, proliferation and vascularisation, so do not lead to native tissue regeneration in the site.

1.2.2.2 Natural Scaffolds

Decellularised ECM (dECM) has been established as an excellent candidate for biomaterial scaffolds due to the fact that it excellently mimics the cell's native environment including mechanical and biological cues[104]. ECM properties differ between different tissues, and so different dECM are suitable for different tissue

engineering scaffolds. Several dECM materials have been investigated for oesophageal tissue engineering with varying degrees of success[104–106].

Small intestinal submucosa ECM (SIS) has been successfully used as a replacement material for oesophageal tissue, but was not able to lead to complete epithelialization after 35 days, and there was a limit to the size of defect that could be regenerated using this scaffold to result in functional tissue[6,7,107].

Urinary bladder ECM (UBM) combined with host skeletal muscle cells, with have also been investigated with moderate success[105,108]. However, these scaffolds were only successful when combined with muscle cells, and alone do not trigger cell reorganisation to generate new tissue.

In general, ECM as a biomaterial scaffold has many advantages; it provides excellent physical and biological cues to cells, exhibits superior biocompatibility and does not trigger an immune response. However, ECM scaffolds are widely variable, have poor mechanical strength once they are decellularized, and cannot be tailored to a specific application. In addition, while some tissues' ECM have an organised and aligned structure, these are difficult to maintain during processing and implantation. Many tissues do not require ECM alignment during normal function, this can be highly beneficial during tissue repair, as it can enhance the migratory capacity of the cells repopulating the scaffold, speeding up revascularisation and tissue regeneration[19].

1.2.2.3 Synthetic Biomaterial Scaffolds

Biomaterial scaffolds are materials that are specifically engineered to enhance tissue regeneration[14,15]. These materials are distinct from the synthetic materials used to restore structural integrity after tissue loss or injury. These scaffolds are designed with the aim of restoring not only anatomical form, but also to actively encourage cellular

migration, differentiation and proliferation as well as vascularisation, which can lead to the deposition of native ECM and tissue to restore function as well as form to the area. One advantage of synthetic scaffolds over natural scaffolds is that they can be tailored to specific applications so that their mechanical properties, surface chemistry and degradation behaviours can be engineered to maximise their suitability for a specific application.

Examples of synthetic scaffolds that have been investigated for use in oesophageal tissue engineering include; poly(L-lactide-co-caprolactone) (PLLC) nanofibrous membranes functionalised with fibronectin or collagen, which supports fibroblast, epithelial cell and smooth muscle cell adhesion and proliferation[109–111], poly(3-hydroxybutyrate-*co*-3-hydroxyvalerate) (PHBV) nanofibres functionalised with gelatin supported oesophageal epithelial cell growth, but the gelatin impacted the long term properties of the scaffold unfavourably[109]. Aligned poly(lactic-co-glycolic acid) (PLGA) was combined with decellularised ECM to improve its material properties and induce directional cell growth, but when implanted *in* vivo, the PLGA fibres caused a foreign body reaction[112].

A successful tissue engineered solution to oesophageal repair could overcome many of the problems associated with current surgical methods; there would be no need for donor tissue to be harvested, they could be tailored to the exact size requirements for each reconstruction, and would remove the risk of an adverse immune response. Some of the most successful biomaterial scaffolds that have previously been investigated have been synthetic electrospun scaffolds with highly aligned fibres[109,112,113].

1.3 Electrospinning

Electrospinning is a versatile material production technique used to produce non-woven fibrous sheets using a strong electric field to draw ultrathin fibres from a viscoelastic fluid. Traditional spinning methods, which typically use mechanical drawing or shearing, are limited in their ability to produce nano-scale fibres. However, modern electrospinning can produce fibred with diameters below 1 nm[114], although they more commonly produced in the range of 10 - 300 nm.

The highly tailorable nature of electrospun materials and suitability for use with a wide range of synthetic, natural, biodegradable and non-degradable polymer and blend melts and solutions means that electrospun materials are useful in a wide range of applications including; filtration membranes[115–117], protective clothing[118,119], UV shielding[120], proton exchange membrane (PEM) fuel cells[121] and drug delivery systems[122,123].

The versatility of electrospinning and its adaptability to various materials have led to a growing interest in the field. Between 2019 and 2022, the number of research papers and reviews on electrospinning published more than doubled [124]. Electrospun fibres have garnered significant interest in the field of tissue engineering and regenerative medicine (TERM), as they can be tailored to produce biomaterial scaffolds that closely mimic the fibrous 3D structure of the ECM, which can be used to influence cellular behaviour and direct tissue regeneration[125,126].

1.3.1 The Process of Electrospinning

Electrospinning was demonstrated as early as 1887 by Charles V Boys, who reported a method for spinning a viscous liquid by connecting it to an electrical supply and collecting a sheet of fibres on a conducting surface nearby[127].

To produce electrospun fibres, the primary components required include a pump, a spinneret (such as a needle) and a grounded conductive collector (illustrated in **Figure 1.4**). During the process, a high voltage is applied to the spinneret, and a polymer solution is fed through it. This causes a charge to accumulate in a droplet of the solution, creating a potential difference between the charged droplet and the grounded collector. Initially, the droplet maintains a spherical shape due to surface tension. Upon reaching a critical voltage, the surface tension is overcome by the localised charges within he droplet, causing it to deform into a conical shape known as the Taylor cone (see **Figure 1.5**). This phenomenon is named after Sir Geoffrey Taylor, who modelled its mechanics in 1964[128]. When the critical voltage is surpassed, the localised charges overcome the surface tension and a charged polymer jet is expelled from the tip of the cone[124,129]. Initially, the jet travels linearly towards the grounded collector for a short distance before bending instability causes the jet to whip and stretch resulting in a decreasing diameter until the solvent evaporates, leaving behind a solid fibre deposited on the grounded collector (see **Figure 1.5D**)[130–132].

The electrospinning process allows for a high level of control over fibre properties such as fibre diameter, porosity, elasticity and fibre alignment. For tissue engineering applications, fibre properties can be optimised to mimic the native ECM of specific tissues, to promote cell attachment, proliferation and differentiation.

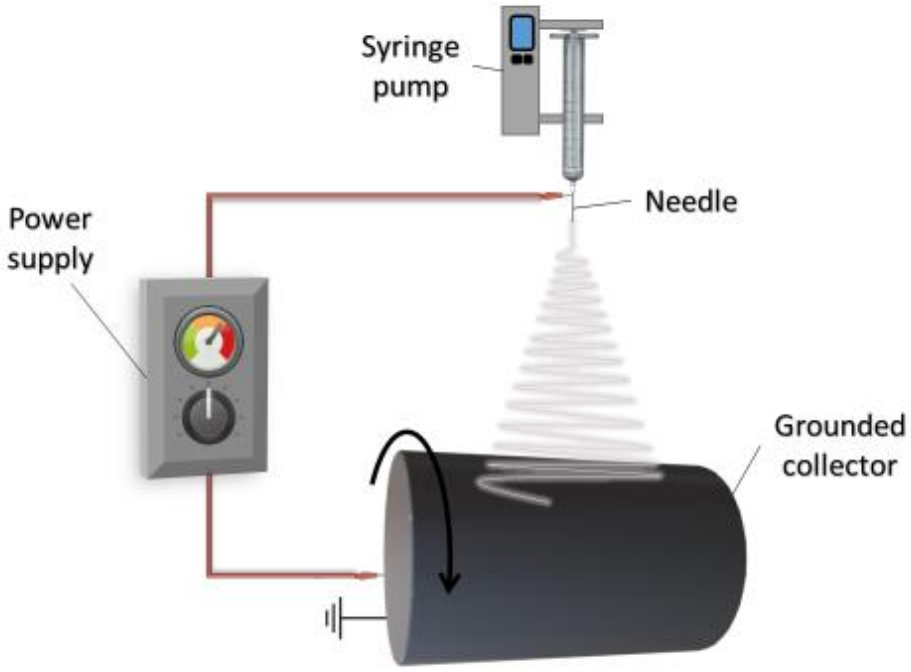

Figure 1.4 Schematic of an electrospinning setup with a rotating mandrel collector. The essential equipment for electrospinning includes a power supply, which applies a high voltage to a spinneret-typically a blunt-tip needle- and a grounded collector for fibre collection. A syringe pump is commonly used to control the flow of the solution. Various stationary and rotating collectors can be used, which influence fibre orientation.

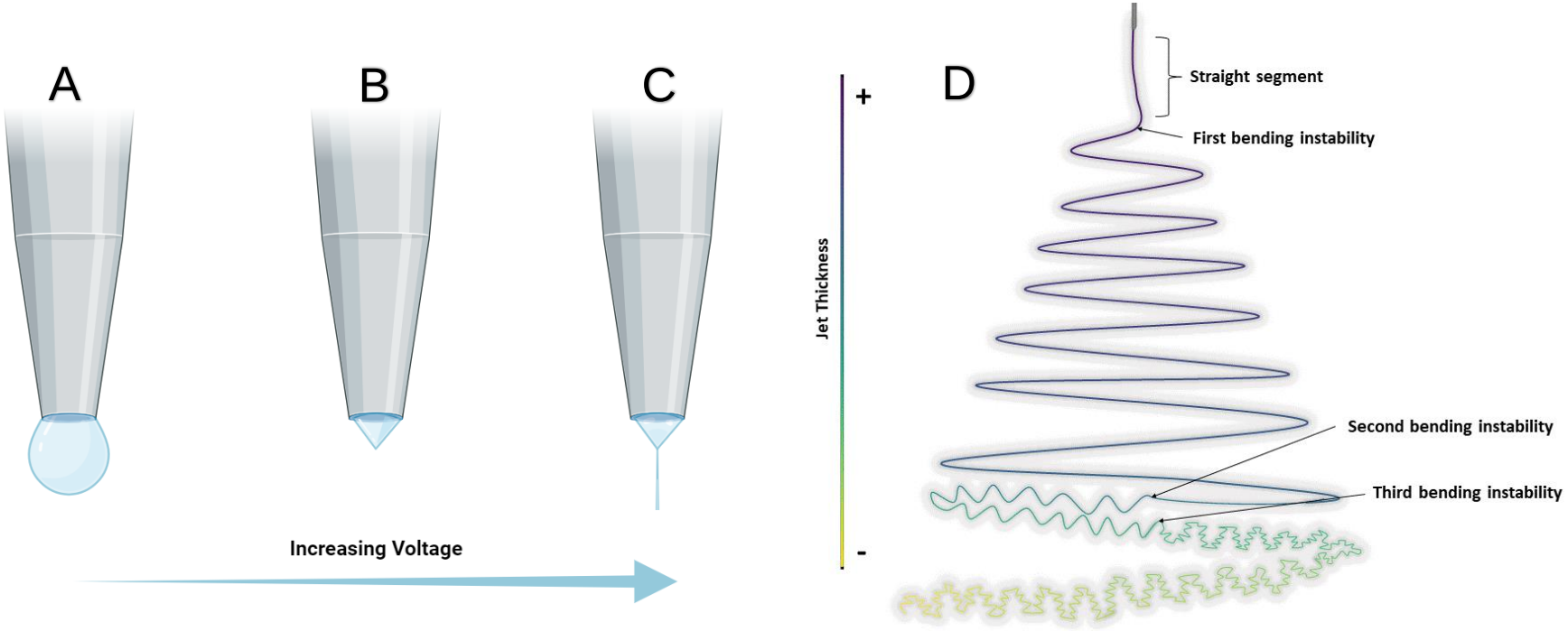

Figure 1.5 Taylor cone formation and jet path. When a droplet of solution forms at the tip of a blunt needle it will naturally form in a spherical shape due to surface tension (A). When a voltage is applied to the needle, a charge will accumulate in the droplet. Once a critical voltage is reached, the charge built up in the droplet and the potential difference between the droplet and the grounded collector will cause it to form a Taylor cone (B). When the applied voltage surpasses the critical voltage, the charges in the droplet will overcome the surface tension, and a jet of solution emerges from the cone, travelling towards the grounded collector (C). This phenomenon was described by Sir Geoffrey Taylor in 1964, and is the basis of electrospinning. Once a jet has left the Taylor cone it travels towards a grounded collector. During its journey, the jet undergoes whipping and stretching, causing its diameter to decrease gradually (D). Finally, the liquid evaporates, leaving behind a solid fibre.

1.3.1 Variables Affecting Electrospun Fibre Morphology

The electrospinning process is affected by a wide range of variables. An understanding of these factors is essential for producing fibres with the desired properties and characteristics for a specific application. Some of the factors affecting fibre formation are under the control of the operator, such as the polymer concentration, flow rate, applied voltage and collector, while others are dictated by environmental factors or inherent properties of the spinning solution, such as ambient temperature and humidity[133].

The flow rate of the spinning solution is crucial for maintaining the stability of the Taylor cone. An optimal flow rate ensures continuous fibre production. An excessively high flow rate can lead to defects such as beading and flattened fibres, as there may not be sufficient time for the solvent to evaporate before the jet reaches the collector. However, the flow rate needs to be sufficient to replace the solution being ejected. Within the optimal range, higher flow rate results in thicker fibres with higher porosity, and reduced flow rates can produce thinner fibres[134].

The voltage applied during the spinning process directly influences the electrostatic forces involved in fibre formation. Higher voltages can produce a wider jet and larger fibres due to increased electrostatic repulsion and mass flow rate within the jet[133,135]. The voltage also determines the position of the Taylor cone, with excessively high voltages leading to beading defects as the fibre is ejected from within the needle tip, which leads to beading defects in the resulting fibres[133,135,136].

The distance between the spinneret and collector affects the available time for the jet to stretch and solidify. Increasing this distance generally leads to fibres with smaller

diameters, but only up to a critical point, beyond which the jet may solidify before reaching the collector[137,138].

Higher polymer concentration, and consequently viscosity, typically results in larger fibre diameters due to increased cohesion and entanglement between polymer chains, which opposes jet elongation[134,135,139]. Polymer concentration also affects fibre morphology. For any polymer solution there is a critical concentration where there is sufficient chain overlap to produce uniform fibres[137,139]. If the concentration is too low or too high, it is difficult to form a stable Taylor cone and jet, and excessive beading defects may occur, or fibres will not form at all.

Fibre diameter can also be affected by adjusting the solution conductivity. This can be achieved by the addition of salts, such as KCL or NaCl, which can increase the droplet surface charge and result in a thinner jet and fibres with smaller diameter[138,140].

Ambient temperature and humidity can also affect the electrospinning process. These primarily affect the solvent evaporation rate[141,142]. High humidity leads to thinner, more variable fibres due to slower solvent evaporation, which allows time for more stretching of the jet, while low humidity results in thicker fibres, as the jet solidifies more quickly. The interaction between humidity and the hydrophilicity of the polymer also plays a significant role in the process, where hydrophobic polymers with develop highly porous structures in humid environments[143]. High temperatures affect the solution's viscosity, while simultaneously influencing the solvent evaporation rate, both of which affect the resulting fibre diameter. These ambient factors are much more difficult to control, so must be understood in order to ensure they do not interfere with the process.

There are a range of collector designs for electrospinning which can determine fibre morphology and orientation. For example, a stationary collector typically results in a

non-aligned mesh of fibres, whereas a rotating collector can be used to produce aligned fibres and simultaneously reduce fibre diameter through mechanical stretching[144].

Controlling these variables allows for the production of highly tailored fibre morphologies, enabling the creation of highly specialised materials suited for specific applications.

1.4 Polycaprolactone for Biomaterial Scaffolds

Polycaprolactone (PCL) is a linear aliphatic thermostatic polymer, with high biocompatibility, hydrophobicity and a semi-crystalline structure. PCL is prepared by ring opening polymerisation of ε-caprolactone (see **Figure 1.6**).

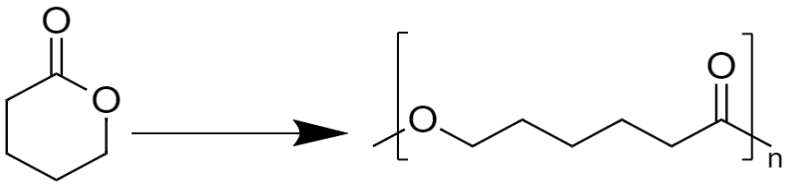

Figure 1.6 Ring-opening polymerisation of ε-caprolactone to form polycaprolactone

The U.S food and drug administration (FDA) approval of several surgical implants and drug delivery devices made from PCL highlights its significant role in tissue engineering and regenerative medicine[145–147]. Electrospun PCL has been investigated as an implantable biomaterial for several applications due to its favourable mechanical properties and degradation kinetics including; tissue engineering of tendons[148], vasculature[149–153], nerve tissue[154] and retina[155,156], wound healing[157–159], dentistry[160,161] and drug delivery[162].

PCL degrades over a period ranging from several months to several years, depending on environmental conditions and production processing. Its degradation involves hydrolysis on both aerobic and anaerobic conditions by lipolytic enzymes such as lipase and esterase, found in various microorganisms like *Firmicutes, Proteobacteria, Penicillium, Aspergillus and Clostridium*[163]. The crystallinity of the polymer significantly affects the rate of biodegradation, with polymers with high crystallinities degrading at a significantly lower rate[164]. This rate can be tailored by blending PCL with other synthetic polymers and carbohydrates, allowing for controlled degradation process suitable for various medical applications[165,166].

In addition to being biocompatible and biodegradable, PCL has highly tailorable mechanical properties depending on processing parameters, making it very useful in the field of tissue engineering and biomaterials.

1.4.1 Electrospinning Polycaprolactone

There are a wide range of parameters that have been successfully used to produce electrospun fibres from PCL. Some recent examples are summarised in **Table 1**.

The concentration of PCL is a critical factor in determining the fibre diameter, lower concentrations typically lead to thinner fibres. Higher PCL concentrations increase solution viscosity, impacting jet stability and fibre diameter. While typically leading to thicker fibres, with the right solvent and processing conditions, thinner fibres are also possible.

The choice of solvent system impacts the solubility of PCL and evaporation rate. Solvents can be mixed to achieve a balance between solubility and volatility and to control fibre morphology. Highly volatile solvents like chloroform and acetone evaporate rapidly, leading to faster solidification of the jet and thicker fibres. However,

lower volatility solvents like DMF evaporate at a slower rate, which can result in fibres that are not fully solidified before they reach the grounded collector, potentially causing flattened fibre morphologies[133,167].

Higher applied voltages can stretch the jet more, potentially producing thinner fibres[150,168]. However, excessively high voltages can affect the fibre uniformity and cause excessive beading, due to affecting the Taylor cone formation[135,136,169].

The desired properties of PCL fibres (mechanical properties, porosity, fibre diameter etc.) depend on their end-use. Optimisation of each production parameter is crucial to tailor the properties of the fibres for specific applications. It is important to note that these parameters are often interdependent, and their combined effects on fibre properties can be complex. The production parameters need to be optimised based on the specific application and desired properties. For tissue engineering scaffolds, parameters can be optimised for enhanced cell attachment and migration and differentiation, with smaller fibre diameters, fibre alignment and elasticity being key considerations.

Table 1.1 Parameters used for PCL electrospinning in published literature

Reference	Concentration/ (% w:v)	Solvent System (v:v)	Voltage (kV)	Tip-Collector Distance (cm)	Charge Density (kV/cm)	Flow Rate/ (mL/h)	Needle Gauge	Speed of mandrel rotation (rpm)	Average Fibre Diameter (nm)*
Li *et al.*[170]	14	DMF/ THF 1:1	12	20	0.6	0.4	18	-	700
Nottelet *et al.*[153]	15	Chloroform/Ethanol 7:3	20	20	1	12	21	4500	200
Piskin *et al.*[171]	15	Chloroform/DMF 1:1	13	10	1.3	-	-	-	250
Wu *et al.*[152]	10	Chloroform/DMF 10:1	18	15	1.2	0.4	21	300	300
Zhu *et al*.[151]	20	Chloroform/DMF 2:1	20	10	2	1	20	700	100
Ma *et al.*[172]	10	Chloroform/ DMF 70:30	15	15	1	0.5	27	1000	200
Liverani *et al.*[173]	10	DMF/ Methanol 70:30	15	11	1.4	0.4	23	500	1600
Kim *et al.*[35]	8	Methylene Chloride/ DMF 80:20	18	20	0.9	2	-	-	760
Gümüşderelioğlu *et al.*[158]	12	DMF/DCM 1:1	22.5	35	0.6	1	20	-	284
Wang *et al.*[174]	14	Chloroform/ DMF 70:30	20	20	1	-	-	-	300

Metwally *et al.* [175]	12	Chloroform/DMSO 90:10	12	15	0.8	0.5	-	-	1900
Seddighian *et al*.[176]	12	Chloroform/DMF 3:1	17	17	1	1	21	350	320
Valerini *et al.* [177]	12	DMF/Chloroform 2:8	25	17	1.5	4	13	-	1830
Karakucuk [178]	-	HFIP	13	15	0.866	3	-	100	1340
Augustine *et al.* [179]	15	Acetone	18	15	1.2	1	21	-	1672
Rabionet *et al.*[180]	7.5	Acetone	7	15	0.466	6	18	-	295.12
Yao *et al.* [181]	8	DCM/DMF 60:40	13	15	0.866	3	18	100	200
Hanas *et al.* [182]	8	Chloroform/Methanol 3:1	-	12	-	0.2	-	-	400
Basar *et al.* [183]	8	Chloroform/Methanol 4:1	20-25	18	1.1-1.4	1.08	-	-	150
Singh *et al.* [184]	15	Acetic Acid/Formic Acid 1:1	15	11	1.4	0.4	21	500	122

*****Some studies reported a range of parameters used. In these cases, the parameters that resulted in the smallest fibre diameters are reported here. If a range of fibre diameters were reported, the smallest diameter is included

1.4.2 Post-production processing of Electrospun PCL Fibres

Electrospun PCL fibres are biocompatible, biodegradable and have excellent mechanical properties. However, their low bioactivity and hydrophobicity has previously limited their usage. These qualities are not ideal for tissue engineering applications, as they prevent adequate cell adhesion and do not actively encourage tissue regeneration. To address this, a range of post-production modifications have been investigated to modify the fibres making them more suitable for tissue engineering applications.

Functionalising the surface of the PCL with ECM proteins and bioactive molecules can be used to increase the bioactivity of the biomaterial. A variety of molecules, including fibronectin, collagen, laminin, bovine serum albumin (BSA), hydroxyapatite and RGD peptides have been successfully utilised to increase cell attachment to PCL biomaterial scaffolds[173,185–190]. Various methods of chemically grafting these bioactive materials onto the surface of various PCL scaffolds including; thiol-halogen and carbodiimide “click” chemistry, glutaraldehyde aminolysis, NaOH hydrolysis, and EDC/NHS catalysed coupling.

Coaxial electrospinning has also been investigated as a method of incorporating bioactive substances such as collagen and silk fibroin into PCL fibres[156,187,191,192]. This can produce fibres with a core of collagen or fibroin, which are gradually released as the PCL degrades, or an outer shell which promotes initial cell attachment. This method offers a controlled release mechanism, which can present different bioactive molecules as the scaffold degrades and interacts with the *in vivo* environment.

A more direct approach involves blending bioactive molecules with the polymer solution before electrospinning. While this method is straightforward, this technique

poses significant challenges; it results in a limited number of molecules being presented on the fibre surface and requires that the bioactivity is not affected by the electrospinning process, which can be difficult given the nature of the solvents typically used for electrospinning[193].

Alternatively, or in addition to, the addition of bioactive molecules, treatments such as plasma treatment, alkaline hydrolysis and the introduction of micro – scale topography have been explored. These methods can be used to introduce functional groups or increase surface wettability and roughness, which can play a crucial role in increasing cell adhesion and directing cell migration and alignment, further improving the electrospun PCL fibres suitability for tissue engineering applications[155,172,188,194–196].

1.5 Fibroblasts in Tissue Engineering

Fibroblasts are cells derived from the mesenchymal lineage and are present in nearly all bodily tissues which play a vital role in tissue homeostasis and repair[72,197,198]. During normal tissue homeostasis, they maintain the ECM and are critical in supporting the stem cell niche in several tissues[38,74]. Fibroblasts also secrete regulatory molecules and crosstalk with other cell populations involved in tissue healing and regulation mechanisms[199,200].

Fibroblasts are among the first cells to migrate to a wound site through contact guidance[201]. They migrate along ECM fibres, particularly fibrin, along fibronectin binding sites through integrin mediated binding sites, which mediate cell-ECM interactions[36,72,202]. Once at a wound site, fibroblasts secrete key ECM components- including collagen and fibronectin- to form a provisional ECM. This provisional structure forms a scaffold for cell adhesion, migration and differentiation, which are essential for tissue regeneration[72,203].

Fibroblasts secrete a variety of growth factors and cytokines- including vascular endothelial growth factor (VEGF), fibroblast growth factor (FGF), angiopoietin 1 (Ang-1) and thrombospondin (TSP)- which promote angiogenesis and vascularisation and contribute to the formation of granular tissue[46,197].

Fibroblasts are also mechanosensitive and can respond and adapt to mechanical stimuli. This allows them to modulate the ECM in response to mechanical cues, ensuring the integrity and functionality of tissues in dynamic environments[204–207].

Understanding how fibroblasts interact with biomaterial scaffolds is pivotal for designing tissue engineering strategies. An optimal scaffold not only promotes fibroblast adhesion and accelerates ECM deposition but also enhances their role in initiating angiogenesis and vascularization[39,45,46,203]. Fibroblasts are central to the development of effective tissue engineering strategies, influencing the scaffold's performance and the overall success of tissue regeneration efforts.

By harnessing the properties and capabilities of fibroblasts, tissue engineering can advance towards creating more effective and functional regenerative solutions, aligning the goals of biomaterial design with the natural processes of tissue repair and regeneration.

1.6 Conclusion

The literature consistently identifies PCL as an excellent candidate for electrospun scaffolds in oesophageal tissue applications[26,35,109,147,208]. PCL’s biocompatibility, biodegradability, and mechanical properties make it particularly suitable for creating scaffolds that can mimic the ECM of soft tissues such as the oesophageal mucosa[35,149,209]. Studies have shown that PCL can be electrospun into fibres with controlled diameters and alignments, providing topographical signals that can guide

cell growth and promote tissue regeneration. In addition, PCL scaffolds that have been functionalised with biochemical signals such as fibronectin, support the adhesion and growth of cells essential to tissue regeneration, including fibroblasts, which are crucial for ECM production and tissue repair[45,173,210–212]. Given these qualities, the aims and objectives of this thesis focus on optimising and characterising electrospun PCL fibres and evaluating their potential for oesophageal tissue engineering.

1.6.1 Aims

The aim of this study is to develop an optimised electrospun material tailored for tissue engineering of the oesophagus mucosal layer.

1.6.2 Objectives

1. To refine electrospinning parameters to produce aligned, uniform, non-beaded PCL fibres with small diameters.
2. To perform comprehensive characterisation of the electrospun PCL fibres, including describing their mechanical properties, morphology and wettability, and compare them with porcine oesophagus mucosa tissue.
3. To assess changes to the fibre morphology, wettability and mechanical properties after incubation *in vitro* under neutral (pH 7) and acidic (pH 4) conditions.
4. To functionalise the electrospun PCL with fibronectin and investigate the effect of the functionalisation on the mechanical properties, wettability and morphology of the fibres.
5. To investigate the effect of ethanol, ethylene oxide, UV radiation and gamma radiation on the mechanical properties, wettability and morphology of the PCL fibres.

6. To investigate morphological changes of primary oesophageal fibroblasts cultured on the surface of electrospun PCL sheets.
7. To add microgrooves to the surface of electrospun PCL sheets, and determine the effect of these grooves, if any, on the morphology of fibroblasts cultured on the fibre sheets.

1.6.3 Chapter summaries

The following “General Materials and Methods” chapter lays out methods that are used in more than one of the experimental chapters of the thesis. Any technique that is only used in one experimental chapter is detailed in that chapter.

This thesis includes 4 experimental chapters, which each address specific objectives that have been laid out above. The first experimental chapter (Chapter 3) describes a design of experiments (DoE) approach to optimising the concentration, solvent system, applied voltage and needle tip-collector distance used to electrospun PCL to produce smooth fibres with small diameters, as fibres with these qualities can be used to direct cell behaviour and encourage tissue regeneration. The speed of the rotating mandrel collector and the volume of polymer solution spun is also investigated. This chapter also describes the characterisation of the optimised electrospun PCL, and compares the biomaterial’s properties to oesophageal mucosa, to determine whether the material is suitable for *in vivo* implantation into the oesophagus.

Chapter 4 of this thesis describes the effect of incubating electrospun PCL fibres *in vitro* in PBS at pH 4 and pH 7 for 12 weeks in order to investigate the degradation behaviour of the biomaterial under conditions similar to the oesophageal environment.

The functionalisation of electrospun PCL fibres with fibronectin with the aim of increasing the fibres’ bioactivity, and the effect of this process on the material’s

properties is described in chapter 5. This chapter also investigates the effect of several sterilisation and disinfection treatments on the material properties of the electrospun PCL, in order to identify a suitable method of sterilisation that does not adversely affect the fibres.

The final experimental chapter (chapter 6) describes the observation of morphological changes to primary oesophageal fibroblasts after culture on electrospun PCL fibres, as changes in fibroblast morphology can indicate a change in behaviour, which may indicate a pro-regenerative phenotype. This chapter also describes the process of adding microgrooves to the surface of electrospun PCL sheets, and investigates whether these grooves have a different effect on the fibroblast morphology than the fibres alone.

The final chapter in this thesis discusses the key findings in the experimental chapters and lays out potential future work that could investigate these findings further.

2.0 General Materials and Methods

2.1 Materials

Table 2.1 Materials and suppliers

Material	Product Code	Supplier
Actin/focal adhesion staining kit	FAK100	Merck Life Science UK Ltd
AlamarBlue cell viability reagent	BUF012B	BIO-RAD laboratories Ltd
Anti-human fibronectin Alexa Fluor®488 antibody	15322090	Fisher Scientific UK Ltd
Bovine Serum Albumin	A7030	Sigma Aldrich Ltd
Chloroform	10607602	Fisher Scientific UK Ltd
D-Chloroform	87153	VWR International Ltd
Dulbecco's Modified Eagle Medium	11965092	Fisher Scientific UK Ltd
Fetal Bovine Serum	10082147	Fisher Scientific UK Ltd
Human Fibronectin	354008	Scientific Laboratory Supplies Ltd
Human Primary Oesophageal Fibroblasts	H-6272	Generon Ltd
IgG-FITC	AP504F	Scientific Laboratory Supplies Ltd
Live/Dead staining kit	15519340	Invitrogen, UK
MES Hydrate	M8250	Merck Life Science UK Ltd
N-(3-dimethylaminopropyl)-N-ethyl carbodiimide hydrochloride	39391	Scientific Laboratory Supplies Ltd
N,N-Dimethylformamide	11420034	Fisher Scientific UK Ltd

N-Hydroxy succinimide	804518	Merck Life Science UK Ltd
Paraformaldehyde	10342243	Fisher Scientific UK Ltd
Phosphate Buffered Saline	10091403	Fisher Scientific UK Ltd
Penicillin/Streptomycin	15140122	Fisher Scientific UK Ltd
Polycaprolactone	440744	Merck Life Science UK Ltd
Porcine oesophagus	_	MedMeat Ltd
Triton X-100	A16046	Fisher Scientific UK Ltd
Trypan blue	T8154	Sigma Aldrich Ltd
Trypsin-EDTA	T4049	Sigma Aldrich Ltd
Tween 20 Technical	817072	VWR International Ltd

2.2 Methods

This chapter describes general methods that are used in several of the subsequent chapters. Any methods used only in one chapter are described in the appropriate chapter.

2.2.2 Electrospinning

Post-optimisation, a 10% w/v solution of PCL was prepared in a 50:50 chloroform, dimethylformamide (DMF) solvent system. The solution was stirred for 24 hours at room temperature to ensure complete dissolution and produce a homogenous solution. 5 mL of solution was placed into two syringes, which were fitted with blunt-tip 21-gauge needles (Tong Li Tec., China). The syringes were then loaded into a TL-OMNI electrospinning machine (Tong Li Tec., China) fitted with a grounded rotating mandrel collector (Ø 9.8 cm, 18 cm wide). The needle tip of each syringe was positioned 20 cm above the surface of the collector. The solution was fed through the syringe at a rate of 1 mL/hr, and a voltage of 20 kV was applied to the needle.

Electrospinning was carried out for 8 hours to produce an adequate amount of sample for handling. The fibre sheets were then removed from the mandrel and placed in a vacuum chamber overnight to ensure there was no solvent remaining.

2.2.3 Scanning Electron Microscopy

Samples from each fibre sheet were taken from the centre of the collector where there was the thickest deposition of fibres. Samples were gold sputter coated at 20 mA for 2 minutes to produce a 15 nm thick coat using a sputter Emitech K550X sputter coater (Quorum Technologies, UK). Samples were then imaged using a Hitachi TM3030 desktop scanning electron microscope (SEM) (Hitachi Ltd., Japan), or a Zeiss EVO MA10 SEM (Carl Zeiss AG, Germany). At least 3 images at 10,000 magnification were taken of each sample.

2.2.3.1 SEM Image Analysis

Image J image processing software (National Institute of Health, USA) was used to analyse the SEM images.

Fibre diameters were measured using the Image J measure tool. At least 100 individual measurements were taken from each sample.

Fibre alignment was analysed using the OrientationJ plugin (Biomedical Imaging Group, EPFL, Switzerland). A visual representation of the fibre alignment was generated from an SEM image in the form of a colour survey, where the hue of each fibre corresponded to its degree of alignment with the dominant fibre direction.

OrientationJ was further utilised to produce a histogram depicting the distribution of fibre orientations, which showed the proportion of the fibres that were aligned with the dominant direction. This data was then plotted on a polar histogram using Python in Visual Studio (see **Appendix A** and **Appendix B**).

2.2.4 Mechanical Testing

A Bose ElectroForce 5500 (TA Instruments, USA) was used to conduct tensile testing of electrospun PCL fibres and porcine oesophagus.

For the fibres, 10 x 50 mm specimens were fixed to a cardboard jig to aid sample loading into the instrument grips (see **Figure 2.1**). The tensile grips were aligned with the inside edge of the jig, resulting in a test area of 10 x 30 mm. Initially, the grips were closed directly onto the jig, which lead to a high failure rate at the point where they made contact with the fibres. To avoid this, foam mounting tape was applied to the grips to distribute the force.

The porcine oesophagus mucosal layer was separated from the muscular and submucosal layers, and cut into 10 x 50 mm strips. These strips were then placed directly into the grips of the instrument.

Each sample was measured using digital callipers, and a preload of 0.5 N was applied. The crosshead moved at 0.1 mm/second until sample failure. Stress/strain graphs were produced for each test from the load and displacement data, and these were used to calculate the elastic modulus, ultimate tensile stress (UTS) and maximum extension (%) for each sample.

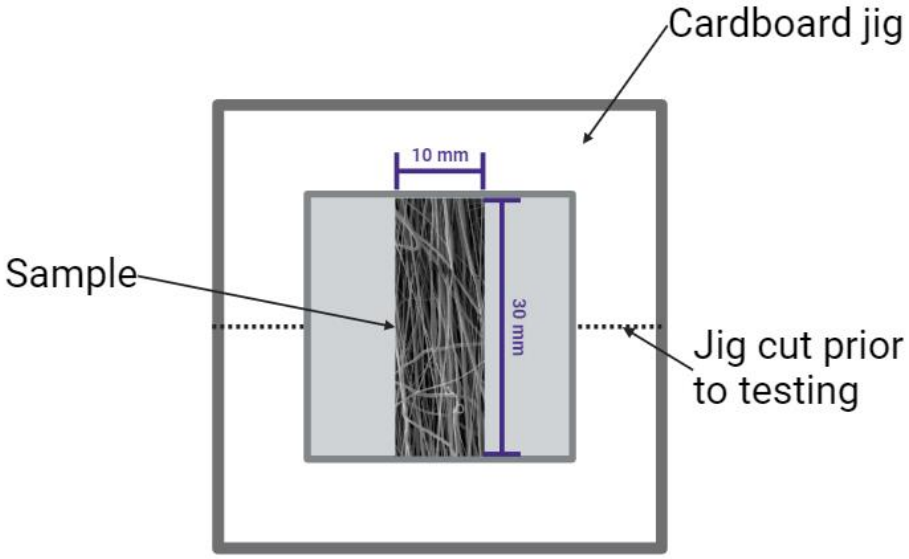

Figure 2.1 Electrospun PCL mounted for tensile testing.

2.2.5 Water Contact Angle

The contact angle of the fibre sheets and decellularised ECM (dECM) of porcine oesophagus mucosa was determined using an Attension Theta Lite (Biolin Scientific AB, Sweden). A 4µL droplet of deionised water was deposited onto the surface of each sample and the contact angle was calculated using OneAttension software. The reported contact angle was taken from six measurements of advancing and receding values measured from three samples of each material.

2.2.6 Raman Spectroscopy

Raman spectra were obtained of the PCL as obtained from the supplier, the electrospun PCL fibres, and fibronectin using a WITec alpha 300R Raman imaging microscope spectrophotometer (Oxford Instruments, UK). Raman spectra were used to determine the crystallinity of materials. This was achieved by deconvoluting the band in the 1710-1750 cm^{-1} region of the spectra, which corresponds to C=O stretching, into to peaks centred at 1724 cm^{-1} and 1732 cm^{-1}, which correspond to the

crystalline and amorphous domains[213,214]. The crystalline fraction could then be calculated using the integrated intensities of the crystalline and amorphous peaks.

2.2.7 Cell Culture

Tissue culture was conducted in a Safe 2020 class II biological safety cabinet (Thermo Fisher Scientific Inc., USA). The hoods were sterilised using 70% industrial methylated spirit (IMS) and inbuilt UV lamps. Human primary oesophageal fibroblasts were procured from Generon limited and cultured in T-175 flasks in high glucose (4500 mg/mL) Dulbecco's modified eagle medium (DMEM) supplemented with L-glutamine, 10% fetal bovine serum (FBS) and 1% penicillin/streptomycin. Fibroblasts were cultured at 37°C and 5% CO_2 until they reached 78-80% confluence. After reaching confluency, cells were detached from the flasks using Trypsin-EDTA, centrifuged, and resuspended in DMEM. Cell counting was performed using a Countess II automated cell counter (Thermo Fisher Ltd, USA). Cells were then seeded onto 6 well plates at a density of $0.5x10^6$ cells/mL. For experiments involving electrospun PCL fibres, cells were seeded onto 40 x 40 mm sections of fibre sheets lining the plates.

2.2.7.1 Live/Dead Staining

Cell viability on aligned PCL fibres after 5 days of incubation was assessed using a calcein AM/ethidium homodimer-1 (EthD-1) live/dead assay (Invitrogen, UK). The stain includes green fluorescent calcein-AM, which indicates intracellular esterase activity- indicating live cells- and ethidium homodimer-1 (EthD-1), which is a membrane impermeable nucleic acid stain and is only able to penetrate plasma membranes of dead cells. Cells were stained with a 2 µM calcein AM and 4 µM EthD-1 PBS solution and incubated at 37°C for 20 minutes After staining, the fibre sheets were carefully transferred into fresh well plates to ensure that only cells on the fibres were imaged, and any cells that had migrated onto the tissue culture plastic were not

included on the analysis. The stained cells were imaged using an FV1000 (Olympus, Germany). Image analysis was performed using ImageJ software (NIH, USA) to quantify the number of live (green) and dead (red) cells. The cell viability was then calculated as the percentage of the total cells that were live.

2.2.8 Statistical Analysis

Statistical analysis of data was performed using Prism version 10.1.2 (GraphPad Software, USA). Statistical evaluations were performed using one-way ANOVA (for three or more groups) or unpaired t-tests (for two groups). Tests were carried out in triplicate (n=3) unless otherwise reported, and all data is reported as mean ± standard deviation (SD) unless otherwise stated.

3.0 Optimisation and Characterisation of Electrospun PCL Fibres

3.1 Introduction

The goal when optimising PCL electrospinning was to minimise the fibre diameter, increase fibre alignment, and find the maximum thickness at which the sheets could be produced without affecting fibre diameter or alignment, in order to improve handleability.

3.1.1 PCL Electrospinning Parameters

Table 3.1 The range of PCL electrospinning parameters found in published literature

Variable	Range in literature	
	Min	**Max**
Concentration (%w/v)	7.5	20
Voltage (kV)	7	25
Distance (cm)	10	35
Flow rate (mL/h)	0.2	12
Needle gauge	18	27
Rotation (RPM)	0	6000

Literature review revealed a broad spectrum of parameters used by various research groups to produce electrospun PCL fibres as summarized in **Table 2.1**[175,176,178–181,183,186,191,192,208,215–217]. The variation between electrospinning set ups, combined with environmental sensitivity means that optimal conditions may vary across different laboratories. Many published studies on PCL electrospinning lack detailed documentation on the optimisation process, or do not employ a systematic approach

to parameter tuning. A significant gap in the literature is the lack of detailed optimisation processes or systematic methodologies used in many of these studies.

3.1.2 Design of Experiments

Design of experiments (DoE) provides a systematic method for studying a response that varies as a function of one or more independent variables[218]. By observing the response produced using a planned matrix of variable settings, a mathematical model can be developed to describe the effect of the variables on the response, identify the main factors and interactions that affect the response, and predict the optimal variable settings in order to produce the desired response.

The traditional method for investigating the effect of several variables on a process response is to study the effect of one variable at a time (OVAT). Unlike traditional methods, DoE assesses multiple variables simultaneously, enabling analysis of interactions and main effects that affect the response[219]. DoE is a more efficient method than OVAT, particularly when investigating complex processes with several variables that may interact with each other, such as electrospinning[220–222].

There are several types of designs that are commonly used in DoE. Designs can be broadly categorised into full factorial designs and partial factorial designs including Taguchi, Placket Burman, Box-Behnken and central composite designs[223]. Each design has unique features and applicability depending on the number of variables and the nature of the experiment. Hybrid designs, which combine elements of these standard approaches, can be tailored to specific experimental needs. The goal is to develop a mathematical model that accurately describes the relationship between variables and the response, which can then be used to predict optimal variable settings for a designed outcome.

This chapter will describe the selection of variables for the optimisation of electrospinning PCL fibres using DoE, and the interpretation of the results that lead to the selection of the optimised parameters. The process of characterising the optimised material will be described, and compared to the properties of porcine oesophageal tissue.

3.2 Methods

3.2.1 Design of Experiments

A fractional factorial design was selected to generate a set of experiments that could be used to produce a model to determine the effect of the applied voltage, solvent system, solvent-collector distance and PCL concentration on the diameter of the electrospun fibres. Minitab statistical software (Minitab LLC, USA) DoE statistical analysis was used to model the effect of individual factors, as well as the interactions of several factors on the fibre diameter. The minimum and maximum for each variable was selected based on literature review, and 6 factor levels were set for each factor (except needle tip-collector distance, which had 3 levels). The order that the experiments were run in was randomised, to eliminate the effect of any unobserved changes e.g. in ambient conditions. The average fibre diameter was then recorded for each experiment and used to construct the mathematical model. The variable settings for each experiment are shown in **Table 3.2**.

Table 3.2 PCL electrospinning optimisation experiments

Experiment #	Solvent system (Chloroform:DMF)	PCL Concentration (%w/v)	Applied voltage (kV)	Needle tip-collector distance (cm)
1	60:40	12.5	17	17.5
2	60:40	22	17	17.5
3	80:20	12.5	17	20
4	80:20	22	17	17.5
5	60:40	12.5	22.5	17.5
6	60:40	22	22.5	20
7	80:20	12.5	22.5	17.5
8	80:20	22	22.5	10
9	70:30	10	20	17.5
10	70:30	25	20	17.5
11	50:50	17.5	20	17.5
12	90:10	17.5	20	17.5
13	70:30	17.5	15	17.5
14	70:30	17.5	25	17.5
15	70:30	17.5	22.5	17.5
16	40:60	17.5	22.5	17.5
17	80:20	5	10	10
18	40:60	5	10	25
19	80:20	20	25	25
20	60:40	12.5	17.5	17.5
21	60:40	12.5	10	17.5

3.2.2 Rheometry

Solution viscosity was investigated using a rotational rheometer (Kinexus Ultra+, Netzsch GmbH, Germany) at 25 °C. Shear viscosity profiles were obtained using a double gap geometry (25mm diameter) between a shear rate of 10 and 0.1 s^{-1} over 5 minutes.

3.2.3 Electrospinning Optimisation Experiments

During the optimisation process, 13 different PCL solutions were prepared with concentrations and solvent systems according to the DoE (see **Table 3.2**). PCL was weighed and placed into the corresponding solvent system in a glass reagent bottle. The solutions were stirred for 24 hours at room temperature to ensure complete dissolution and solution homogeneity. 5 mL of solution was placed into a syringe, which was fitted with a blunt tip needle. The syringe was then fitted into TL-OMNI electrospinning apparatus (Tong Li Tec., China) fitted with a grounded rotating mandrel (Ø 9.8cm, 18cm wide) and the solution was fed through the syringe at a rate of 1 mL/hour. The needle was positioned at a specific distance from the collector according to the experiment design, and the required voltage was applied. Electrospinning was carried out for 5 hours to produce an adequate amount of sample for characterisation. The fibre sheets were then removed from the mandrel and placed in a vacuum chamber overnight to ensure there was no solvent remaining.

3.2.4 Porcine Oesophagus Characterisation

Adult porcine oesophagi were acquired from MedMeat Ltd (Manchester, UK). The mucosal layer was separated from the muscle layer and stored at -20°C until tested.

For mechanical testing, the mucosal layer was separated from the submucosal and muscle layers, which were disposed of. The mucosal layer was then cut to produce

rings, which were then sliced open to produce strips of tissue. These strips were then cut down to 3 cm x 1 cm sections for testing.

For SEM analysis, tissue was decellularised using a solution containing 1% Triton X-100 and 1% SDS. Tissue sections were placed in falcon tubes, covered with the solution and placed on a tube roller for 24 hours until a colour change to white was observed, then washed with PBS, frozen to -80°C and placed in a Lablyo Mini freeze dryer (Wolflabs. UK) for 24 hours. Samples were then gold sputter coated for SEM imaging.

3.3 Results

3.3.1 Optimisation

3.3.1.1 DoE Optimisation of Solvent System, PCL Concentration, Applied Voltage and Needle Tip-Collector Distance

21 electrospinning experiments with variable settings determined by the fractional factorial design were used to produce PCL fibres. Each fibre sheet was imaged using SEM and the average fibre diameter was determined using Image J (see **Figure 3.1**).

The average fibre diameter from each experiment was used to develop a model to describe the relationship between the variables and the fibre diameter (see **Equation 1**). A Pareto chart was created showing the standardised effect of each variable and interaction of pairs of variables on the fibre diameter (see **Figure 3.2**) and response surfaces were predicted by the model (see **Figure 3.3**). The response surfaces show that for each pair of factors there is not necessarily a linear relationship between the inputs and the fibre diameter.

PCL concentration (**B**) had the greatest influence on the fibre diameter, with a standardised effect of 9.98. Lower concentrations generally resulted in thinner fibres.

However, concentrations below 10% w/v did not reliably spin successfully (see Experiment 17 and 18 in **Figure 3.1**). 10% w/v was determined to be the optimal PCL concentration for producing the thinnest fibres.

The ratio of chloroform to DMF used in the solvent (**A**) had the next greatest effect on fibre diameter with a standardised effect of 8.88. Lowering the amount of chloroform on the solution lead to thinner fibres until a critical point of 50%. Therefore, a 50:50 chloroform: DMF solvent system was selected.

The applied voltage (**C**) and needle tip-collector distance (**D**) had a standardised effect on the fibre diameter of 4.25 and 3.73 respectively, and their interaction (**CD**) had an effect of 3.74. In addition, the effect of the interaction between the solvent system and needle tip-collector distance (**AD**) was 5.95. The applied voltage and needle tip-collector distance selected were 20 kV and 20 cm respectively, as this produced the thinnest fibres with the least variation.

The effects of the PCL concentration, solvent system, applied voltage, needle tip-collector distance, and the interactions of needle tip-collector distance, with the solvent system and the applied voltage explained 92.1 % of the variation in fibre diameter.

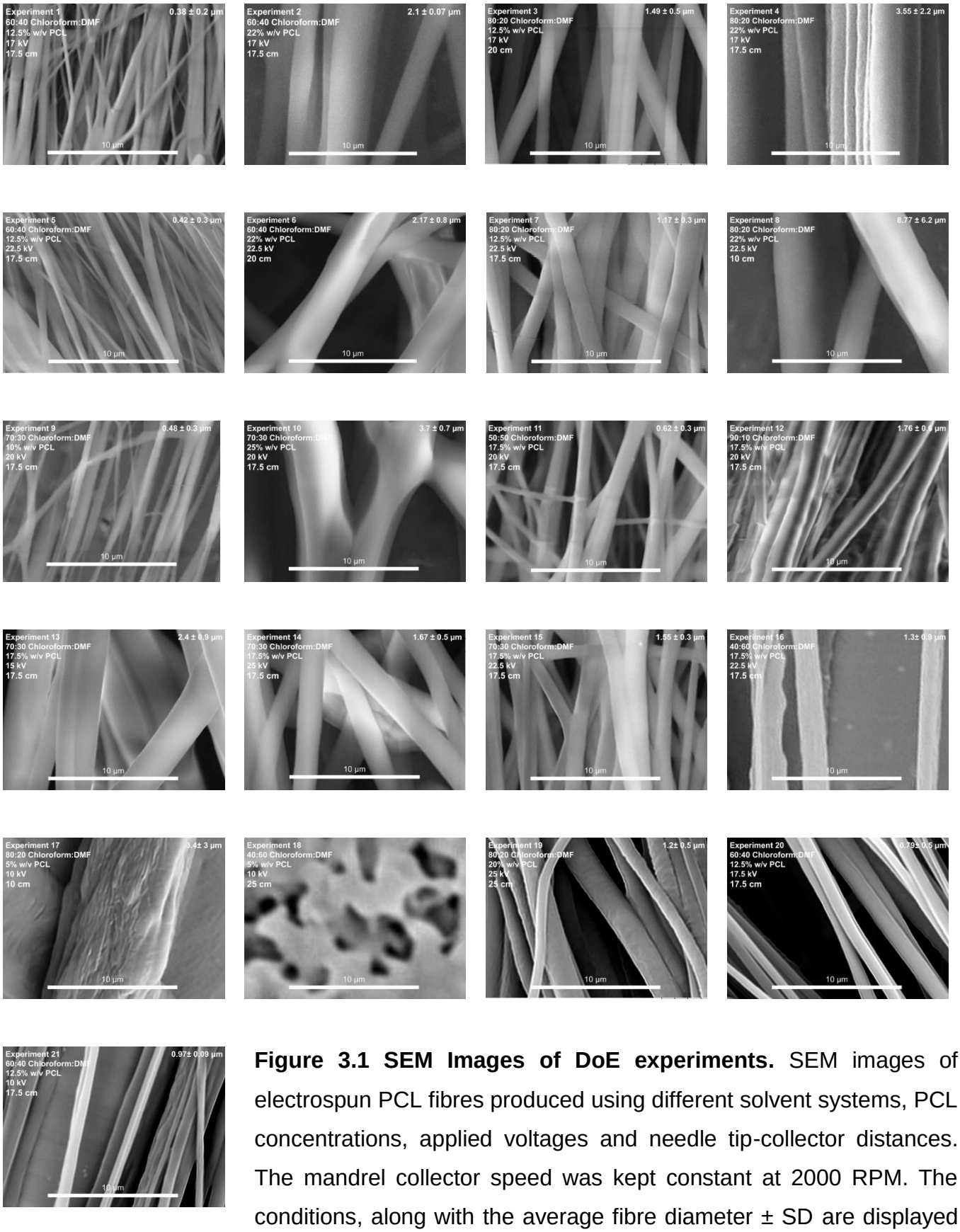

Figure 3.1 SEM Images of DoE experiments. SEM images of electrospun PCL fibres produced using different solvent systems, PCL concentrations, applied voltages and needle tip-collector distances. The mandrel collector speed was kept constant at 2000 RPM. The conditions, along with the average fibre diameter ± SD are displayed for each experiment (N=3, n=100).

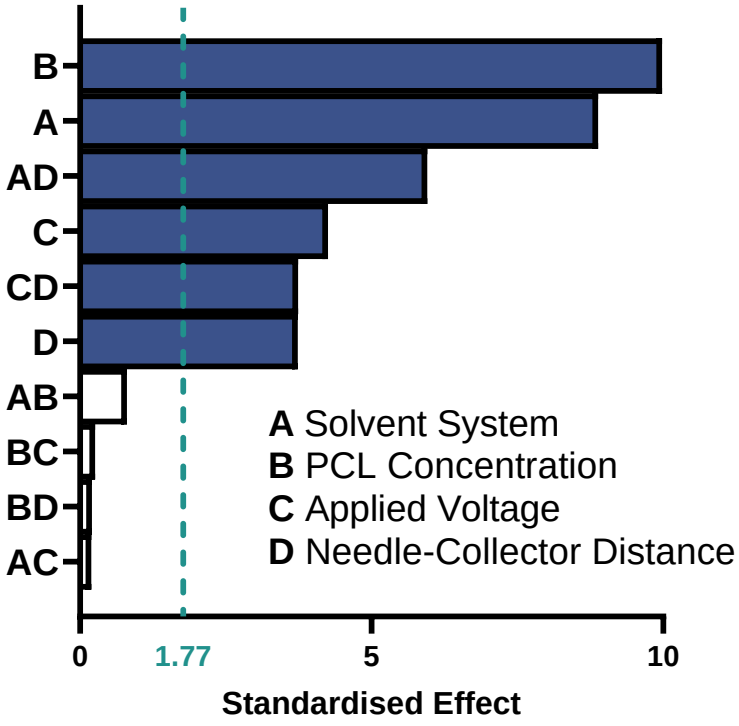

Figure 3.2 Standardised effects of variables on electrospun PCL fibre diameter. Pareto chart showing the standardised effect of each variable and interaction of pairs of variables on the fibre diameter. The reference line at 1.77 represents the point at which p=0.05. Bars that exceed the reference line represent variables which had a significant effect on the fibre diameter. (N=21, n=100).

Equation 1

$$\text{Fibre diameter } (\mu m) = -9.97 + 0.2586\mathbf{A} + 0.2111\mathbf{B} - 0.3946\mathbf{C} + 0.378\mathbf{D} - 0.01273\mathbf{AD} + 0.01940\mathbf{CD}$$

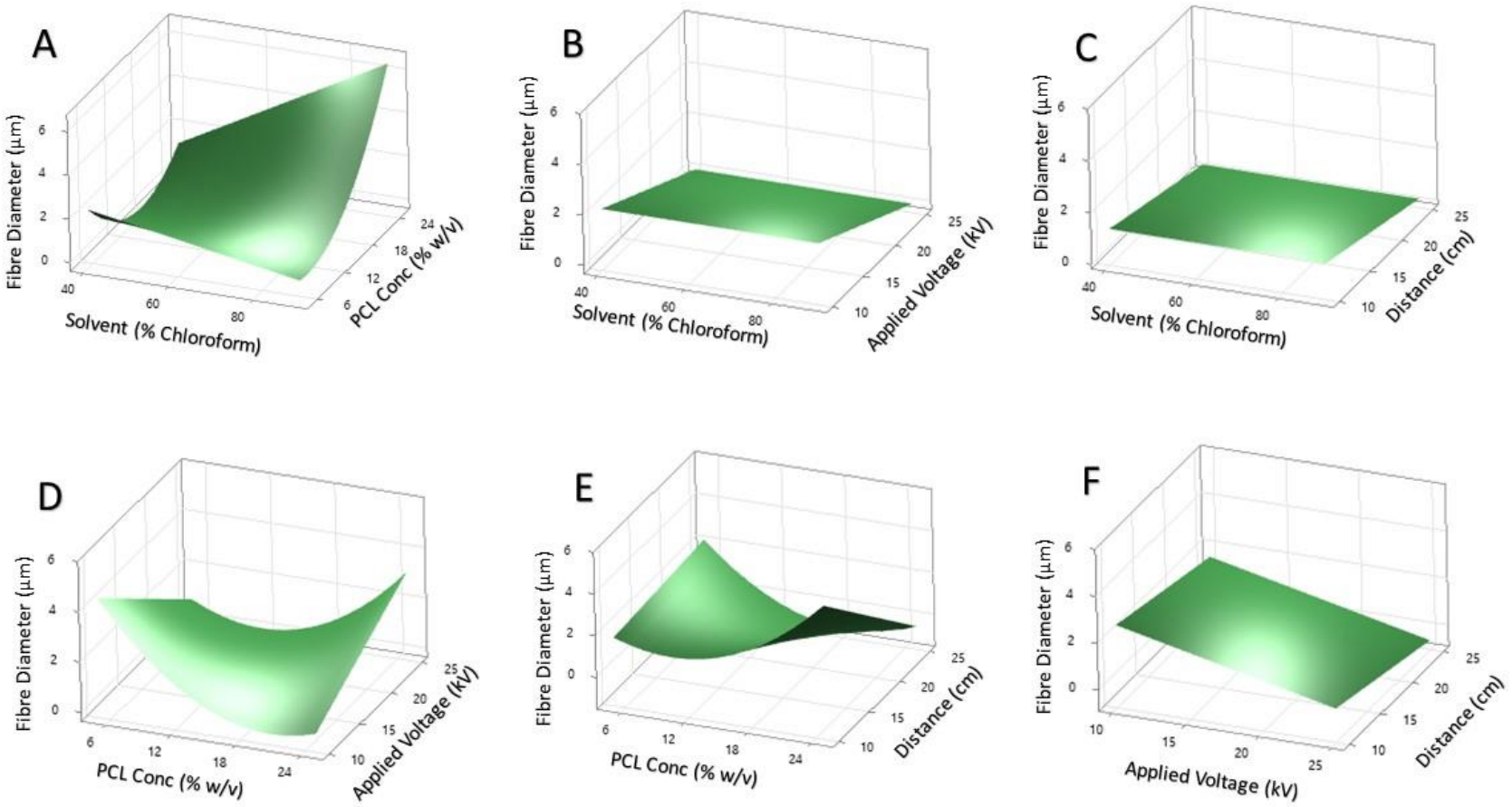

Figure 3.3 Response surface plots showing the effects of PCL concentration, solvent system, applied voltage and needle-collector distance on fibre diameter

For each surface plot there were two factors not varied. The hold value for each factor when they were not included in the response surface was as follows: voltage- 17.5 kV, distance- 17.5 cm, PCL concentration- 15 % w/v, solvent- 65 % chloroform.

3.3.1.2 Solution Viscosity

The solution parameters (PCL concentration and solvent system) had the greatest effect on the fibre diameters. Given that this was likely due to the solution viscosity, the viscosity of each solution used for the DoE optimisation was determined via rheometry (see **Figure 3.4**). The main factor affecting solution viscosity was PCL concentration, with higher concentrations resulting in higher viscosities. However, the ratio of chloroform to DMF used in the solvent system also affected the solution viscosity, with higher proportions of chloroform leading to more viscous solutions.

While chloroform has a slightly lower viscosity at 25°C than DMF, it is also much more volatile (see **Table 3.3**), meaning that the solution is more unstable at higher chloroform concentrations, and the solvent volatility will affect the true concentration of the solution[224–226]. However, this is much less apparent at lower PCL concentrations.

Table 3.3 Solvent properties

	Viscosity at 25°C (Pa s)	**Boiling Point (°C)**
Chloroform	0.536	61
DMF	0.796	153

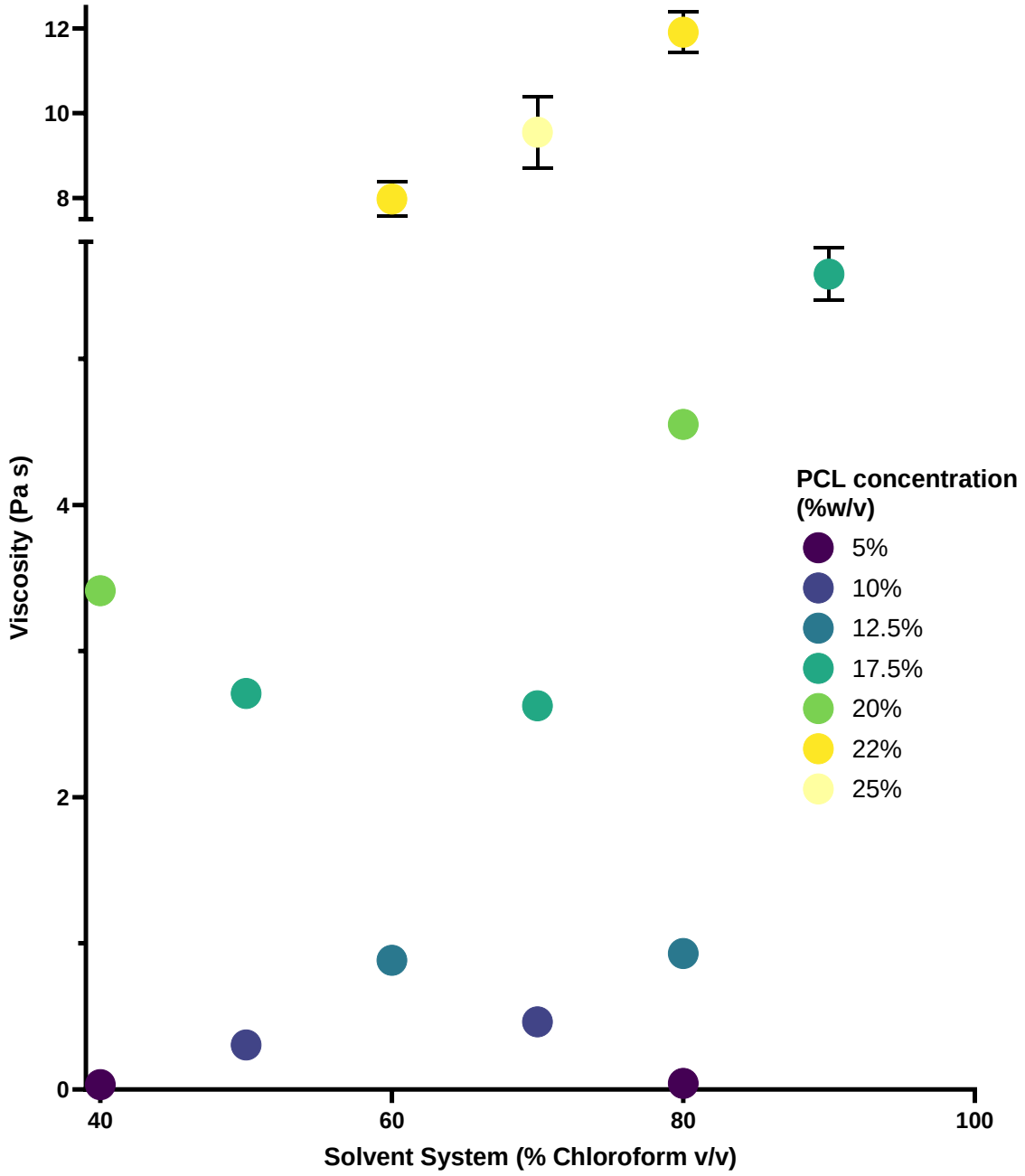

Figure 3.4 The effect of solution parameters on viscosity. The viscosity of each of the solutions used in the DoE optimisation experiments was determined using rheometry (n=3).

With each increase in PCL concentration, there was a stepwise increase in solution viscosity with the exception of 25 % w/v PCL solution in 70:30 chloroform:DMF, which had a viscosity between that of the two 22 % w/v solutions in 60:40 and 80:20 solvent systems. At concentrations of 12.5 % w/v and below, changing the solvent system did not affect the viscosity. However, once the solution concentration exceeded 12.5 % w/v, there was a marked increase in solution viscosity when the amount of chloroform in the solvent system was increased.

The Hansen Solubility parameters (HSP) can explain the solubility of PCL in chloroform, DMF and mixtures of these solvents. HSP can also provide insights into the solution viscosity. HSP are composed of three components, dispersion forces (δ_d), polar forces (δ_p) and hydrogen bonding (δ_h), and the HSP approach predicts solubility based on “like dissolves in like”, meaning that a solute is likely to dissolve in a solvent with similar properties

Chloroform has a relatively close match in HSP with PCL, suggesting good solubility driven mainly by dispersion forces (see **Table 3.4**)[227–229]. However, chloroform is highly volatile, which can lead to rapid changes in concentration, which will affect the electrospinning process. DMF has more dissimilar HSPs to PCL, suggesting lower solubility, although PCL can still dissolve effectively in DMF. DMF is much less volatile than chloroform, which is beneficial in maintaining a stable solution during electrospinning, which is crucial for producing consistent fibres.

Table 3.4 Hansen solubility parameters of PCL, chloroform and DMF

Hansen solubility parameters	**δ_d** $(MPa)^{1/2}$	**δ_p** $(MPa)^{1/2}$	**δ_h** $(MPa)^{1/2}$
Chloroform	17.8	3.1	5.7
DMF	17.4	13.7	11.3
50:50 Chloroform DMF	17.6	8.4	8.5
PCL	17.7	5	8.4

A 50:50 mixture of chloroform and DMF offers a balance between the higher PCL solubility of chloroform, but the lower volatility of DMF resulting in a more stable, less volatile solution. The characteristics of this mixture result in a more controlled and consistent electrospinning process, leading to more uniform fibres. In order to confirm this, the viscosity of each solution was compared to the resulting fibre diameter when it was used to produce electrospun fibres (see **Figure 3.4**).

There was a correlation between higher viscosities and larger fibre diameters. However, there was also a critical point, below which electrospinning failed to produce fibres at all, or produced thicker fibres with large variability. This is likely due to destabilisation of the Taylor Cone, which is dependent on surface tension to form[230]. The result of using PCL solutions below the critical viscosity can be seen clearly in experiments 17 and 18 which used 5 % w/v PCL solutions (see **Figure 3.1**).

In addition to producing fibres with the smallest diameters, the optimised solution (10 % w/v, 50:50 Chloroform:DMF) suggested by the previously described DoE process also had much less variability than any of the other solutions used.

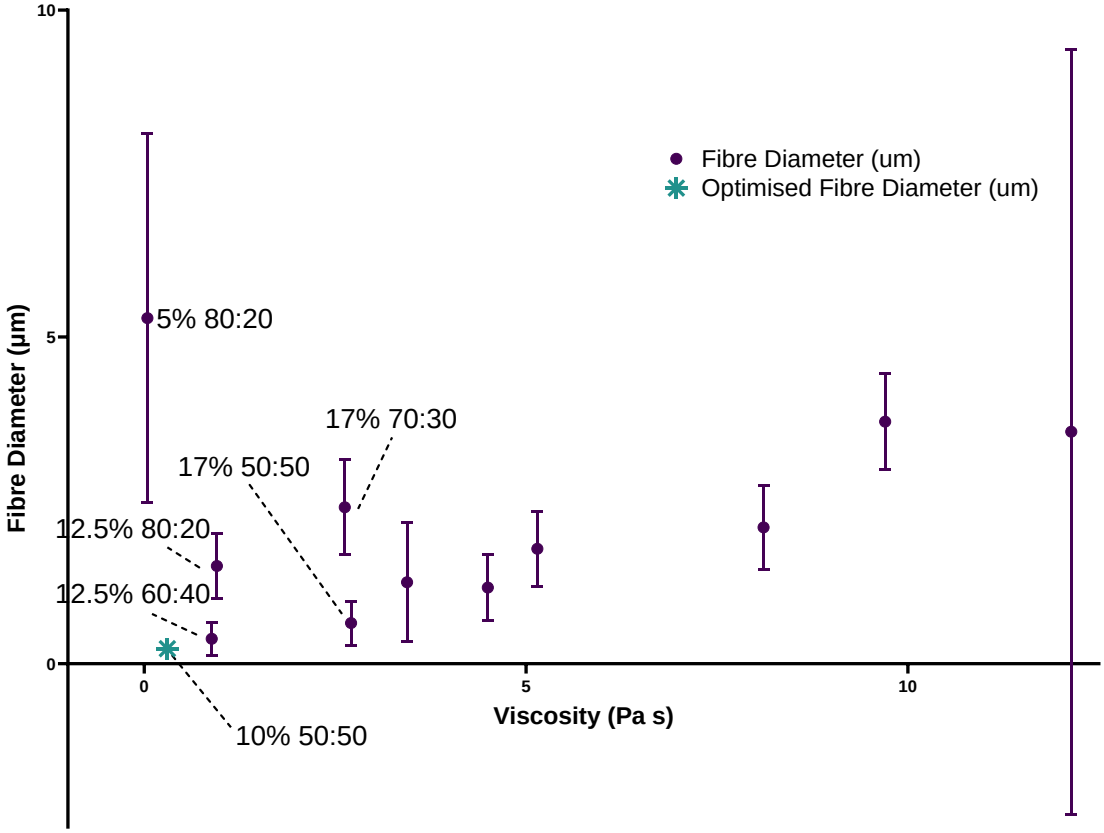

Figure 3.5 The effect of solution viscosity on electrospun PCL fibre diameter. The viscosity of each solution used in the DoE optimisation determined using rheometry plotted against the resulting fibre diameters (N=3, n=100).

3.3.1.3 Mandrel Speed

To investigate the effect of the rotating mandrel collector speed on the fibres, the mandrel speed was varied in isolation from the other factors. SEM images of the resulting fibres show an increase in alignment as the speed of the mandrel is increased (see **Figure 3.6**).

At mandrel speeds of 0 RPM (stationary) and 500 RPM, the fibres showed no visible alignment. The 1000 RPM and 2000 RPM mandrel speeds produced highly aligned fibres. The higher mandrel speeds also resulted in thinner fibres, which was analysed using Image J (see **Figure 3.7**). There was no other visible difference between the fibres, which were all smooth and showed no beading.

The distribution of fibre alignment produced using the different mandrel speeds was analysed using the Orientation J plugin for Image J. Colour surveys confirmed that the fibre alignment increased with mandrel speed (see **Figure 3.8**). The Orientation J plug-in for Image J was used to analyse the alignment of fibres in each SEM image. This data was plotted on polar histograms (see **Figure 3.9**). One-way ANOVA performed using GraphPad Prism showed that the proportion of fibres aligned with the dominant fibre direction increased significantly with mandrel speed from 6.1 ± 0.7 % (0 RPM) to 40 ± 3 % (2000 RPM). Increased mandrel speeds produced more highly aligned fibres, therefore the highest mandrel speed was chosen as the optimal setting.

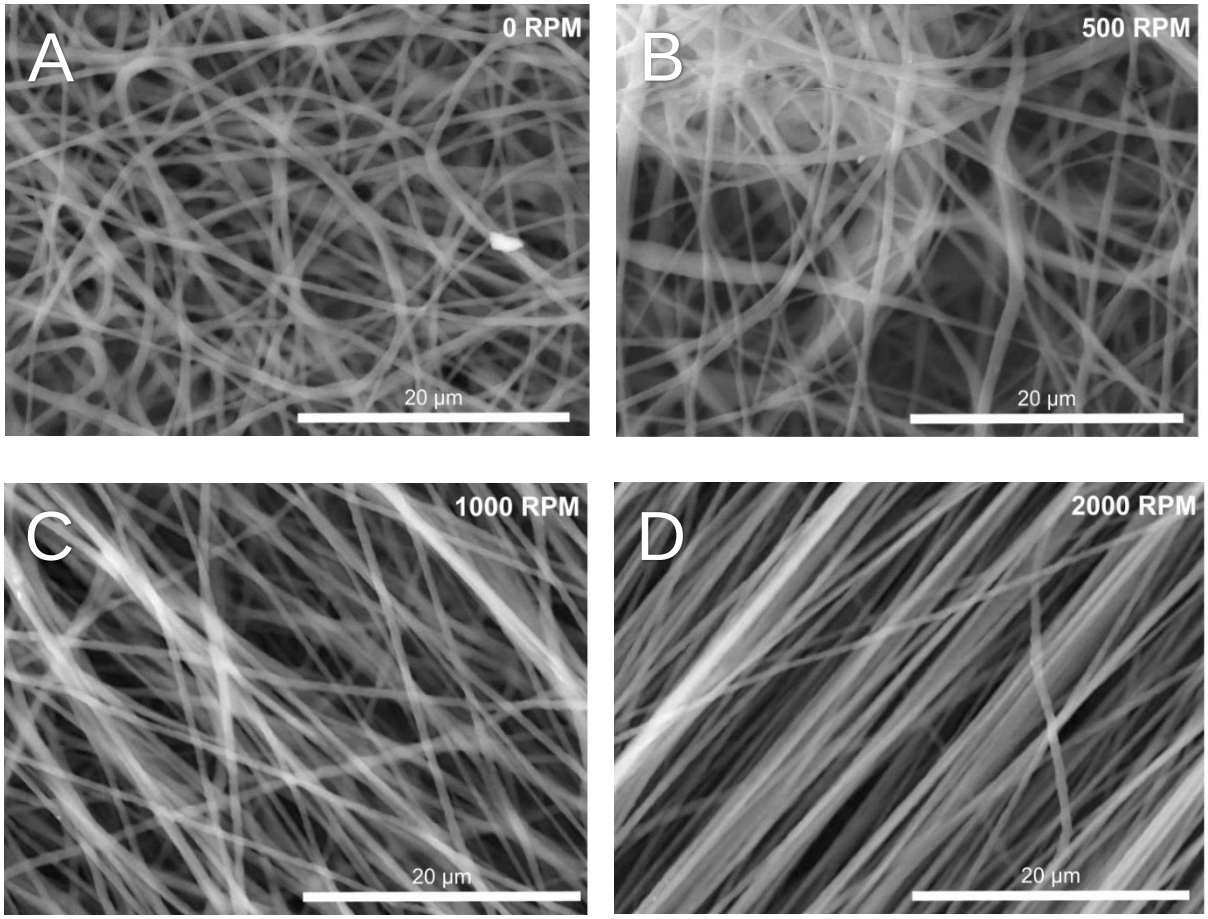

Figure 3.6 SEM images of fibres produced using different mandrel speeds. To investigate the effect of the rotating mandrel collector speed on the electrospun fibres, 10% w/v PCL solution in a 50:50 chloroform:DMF solvent system was electrospun with an applied voltage of 20 kV, a needle tip-collector distance of 20 cm, with the mandrel speed set at **A** 0 RPM (stationary), **B** 500 RPM, **C** 1000 RPM and **D** 2000 RPM.

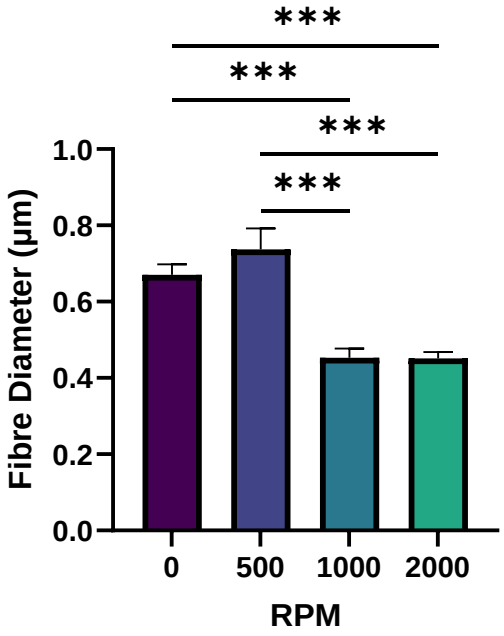

Figure 3.7 The effect of mandrel speed on electrospun PCL fibre diameter. There was not a significant difference in the fibre diameter when the mandrel speed was increased from 0 to 500 RPM. When the mandrel speed was increased to 1000 RPM there was a significant decrease in the fibre diameter, but when the speed was increased further to 2000 RPM there was no further decrease in fibre diameter. Graph shows mean ± SE (N=3, n=100), with one-way ANOVA statistical test (***p≤0.001).

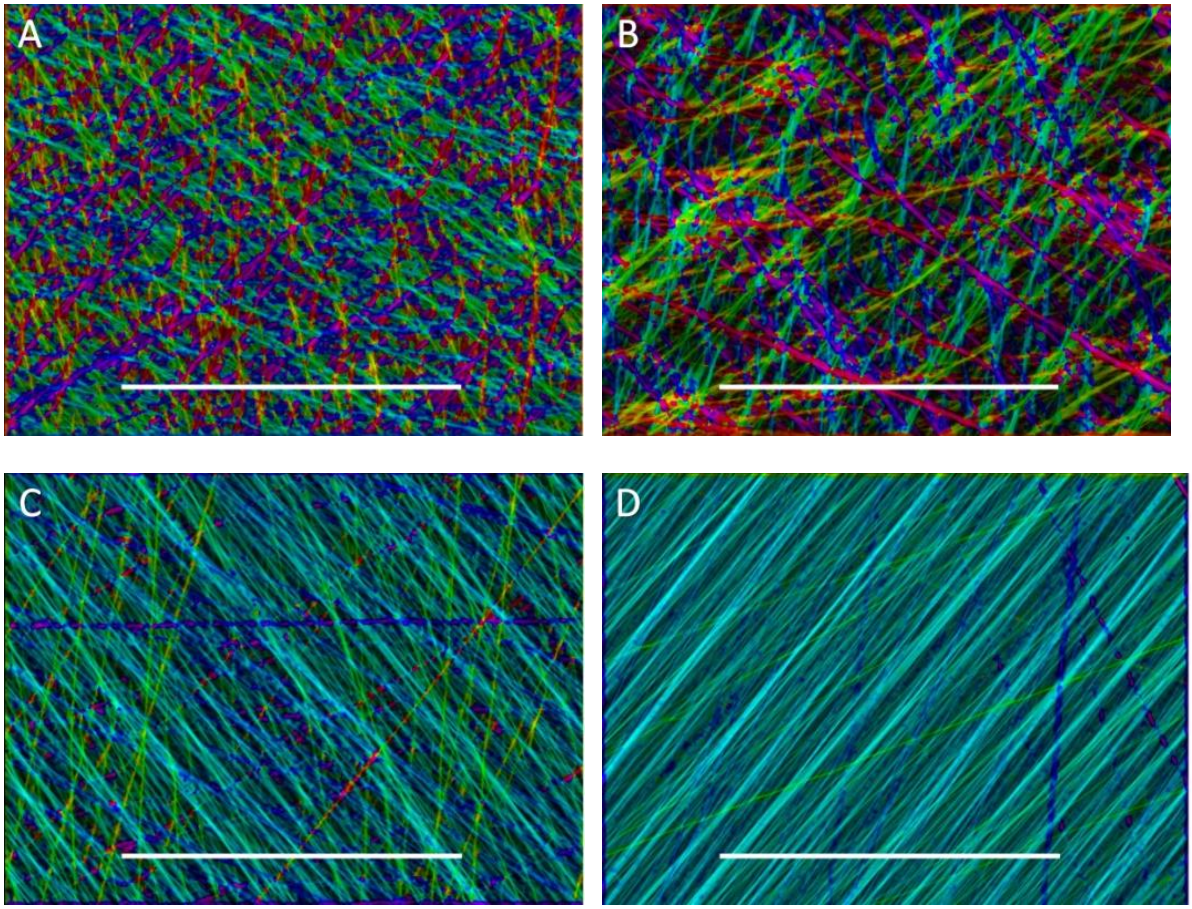

Figure 3.8 The effect of mandrel speed on fibre alignment. Colour surveys produced using Image J showing fibre alignment when using different rotating mandrel collector speeds: **A** 0 RPM (stationary) **B** 500RPM, **C** 1000 RPM and **D** 2000 RPM. Scale bars: 100 µm. The hue changes with the orientation, with the dominant direction being represented by cyan (rgb (0,255,255)) and perpendicular fibres being shown in red (rgb (255,0,0)).

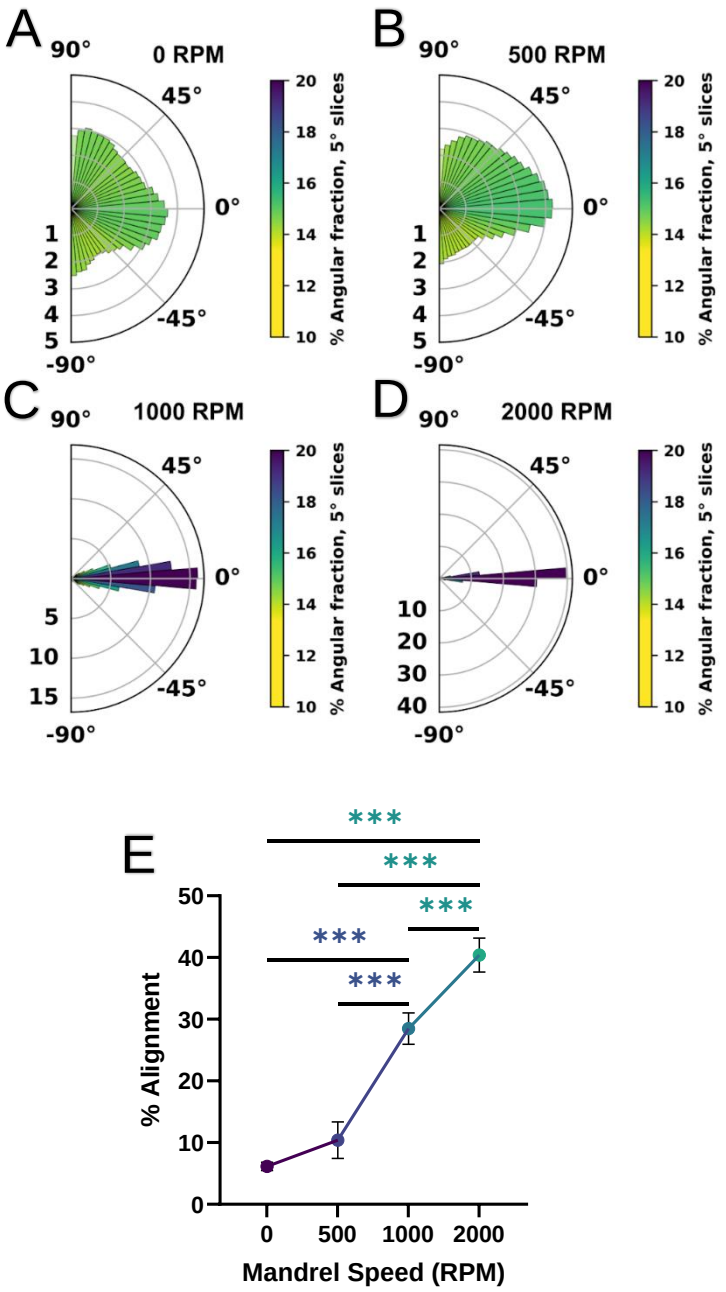

Figure 3.9 The effect of mandrel speed on electrospun PCL fibre alignment. Polar histograms produced using Python showing the distribution of alignment of fibres produced using a rotating mandrel speed of **A** 0 RPM (stationary), **B** 500 RPM, **C** 1000 RPM and **D** 2000 RPM. The Orientation J plug-in for Image J was used to analyse the alignment of fibres in each SEM image. This data was plotted on a polar histogram. Each bar represents a 5° slice of the SEM image, with 0° representing the dominant fibre direction. The length of the bar represents the proportion of the image (%) that is aligned with the dominant fibre direction. Darker coloured bars are longer. Graph (E) shows the mean % alignment ± SD (n=5), with one-way ANOVA statistical t-test (*** $p \leq 0.001$).

3.3.1.4 Electrospinning Time

To assess how the total volume of electrospun solution affects the fibres, two conditions were examined. Initially the minimum volume was used that could produce fibre sheets which could be completely removed from the collector, which was achieved by running the electrospinning process for 5 hours with a single syringe loaded into the apparatus resulting in 5 mL of electrospun solution. For the other extreme, the longest feasible operation time was determined to be 8 hours, during which two syringes were loaded into the apparatus, allowing for 16 mL of electrospun PCL solution. This allowed the investigation of the effects of operating at both the minimum and maximum capacity.

The minimum and maximum sheet thicknesses were 42 ± 13 µm and 70 ± 10 µm respectively (see **Figure 3.11**). The 16 mL sheet was significantly thicker than the 5 mL sheet, and was sufficiently robust to handle.

To ensure that the increased electrospinning time did not adversely affect the fibres, the fibre diameters were compared (see **Figure 3.10**). The 5 mL and 16 mL sheets had average fibre diameters of 0.23 ±0.09 µm and 0.21 ±0.07 µm respectively, which were not significantly different from each other. This confirmed that electrospinning the maximum volume of 16 mL produced robust, thicker fibre sheets without compromising fibre diameter.

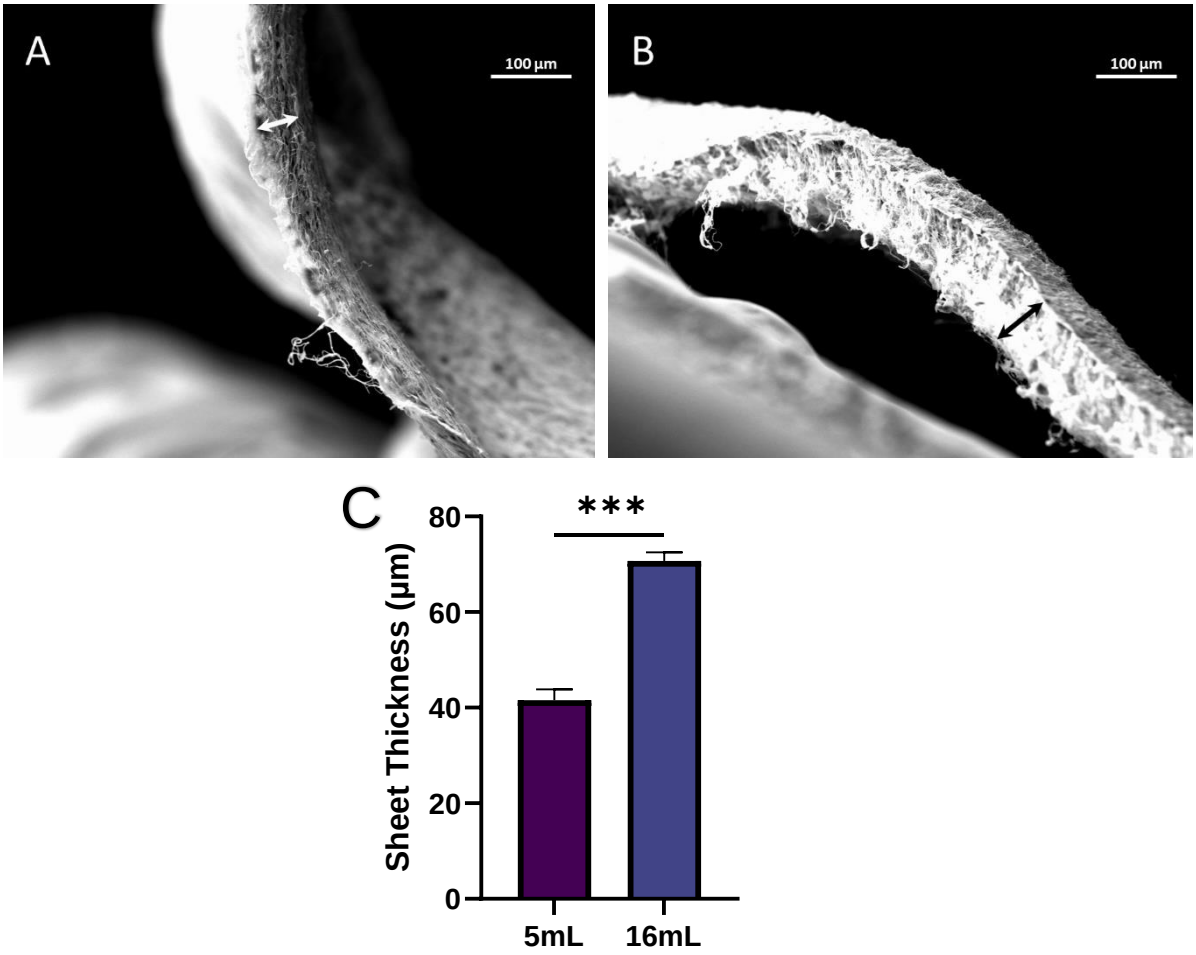

Figure 3.10 The effect of electrospinning volume on sheet thickness. SEM images of fibre sheets produced by electrospinning **A** 5 mL and **B** 16 mL of 10 % w/v PCL solution in a 50:50 chloroform:DMF solvent system with an applied voltage of 20 kV, a needle tip-collector distance of 20 cm, and a mandrel collector speed of 2000 RPM show that electrospinning larger volumes of solution lead to thicker fibre sheets. **C** Comparison of sheet thickness after electrospinning 5 mL and 16 mL of PCL solution. Graph shows the mean ± SE N=3, (n=10), with unpaired t-test (*** $p \leq 0.001$).

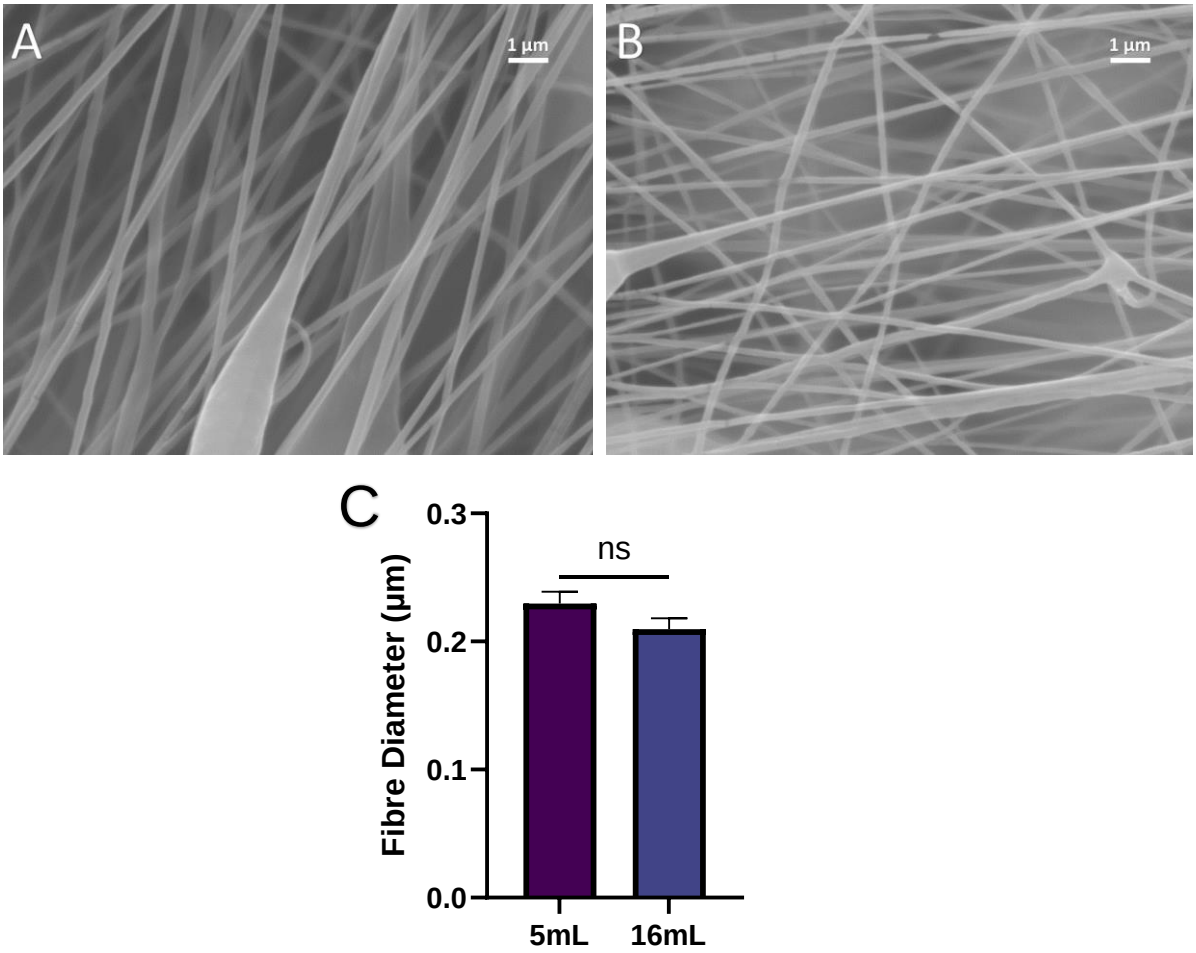

Figure 3.31 The effect of electrospinning time on fibre diameter. SEM images of fibres produced by electrospinning **A** 5 mL and **B** 16 mL of 10 % w/v PCL solution in a 50:50 chloroform:DMF solvent system with an applied voltage of 20 kV, a needle tip-collector distance of 20 cm, and a mandrel collector speed of 2000 RPM show that the fibre diameter is not affected by the volume of solution electrospun. **C** Comparison of the average fibre diameter after electrospinning 5 mL and 16 mL of PCL solution. Graph shows the mean ± SE (N=3, n=100), with unpaired t-test (ns $p \geq 0.05$).

3.3.2 Electrospun PCL Fibre Characterisation

3.3.2.1 Fibre Morphology

Once the electrospinning process had been optimised, the resulting PCL fibres were extensively characterised.

SEM images of fibres produced using the optimised conditions showed highly aligned, smooth fibres free from beading with an average fibre diameter of 0.22 ± 0.06 µm (see **Figure 3.12**).

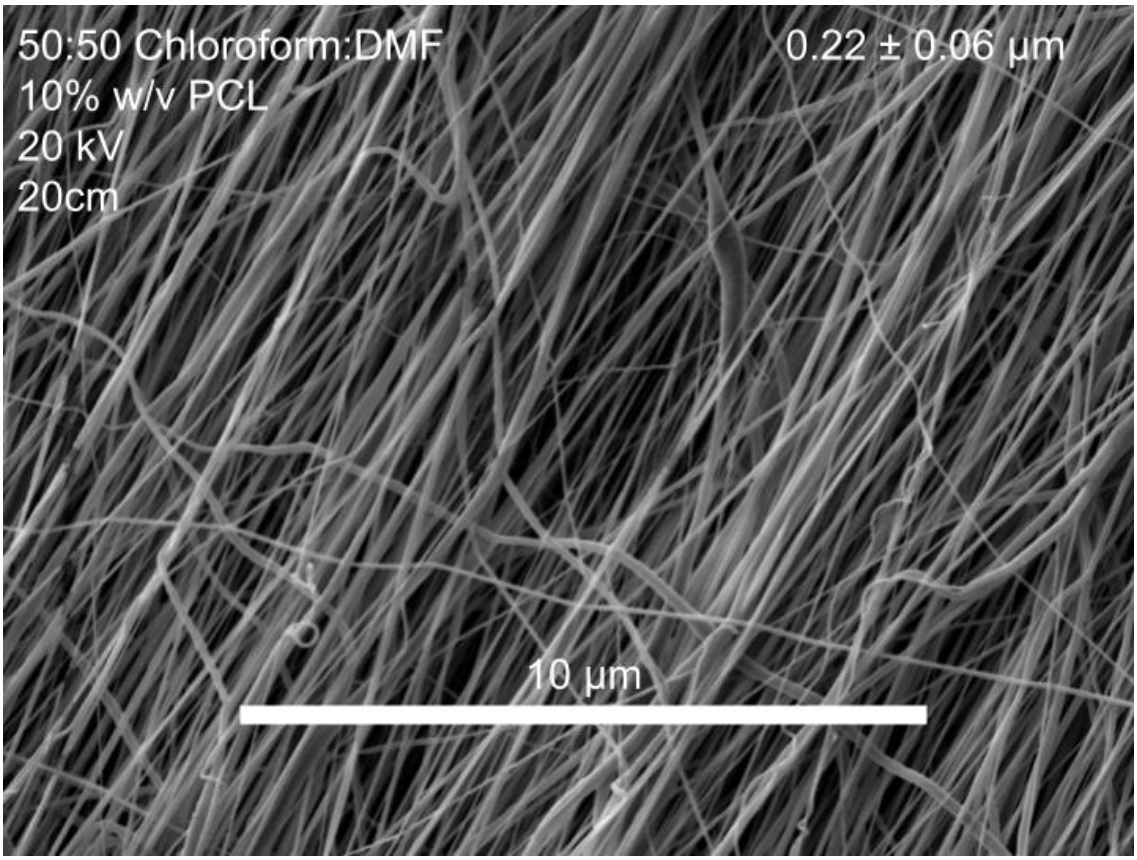

Figure 3.42 Optimised electrospun PCL fibres. Representative SEM image of electrospun PCL fibres produced using the optimised conditions; a 50:50 chloroform: DMF solvent system, 10% PCL w/v, an applied voltage of 20kV, a needle tip- collector distance of 20cm, a mandrel collector speed of 2000 RPM and 16 mL of solution.

3.3.2.2 Mechanical Properties

Mechanical testing of the electrospun PCL fibre sheets revealed that they exhibited anisotropy. The elastic modulus parallel and perpendicular to the fibres was 33.0 ± 13 MPa and 1.1 ± 0.5 MPa respectively, which were significantly different to each other (see **Figure 3.13A**). The sheets also had a significantly higher modulus than the tissue parallel to the fibre direction, but were not significantly different in the perpendicular direction.

The UTS parallel and perpendicular to the fibre direction was 6.0 ± 0.6 µm and 0.4 ± 0.3 µm respectively. These were significantly different from both each other and the tissue (see **Figure 3.13B**). The maximum extension parallel to the fibres was 40 ± 20 µm, and 100 ± 20 µm perpendicular to the fibre direction (**Figure 3.13C**). These were also significantly different form both each other and the tissue.

Anisotropy is an important aspect of creating a biomaterial scaffold that mimics the natural ECM[37]. By mimicking tissue anisotropy, biomaterials can recreate one facet of the mechanical signal transduction facilitated by the ECM. Mimicking tissue anisotropy allows a biomaterial to recreate the directional mechanical cues present in native tissues, thereby promoting cell alignment, tissue organisation and ultimately enhancing the biomimicry of the engineered scaffold[231,232].

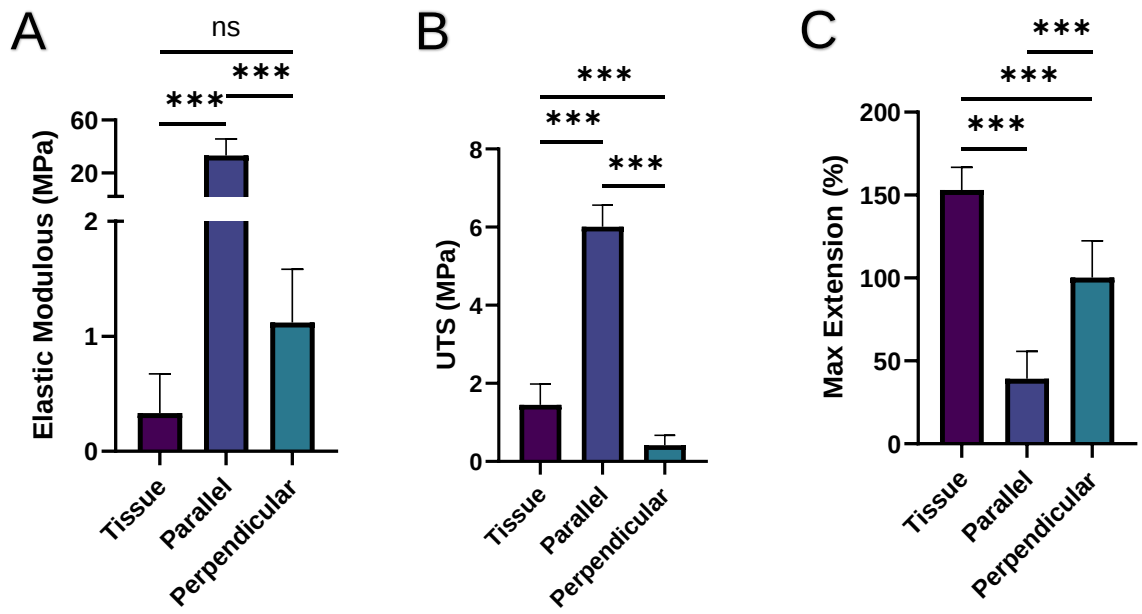

Figure 3.13 Mechanical properties of electrospun PCL fibre sheets parallel and perpendicular to fibre alignment. Graphs comparing **A** the elastic modulus, **B** the UTS and **C** the maximum extension of electrospun PCL fibre sheets parallel and perpendicular to the fibre direction, compared to porcine oesophagus tissue. Graphs show mean ± SD (n=5), with one-way ANOVA statistical test (*** $p \leq 0.001$, ns $p \geq 0.05$).

3.3.2.3 Wettability

The water contact angle (θ) for the fibre sheets was determined in order to investigate the hydrophilicity of the material (**Figure 3.14**). The water contact angle of the decellularised porcine oesophagus ECM (dECM) was 67 ± 5°. The θ of the electrospun PCL fibre sheets was 142 ± 12°, which was significantly higher than that of the ECM, indicating hydrophobicity.

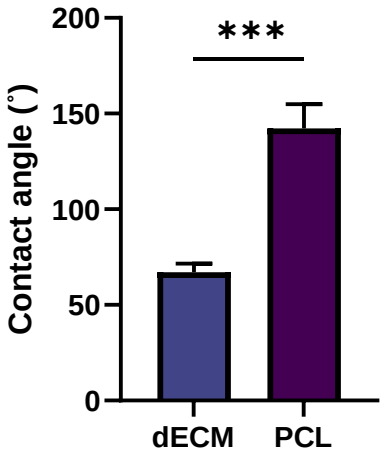

Figure 3.14 Electrospun PCL fibre water contact angle. Comparison of the water contact angle of porcine dECM and electrospun PCL fibres. Graph shows the mean ± SD (N=3, n=6), with unpaired t-test (*** $p \leq 0.001$).

3.3.2.4 Raman Spectra

Raman spectra of the PCL before and after electrospinning showed peaks characteristic of PCL[233–235]. These characteristic peaks remained after electrospinning (see **Figure 3.15**). Raman shift peak assignments are shown in **Table 3.5**.

In order to determine the crystallinity of the electrospun PCL fibres, the band in the region 1710-1750 cm^{-1}, which corresponds to C=O stretching) was deconvoluted into two gaussian peaks centred at 1724 cm^{-1} (corresponding to the crystalline phase) and at 1732 cm^{-1} (which corresponds to the amorphous phase). These peaks were integrated, and these values were used to calculate the fraction of crystalline phase (see **Figure 3.16**). The crystalline phase of the PCL before and after electrospinning was found to be 61 ± 2 % and 60 ± 3 % respectively. An unpaired t-test (n=3) showed that these values were not significantly different from each other, indicating that the electrospinning process did not affect the crystallinity of the PCL.

Table 3.5 Raman shift peaks of the PCL spectrum

Peak shift (cm^{-1})	**Assignment**
1110	ν(COC)
1306	ω(CH_2)
1442	δ(CH_2)
1725	ν(C=O)

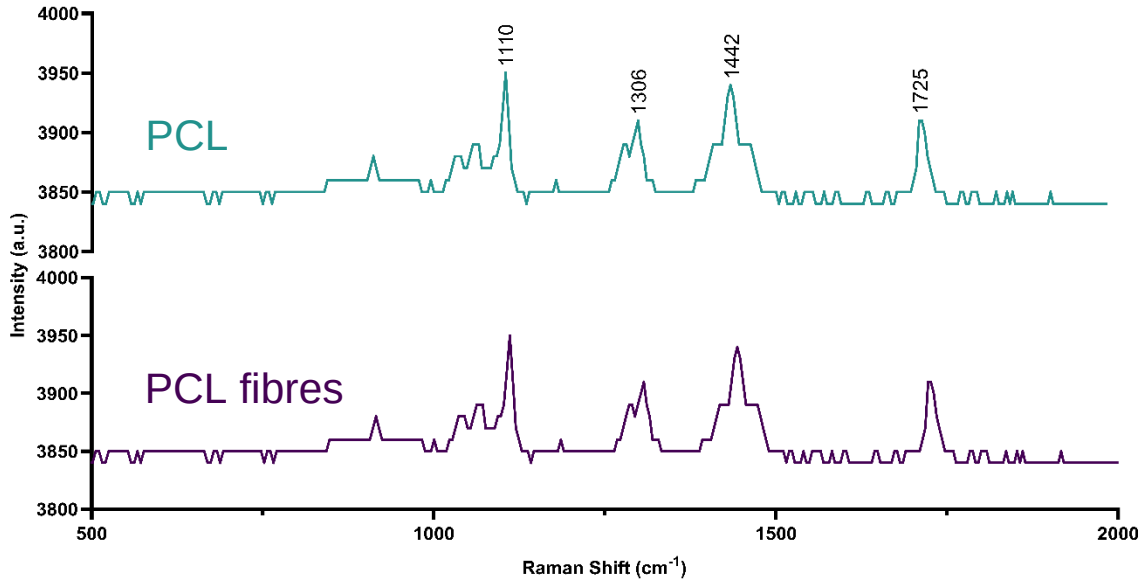

Figure 3.55 PCL Raman spectra. Raman spectra of PCL before and after electrospinning between 500 and 2000 cm^{-1}, 785nm laser line. Peaks were identified at 110, 1306, 1442 and 1725 on both spectra, indicating that the electrospinning process did not change the chemical structure of the PCL.

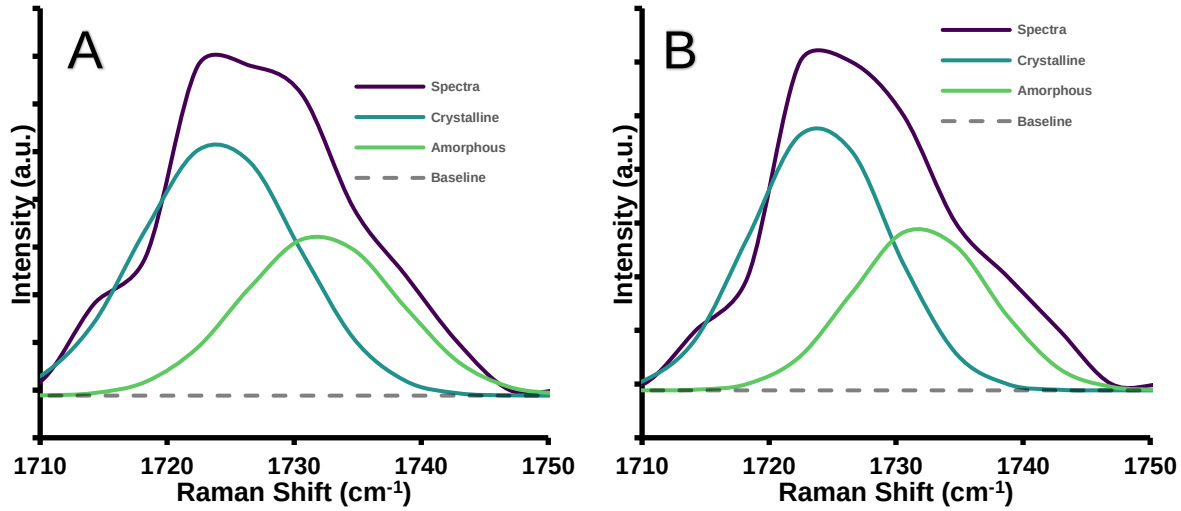

Figure 3.16 The effect of electrospinning on PCL crystallinity. Representative Raman spectral region 1710-1750 cm^{-1} of PCL **A** before and **B** after electrospinning, showing the contribution of the crystalline and amorphous fractions.

3.3.3 Porcine Oesophagus Characterisation

Porcine oesophagus was chosen as a comparison to evaluate the suitability of electrospun PCL fibres for oesophageal tissue engineering, as it shares morphological and histological similarities to human oesophageal tissue and has been established as an excellent model for human oesophagus[236,237].

SEM imaging shows the ECM of decellularised porcine oesophagus tissue (see **Figure 3.17**). Individual ECM fibres can be seen, along with clusters of fibres.

Porcine oesophagus was mechanically tested in the longitudinal (parallel to the direction of bolus travel) and transverse (perpendicular to bolus travel) directions (see **Figure 3.18**). The average thickness of the porcine oesophagus mucosal layer was 1.2 ± 0.4 cm. Mechanical testing revealed that the elastic modulus of the transverse and longitudinal samples was 0.1 ± 0.1 MPa and 0.3 ± 0.3 MPa respectively. The UTS of the transverse samples was 0.08 ± 0.1 MPa and of the longitudinal samples was 1.3 ± 0.6 MPa.

Both the elastic modulus and tensile strength were significantly greater in the longitudinal direction, indicating that the tissue is highly anisotropic. For comparison with electrospun PCL fibres, the transverse elastic modulus and the longitudinal UTS were used, as they indicated the highest elasticity and strength respectively.

153 ± 16 % and 87 ± 17 % were the maximum extensions reached in the transverse and longitudinal directions respectively. The transverse extension was used for comparison with PCL fibres.

The tissue exhibited significant anisotropy, characterised by greater elasticity in the transverse direction, a trait which has been previously reported of the oesophagus mucosal layer[238,239]. The elasticity in the transverse direction is crucial in

accommodating bolus passage during swallowing. The anisotropy of the tissue also suggests a higher degree of alignment of the ECM fibres in the transverse direction[239].

Given that the mucosal layer typically exhibits greater mechanical properties compared to the muscular layer[238], the mucosal layer was chosen for comparison to the electrospun PCL fibres to ensure that the material had sufficient mechanical properties to withstand the physiological forces experienced by the tissue *in vivo*.

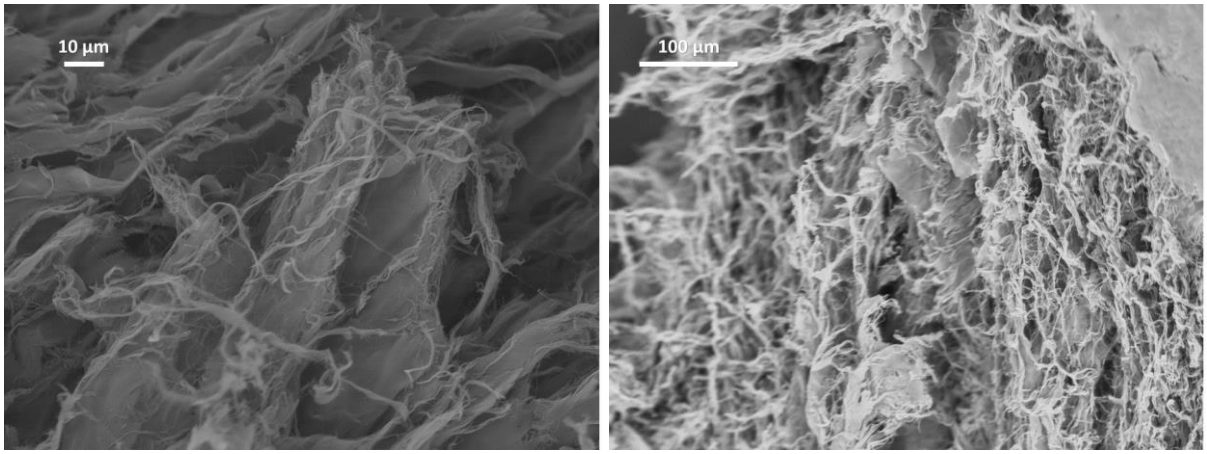

Figure 3.67 SEM images of decellularised porcine oesophagus. Porcine oesophagus was decellularised using a 1% Triton-X and 1% SDS solution. SEM imaging was used to visualise the decellularised tissue. Individual ECM fibres can be seen, with an average fibre diameter of 0.4 ± 0.2 µm.

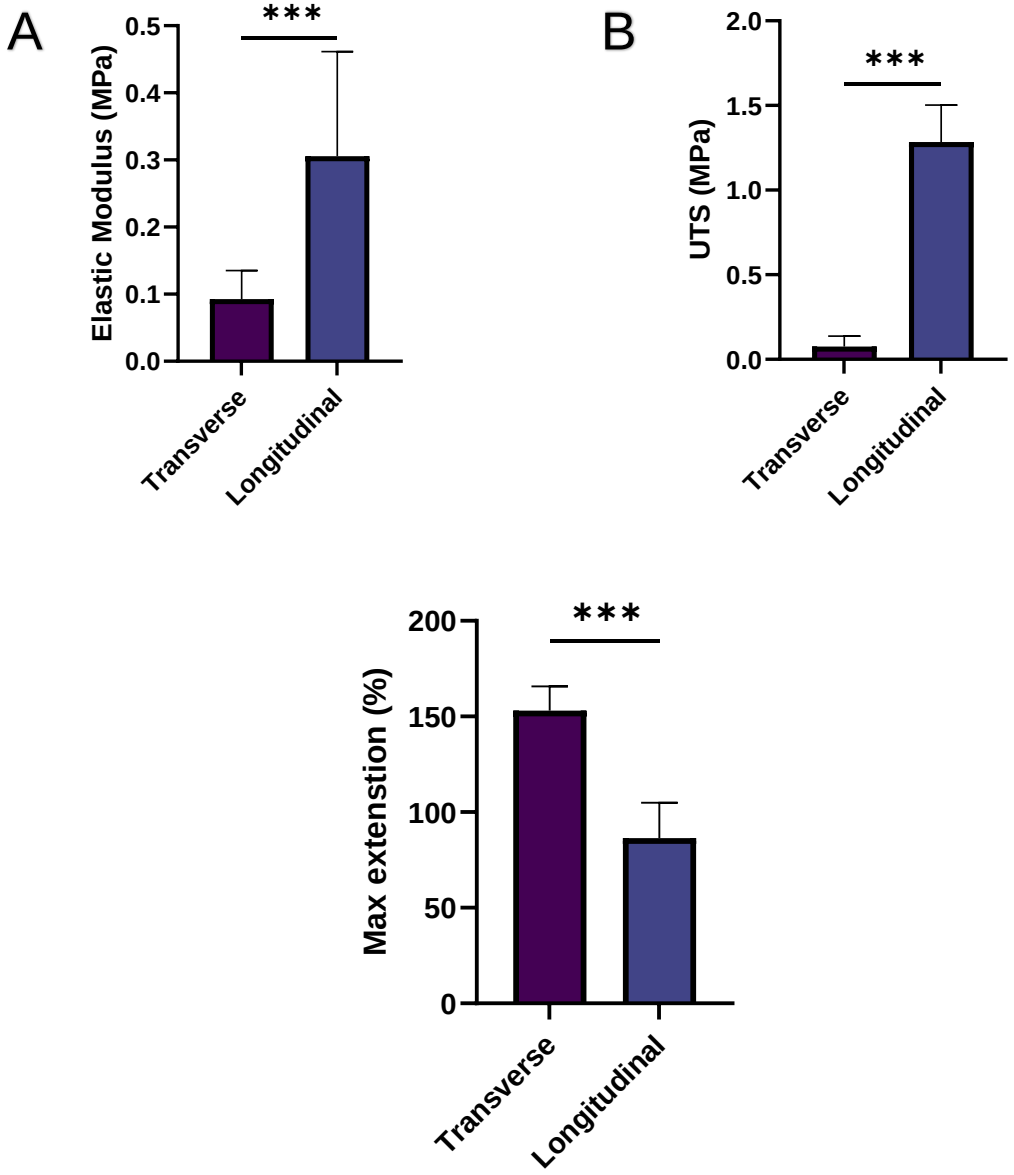

Figure 3.18 Mechanical properties of porcine oesophageal tissue. Graphs comparing **A** the elastic modulus, **B** the UTS and **C** the maximum extension of porcine oesophagus tissue tested in the longitudinal (parallel to the direction of bolus travel) and transverse (perpendicular to bolus travel) directions. Graph shows the mean ± SD (n=5), with unpaired t-test (*** $p \leq 0.001$).

3.4 Discussion

This chapter describes the determination of the optimal parameters for producing highly aligned electrospun PCL fibres with small diameters and minimal beading. The optimised process used a 10 % w/v PCL solution in a 50:50 chloroform: DMF solvent system. The process used an applied voltage of 20 kV, a needle tip-collector distance of 20 cm, a rotating mandrel collector speed of 2000 RPM and 16 mL of solution in two syringes spun for 8 hours to produce a 70 ± 10 µm thick sheet of 0.22 ± 0.06 µm diameter fibres that were highly aligned and exhibited minimal beading (**Figure 3.11**).

The diameter of electrospun PCL fibres found in literature ranged from 0.1 to 2.5 µm (see **Table 1.1**) [151,175,184]. The fibres described here are within this range and are among the thinnest reported electrospun PCL fibres. While fibre alignment is often unreported in published studies, this optimised method achieves consistent alignment, which produces an anisotropic material that replicates the anisotropy of the oesophageal mucosa. This replication is crucial for replicating the *in vivo* environment, which is essential for successful tissue engineering applications [240,241].

It was determined that the solution parameters, namely PCL concentration and solvent system, had the greatest impact on the electrospinning process and the resulting fibre diameter. Previous studies have shown that viscosity is an important factor determining smooth unbeaded fibres, with lower viscosities being shown to produce fibres with smaller diameters [133,139,141]. The optimised PCL solution had a viscosity of 0.304 ± 0.008 Pa s. Lower viscosities led to reduced fibre diameters, however, it was noted that if the viscosity fell below a critical point, electrospinning would not succeed. This is due to the disruptive effects of surface tension on the jet during the electrospinning process, which attempts to reduce the surface area: volume ratio by forming solution droplets [133,242,243]. By using solutions with higher viscosities, the

viscoelastic forces counter the effects of surface tension, allowing smooth, continuous jet formation.

Tensile testing revealed the mechanical properties of the fibre sheets and enabled a comparative analysis with porcine oesophageal mucosa. The fibre sheets were highly anisotropic, with an elastic modulus of 33.0 ± 13 MPa parallel to the fibre direction, which was significantly stiffer than the porcine oesophageal tissue. However, when tested in the direction perpendicular to the fibre alignment, the fibre sheets had an elastic modulus of 1.1 ± 0.5 MPa, which was similar in elasticity to the tissue.

The PCL fibre sheets displayed higher strength compared to the oesophageal tissue when tested parallel to the fibre orientation, meaning that the material had sufficient strength to withstand the forces experienced by the tissue, a crucial consideration for implantable biomaterials[244,245].

The maximum extension of both the fibres and the tissue is a critical factor, especially in dynamic biological environments. While the fibre sheets have a lower maximum extension than the tissue in both directions, it is notable that the native tissue exhibits more elasticity than required *in vivo*. This "biorelevant stretch" is a key consideration; the tissue's natural elasticity far exceeds typical physiological demands, suggesting that the fibre sheets, while less extensible, may still be sufficient for practical applications.

For *in vivo* implantation, the layering and fibre orientation must be carefully considered, in order to maximise the mechanical properties of the fibre sheets. Combining layers of fibre sheets in various orientations could combine the favourable strength of the fibres in parallel with the elasticity of the perpendicular fibre sheets, and control the degree of anisotropy to match that of specific tissues[246].

Raman spectroscopy of unprocessed PCL and electrospun PCL fibres both showed characteristic peaks of PCL, and the crystalline fraction was not significantly different after electrospinning. This confirms that the electrospinning process does not affect the structure or crystallinity of the PCL. This preservation of PCL crystallinity indicates long-term stability *in vivo*, a crucial aspect for biomedical applications where polymer degradation rate plays a significant role [247,248].

In conclusion, the electrospinning optimisation for PCL fibres, through careful consideration of solvent properties and process variables, has led to the production of fibres with desirable mechanical properties. While there are differences in elasticity, strength, and maximum extension between the PCL sheets compared to natural tissue, the electrospun PCL fibre sheets show promising characteristics for biomedical applications, particularly in replicating the directional mechanical properties of native tissues.

4.0 Degradation of Electrospun PCL Fibres *In Vitro*

4.1 Introduction

Understanding the degradation behaviour of implantable biomaterials is crucial in determining their suitability for *in vivo* applications. A key requirement of biomaterial scaffolds for tissue engineering is the ability to retain mechanical integrity long enough to support new tissue formation, but eventually degrade to facilitate complete tissue regeneration. The balance between degradation rate and mechanical properties is critical in scaffold design, and must be tailored to ensure the implant maintains strength until the newly formed tissue can assume the mechanical support

4.1.1 Factors in PCL Degradation

The degradation rate of PCL is influenced by several factors, including the accessibility of water to the ester bond. This accessibility is determined by various properties of the polymer including; hydrophobicity, crystallinity, molecular weight, glass transition temperature and bulk sample dimensions[249–251].

Polycaprolactone (PCL) is a semi crystalline, aliphatic polyester, with a low melting point of approximately 60°C. PCL is a bioresorbable thermoplastic, which can be degraded by both microbial action and hydrolytic mechanisms under physiological conditions[252,253]. However, the degradation of PCL *in vivo* is very slow, generally taking between 1 and 2 years, which is attributed to its high crystallinity and hydrophobicity[247,254]. For up to six months, PCL retains its mechanical properties before gradually losing stiffness and strength until it is completely metabolised over a two-year period.

The initial stages of PCL degradation involve non-enzymatic random hydrolysis, a process catalysed by the polymer's carbonyl end groups. This stage continues until

the molecular weight decreases to approximately 5-10 kDa M_n. At this point, hydrolytic activity diminishes, and bulk weight loss begins, primarily through oligomeric diffusion[255]. Once this begins, the polymer becomes susceptible to fragmentation due to compromised mechanical stability, with enzymatic surface erosion and phagocytosis contributing to the absorption process. Complete fragmentation occurs in phagosomes, macrophages and fibroblasts[256]. All PCL products have been demonstrated to be absorbable, with hydrolysis being the rate-limiting stage of the degradation process[257].

A major factor that influences the degradation rate of PCL is pH, with extreme acidic (below 3) or basic (above 11) conditions accelerating degradation through catalysis of ester hydrolysis[258]. The physical characteristics of a PCL construct, such as porosity and fibre diameter, can also affect its degradation rate. For instance, thinner fibres lead to an increased rate of degradation, due to increased water infiltration[259]. This suggests that a controlled degradation rate can be achieved through manipulating the biomaterial topography.

4.1.2 Characterising Electrospun Fibre Degradation

PCL degradation can be characterised in several ways; changes in molecular weight, bulk weight loss and the deterioration of mechanical properties. Typically, changes in molecular weight and mechanical properties are apparent before bulk weight loss, as only the monomer degradation products are soluble[260].

4.1.3 Oesophageal conditions affecting degradation

The normal pH in the oesophagus is around 7.0. However, this level fluctuates over a 24-hour period due to the oesophagus' proximity to the stomach and exposure to external factors such as food, which can cause temporary pH changes. The generally

accepted threshold for oesophageal reflux is a pH of 4.0. The duration of acidic pH exposure in the tissue varies depending on its position within the oesophagus, with the distal portion (5 cm above the OGJ) experiencing pH levels below 4.0 for up to 6.3 % of the time, but the distal portion (20cm above the OGJ) experiencing decreased pH for less than 0.9 %[261].

This chapter will outline an experimental approach to investigating the degradation behaviour of the electrospun PCL fibres that were developed in the previous chapters. Degradation was characterised through investigating changes in molecular weight, mechanical properties and fibre morphology at pH levels of 4.0 and 7.0.

4.2 Methods

4.2.1 In Vitro Degradation

0.1M Phosphate buffered saline (PBS) was prepared at pH 4 and pH 7. The components, namely sodium chloride (NaCl), potassium chloride (KCl), sodium phosphate dibasic (Na_2HPO_4) and potassium phosphate monobasic (KH_2PO_4), were dissolved in diH_2O to achieve the concentrations outlined in **Table 4.1**. The pH was adjusted using 0.1 M HCl or 0.1 M NaOH to obtain the desired pH levels (4 or 7). Sodium azide was added to a final concentration of 0.05% w/v to inhibit bacterial growth during incubation.

Table 4.1 Concentrations of components in PBS solutions at pH 4 and pH 7

		pH 4	**pH 7**
Concentration (M)	**NaCl**	0.137	0.137
	KCl	0.0027	0.0027
	Na_2HPO_4	0.0005851	0.01
	KH_2PO_4	0.01141	0.0018

Samples of electrospun PCL fibres were immersed in phosphate buffered saline (PBS) at pH 4 and pH 7, and incubated at 37°C for 4, 8 and 12 weeks. For mechanical testing, due to batch-to-batch variability, samples and controls for each condition were taken from a single sheet of electrospun fibres.

4.2.2 Accelerated Degradation

300 mg of PCL fibres were placed in 100 mL of 1M NaOH. The reaction was terminated after 72 hours when the fibres were no longer visible. The solution was

neutralised with 100 mL of 1M HCL. The degraded PCL was extracted into deuterated chloroform ($CDCL_3$), for nuclear magnetic resonance (NMR) analysis.

4.2.3 Nuclear Magnetic Resonance Spectroscopy

Nuclear magnetic resonance (NMR) analysis was performed to determine changes in the molecular weight of PCL fibres following *in vitro* degradation (see **Figure 4.1B**). ^{1}H-NMR spectra were recorded at 25°C using a Bruker AVIII-300 MHz instrument in $CDCl_3$. The data was processed with MestreNova software (Mestrelab Research, Spain). Chemical shifts (δ) were reported in parts per million (ppm), referenced to the solvent resonance ($CDCl_3$ ^{1}H δ= 7.26ppm)[262].

The degree of polymerisation (DP) was estimated by analysing the peaks corresponding to the **a** and **e** protons, as assigned in **Figure 4.1A**. The **a** proton peak is unaffected by the DP due to its location furthest from the chain end, whereas the **e** proton peak depends on the DP. The **e** proton peak diminishes with decreasing DP, being replaced by **e'** protons that exhibit a different δ due to their position at the polymer end. (see **Figure 4.1**). **Equation 2** was be used to estimate the DP from the integrated peaks.

Equation 2

$$DP = \int_{3.9}^{4.1} a \Big/ \int_{3.9}^{4.1} a - \int_{2.2}^{2.4} e$$

The calculated DP, along with the molecular weight of the PCL monomer (114 g/mol) was then used to estimate the molecular weight of the polymer.

A

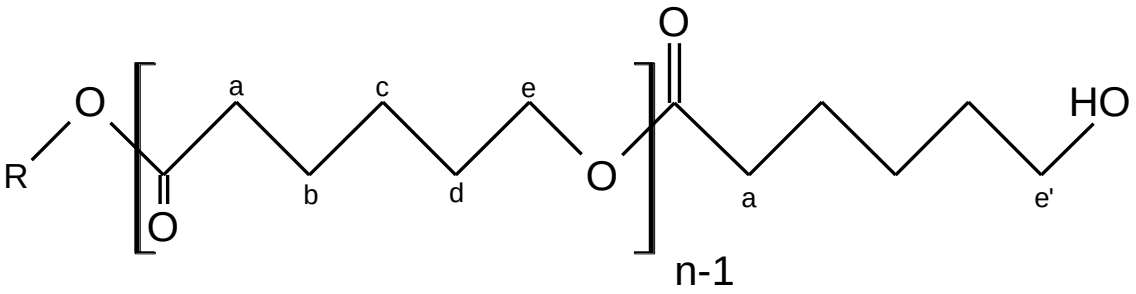

B

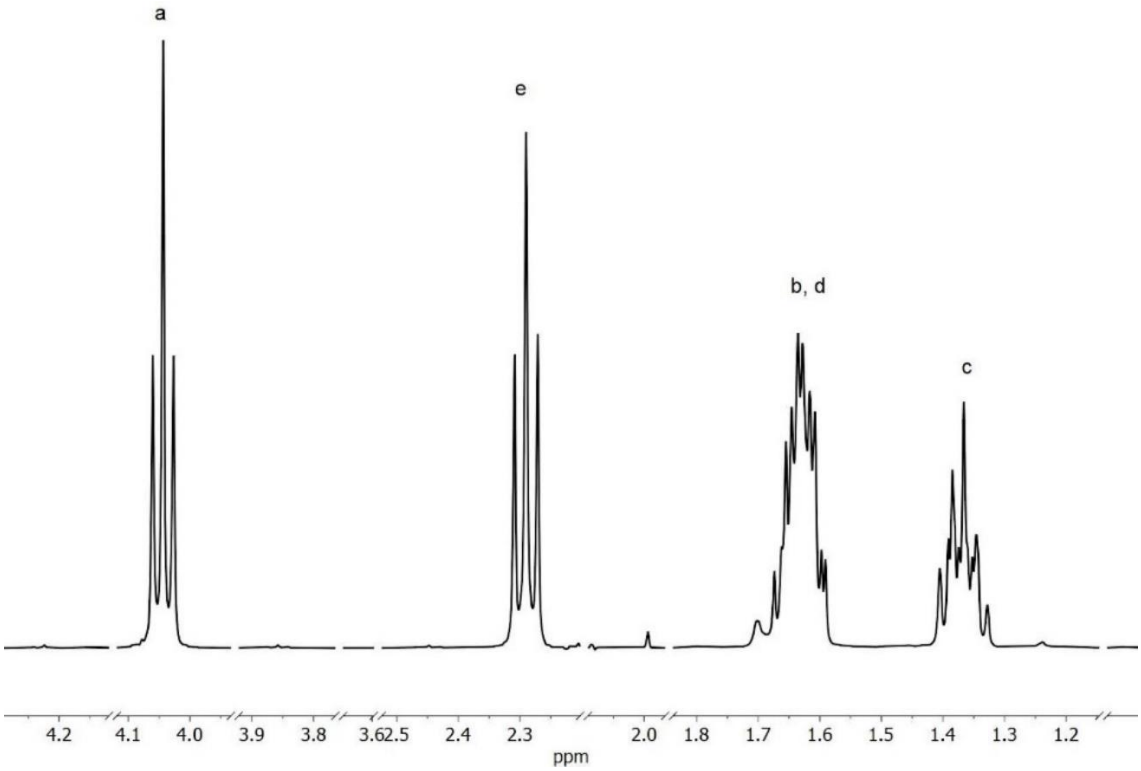

Figure 4.1 PCL NMR Peaks A Polycaprolactone with proteins denoted a-e **B** ^{1}H-NMR spectrum of PCL in $CDCl_3$ (300 MHz, 25°C), with peaks corresponding to PCL protons a-e identified.

4.2.4 Bulk Weight Loss

Prior to the *in vitro* incubation, each individual sample was weighed using a Sartorius Quintx semi-micro balance (Sartorius Lab Instruments GmbH, Germany). After the samples were removed at each time point, they were rinsed thoroughly in deionised water (DI) to remove any residual salts and dried in a vacuum oven overnight. Once completely dry, the samples were then weighed again on the same balance. The % weight difference was then calculated for each sample.

4.3 Results

4.3.1 Topographical Changes

SEM images were obtained of PCL fibres after incubation in PBS at pH 4 and pH 7 for 4, 8 and 12 weeks, as shown in **Figure 4.2**. Fibre diameters were visibly smaller at weeks 8 and 12 in both pH 4 and pH 7.

Fibre diameters were measured using ImageJ (see **Figure 4.3**). The fibres had an average diameter of 0.37 ± 0.13 µm prior to incubation. When incubated in pH 4 PBS, decreased significantly at each time point, and by week 12 had decreased to 0.14 ± 0.17 µm. In pH 7 PBS, the fibre diameter decreased until week 8, and did not continue to decrease after this point. The final fibre diameter of the samples incubated at pH 7 was 0.17 ± 0.05 µm. The fibre diameters in both pH conditions decreased at a similar rate until week 8, after which the fibres in the pH 4 environment continued to degrade.

This result suggests that the rate of degradation of the PCL fibres in both pH 4 and pH 7 is similar for 8 weeks, after which the fibres in pH 4 degrade more quickly.

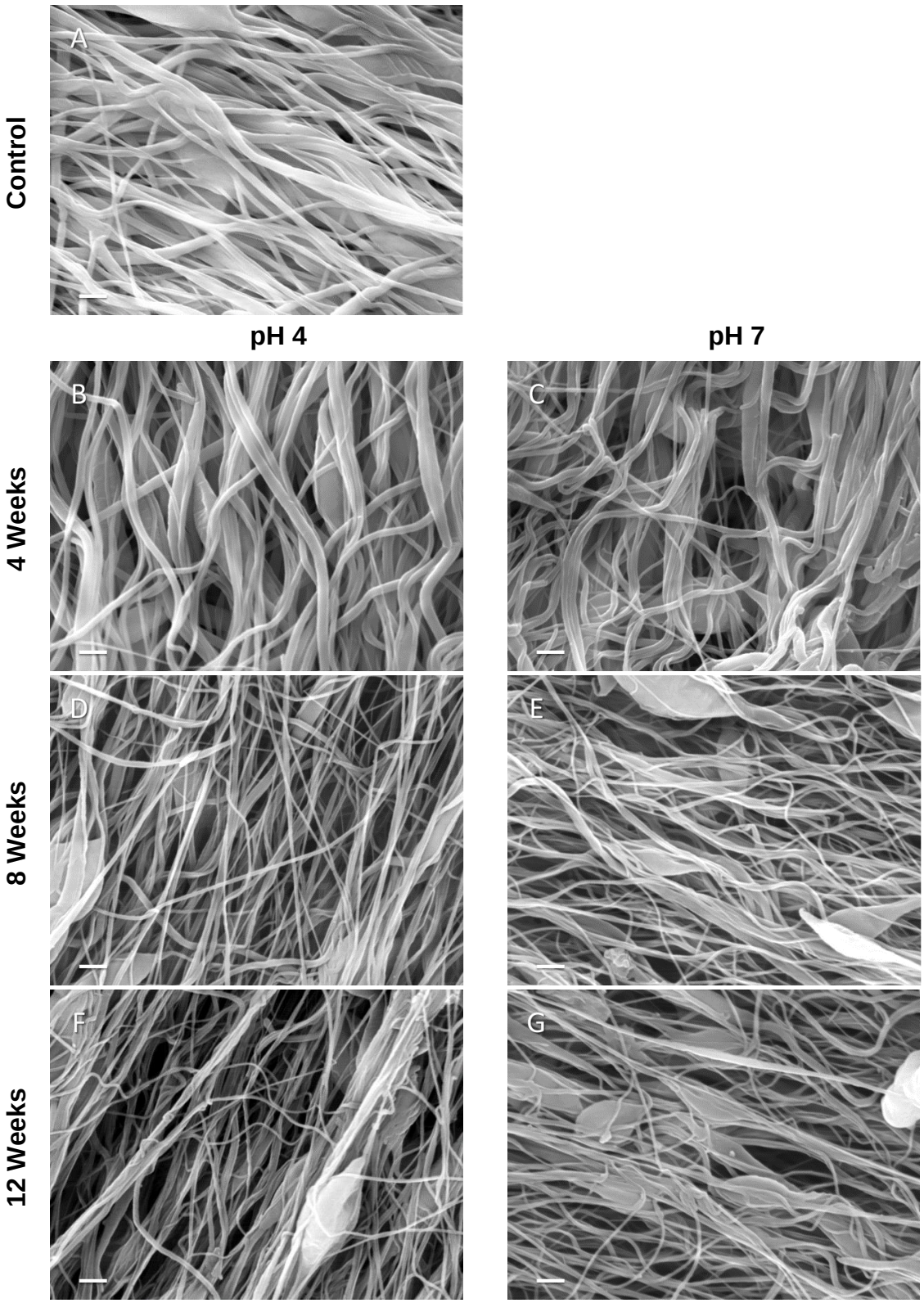

Figure 4.2 SEM images of electrospun PCL fibre degradation. SEM images of **A** control electrospun PCL fibres, and fibres after incubation at 37°C for B-C 4 weeks, **D-E** 8 weeks and **F-G** 12 weeks in **B**, **D**, **F** pH 4 PBS and **C**, **E**, **G** pH 7 PBS. Scale bar: 2 µm

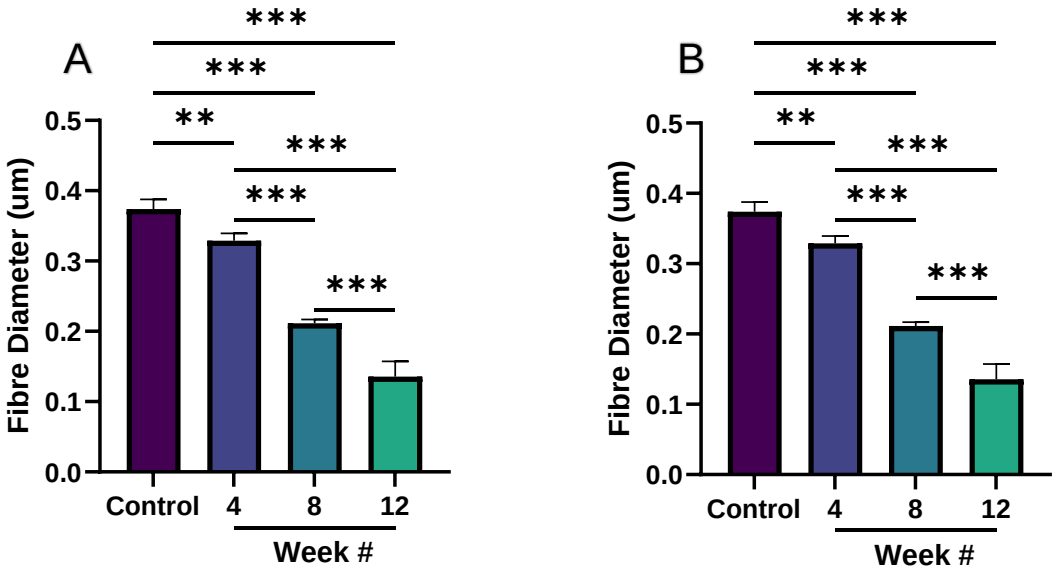

Figure 4.3 Degradation of electrospun PCL fibre diameter during *in vitro* degradation. Graphs comparing average diameters of electrospun PCL fibres after incubation at 37°C in PBS at **A** pH 4 and **B** pH 7 for 4, 8 and 12 weeks. Data presented as mean ± SE (N=3, n=100) with one-way ANOVA statistical test (** $p < 0.002$, *** $p < 0.001$).

4.3.2 Wettability

The wettability of the PCL fibres was determined via water contact angle testing after 4, 8 and 12 weeks of incubation in pH 4 and pH 7 PBS (see **Figure 4.4**).

Initially, the water contact angle (θ) of the control PCL fibres was 89 ± 9°. Following 4 weeks of incubation in pH 4 PBS, θ reduced significantly to 62.9 ± 3.1° and did not significantly change further. Incubation in pH 7 PBS for 4 weeks did not significantly alter the contact angle, but by week 8, a significant reduction 70 ± 4° was observed, with no further significant changes recorded thereafter.

After 8 weeks of *in vitro* degradation, neither the pH 4 or pH 7 exhibited significantly different wettability compared to the dECM, although the pH 4 fibres exhibited a more rapid decrease in contact angle.

After incubation in PBS, the water contact angle had reduced significantly, and the material exhibited hydrophilicity (θ ≤ 90°). These findings align with the known acceleration of hydrolysis under acidic conditions, which results in an increase in wettability[210].

Overall, these findings demonstrate the transition of the initially hydrophobic PCL material to a hydrophilic state upon incubation in PBS, with the rate of wettability alteration influenced by the pH of the medium due to its impact on the rate of hydrolysis.

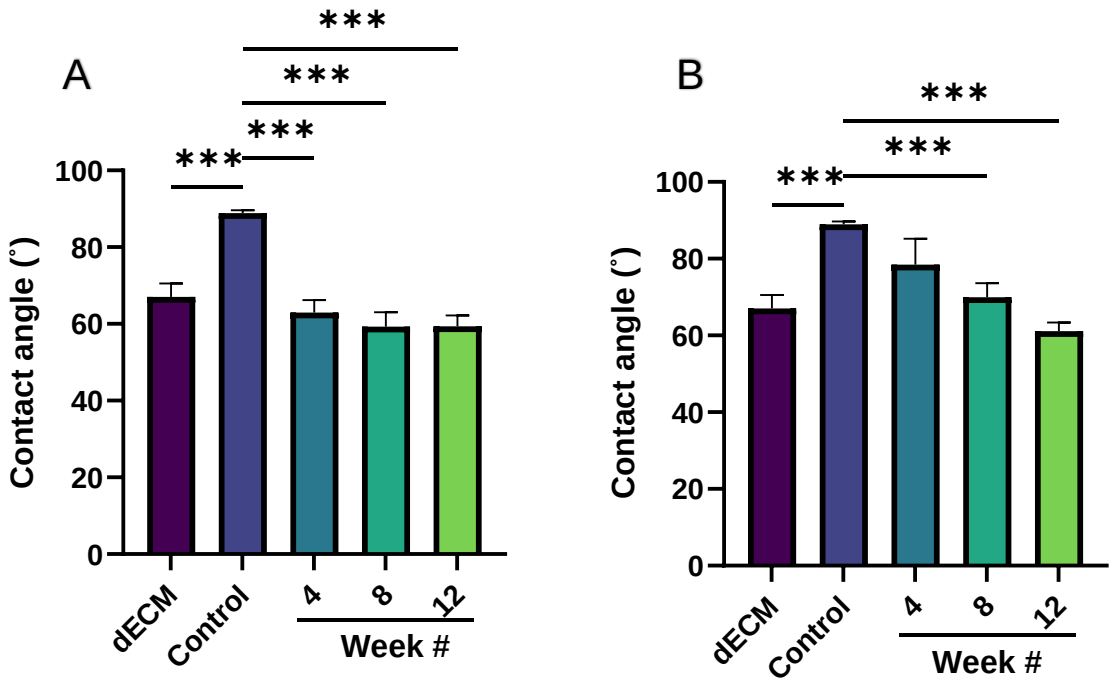

Figure 4.4 Changes in electrospun PCL fibre wettability during *in vitro* degradation. Graphs comparing the contact angle (θ) of PCL fibres after incubation at 37°C in PBS at **A** pH 4 and **B** pH 7 for 4, 8 and 12 weeks. Data presented as mean ± SD (N=6) with one-way ANOVA statistical test (*** $p < 0.001$).

4.3.3 Mechanical characterisation

The mechanical characteristics of electrospun PCL fibre sheets after *in vitro* degradation in both pH 4 and pH 7 PBS were assessed using tensile testing.

The elastic modulus of the tissue was previously found to be 0.3 ± 0.3 MPa. The control sample for the pH 4 condition had an elastic modulus of 42 ± 7 MPa (see **Figure 4.5A**). After 4 weeks this had significantly decreased to 30 ± 4 MPa. Subsequent to week 8, the elastic modulus had significantly decreased further to 8 ± 2 MPa, and did not significantly decrease any further. However, by 12 weeks the elastic modulus was 4 ± 3 MPa, which was not statistically significantly different to the tissue.

The control sample for the pH 7 condition had an elastic modulus of 26 ± 10 MPa (see **Figure 4.5B**). At week 4 this had significantly dropped to 8 ± 2 MPa and did not significantly decrease any further. However, the elastic moduli after 8 and 12 weeks were 6.5 ± 0.9 MPa and 7 ± 1 MPa respectively which, while still greater, were not statistically significantly different from the tissue.

The UTS of the tissue was previously found to be 1.4 ± 0.5 MPa. The control sample for the pH 4 condition had a UTS of 2.7 ± 0.7%, which was significantly greater than that of the tissue (see **Figure 4.6A**). After 4 and 8 weeks this had not significantly changed. However, after 12 weeks of incubation the UTS had significantly dropped to 0.67 ± 0.2, which was also significantly different from the week 4 sample. The samples incubated for 4, 8 and 12 weeks had a UTS that was not significantly different from that of the tissue.

For the pH 7 condition, the control sample had a UTS of 2 ± 1 MPa (see **Figure 4.6B**). This had dropped after 4 and 8 weeks, although not significantly. After 12 weeks of

incubation the UTS had dropped to 0.84 ± 0.4 MPa. The UTS of the samples incubated for 4, 8 and 12 weeks was not significantly different from that of the tissue.

Changes in the maximum extension of the electrospun PCL fibres during *in vitro* degradation were also investigated (see **Figure 4.7**). The maximum extension of the tissue was 140 ± 10 %.

For the pH 4 condition, the control sample had a maximum extension of 53 ± 9 %. Over 4 and 8 weeks, there was a reduction in maximum extension, although this change was not statistically significant. However, after 12 weeks of incubation, the maximum extension had significantly decreased to 20 ± 10%.

For the pH 7 condition, the control sample had a maximum extension of 20 ± 10%. After 4, 8 and 12 weeks there were no significant changes in maximum extension observed. The control samples and therefore those at each timepoint had a significantly lower maximum extension than the porcine oesophageal tissue.

These findings underscore the previous observation that the degradation of the PCL fibres was accelerated in the pH 4 condition, attributable to the increased rate of hydrolysis.

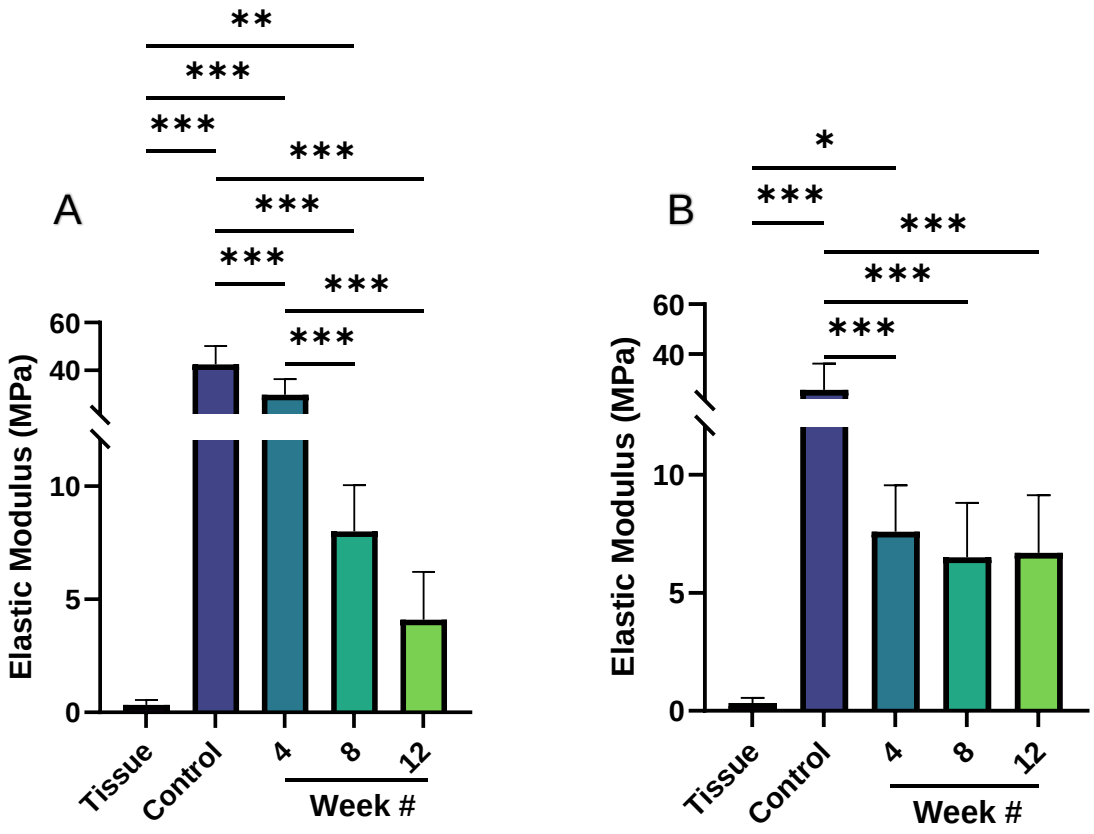

Figure 4.5 Changes in elasticity of electrospun PCL fibres during *in vitro* degradation. Graphs comparing the elastic modulus (E) of PCL fibres after incubation at 37°C in PBS at **A** pH 4 and **B** pH 7 for 4, 8 and 12 weeks. Data presented as mean ± SD (n=5) with one-way ANOVA statistical test (* $p < 0.003$, *** $p < 0.001$).

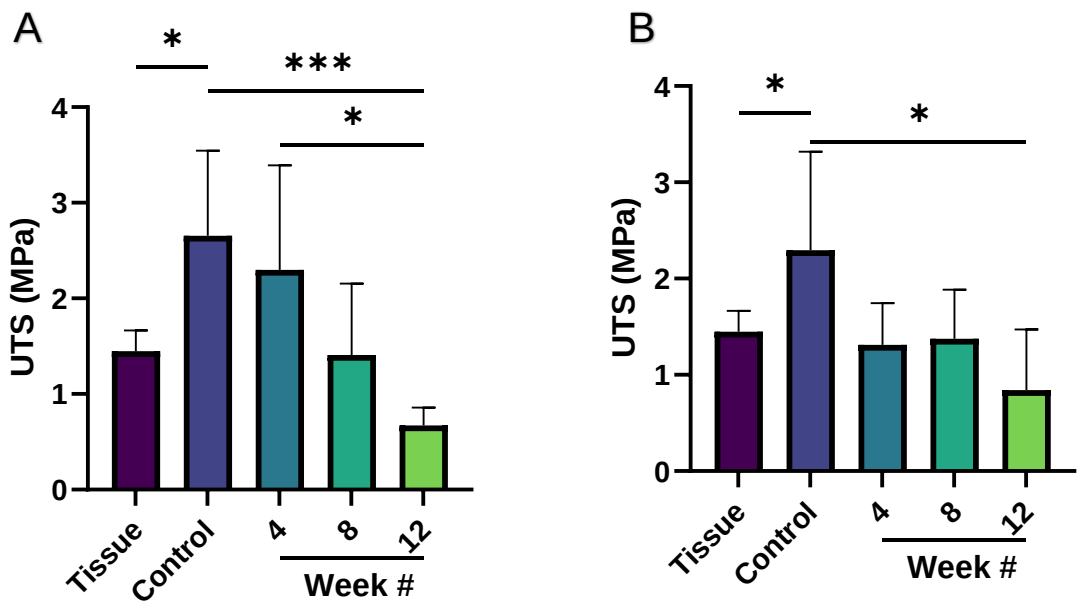

Figure 4.6 Changes in UTS of electrospun PCL fibres during *in vitro* degradation. Graphs comparing the UTS of PCL fibres after incubation at 37°C in PBS at **A** pH 4 and **B** pH 7 for 4, 8 and 12 weeks. Data presented as mean ± SD (n=5) with one-way ANOVA statistical test (* $p < 0.003$, *** $p < 0.001$).

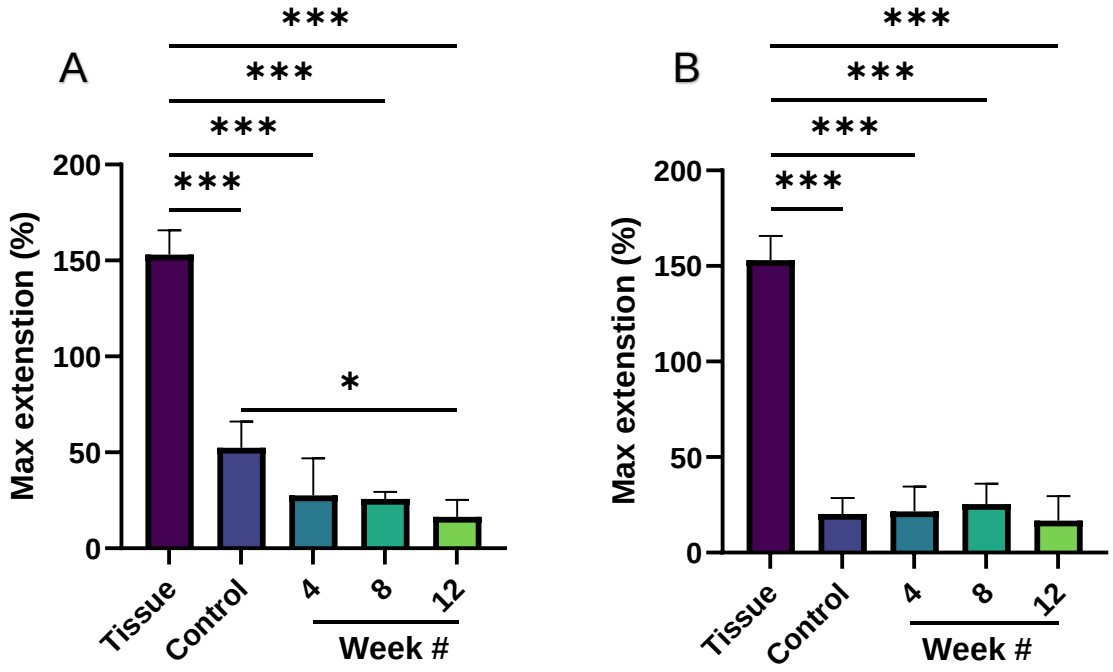

Figure 4.7 Changes in maximum extension of electrospun PCL fibres during i*n vitro* degradation. Graphs comparing the maximum extension of PCL fibres after incubation at 37°C in PBS at **A** pH 4 and **B** pH 7 for 4, 8 and 12 weeks. Data presented as mean ± SD (n=5) with one-way ANOVA statistical test (* $p < 0.003$, *** $p < 0.001$).

4.3.4 Weight loss

Before *in vitro* degradation, each PCL fibre sample was weighed. After the samples were removed for each time point they were rinsed, dried and weighed again. The % weight difference was calculated for each individual sample (see **Figure 4.8**). There was no observable bulk weight loss at either the pH 4 or pH 7 condition, and there was no significant difference between the two conditions.

However, to determine if there was any change in the molecular weight of the fibres during the degradation, NMR spectroscopy was carried out. The degree of polymerisation was estimated for each sample by analysing the NMR spectra, which could be used to estimate the molecular weight of the PCL.

The control fibres had a molecular weight of 277 ± 9 kg/mol. After forced degradation via hydrolysis in 1M NaOH the molecular weight was 10 ± 1 kg/mol.

After incubation in PBS at pH 4 for 4 and 8 weeks the molecular weight had significantly reduced to 150 ± 8 kg/mol and 77 ± 11 kg/mol, respectively. Both the week 4 and 8 molecular weights were significantly different from the hydrolysed sample. By week 12, the pH 4 sample had degraded further to 30 ± 3 kg/mol, which was no longer significantly different from the hydrolysed PCL.

In contrast, after incubation at pH 7 for 4 weeks, the molecular weight of the PCL was 256 ± 6 kg/mol, which had not significantly changed from the control sample. However, after 4 and 8 weeks, the molecular weight was 235 ± 5 kg/mol and 88 ± 3 kg/mol respectively, both of which had significantly reduced from the control sample. All the pH 7 time points were significantly larger than the hydrolysed PCL.

In addition to the differences from the controls, the time points all had significantly different molecular weights from each other.

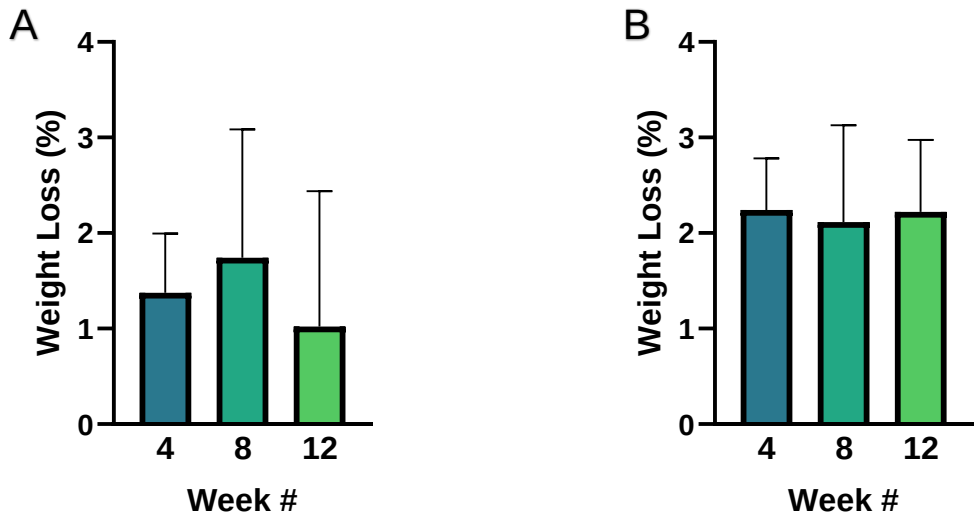

Figure 4.8 Bulk weight loss of electrospun PCL fibres during *in vitro* degradation. Graphs comparing the % weight loss of PCL fibre sheets after incubation at 37°C in PBS at **A** pH 4 and **B** pH 7 for 4, 8 and 12 weeks. Data presented as mean ± SD (n=6).

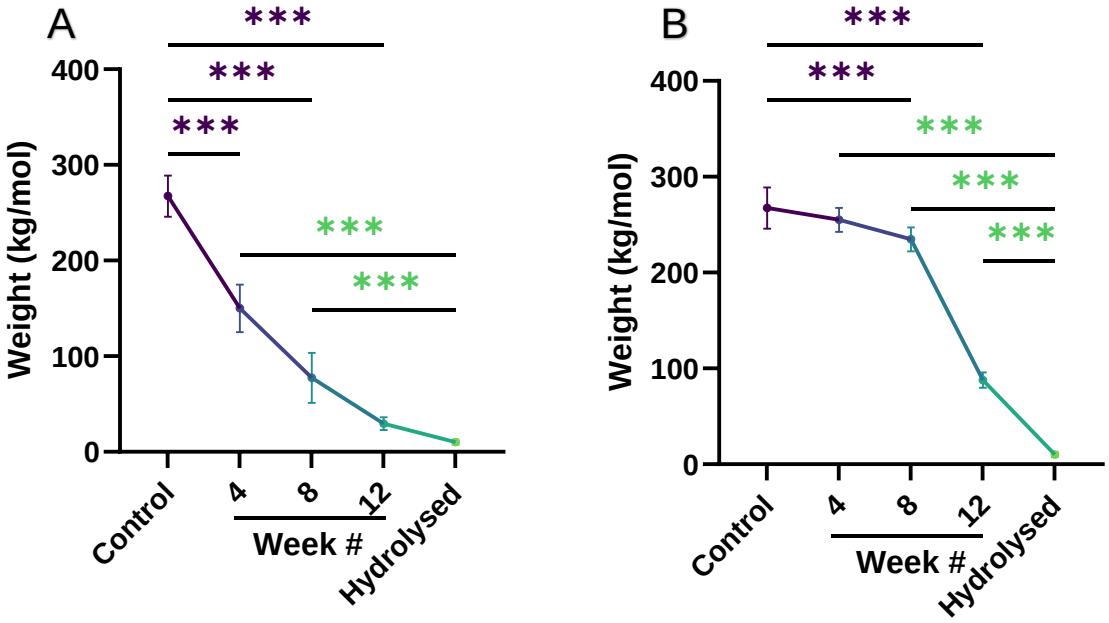

Figure 4.9 Molecular weight loss of PCL fibres during *in vitro* degradation. Graphs comparing the molecular weight of PCL fibres after incubation at 37°C in PBS at **A** pH 4 and **B** pH 7 for 4, 8 and 12 weeks. Data presented as mean ± SD (n=3), with one-way ANOVA statistical test (*** $p < 0.001$).

4.4 Discussion

This study of the electrospun PCL fibres' degradation under different pH conditions has revealed crucial insights relevant to their application in biomedical environments where there is a fluctuation in pH, such as the oesophagus.

There was an observed decrease in fibre diameter over time in both pH 4 and pH 7, with a more dramatic and prolonged degradation in pH 4. This aligns with previous findings that acidic conditions will accelerate the hydrolysis stage of PCL degradation[258].

The change from hydrophobic to hydrophilic of the PCL fibre sheets is also notable. Initially, the PCL material was hydrophobic ($\theta \geq 90°$), but after incubation in PBS this had reduced significantly and the material exhibited hydrophilicity ($\theta \leq 90°$). After 4 weeks of incubation at both pH 4 and pH 7, the contact angle of the PCL fibres was similar to that of decellularised porcine oesophagus ECM. This shift is beneficial for biomaterial scaffolds, as hydrophilic surfaces enhance cell attachment and proliferation, while hydrophobic surfaces can prevent cell attachment[263–265]. This effect could potentially improve the PCL fibres' suitability for use as tissue engineering scaffolds, especially considering the similarity of the resulting contact angle to that of oesophageal dECM.

The decrease in the elastic modulus of PCL fibre sheets, which approach that of the natural tissue over the incubation period is another point of interest. Pre-incubation, the fibres were much stiffer than the oesophageal tissue, as indicated by the elastic modulus of the fibres. After incubation in PBS, the fibres became less stiff. This effect was more dramatic, and continued for a longer period at pH 4 than at pH 7.

The increase in elasticity is likely due to increased porosity of the bulk material, which is evident through the decrease in fibre diameter[258]. This is promising as it brings the stiffness of the fibres in the parallel direction more in line with that of the oesophageal tissue, which represents the potential for the material to become increasingly biomimetic of the native tissue over time, which could help its suitability for implantation.

However, it is important to note the decrease in the ultimate tensile strength (UTS) and maximum extension, particularly in the pH 4 environment.

The UTS of the PCL fibres prior to incubation was significantly higher than the tissue. During *in vitro* incubation, the UTS decreased, but after 12 weeks was not lower than the tissue in either pH 4 or pH 7.

The maximum extension of the PCL fibres was significantly lower than the tissue, however the tissue is redundantly elastic, meaning that it never stretches to its maximum capacity *in situ*. The maximum extension changed very slowly over time, only significantly decreasing from the control sample after 12 weeks of incubation in pH 4 PBS.

While the UTS aligns with that of the tissue after 12 weeks, the significant reduction in maximum extension in both environments may raise concerns about the mechanical suitability of the fibres in long-term conditions. Determining the rate of tissue regeneration, and determining if there is enough ECM deposition to replace the structural support lost by this degradation would be important next steps to determining appropriate use of the material.

The degradation of the PCL is most apparent at the molecular scale, with significant degradation being apparent from week 4 in pH 4 PBS.

The observed degradation patterns of PCL fibres in different pH environments highlight the impact of pH on PCL stability and degradation rate, which is crucial for biomedical applications. The faster degradation in acidic conditions (pH 4) aligns with the general understanding that acidic environments accelerate hydrolysis. This has implications for their use in environments where the pH may vary, such as the oesophagus.

While this study provides valuable insights into the degradation behaviour of PCL fibres under different pH conditions, it is important to acknowledge that it does not completely model all *in vivo* conditions that an oesophageal implant would experience. One significant factor is the mechanical forces that are present in the oesophageal environment. Mechanical stretching due to the peristaltic action of the surrounding tissue, as well as the movement of food boluses, could contribute to implant erosion and impact the mechanical integrity of the scaffold. These dynamic mechanical forces are a critical aspect of the *in vivo* environment that were not replicated in this *in vitro* study, and they could significantly affect the long-term performance and degradation behaviour of the PCL fibres.

Studies of other stromal cell-seeded oesophageal regeneration biomaterials provide valuable insights into the tissue regeneration timeline. Neo-tissue has been observed as early as 30 days post-implantation in some studies, with complete epithelialisation achieved by 90 days[266]. Interestingly, the regenerated tissue appeared almost identical to normal oesophagus at 365 days, indicating a prolonged remodelling phase, However, the complete regeneration of muscle layers had not been achieved even at

this stage. This prolonged remodelling period extending to at least a year, underscores the importance of understanding the long-term behaviour of biomaterials for oesophageal regeneration.

Given these considerations, future research should focus on *in vivo* studies that can replicate these mechanical and biological aspects of the oesophageal environment. This could provide a more comprehensive understanding of the performance of PCL fibres as scaffolding materials in oesophageal tissue engineering. Additionally, investigating the interaction of these fibres with various cellular components under dynamic, mechanical conditions akin to those in the human oesophagus would offer further insights into their suitability for clinical applications.

In conclusion, this study sheds light on the *in vitro* degradation behaviour of electrospun PCL fibres, revealing important insights into their suitability for biomedical applications, particularly in oesophageal tissue engineering. These findings demonstrate that observable effects of degradation can appear as early as 4 weeks into the degradation process. Analysis of the molecular weight of PCL fibres indicates that while bulk properties such as strength, fibre diameter and weight degrade slowly over a 12-week period, molecular weight degradation occurs significantly earlier, especially in acidic conditions, suggesting a critical stage in the degradation process that precedes macroscopic changes.

Furthermore, this study highlights the influence of environmental pH conditions on the degradation kinetics of PCL fibres. We observed that acidic conditions mimicking the oesophageal environment accelerate the degradation of PCL fibres over the first 12 weeks of in vitro degradation. This underscores the importance of considering pH

variations in biomedical applications where PCL scaffolds may be exposed to fluctuating pH levels.

While this study provides valuable insights into the degradation behaviour of PCL fibres, it is essential to acknowledge its limitations. The *in vitro* model used in this study may not fully replicate the complex *in vivo* conditions of the oesophageal environment, particularly regarding mechanical forces and dynamic cellular interactions. Future research should focus on *in vivo* studies to validate these findings and explore the long-term performance of PCL fibres in realistic physiological conditions.

5.0 Functionalisation and Sterilisation

5.1 Introduction

Polycaprolactone (PCL) has excellent mechanical properties, biodegradation behaviour and processability, making it an excellent material for biomedical engineering. However, the inherent lack of bioactivity of PCL presents a significant limitation, particularly in the context of tissue engineering, where directing cell responses can be pivotal for successful integration and regeneration[267,268]. An ideal bioactive scaffold provides a microenvironment that mimics the extracellular matrix (ECM), which not only ensures cell attachment and proliferation, but can also influence cell differentiation, ultimately contributing to the functional restoration of the tissue[269]. PCL is very stable and durable, however, in tissue engineering, where the ultimate goal is the integration of biomaterial scaffolds with the host tissue, physical support is not sufficient[147,270]. This lack of bioactivity exhibited by PCL restricts its ability to actively engage with host cells, limiting its influence on cell adhesion, migration and proliferation.

To address the lack of bioactivity of PCL, functionalisation with biomolecules has become a promising strategy. Among these molecules, fibronectin, which is a key ECM protein, plays a crucial role in cell adhesion and migration. By introducing fibronectin to PCL surfaces, a scaffold can become more bioactive, encouraging cell-material interactions[43,111,271,272]. Fibronectin is an adhesive glycoprotein with multiple binding sites that several cell types, including fibroblasts, interact with[271,273]. Fibronectin has been shown to promote fibroblast adhesion and migration into artificial ECM, and is also thought to play a role in cell-cell adhesion by serving as a bridge for integrin-integrin interactions[202,274]. Therefore, fibronectin has been explored as a suitable candidate for functionalisation of biomaterials lacking in bioactivity, and

several studies have shown that incorporating fibronectin onto polymer surfaces can have favourable effects on the responses of several cell types to the material[43,110,173,272,275].

Sterilisation is a pivotal step in developing an implantable biomaterial. Sterilisation is defined as the complete eradication of all microorganisms including bacteria, viruses and yeasts. This is distinct from disinfection, which is the elimination of all microorganisms with the exception of bacterial spores[276–278]. During preliminary research and development, disinfection is often adequate to prepare a biomaterial for use in cell culture. However, once an implantable biomaterial reaches the clinic, sterilisation is essential. Given that the material properties of these biomaterials have usually been finely tuned to be optimal for their purpose, it is important to determine what effects, if any, the sterilisation or disinfection methods used have on a material's properties.

There is a wide range of sterilisation and disinfection methods used in biomaterial research[279–282]. Gamma radiation and ethylene oxide are both widely used to sterilise implantable medical devices[283]. However, these methods are often unsuccessful when used to sterilise biomaterial scaffolds due to their effects on the highly tailored material properties. By exploring these effects early in the biomaterial development process, it may be possible to incorporate them into the design of the material. Prior to *in vitro* testing, disinfection methods including 70% ethanol and UV radiation are commonly used, but their effects on material properties are often overlooked or unreported[277,282,284]. Given that PCL has a relatively low melting point of around 60°C, low temperature sterilisation is essential. Therefore, autoclaving, which is another commonly used sterilisation technique was deemed not suitable for use with the material[281,285].

Gamma radiation is an ionising radiation technique, that usually uses a cobalt-60 (^{60}Co) source to produce a dose of radiation in the range of 10-30 kGy/h[286]. The high energy gamma rays emitted by the source pass through a material and directly damage DNA and RNA strands, while generating reactive oxygen species (ROS). This radiation is able to eliminate bacteria, yeasts, viruses and bacterial spores, and results in sterilisation[283,287]. Gamma radiation has been shown to affect PCL properties in various ways including; decreasing molecular weight[288] and increased maximum stress[289].

Ethylene Oxide is a gas that causes permanent alkylation of molecules that contain amino, carboxyl thiol, hydroxyl and amide groups, which inactivates cell metabolism and division and is often used to sterilise medical devices[283]. This sterilisation method is advantageous as it is suitable for heat-sensitive materials. However, the gas itself is highly toxic, which introduces a problem if any residual gas remains after sterilisation, which is likely in highly porous materials[279]. Ethylene oxide is known to have significant effects on polymer properties including; decreased yield strength and an increase in degradation rate[283].

Ultraviolet-C (UV-C) radiation in the range of 200-300 nm inactivates cells by destroying DNA, making it an effective technique for eliminating viruses, bacteria and fungi. UV is a widely available and cheap disinfection method, and has been shown to have very little effect on the mechanical properties of PCL[290]. Ethanol is also a commonly used and cost-effective method for disinfection in *in vitro* testing. Ethanol disinfection has previously been reported to have very little effect on the mechanical properties of bulk PCL. There is less published data on the effects of UV and ethanol treatments on PCL properties, which is likely due to the fact that they are not suitable for terminal sterilisation. It is also important to consider that the reported changes in

properties after post-production processing are highly varied and often contradictory, seemingly due to variation in PCL molecular weight and processing parameters. It is also likely that the surface area to volume ratio of a material will impact how susceptible it is to the effects of these treatments.

This chapter will describe the functionalisation of electrospun PCL fibres with fibronectin, and investigate the effects of ethanol, ethylene oxide, UV and gamma treatment on the material's properties.

5.2 Methods

5.2.1 Functionalisation

The fibronectin functionalisation was based on two previously published protocols[43,173] Bovine fibronectin was diluted to 10 µg/mL in 1M (2-(N-Morpholino) ethane sulfonic acid hemisodium salt) MES buffer. Electrospun PCL fibres were immersed in 0.01M NaOH for 20 minutes at room temperature to hydrolyse the surface of the fibres. The fibres were then rinsed twice in MES and immersed in 0.01M HCl for 30 minutes at room temperature, followed by 2 further rinses in MES.

N-hydroxy succinimide (NHS) was attached via an N-(3-dimethylaminopropyl)-N'-ethyl carbodiimide hydrochloride (EDC) coupling through submersion in a 75 mg/mL NHS, 1.15 mg/mL NHS solution 0.1M MES buffer solution. An NHS ester is formed by a reaction between the PCL carboxylate and the NHS to form an unstable reactive O-acylisourea ester which has an activated leaving group. This unstable ester then reacts with the EDC, to form a semi-stable NHS ester, with an NHS leaving group.

The PCL fibres were then immersed in 3 mL of the fibronectin solution for 24 hours at 37°C. The NHS ester is highly reactive with amine nucleophiles (-NH_2 groups) and so the NHS leaving group is replaced by the fibronectin, forming a stable amide bond (see **Figure 5.1**). The fibres were rinsed and stored in 0.1M MES buffer at 4°C until required.

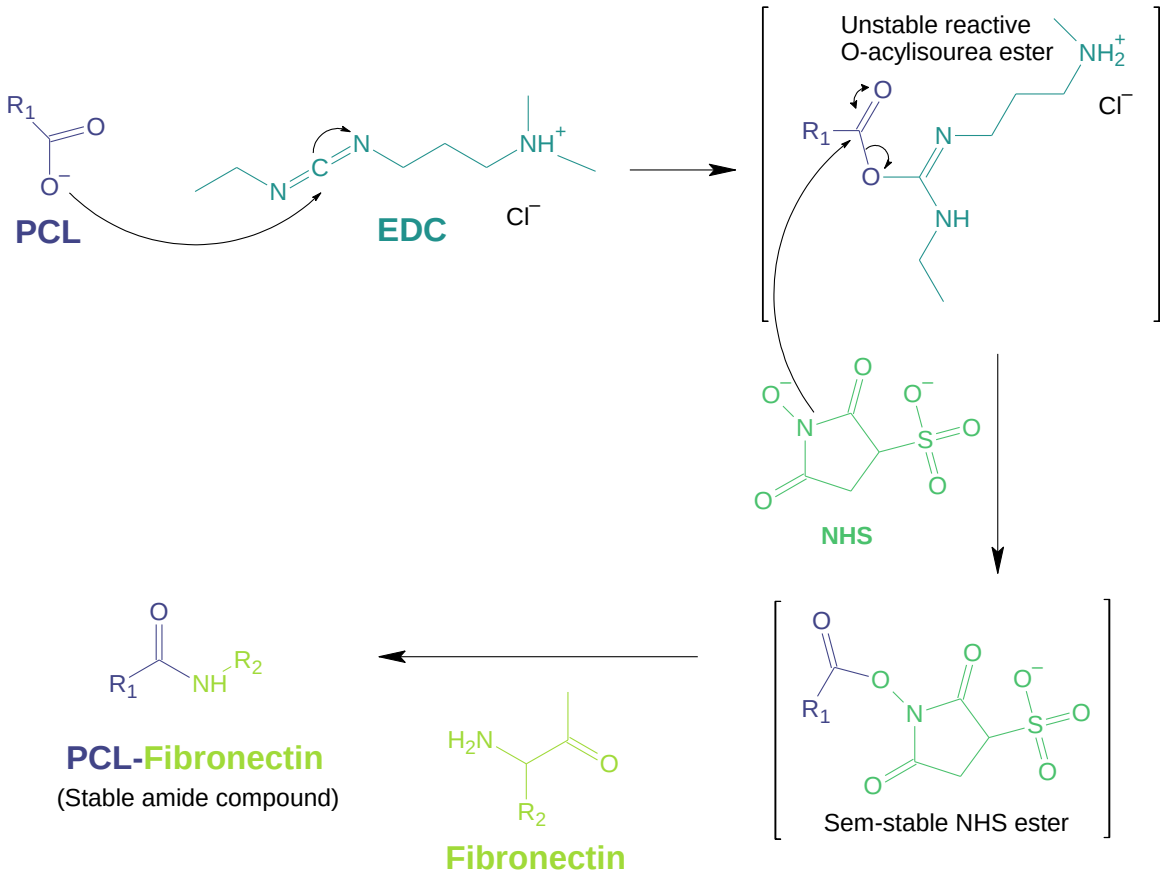

Figure 5.1 Mechanism of amine nucleophilic substitution for PCL functionalisation with fibronectin

5.2.2 Fluorescent Microscopy

To confirm the fibronectin functionalisation, pre- and post-functionalisation samples were immersed in a 1% BSA blocking buffer for 30 minutes at 37°C, followed by rinsing twice in PBS for 5 minutes. An Alexa Fluor® 488 tagged mouse anti-human fibronectin antibody was diluted to 2% v/v in the blocking buffer. Blocked samples were immersed in the antibody solution for 2 hours at room temperature on a rocking shaker. The stained samples were then rinsed twice in PBS for 5 minutes and imaged using an EVOS M500 fluorescent microscope.

5.2.2.1 Fluorescent Image Analysis

To quantify the fluorescence of the stained fibres, the fluorescent intensity of each image was determined using Image J. Each image was split into RGB channels, and the green channel was selected for analysis as it corresponded to the fluorescence of the tagged antibody. The Intensity of the image was determined using Image J. To account for background fluorescence, images of unstained fibres were captured under the same conditions. The green intensity of these unstained fibres was subtracted from the stained fibre images.

5.2.3 BCA Assay

A bicinchoninic acid (BCA) assay was used to detect changes in protein concentration in the fibronectin solution after it was used for electrospun fibre functionalisation. Once the functionalisation was complete, the fibronectin solution was removed and diluted to 3 mL (the original volume that was used) and two 3 mL PBS washes were retained. The BCA working reagent was added to triplicates of the fibronectin solutions and a set of BSA standards, and incubated at 37 °C for 30 minutes according to the supplier's recommendation. The colourimetric change of each replicate was determined by measuring the absorbance at 562 nm after the samples had cooled to room temperature. A Tecan Spark® microplate reader (Tecan Trading AG, Switzerland) was used to take these measurements. A standard curve was plotted using the absorbances of the BSA standards, which was then used to determine the protein concentration of each unknown sample.

5.2.4 Ethanol Treatment

Samples were placed in 70 % ethanol for 20 minutes at room temperature, and then washed in sterile PBS twice for 5 minutes, Samples were then placed in a desiccator cabinet overnight.

5.2.5 Ethylene Oxide Treatment

Samples were exposed to at least 450 mg/L of ethylene oxide at 37°C for at least 1 hour under vacuum.

5.2.6 UV Treatment

Samples were placed in the centre of a Thermo Scientific Safe 2020 Class II Biological Safety Cabinet (Thermo Scientific, USA), which was fitted with two lamp housing fitted with two UV lamps each. Samples were exposed to UV radiation for 30 minutes on each side, at a distance of 1m from each set of UV lamps, which had a wavelength of 253 nm.

5.2.7 Gamma Irradiation Treatment

Samples were sealed in sterilisation pouches and sent to Gargrave Sterilisation Services and irradiated at 30.9-33.0 kGy at 34.4 °C. This is above the minimum amount required to ensure appropriate sterility[291].

5.3 Results

5.3.1 Functionalisation

5.3.1.1 Topographical Characterisation of Functionalised Fibres

Electrospun PCL fibres were functionalised with fibronectin, as described above, in order to improve the material bioactivity and enhance cell-biomaterial interactions. Changes in fibre morphology after functionalisation were determined using SEM. No visual differences in fibre morphology were observed between non-functionalised and fibronectin-functionalised fibres (see **Figure 5.2**).

The average fibre diameter of the non-functionalised fibres was 0.4 ± 0.2 µm, and after functionalisation was not significantly different from the control fibres (see **Figure 5.3**). The functionalisation process did not affect the average diameter of the electrospun PCL fibres.

The functionalisation process did not visually affect the alignment of the fibres. This was investigated using the ImageJ plug-in OrientationJ, which generated data describing the alignment of fibres in each SEM image (see **Figure 5.4**). The image analysis showed that the initial fibre alignment was 42 ± 6 % and post-functionalisation the alignment was 39 ± 8 %, which was determined to not be significantly different from the control by an unpaired t-test.

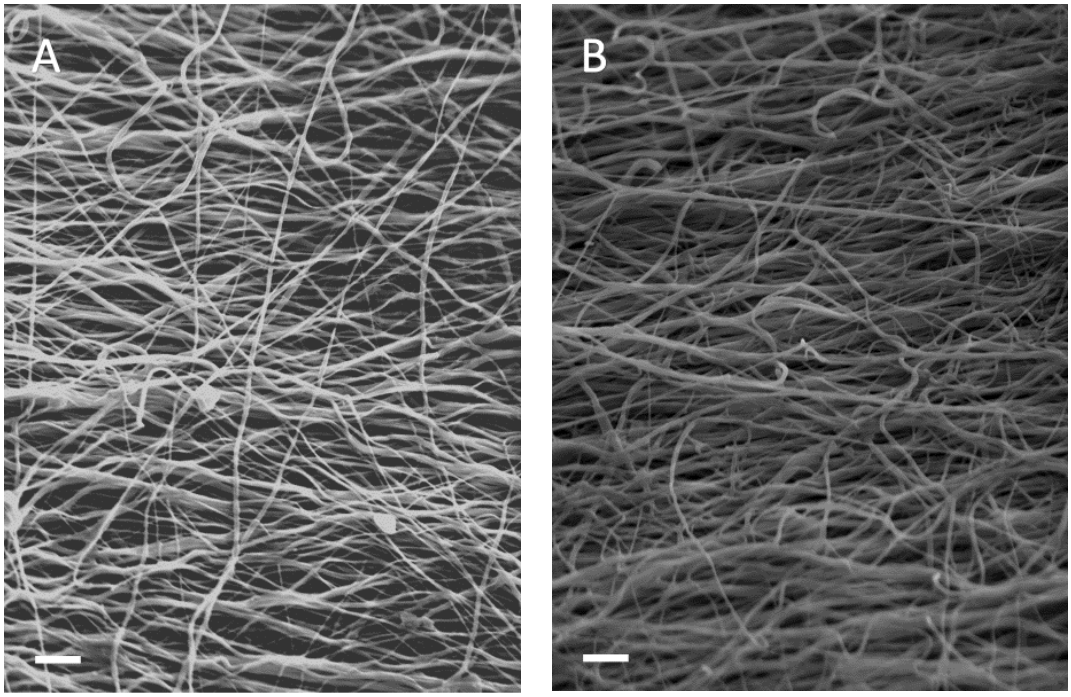

Figure 5.2 The effect of fibronectin functionalisation on electrospun PCL fibre morphology. SEM images of **A** non-functionalised electrospun PCL fibres and **B** fibronectin-functionalised electrospun fibres. Scale bar: 10 µm

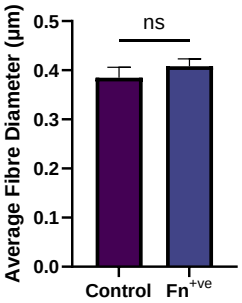

Figure 5.3 The effect of fibronectin functionalisation on electrospun PCL fibre diameter. Graph comparing the fibre diameters of electrospun PCL fibres pre- and post-functionalisation. Data presented as mean ± SE (N=3, n=100), with unpaired t-test test (ns p ≥0.05). The average fibre diameter of the non-functionalised fibres was 0.4 ± 0.2 µm. Post functionalisation, the average fibre diameter was 0.4 ± 0.2 µm.

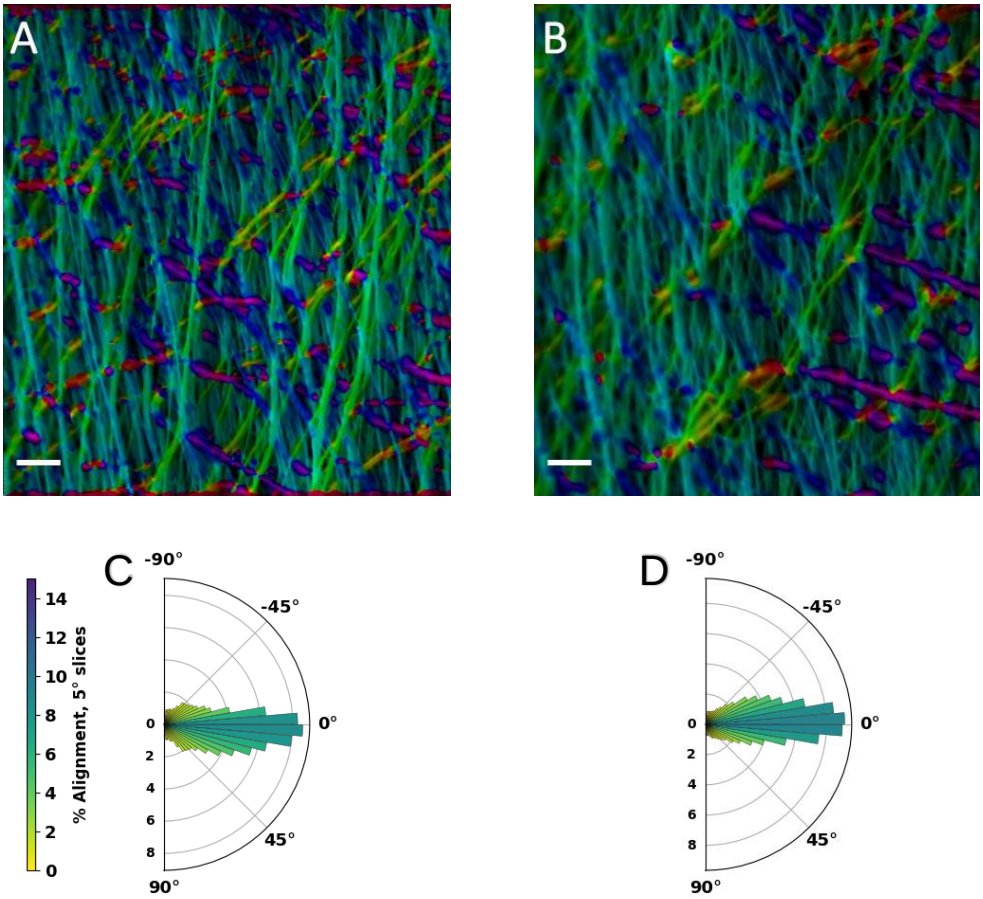

Figure 5.4 The effect of fibronectin functionalisation on electrospun PCL fibre alignment. Colour surveys produced using Image J showing fibre alignment of **A** non-functionalised and **B** fibronectin-functionalised electrospun PCL fibres Scale bars: 10 µm. The hue changes with the orientation, with the dominant direction being represented by cyan (rgb (0,255,255)) and perpendicular fibres being shown in red (rgb (255,0,0)).

The Orientation J plug-in for Image J was used to analyse the alignment of fibres in each SEM image. This data was plotted on a polar histogram **C** non-functionalised fibres and **D** fibronectin-functionalised fibres. Each bar represents a 5° slice of the SEM image, with 0° representing the dominant fibre direction. The length of the bar represents the proportion of the image (%) that is aligned with the dominant fibre direction. Darker coloured bars are longer.

One-way ANOVA performed using GraphPad Prism showed that the proportion of fibres aligned with the dominant fibre direction did not change significantly after functionalisation (n=3).

5.3.1.2 Mechanical Characterisation of Functionalised PCL Fibres

The mechanical properties of the electrospun PCL fibres were determined via tensile testing parallel to the direction of the fibre alignment, and compared to the properties of porcine oesophageal mucosa. The tissue had an elastic modulus (E) of 0.3 ± 0.3 MPa, while that of the non-functionalised fibres was 33 ± 4 MPa, which was significantly higher. After functionalisation, E was 35 ± 8 MPa, which was not significantly different from the non-functionalised fibres, and remained significantly higher than the tissue (see **Figure 5.5 A**).

The tissue had a UTS of 1.4 ± 0.5 MPa. The non-functionalised fibres had a UTS of 5.4 ± 0.5 MPa, which was significantly higher than the tissue (see **Figure 5.5 B**). After functionalisation, the UTS increased to 9 ± 2 MPa, which was significantly increased from the control fibres and the tissue.

The maximum extension of the tissue was 153 ± 27 %, which was significantly higher than that of the non-functionalised fibres (39 ± 18 %) (see **Figure 5.5C**). After functionalisation, the maximum extension was 51 ± 11 %, which was not significantly different from the control fibres, and remained significantly lower than the tissue.

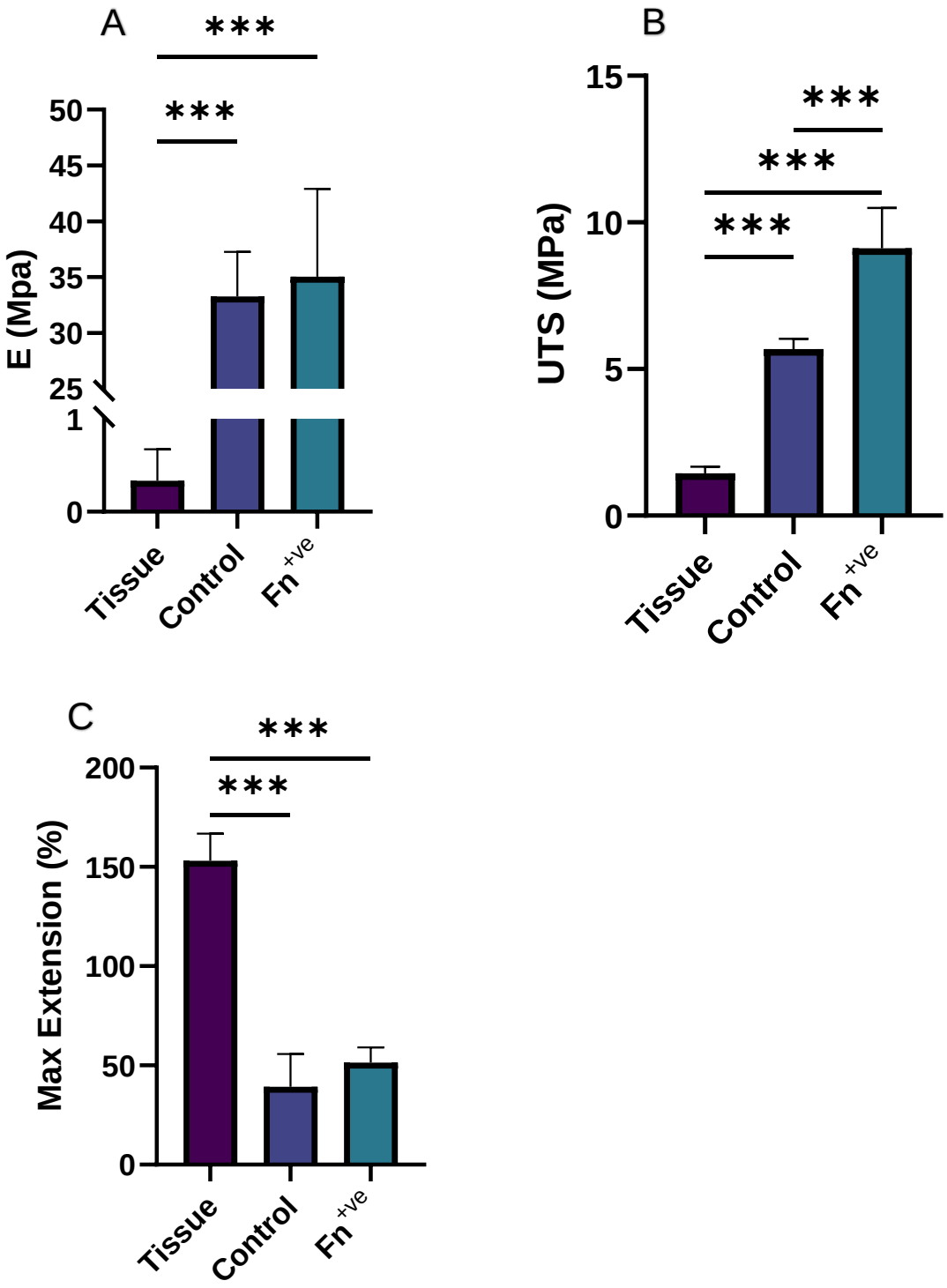

Figure 5.5 The effect of fibronectin functionalisation on the mechanical properties of electrospun PCL fibres. Graphs comparing **A** elastic modulus (E), **B** UTS and **C** of PCL fibres pre- and post- fibronectin functionalisation with porcine oesophageal tissue. Data is presented as mean ± SD (n=5) with one-way ANOVA statistical test (*** p <0.001).

5.3.1.3 Wettability of Functionalised PCL Fibres

Contact angle can be used as an indicator of the hydrophilicity of a material surface. PCL is known to be a hydrophobic material which hinders cell attachment, whereas fibronectin has been shown to increase hydrophilicity. The contact angle (θ) of the PCL fibres, functionalised fibres and porcine oesophageal dECM was determined (see **Figure 5.6**). The θ of the dECM was 67 ± 5°. The control PCL fibres had a θ of 141 ± 26°, which was significantly higher than that of the dECM. After functionalisation, θ dropped significantly to 89 ± 9°, which was not statistically significantly different than that of the dECM.

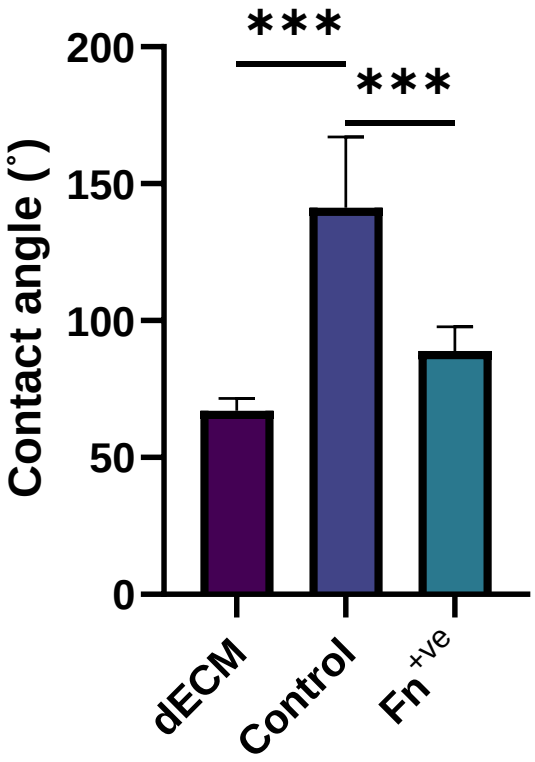

Figure 5.6 The effect of fibronectin functionalisation on the water contact angle of electrospun PCL fibres. Graph comparing the contact angle (θ) of control (non-functionalised) PCL fibres, fibronectin-functionalised fibres and porcine oesophageal dECM. Data is presented as mean ± SD (n=6) with one-way ANOVA statistical test (*** p <0.001).

5.3.1.3 Confirmation of Fibronectin Functionalisation

The fibronectin functionalisation was confirmed using fluorescent microscopy. After the functionalisation protocol was complete, the fibres were stained using a fluorescent tagged anti-fibronectin antibody to visualise the fibronectin. Non-functionalised samples were also stained and used as controls. When visualised using fluorescent microscopy, the control fibres showed a degree of fluorescence. However, the fluorescence was visually increased post-functionalisation (see **Figure 5.7 A-B**).

The fluorescent intensity of the functionalised fibres ($8.1 \times 10^7 \pm 0.9 \times 10^7$ a.u.) was significantly higher than that of the non-functionalised fibres ($0.3 \times 10^7 \pm 0.3 \times 10^7$ a.u.) (see **Figure 5.7 C**).

A BCA protein assay was used to determine the concentration of the fibronectin solutions at various points throughout the functionalisation process (see **Figure 5.8**). Before carrying out the functionalisation, the protein concentration in the fibronectin solution was 11.7 ± 0.2 µg/mL. Once the PCL fibres had been incubated in the fibronectin solution for 24 hours, the solution was removed and it was determined that it had a concentration of 3.5 ± 0.4 µg/mL, which was significantly less concentrated that the original solution. Subsequently, the fibres were washed twice in PBS to remove any unbound fibronectin. Each of these washes were determined to have a protein concentration of 1.4 ± 0.2 µg/mL and 0.4 ± 0.05 µg/mL respectively. The total fibronectin remaining on each PCL fibre sample post-functionalisation was around 18.6 µg per sample. \

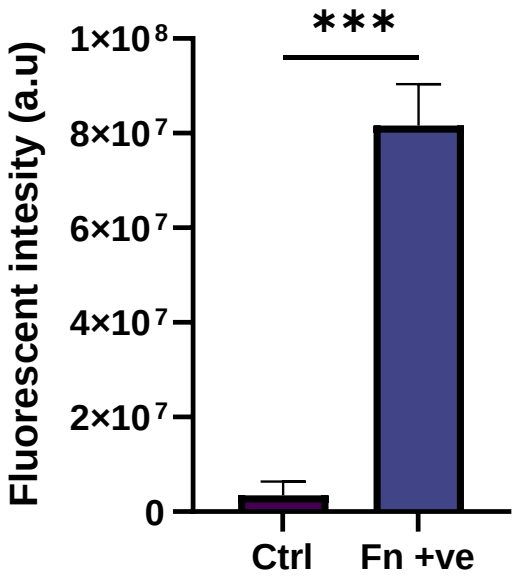

Figure 5.7 Fluorescent intensity of fibronectin-functionalised electrospun PCL fibres stained with a fluorescent-tagged anti-fibronectin antibody. Graph comparing the fluorescent intensity of control and functionalised fibres. Data presented as mean ± SD (n=3), with unpaired t-test test (*** p <0.001).

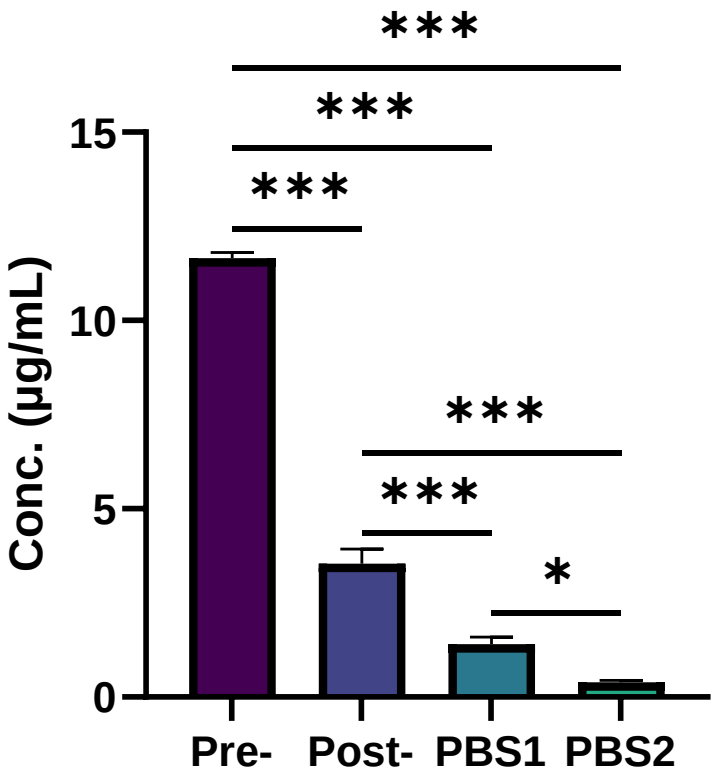

Figure 5.8 Graph comparing the protein concentration of the fibronectin solution used for functionalisation of electrospun PCL fibres. A BCA protein assay was carried out to determine the concentration of the fibronectin solution at various points throughout the functionalisation process. The protein concentration of the solution prior to functionalisation (pre-) was 11.7 ± 0.2 µg/mL. After incubation on the electrospun PCL fibres (post-), the concentration of the solution was to 3.5 ± 0.4 µg/mL. Two PBS washes (PBS1 and PBS2) were then used to remove any unbound fibronectin. These washes had concentrations of 1.4 ± 0.2 µg/mL and 0.4 ± 0.05 µg/mL respectively. Data is presented as mean ± SD (n=3), with one-way ANOVA statistical test (* $p < 0.033$, *** $p < 0.001$).

Raman spectra were obtained of the fibronectin, the PCL prior to electrospinning and the electrospun PCL fibres (see **Figure 5.9**). In the PCL spectrum, there are defined peaks at 2914cm-1 (CH stretching), 1723cm-1, (C=O stretching), 1441cm-1 (CH2 bending), 1304cm-1 (CH2 twisting), 913cm-1 (C-COO stretching) and a set of peaks between 1003 and 1110 cm-1 (C-C stretching). This spectrum is characteristic of PCL[233,234,292].

In the fibronectin spectrum, there were defined peaks at 2914 cm-1 (C-H stretching) and 790 cm-1, which was identified as Si-O-Si stretching, and was explained by the glass coverslip which the fibronectin had been isolated on. In the fibronectin spectrum there were also peaks between 1003 and 1110cm-1 (C-C stretching), which showed a slightly different pattern from the peaks in the same range in the PCL spectrum.

The functionalised PCL spectrum included all of the characteristic peaks of PCL, but the 2914 cm-1 peak, which represents the vCH bond stretching, was higher in the functionalised PCL than either of the other two spectra.

Given that the fibronectin and PCL spectra have characteristic peaks in similar areas, they could not be used to confirm the presence of fibronectin on the functionalised fibres, as the fibronectin peaks could be masked by the stronger PCL shifts in the same regions. However, this is useful as it shows that the PCL retains it characteristic peaks after the functionalisation process.

In order to determine the crystallinity of the electrospun PCL fibres, the band in the region 1710-1750 cm^{-1}, which corresponds to C=O stretching) was deconvoluted into two gaussian peaks centred at 1724 cm^{-1} (corresponding to the crystalline phase) and at 1732 cm^{-1} (which corresponds to the amorphous phase)[213,293]. These peaks were integrated, and these values were used to calculate the fraction of crystalline phase

(see **Figure 5.10**). The crystalline phase of the non-functionalised and fibronectin-functionalised fibres were found to be 61 ± 2 % and 60.4 ± 0.6 % respectively. These values were not significantly different from each other, which confirms that the functionalisation did not affect the crystalline fraction of the electrospun PCL fibres.

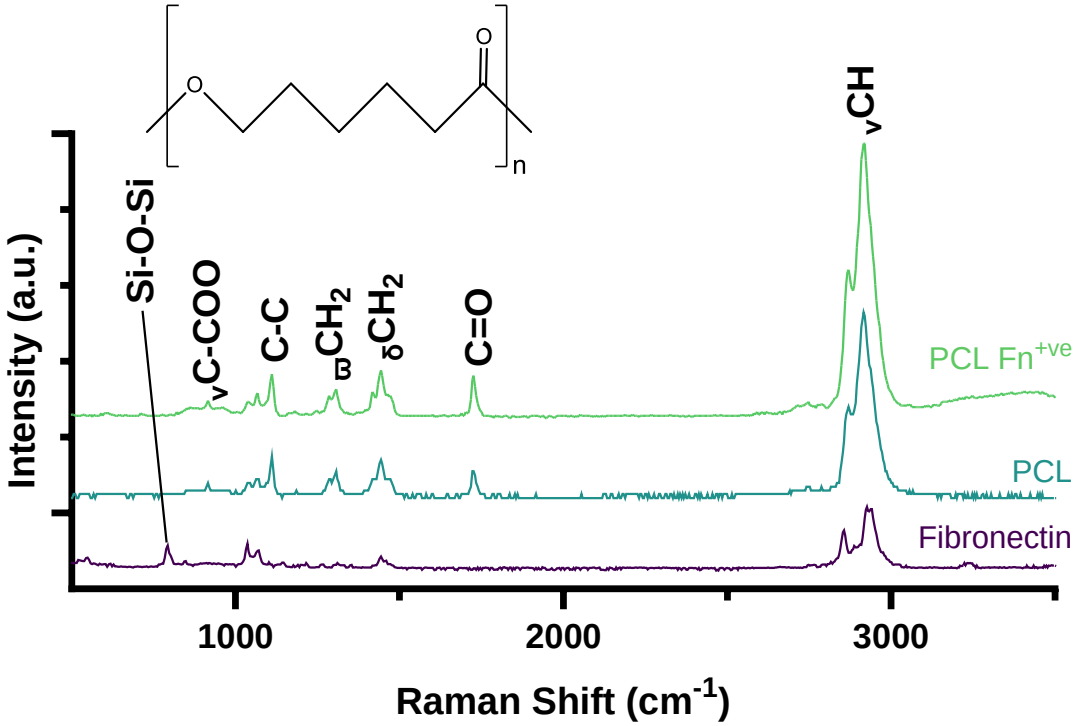

Figure 5.9 Raman spectra of fibronectin-functionalised PCL fibres. Raman spectra analysis of fibronectin, non-functionalised PCL and functionalised PCL in the spectral range of 0-4000 cm^{-1}, 532nm laser line. Inset: PCL structure.

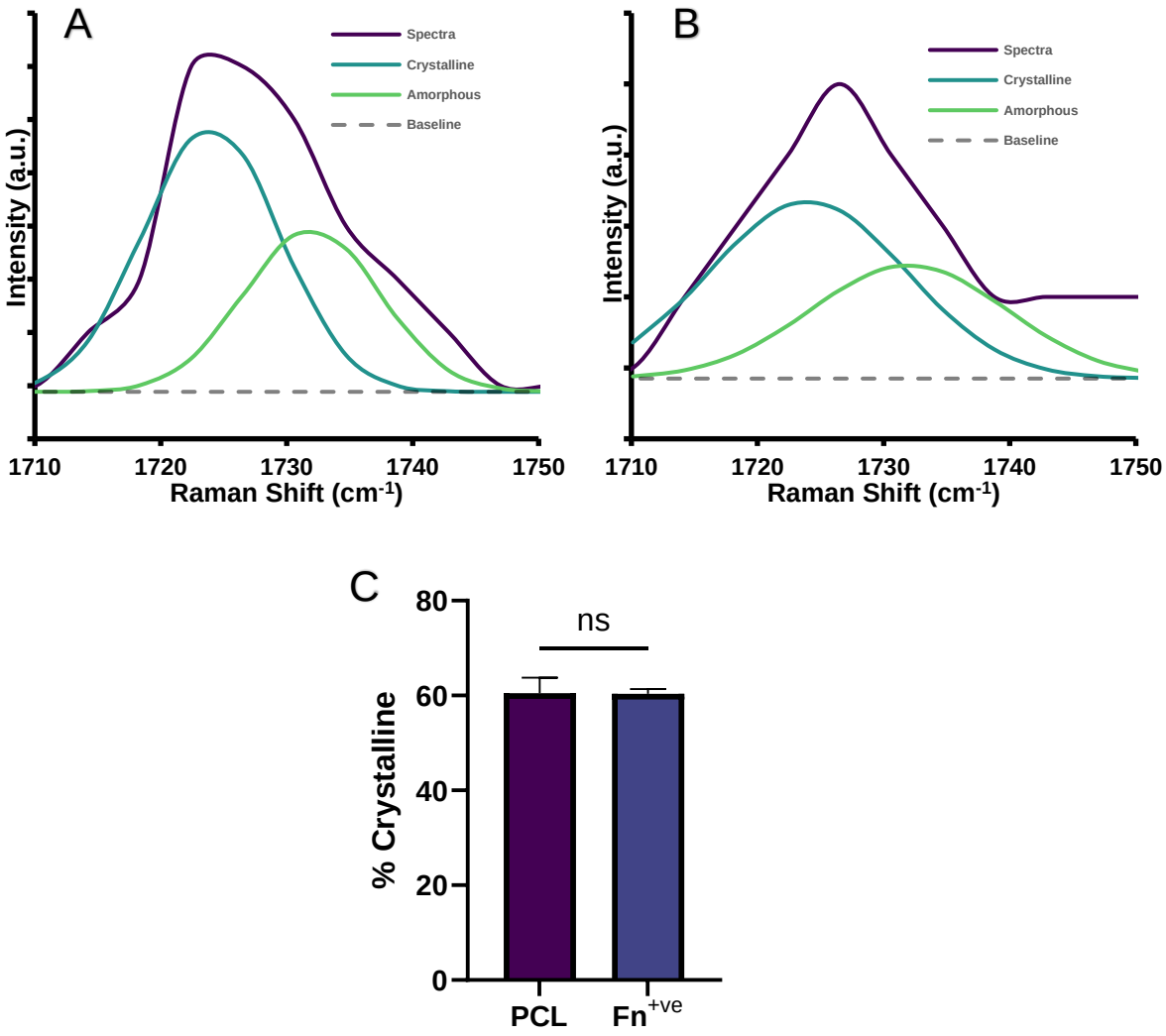

Figure 5.10 The effect of fibronectin functionalisation on electrospun PCL fibre crystallinity. Raman spectral region 1710-1750 cm^{-1} of **A** non-functionalised and **B** fibronectin-functionalised electrospun PCL fibres, showing the contribution of the crystalline and amorphous fractions. **C** Graph showing the crystalline fractions of electrospun PCL fibres. Data presented as mean ± SD (n=3), with unpaired t-test test (ns $p \geq 0.05$).

5.3.1.4 Cell Viability on Functionalised PCL Fibres

Primary oesophageal fibroblasts were cultured on electrospun PCL fibres functionalised with fibronectin to investigate their viability compared to cells cultured on tissue culture plastic and non-functionalised fibres. Cells were cultured on each material for five days at 37°C, at which point the fibre samples were moved into new wells.

Fluorescent microscopy images were generated of the stained cells (see **Figure 5.11**). ImageJ software was used to determine the number of live and dead cells in each image. The cell viability was calculated as a percentage of live cells of the total number of cells in each image. The viability of the fibroblasts cultured on tissue culture plastic was 85 ± 6 % after 5 days. On the non-functionalised PCL fibres, the viability dropped significantly to 34 ± 12 %, but when cultured on the fibronectin-functionalised fibres, the cell viability was 78 ± 10 % after 5 days, which was not significantly different than the fibroblasts cultured on the tissue culture plastic. This demonstrates that the addition of fibronectin to the electrospun PCL fibres enhances cell viability. The significant drop in cell viability observed on the non-functionalised fibres suggests that the surface properties of the material alone do not support optimal cell attachment and survival. The presence of fibronectin, known for its role in cell adhesion and proliferation, promotes enhanced cell-material interactions, thereby fostering a more favourable microenvironment for cell growth and viability.

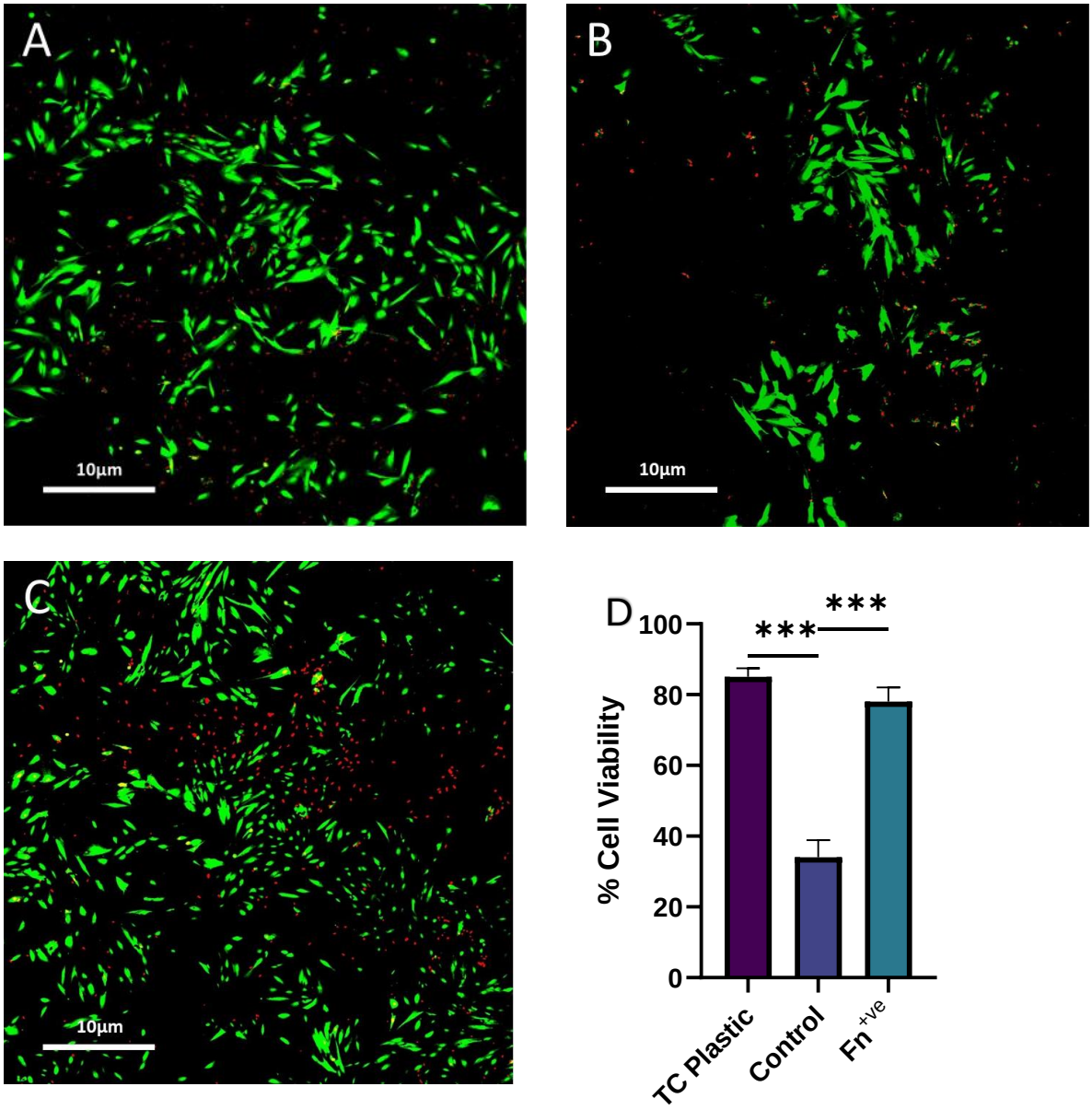

Figure 5.11 Live/Dead staining of fibroblasts cultured on electrospun PCL fibres after 5 days. Representative images of primary oesophageal fibroblasts cultured on **A** tissue culture plastic (control), **B** non-functionalised electrospun PCL fibres and **C** fibronectin-functionalised PCL fibres for 5 days, stained with calcein AM and EthD-1. Live cells are stained green, dead cells are stained red. **D** Graph comparing the % cell viability of fibroblasts cultured on tissue culture plastic, non-functionalised and functionalised electrospun PCL fibres. Data presented as mean ± SEM (n=6), with one-way ANOVA statistical test (*** p <0.001).

5.3.2 Sterilisation

5.3.2.1 Effects of Sterilisation Treatments on PCL Fibre Topography

Electrospun PCL fibres were treated with four disinfection and sterilisation methods; ethanol, ethylene oxide, gamma irradiation and UV radiation.

SEM images revealed the effects of these treatments on non-functionalised fibre morphology (see **Figure 5.12**). Untreated non-functionalised fibres displayed smooth, aligned morphology and were free from beading. Non-functionalised fibres treated with ethanol and ethylene oxide exhibited a slightly melted appearance and disrupted fibre alignment. Non-functionalised fibres treated with gamma and UV radiation retained a smooth surface morphology comparable to the untreated fibres, with no observable melting effects.

SEM was also used to investigate the effects of the treatments on fibronectin-functionalised fibres (see **Figure 5.13**). The treatments had a very similar effect on the visible morphology as the non-functionalised fibres. The ethanol and ethylene oxide treated fibres had a melted appearance, with beads of PCL appearing where fibres had fused together.

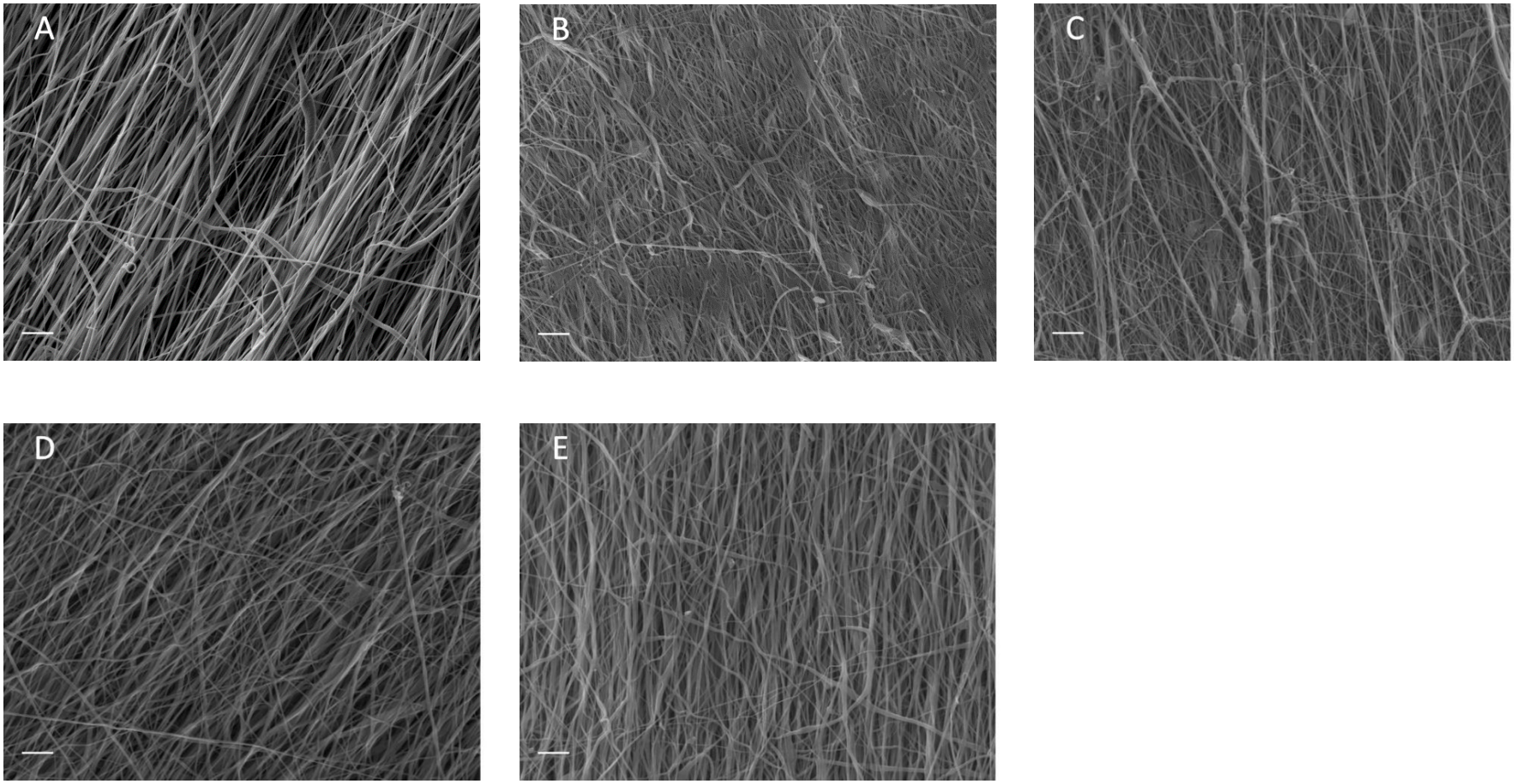

Figure 5.12 The effect of sterilisation on non-functionalised PCL fibre morphology. SEM images showing sterilisation effects on non-functionalised electrospun PCL fibres; **A** untreated non-functionalised fibres, **B** fibres treated with ethanol **C** fibres treated with ethylene oxide, **D** fibres treated with UV radiation, and **E** fibres treated with gamma radiation. Scale bars: 10 µm.

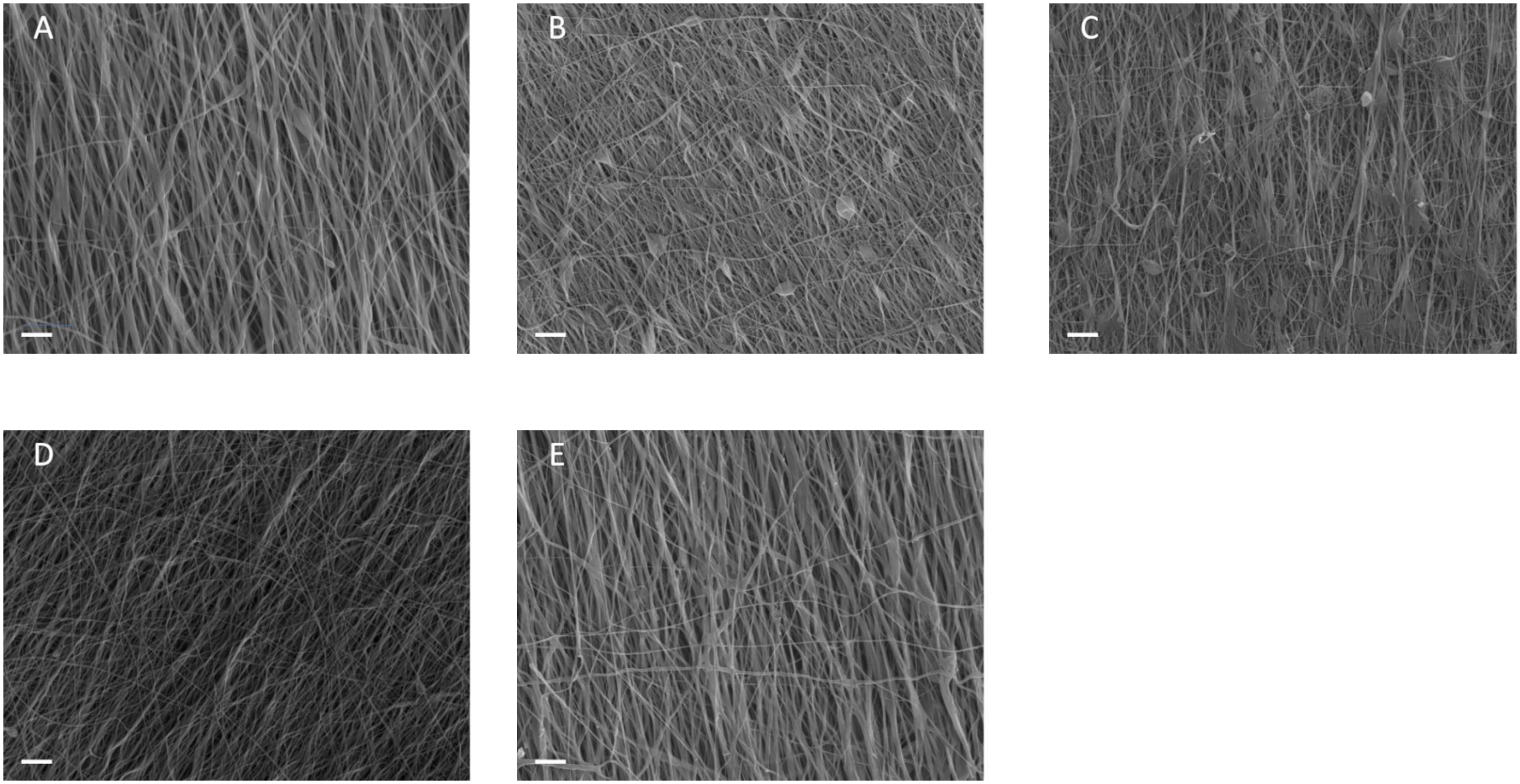

Figure 5.13 The effect of sterilisation on fibronectin-functionalised electrospun PCL fibre morphology. SEM images showing sterilisation effects on fibronectin-functionalised electrospun PCL fibres; **A** untreated fibronectin-functionalised fibres, **B** fibres treated with ethanol **C** fibres treated with ethylene oxide, **D** fibres treated with UV radiation, and **E** fibres treated with gamma radiation. Scale bars: 10 µm.

ImageJ was used to determine the average fibre diameter of the fibres after each treatment (see **Figure 5.14**).

The untreated non-functionalised control had a fibre diameter of 0.38 ±0.12 µm. After ethanol, UV and ethylene oxide treatments the fibre diameters were not significantly different from the control. After gamma radiation treatment, the fibre diameter was 0.28 ±0.11 µm, which was significantly reduced from the control fibres.

The functionalised control fibres had a diameter of 0.4 ±0.2 µm, which was significantly decreased after ethanol and ethylene oxide treatment to 0.26 ± 0.06 µm and 0.3 ± 0.2 µm respectively, both of which were significantly less than the functionalised control. UV and gamma treatments did not affect the fibre diameters.

The effect of the treatments on the fibre alignment was investigated using the OrientationJ plug-in for ImageJ, which was used to produce data describing the alignment of fibres in each SEM image. This data was then plotted on a polar histogram to visualise the distribution of fibre alignments (see **Figure 5.15**).

The total alignment was also calculated by OrientationJ, which showed that for both the non-functionalised and fibronectin-functionalised fibres, the ethanol and ethylene oxide treatments led to a significant reduction in the fibre alignment, but the UV and gamma treatments did not have a significant effect (see **Figure 5.16**).

The significant alterations in the topography of both functionalised and non-functionalised fibres following treatment with ethanol and ethylene oxide can be attributed to mechanical disruption induced by these sterilisation methods. During these sterilisation processes, the porous structure of the fibre sheets allows ethanol liquid and ethylene oxide gas to infiltrate, leading to the suspension of individual fibres

within either the liquid or gas phase. Upon drying, the fibres lose their alignment, resulting in the observed disruption of the fibre arrangement.

Furthermore, the slight melted appearance of the fibres may arise from the partial dissolution of the fibre surface in ethanol. Ethanol, being a polar solvent, can interact with the polymer chains of the fibres, causing them to partially dissolve and lose their structural integrity. Additionally, the alkylation of hydroxyl and amide groups within the fibres by ethylene oxide may have a similar effect. Notably, the functionalised fibres, containing both hydroxyl and amide groups due to the presence of fibronectin, exhibit a greater susceptibility to the effects of ethylene oxide compared to non-functionalised fibres, which only contain the hydroxyl groups present in PCL.

The observed minimal impact of UV and gamma treatments on the fibre topography implies that these sterilisation methods hold promise as suitable candidates for sterilising electrospun PCL fibres. Unlike ethanol and ethylene oxide treatments, which induced significant alterations in fibre topography, UV and gamma treatments maintained the structural integrity of the fibres. This preservation of fibre topography suggests that UV and gamma radiation effectively sterilise the fibres without causing substantial physical changes, making them potentially favourable options for sterilisation of electrospun PCL biomaterials.

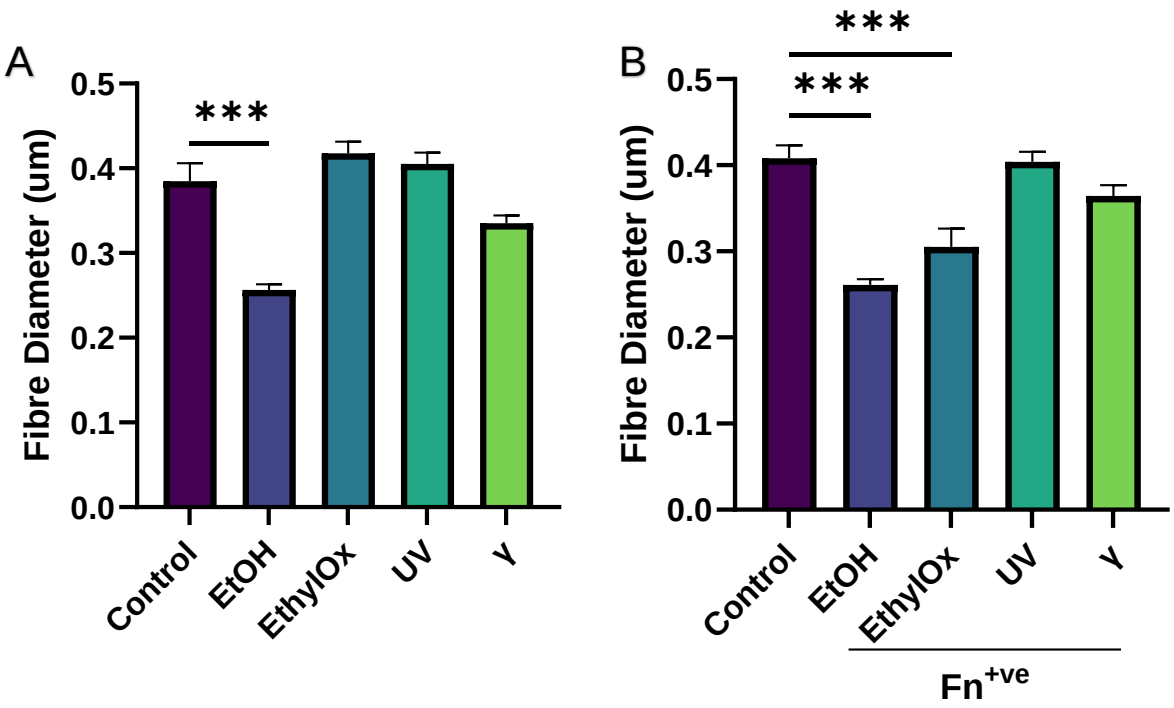

Figure 5.14 The effect of sterilisation treatments on electrospun PCL fibre diameters. Graphs showing the average fibre diameters of **A** non-functionalised and **B** fibronectin-functionalised electrospun PCL fibres following treatment with ethanol (EtOH), ethylene oxide (EthylOx), UV radiation (UV) and Gamma radiation (γ). Data is presented as mean ± SE (N=3, n=100) with one-way ANOVA statistical test (*** $p < 0.001$).

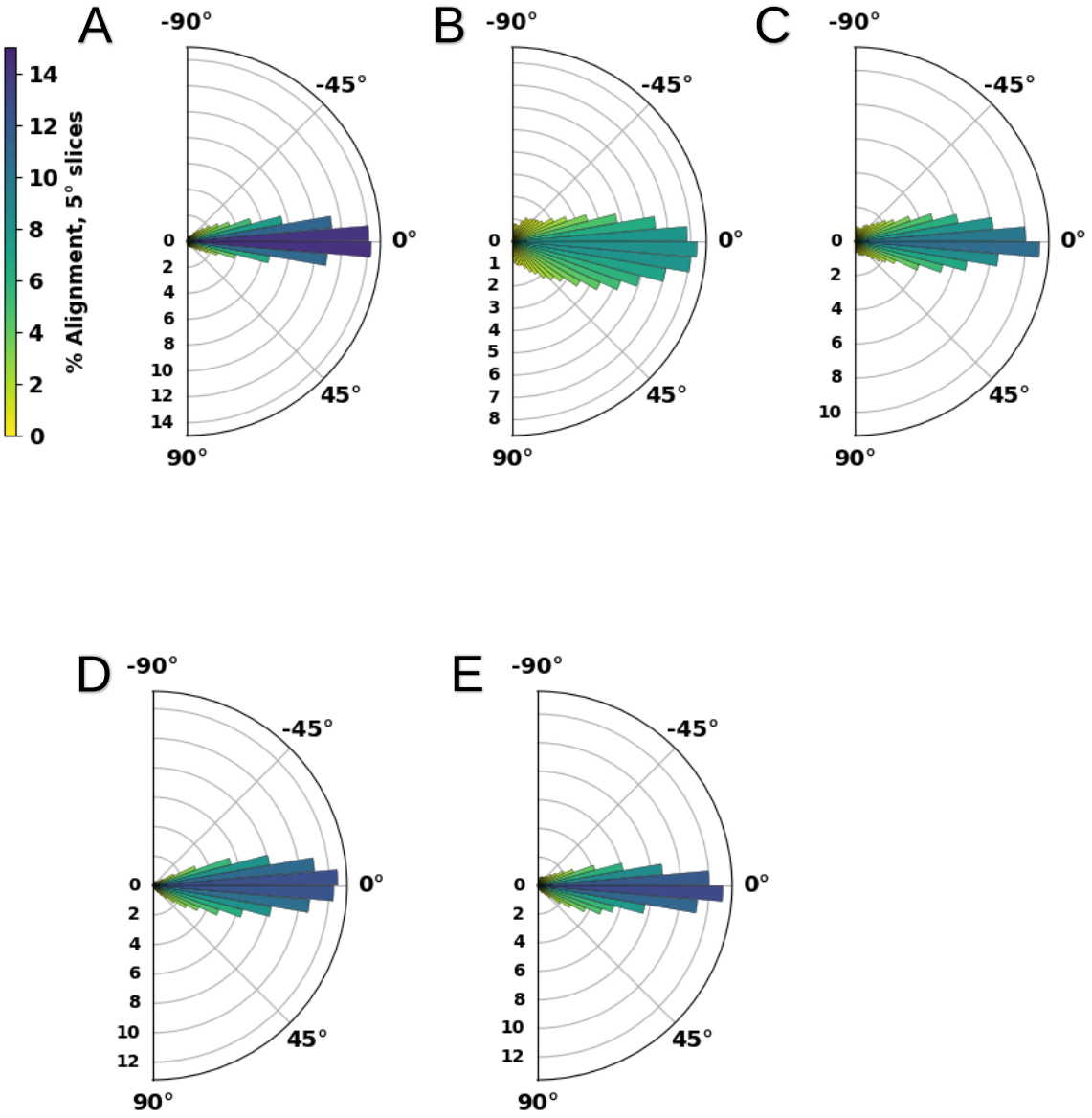

Figure 5.15 The effect of sterilisation treatments on electrospun PCL fibre alignment. Polar histograms produced using Python showing the distribution of alignment of **A** control electrospun PCL fibres, and fibres after treatment with **B** ethanol, **C** ethylene oxide, **D** UV and **E** gamma irradiation. The Orientation J plug-in for Image J was used to analyse the alignment of fibres in each SEM image. This data was plotted on a polar histogram. Each bar represents a 5° slice of the SEM image, with 0° representing the dominant fibre direction. The length of the bar represents the proportion of the image (%) that is aligned with the dominant fibre direction. Darker coloured bars are longer.

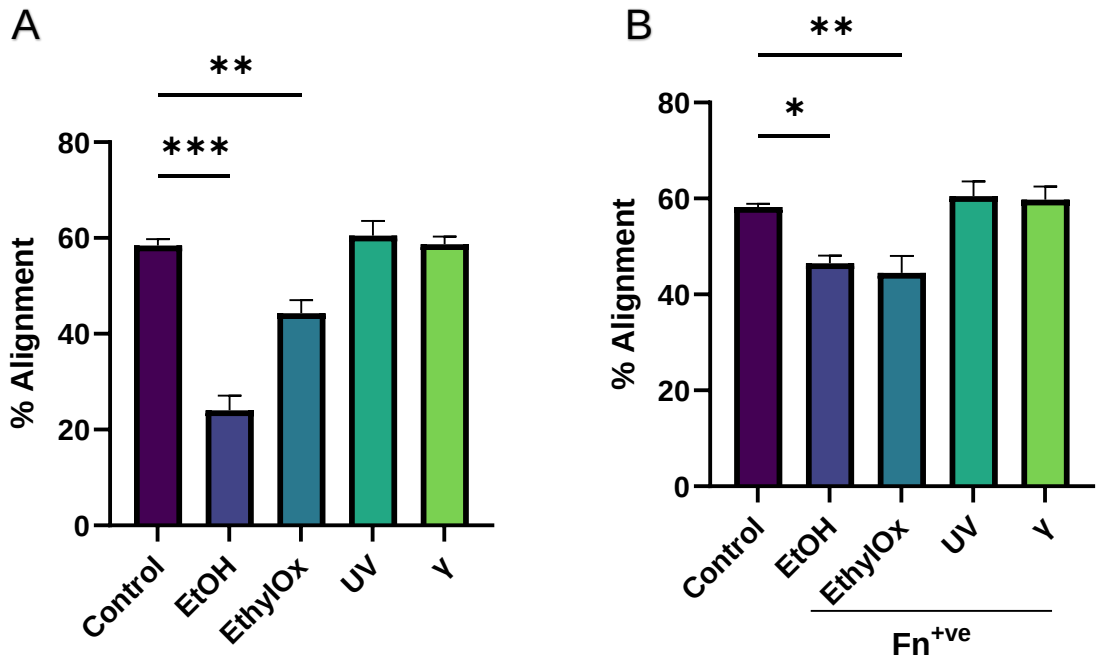

Figure 5.16 The effect of sterilisation treatments on alignment of non-functionalised and fibronectin-functionalised electrospun PCL fibres. Graphs comparing the alignment of **A** non-functionalised and **B** fibronectin-functionalised electrospun PCL fibres. Data presented as mean ± SD (n=5). with one-way ANOVA statistical t-test (*** $p < 0.001$, ** $p < 0.002$, * $p < 0.003$).

5.3.2.2 Effects of Sterilisation Treatments on PCL Fibre Mechanical Properties

The mechanical properties of the electrospun PCL fibres treated using various sterilisation methods were determined via tensile testing, and compared to the properties of porcine oesophageal tissue.

The tissue had an elastic modulus (E) of 0.3 ± 0.3 MPa. The non-functionalised control fibres had an elastic modulus of 33 ± 4 MPa, which was significantly larger than the tissue. After all of the treatments the elastic modulus of the non-functionalised fibres remained significantly higher than the tissue, and all were significantly larger than the non-treated fibres (see **Figure 5.17A**).

The fibronectin-functionalised control fibres had an elastic modulus of 35 ± 8 MPa, which was also significantly larger than the tissue. After ethanol and gamma irradiation treatment the elastic modulus increased to 65 ± 14 MPa and 76 ± 11 MPa respectively. Both of these were significantly higher than the non-treated functionalised fibres. After UV and ethylene oxide treatment, the elastic modulus of the functionalised fibres was 22 ± 1 MPa and 36 ± 8 MPa, which were not significantly different from the functionalised controls, but remained significantly higher than the tissue (see **Figure 5.17B**).

The tissue had a UTS of 1.4 ± 0.5 MPa. The non-functionalised control fibres had a UTS of 5.4 ± 0.3 MPa, which was significantly larger than the tissue. After each of the treatments the UTS of the non-functionalised fibres remained significantly higher than the tissue (see **Figure 5.18A**). The ethylene oxide and gamma treatments caused significant increases in the UTS of the fibres, raising the UTS to 14 ± 1 MPa and 15 ± 2 MPa respectively.

The fibronectin-functionalised control fibres had a UTS of 10 ± 2 MPa, which was also significantly larger than the tissue. The UTS of the fibres remined significantly larger than the tissue after all of the treatments see (**Figure 5.18B**). The ethylene oxide treatment did not change the UTS of the fibres to any level of statistical significance. After ethanol and gamma treatment, the UTS had significantly increased to 10 ± 2 MPa and 15 ± 2 MPa respectively. The UV treatment led to a decrease in the UTS to 5 ± 2 MPa, but it remained significantly larger than that of the tissue.

The tissue had a maximum extension of 153 ± 27%. The non-functionalised control had a maximum extension of 39 ± 18%, which was significantly lower than the tissue. After each of the treatments the maximum extension remained significantly lower than that of the tissue, and did not change to a significant level from the non-treated control (see **Figure 5.19A**).

The fibronectin-functionalised control had a maximum extension of 51 ± 11%, which was significantly lower than the tissue. After ethylene oxide, UV and gamma treatments, the maximum extension remined significantly less than the tissue, but was not significantly different that the control fibres. The maximum extension of the ethanol treated fibres was decreased compared to the untreated fibres to 23 ± 11% (see **Figure 5.19B**).

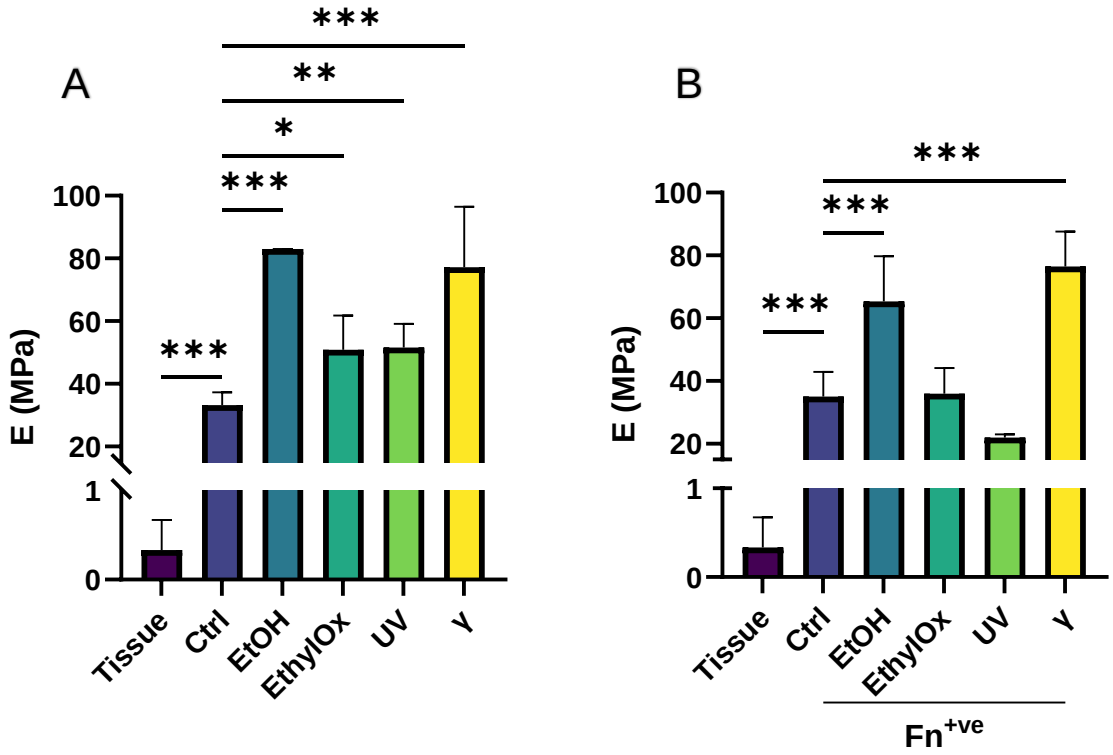

Figure 5.17 The effects of sterilisation treatments on PCL fibre elasticity. Graphs comparing the elastic modulus (E) of **A** non-functionalised and **B** fibronectin-functionalised electrospun PCL fibres after treatment with 70% ethanol (EtOH), UV radiation (UV), Ethylene Oxide (EthylOx) and gamma radiation (γ) with porcine oesophageal tissue. Data presented as mean ± SD (n=5). with one-way ANOVA statistical t-test (*** $p < 0.001$, ** $p < 0.002$, * $p < 0.003$).

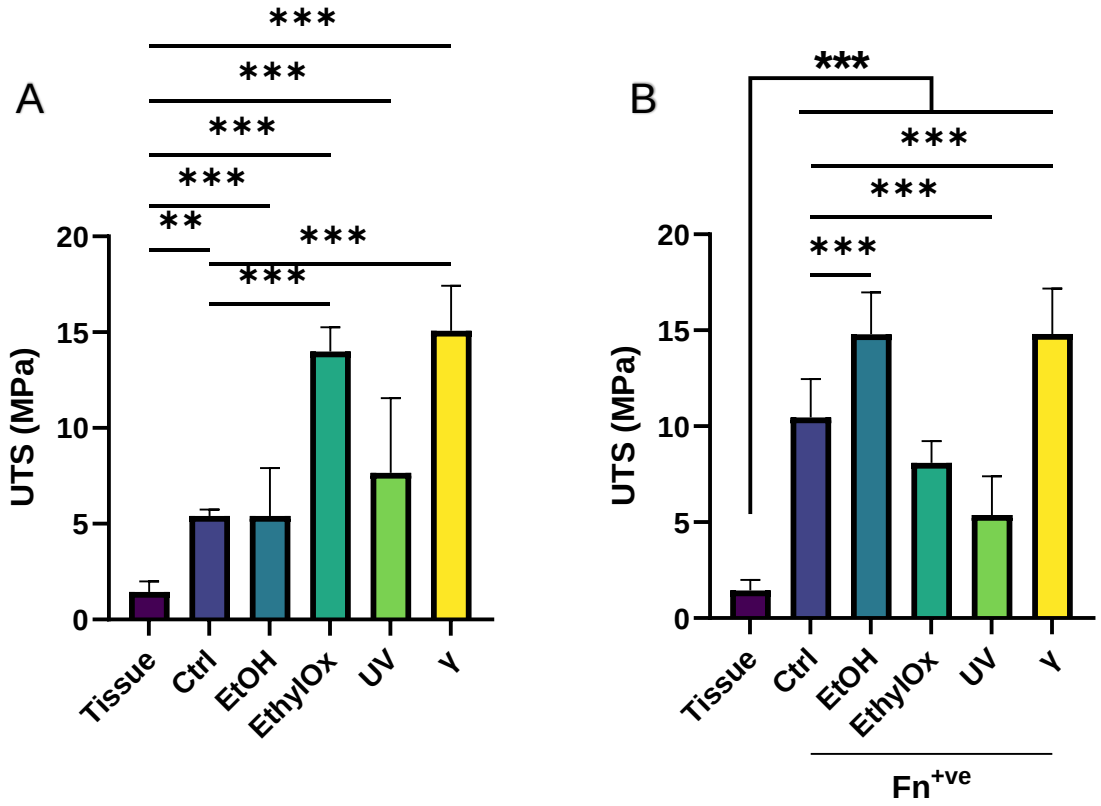

Figure 5.18 The effect of sterilisation methods on PCL fibre UTS. Graphs comparing the UTS of **A** non-functionalised and **B** fibronectin-functionalised electrospun PCL fibres after treatment with 70% ethanol (EtOH), UV radiation (UV), Ethylene Oxide (EthylOx) and gamma radiation (γ) with porcine oesophageal tissue. Data presented as mean ± SD (n=5). with one-way ANOVA statistical t-test (*** $p < 0.001$, ** $p < 0.002$, * $p < 0.003$).

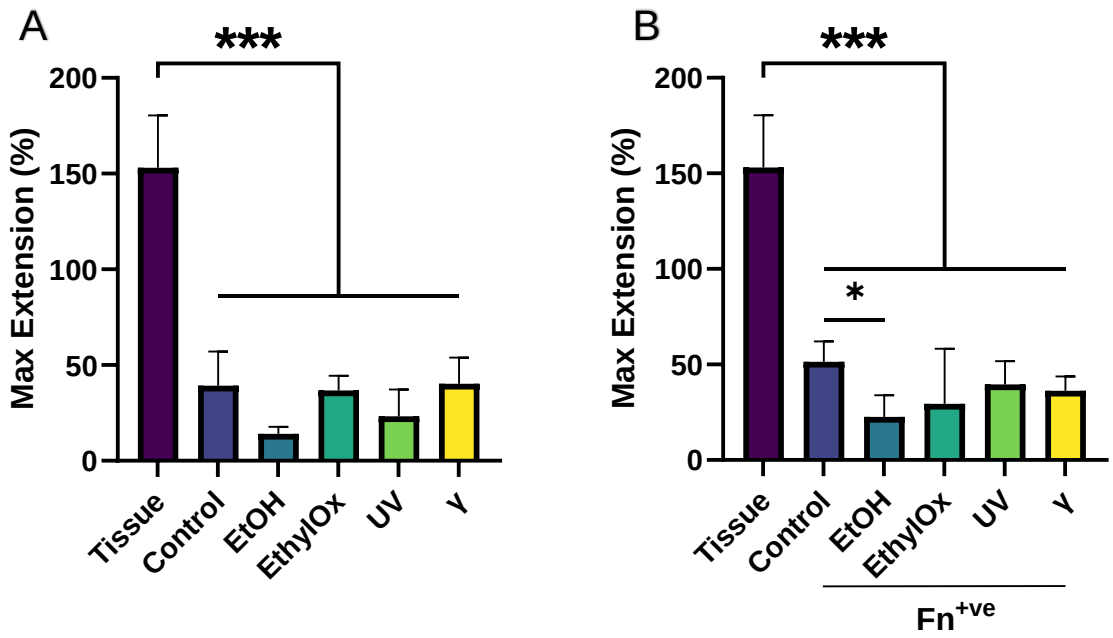

Figure 5.19 The effect of sterilisation methods on PCL fibre extension. Graphs comparing the maximum extension of **A** non-functionalised and **B** fibronectin-functionalised PCL fibres after treatment with 70% ethanol (EtOH), UV radiation (UV), Ethylene Oxide (EthylOx) and gamma radiation (γ) with porcine oesophageal tissue. Data presented as mean ± SD (n=5). with one-way ANOVA statistical t-test (*** $p < 0.001$, * $p < 0.003$).

5.3.2.3 Effects of Sterilisation Treatments on PCL Fibre Wettability

The water contact angle was determined for each type of the treated PCL fibres, and compared to the contact angle of decellularised ECM (dECM) from porcine oesophagus (see **Figure 5.20**). The dECM had a θ of 67 ± 5°.

The non-functionalised and untreated PCL fibres had a θ of 141 ± 26°, which was significantly higher than the dECM. After treatment with ethylene oxide and gamma radiation, the θ of the fibres were 124 ± 17° and 124 ± 12° respectively. These were significantly lower from the untreated fibres, but were both significantly higher than the dECM. The ethanol and UV treatments resulted in a θ of 74 ± 12° and 81 ± 15° respectively, which were both significantly lower than the untreated fibres, and were not significantly different to the dECM. In addition, the ethanol and UV treatments reduced the θ of the fibres to below 90°, which is considered hydrophilic.

The fibronectin-functionalised, but untreated, fibres had a θ of 88 ± 9°, which was significantly higher than that of the dECM. The ethanol and gamma radiation treatments produced a θ of 93 ± 17° and 90 ± 14° respectively. These were not significantly changed from the control fibres, and remained significantly higher than the dECM.

The functionalised fibres treated with ethylene oxide and UV had a θ of 77 ± 16° and 67 ± 23° respectively, which were significantly lower than the control fibres, and were not significantly different from the dECM.

The relatively reduced impact of the sterilisation methods on the contact angle of the functionalised fibres is due to the fact that the functionalisation process itself decreases the contact angle significantly. The UV is the only method that reduces both the non-functionalised and fibronectin-functionalised fibres enough to be similar to that

of the dECM. This highlights UV sterilisation as a good candidate for PCL fibre sterilisation, as a reduced contact angle can indicate an increase in bioactivity, as it is known to increase cell adhesion[155,188,194,195].

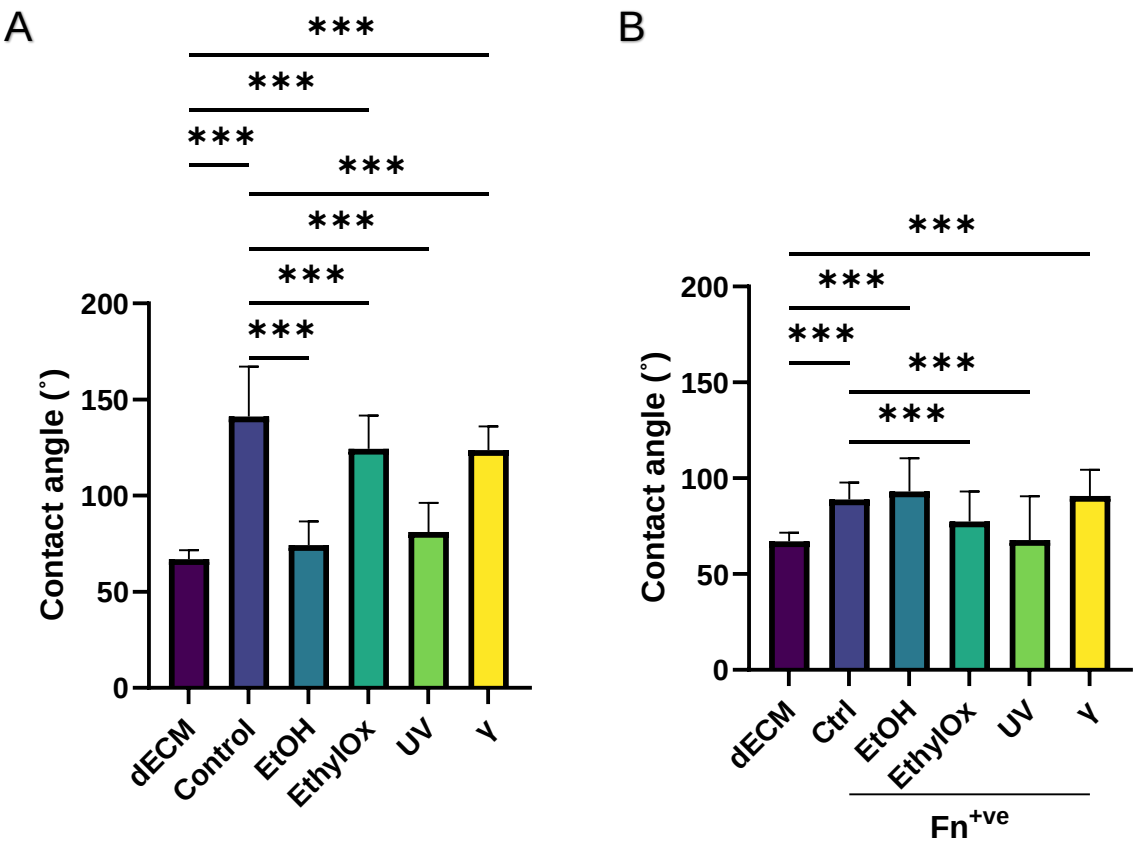

Figure 5.20 The effect of sterilisation treatments on the water contact angle of PCL fibres. Graphs comparing the water contact angle (θ) of porcine dECM with **A** non-functionalised and **B** fibronectin-functionalised electrospun PCL fibres after treatment with 70% ethanol (EtOH), UV radiation (UV), Ethylene Oxide (EthylOx) and gamma radiation (γ) with porcine oesophageal tissue. Data is presented as mean ± SD (n=6) with one-way ANOVA statistical t-test (*** $p < 0.001$).

5.4 Discussion

The aim of this chapter was to successfully functionalise electrospun PCL fibres with fibronectin, to increase the fibre bioactivity for tissue engineering applications. Fibronectin was selected as it plays a crucial role in cell adhesion and migration, and has been shown to enhance tissue regeneration when grafted onto several polymer types[41,111,186,271,272,275].

The presence of fibronectin on the functionalised fibres was confirmed by fluorescent microscopy and BCA assay. The functionalisation did not have any effect the fibre diameter or degree of alignment. Given that the characteristic peaks of the fibronectin and PCL appear at similar Raman shifts, the spectra of the fibronectin-functionalised PCL fibres was not different enough to be distinctive from the two materials. Therefore, this method could not be used to confirm the presence of the fibronectin on the PCL fibres. However, the Raman spectra showed that the functionalisation process did not alter the chemical structure or crystallinity of the PCL fibres.

Live/dead staining revealed high cell viability, with 78 ± 10% of human oesophageal fibroblasts cultured on aligned PCL fibres functionalised with fibronectin remaining viable after 5 days. This result confirms the biocompatibility of the fibres and their suitability as a biomaterial scaffold for oesophageal tissue engineering.

The functionalisation did, however, affect the physical properties of the material. The water contact angle of the fibre sheets was significantly reduced after the process, not statistically different from that of decellularised ECM, showing that the material had become hydrophilic. This is due to the hydrolysis step of the functionalisation process, which is known to enhance PCL wettability through increased surface are and the creation of functional surface groups (-OH, -COOH, $-NH_2$)[210,294,295] This is a welcome

side effect of the functionalisation process, as hydrophilicity promotes cell adhesion through enhanced protein adsorption, which in turn increases the bioactivity of a biomaterial[263,296].

In terms of mechanical properties, the elasticity and maximum extension of the material both remained significantly lower to that of porcine oesophageal tissue, with no additional changes post-functionalisation. However, the UTS of the material at break did increase further after the functionalisation.

These findings underscore the successful integration of fibronectin onto PCL fibres without compromising their structural integrity. In addition, the enhanced hydrophilicity highlights the potential of this approach to improve the bioactivity of the material beyond that introduced by the fibronectin alone. This not only promotes better cell-material interactions but also creates a microenvironment more conducive to cellular attachment, proliferation, and ultimately tissue regeneration.

In addition to the physical and mechanical properties discussed, it's crucial to consider the biocompatibility of the functionalised PCL fibres. The investigation of cell viability revealed that fibroblasts cultured on fibronectin-functionalised PCL fibres exhibited significantly higher viability compared to those cultured on non-functionalised fibres, with viability levels comparable to cells cultured on tissue culture plastic. This underscores the importance of surface modification with fibronectin in promoting favourable cell-material interactions, ultimately enhancing the potential of these fibres for tissue engineering applications.

The sterilisation of electrospun PCL fibres, both non-functionalised and fibronectin-functionalised, using various methods revealed distinct effects on their physical properties. These findings provide insights for the application of electrospun PCL

fibres in tissue engineering and regenerative medicine, where sterilisation is essential for clinical applications. These effects are summarised in **Table 5.1**.

Table 5.1 Summary of the effects of sterilisation treatments on PCL fibres

The effects of ethanol (EtOH), UV radiation (UV), Ethylene Oxide (EthylOx) and gamma radiation (γ) treatments on non-functionalised (purple) and fibronectin-functionalised (green) PCL fibres.

	EtOH	EthylOx	UV	γ
Topography	✗ ✗	✗ ✗	✓ ✓	✓ ✓
Fibre Diameter	↓ ↓	- ↓	- -	↓ -
Alignment	↓ ↓	- -	- -	- -
Θ	↓ -	↓ ↓	↓ ↓	↓ -
E	↑ ↑	↑ -	↑ -	↑ ↑
UTS	- ↑	↑ -	- ↓	↑ ↑
Max extension	- ↓	- -	- -	- -

The fibre diameter measurements post-sterilisation revealed significant reduction after ethanol treatment of both non-functionalised and fibronectin-functionalised fibres, with the effect being greater on the functionalised fibres. This could be related to the partial dissolution of the fibre surface, leading to fibre thinning. This effect may be greater on the functionalised fibres due to the hydrolysis during the functionalisation process, which creates more polar groups on the fibre surface. While PCL is not soluble in ethanol at high concentrations due to their very different solubility parameters (see **Table 5.2**), it is possible that very small amounts of polymer from the fibre surface may dissolve in the solvent.

Table 5.2 Hansen solubility parameters of chloroform, ethanol and PCL [227–229].

Hansen solubility parameters	**δ_d** $(MPa)^{1/2}$	**δ_p** $(MPa)^{1/2}$	**δ_h** $(MPa)^{1/2}$
Chloroform	17.8	3.1	5.7
Ethanol	15.8	8.8	19.4
PCL	17.7	5	8.4

The mechanism behind ethylene oxide-induced fibre thinning could be due to cross-linking of polymer chains, leading to shrinkage of the fibres, an effect which has been observed previously in electrospun PLLA, PEG and PLCL sheets and explained by esterification of carboxyl groups and an increase in polymer crystallinity[279,297,298]. This effect could also explain the slight loss of fibre alignment after ethylene oxide treatment.

The contact angle measurements indicated an increase in hydrophilicity following all treatments for the non-functionalised fibres, and following the ethylene oxide and UV treatments for the functionalised fibres. This is likely due to increased surface roughness and surface energy of the fibres[280,299,300]. The increase is less on the functionalised fibres as they are more hydrophobic initially. The increase in wettability suggests an increase in bioactivity, as it could improve cell attachment and proliferation[43,263,264].

The sterilisation treatments variably affected the mechanical properties of the fibres. Notably, the stiffness and UTS of the fibronectin-functionalised fibres increased significantly after ethanol and gamma treatments. This improvement in mechanical properties could be attributed to cross-linking induced by the radiation, which could enhance the load-bearing capacity of the fibres[286,288,289].

In conclusion, the choice of sterilisation technique could significantly impact the physical and mechanical properties and the bioactivity of the PCL fibres. UV and gamma radiation emerge as favourable methods for preserving fibre morphology and alignment, and enhancing hydrophilicity and mechanical properties. UV radiation was selected for use in *in vitro* testing in the next stage of this project.

6.0 Cell response to Electrospun PCL Fibres

6.1 Introduction

In tissue engineering and regenerative medicine, understanding the cues influencing cellular responses to biomaterial is fundamental for optimising their properties. Biological and chemical cues, such as hormones, growth factors and proteins, are typically used to fulfil the “signals” component of the tissue engineering triad, and are often incorporated into biomaterials to enhance bioactivity and influence cell adhesion, migration and differentiation. In addition, physical cues in the form of topographical features can play a significant role in affecting cell responses to a material. In natural tissue, cells experience physical cues from the 3D structure of the ECM, which exhibits differing micro- and nanoscale topographies and stiffnesses, varying between tissue types, developmental stages and depending on tissue health as well during stages of regeneration[34].

Engineered topographies have been successfully used to direct cell alignment and the orientation of secreted ECM components, which can enhance the organisation and mechanical properties of regenerated tissue while reducing scarring [39]. While it has been demonstrated that the size, shape and alignment of topographical features can have significant effects on cell adhesion, migration and differentiation, these responses are not yet fully understood.

Aligned electrospun fibres introduce nanoscale topography (~100 nm) that closely mimics the ECM of natural tissues. This nanoscale environment has been shown to significantly affect cell alignment, elongation, proliferation and motility, and differentiation[48,113,142,151,159,188,301,302]. Specifically, aligned fibres can direct the organisation of cells along the fibres, promoting a more organised tissue architecture.

For instance, the degree of fibre alignment has been shown to influence the integrin β1 signalling pathway in fibroblasts[38]. This pathway is crucial for cell adhesion, migration and differentiation, suggesting that electrospun fibre alignment can enhance fibroblast functionality and contribute to the differentiation process. This directed differentiation is effective in promoting effective tissue repair.

On the microscale (~100 µm), topographical features such as grooves, pillars and pits can significantly enhance cell spreading, proliferation and alignment [32,33,303–305]. These features can be engineered to influence cell behaviour to promote tissue-specific outcomes. For example, induced pluripotent stem cell (iPSC) gene expression is notably altered when cultured on micropatterned surfaces[306], indicating that microscale topographies can direct stem cell fate and potentially guide the formation of specific tissue types. Similarly, microgrooved surfaces (~100 µm) have been observed to significantly affect osteoblast gene and protein expression, highlighting the potential for microscale topographies to enhance bone tissue engineering by directing osteogenic differentiation[307].

The effects of nano- and microscale topographies offers a powerful tool for tissue engineering and regenerative medicine, enabling several levels of control over the guidance of cell behaviour by a biomaterial. These topographical cues can accelerate the rate at which biomaterial scaffolds become populated with cells, which is crucial for the early stages of tissue regeneration, as it leads to the effective deposition of ECM and the subsequent growth of new tissue. Cells experience multiple types of topographical cues simultaneously *in vivo*, ranging from nanoscale (~100 nm) to microscale (~100 µm). By incorporating topographical cues at different scales in one biomaterial, this complexity could be mimicked, and the interaction of several types of cues could be examined.

Fibroblasts are an important cell type in tissue engineering and regenerative medicine due to their crucial role in tissue repair and regeneration process. These cells are not only fundamental in the production of new ECM, providing structural support to tissues, but also for coordinating the repair process through the production of various regulatory molecules and interactions with other cell populations necessary for tissue repair and regeneration[73,308]. Furthermore, fibroblasts exhibit proliferative capacities and contribute to angiogenesis and the development of granulation tissue, which serves as a scaffold for tissue regeneration[197].

In the context of biomaterials and tissue engineering, fibroblast interactions can significantly influence the outcome of tissue repair[72,73,197,198,203,210]. The surface properties of biomaterials, including their chemistry, topography, and mechanical stiffness, can affect fibroblast adhesion, proliferation, and differentiation[206,231]. For instance, biomaterials designed to mimic the natural ECM in terms of biochemical composition and physical structure can enhance fibroblast functionality, promoting more effective tissue regeneration. Moreover, fibroblast elongation and alignment in response to biomaterial cues, such as those provided by electrospun fibres or microgrooved surfaces, is critical for the directional growth of tissues[32,39,40,207,231].

Assessing fibroblast behaviour on biomaterials, through measures of cell morphology, metabolic activity and viability, provides crucial insights into the material's bioactivity and its potential to enhance tissue regeneration. Morphological changes, such as elongation and alignment, offer insights about the material's ability to guide cell migration and tissue organisation, while evaluating the cell metabolic rate and viability can provide insights into its support for sustained cell growth[32,33,40,207,309–312].

This chapter will describe the evaluation of fibroblast responses to electrospun PCL fibres functionalised with fibronectin, as previously described. The impact of adding microgrooves to the fibre sheets on the fibroblast response to the material will also be investigated.

6.2 Methods

6.2.1 AlamarBlue Assay

AlamarBlue assays were conducted on cells cultured on PCL fibre sheets for 1, 3 and 7 days. Following incubation, cells were washed with PBS and incubated with AlamarBlue and DMEM for 4 hours at 37°C. Absorbance was measured at 570 nm using a Tecan Spark microplate reader (Tecan Life Sciences, Switzerland).

6.2.2 Immunostaining

Cell-seeded fibre sheets incubated for 5 days were fixed with 4% PFA, permeabilised with 0.1% Triton X-100 and blocked in 1% bovine serum albumin (BSA). Vinculin staining was carried out using a vinculin monoclonal antibody (1:400), followed by a secondary antibody (FITC conjugated IgG, 1:200, green) and TRITC conjugated phalloidin (1:200, red). Nuclei were counterstained with DAPI (1:1000, blue) for 5 minutes. Between each step of the staining, samples were washed twice with a wash buffer (0.05% Tween-20 in PBS). Fluorescence microscopy of fluorescently labelled samples was carried out using an FV1000 (Olympus, Germany). Image analysis was performed using ImageJ (NIH, USA). The length and width of each visible cell was measured, and used to determine its aspect ratio (AR).

6.2.3 Microgroove Imprinting

Computer aided drawing (CAD) models were created using Fusion 360 software (Autodesk, Inc., USA) to design stamps for imprinting microgrooves into electrospun PCL fibre sheets. Three types of stamps were designed; a stamp with 250 µm grooves, a stamp with 50 µm grooves and a stamp with angled grooves (see **Figure 6.1**). The stamps were fabricated using water-soluble UV-cured 3D printer resin with a Mars 3 3D printer (Elegoo, China). Once printed, stamps were cured under an Elegoo Mercury

Plus curing lamp (Elegoo, China) and used to imprint grooves onto sheets of PCL fibres, either parallel or perpendicular to the direction of the fibre alignment.

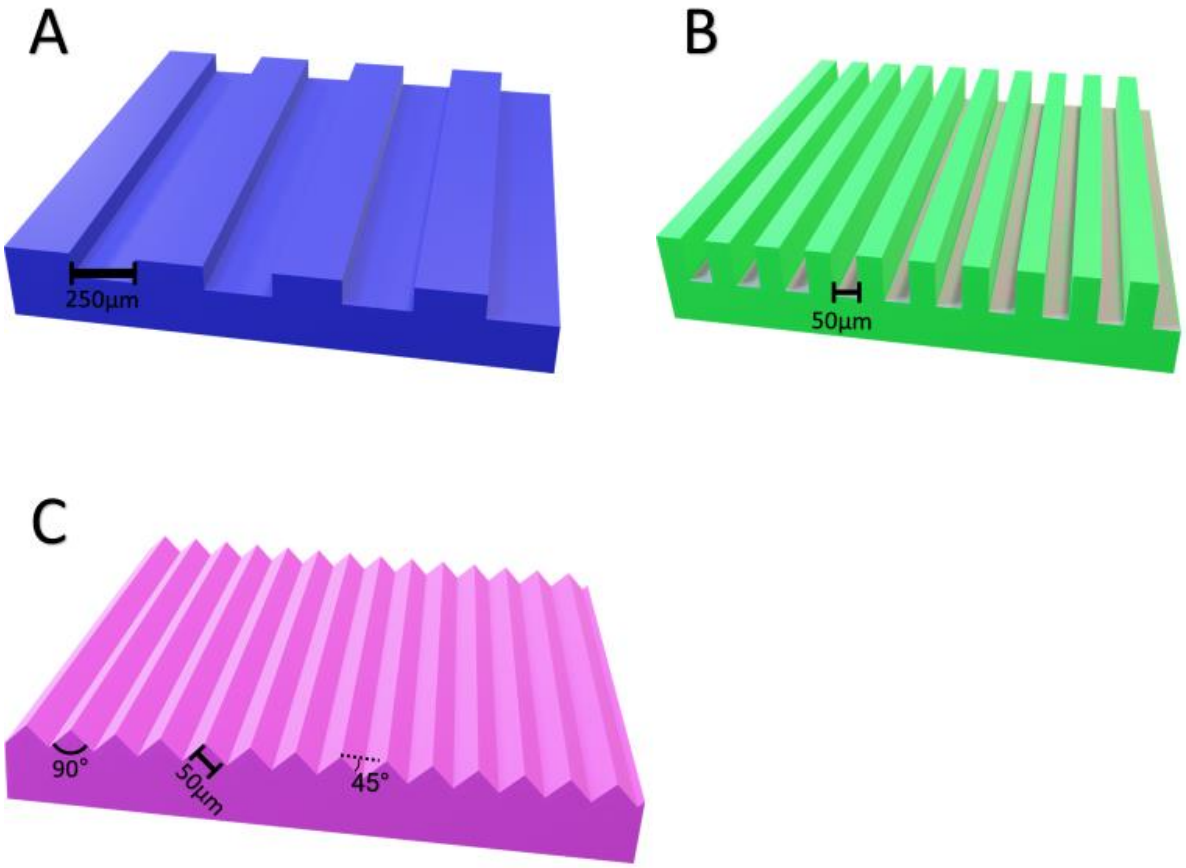

Figure 6.1 3D drawings used to produce stamps for imprinting of A 250µm, B 50µm and C angled grooves

6.3 Results

6.3.1 Topography of PCL Fibre Sheets Imprinted with Microgrooves

To imprint microgrooves onto electrospun PCL fibre sheets, 3D printed stamps with 250 µm, 50 µm and angled grooves were used. Microgrooves were stamped parallel to the direction of the fibre alignment.

SEM images of the imprinted sheets were obtained to investigate the microgroove topography and the effect of the imprinting on fibre morphology as illustrated in **Figure 6.2**. The analysis revealed that the average diameter of the grooves produced with the 250 µm stamp was 241 ± 25 µm, while those from the 50 µm stamp measured 75 ± 8 µm and the angled stamp produced grooves with an average diameter of 156 ± 24 µm.

Notably, the grooves produced by the 50 µm stamp appeared larger than the dimensions of the stamp itself. This discrepancy was attributed to material relaxation post-stamping. Despite this, the resulting grooves still fell within the range of topographical scale known to influence fibroblast behaviour. To produce 50 µm grooves, a stamp could be produced with smaller groove diameters to account for the material relaxation. However, the 50 µm stamp is the smallest that could be achieved with the available equipment. While the groove diameters were not precisely aligned with the stamp dimensions, they were categorised as “250 µm”, “50 µm” and “angled” for reference and consistency.

Additionally, the average fibre diameter of each stamped sheet was determined using ImageJ. Results indicated that the fibre diameter of the control sheet was 0.25 ± 0.06 µm, with the sheets stamped with 250 µm, 50 µm and angled grooves had average fibre diameters of 0.23 ± 0.06 µm, 0.24 ± 0.06 µm and 0.22 ± 0.05 µm respectively.

Statistical analysis through one-way ANOVA testing (N=3, n=100) showed that none of the fibre sheets had significantly different fibre diameters, indicating that the imprinting of microgrooves did not have a notable effect on fibre morphology. These findings show the success of the imprinting procedure on introducing microscale features onto electrospun PCL fibre sheets while preserving the fibre morphology.

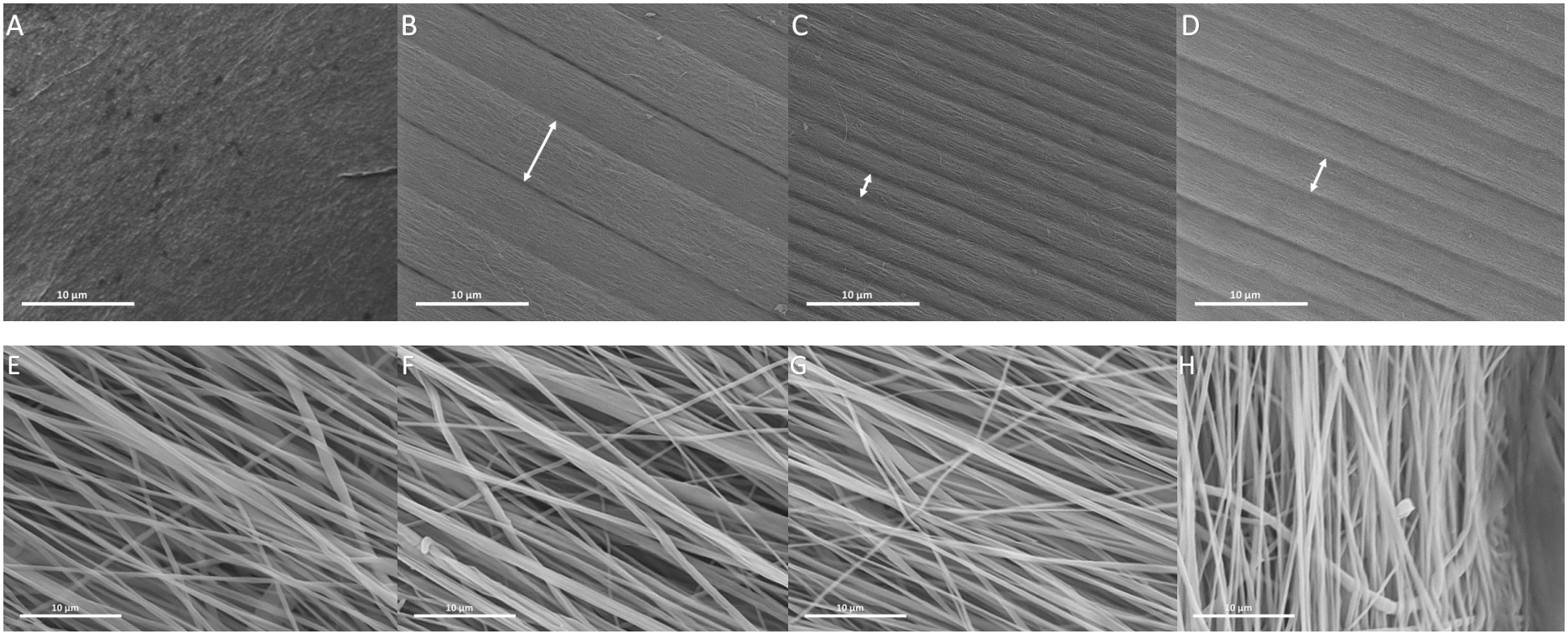

Figure 6.2 SEM of PCL fibre sheets with microgrooves. SEM images of **A, E** control PCL fibre sheets, and fibre sheets imprinted with **B, F** 250 µm, **C, G** 50 µm and **D, H** angled microgrooves. **B** and **C** show 250 µm and 50 µm microgrooves with well-defined edges, while **D** shows that the angled grooved have less well-defined edges. **E-H** show higher magnification images allowing individual fibre morphology to be examined. There was no visible difference in fibre morphology or alignment.

6.3.2 Mechanical Characterisation of Imprinted PCL Fibre Sheets

Tensile testing was conducted to investigate the impact of microgroove imprinting on the mechanical properties of the electrospun PCL fibre sheets (see **Figure 6.3**). Microgrooves were imprinted both parallel and perpendicular to the direction of the fibre alignment and compared to a control without microgrooves.

Initially, the control had an elastic modulus of 46 ± 9 MPa. After microgroove imprinting both parallel and perpendicular to the fibre alignment, the elastic moduli of the fibre sheets were 40.27 ± 15 MPa and 40 ± 21 MPa respectively. These were not significantly different from the control.

The control fibre sheets had a UTS of 4 ± 1 MPa. Once the parallel and perpendicular microgrooves had been imprinted, the fibre sheets had a UTS of 2.9 ± 0.5 MPa and 3.2 ± 1 MPa respectively, neither of which were significantly different from the control.

The maximum extension of the control fibre sheets was 29 ± 11 %. The maximum extension after imprinting microgrooves parallel and perpendicular to the fibre direction was 26 ± 3 % and 29 ± 3 % respectively. There was no significant difference between the maximum extension of the control and imprinted fibre sheets.

These finding collectively show that the imprinting of microgrooves onto electrospun PCL fibre sheets did not significantly alter their mechanical properties. Therefore, the addition of microgrooves, both parallel and perpendicular to the fibres, did not compromise the mechanical stability of the fibres.

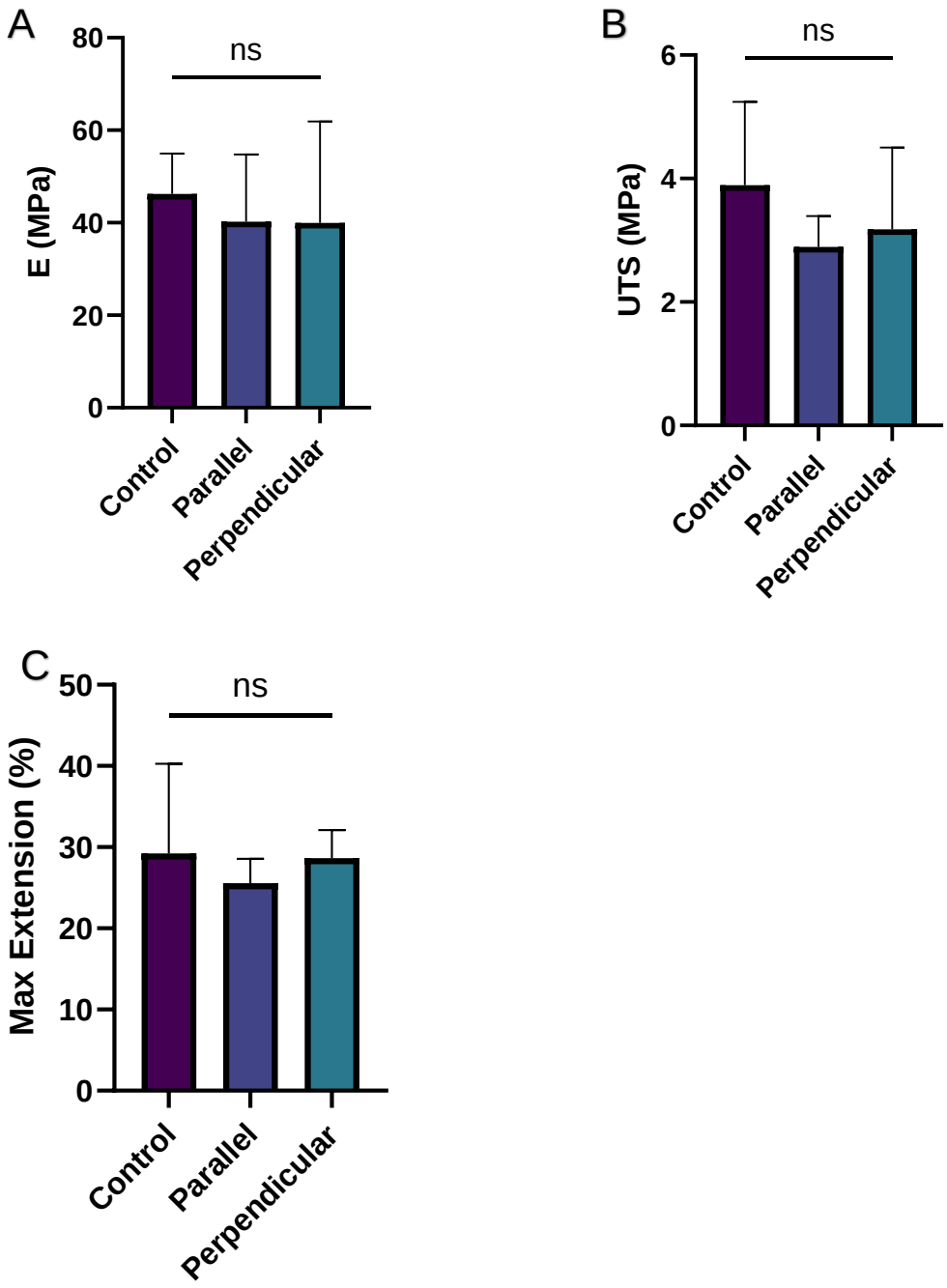

Figure 6.3 The effect of imprinting microgrooves on the mechanical properties of PCL fibre sheets. Graphs comparing the **A** elastic modulus (E), **B** UTS and **C** maximum extension of unstamped PCL sheets with sheets imprinted with microgrooves parallel and perpendicular to the direction of PCL fibre alignment. Data presented as mean ± SD (n=6) with one-way ANOVA statistical t-test (ns $p \geq 0.05$).

6.3.3 Metabolic Rate of Fibroblasts Cultured on Imprinted PCL Fibre Sheets

The metabolic rate of fibroblasts cultured on electrospun PCL fibres was assessed using an AlamarBlue assay at 1, 3 and 7 days (see **Figure 6.4**). To provide context, tissue culture plastic was used as a control surface, while fibronectin-functionalised, non-aligned electrospun PCL fibres were included to investigate the effect of fibre alignment. A one-way ANOVA statistical test was used to compare the metabolic activity of each group at day 7 (see **Figure 6.5**).

The metabolic assay indicated that by day 3 cells cultured on the non-aligned fibres had increased metabolic activity compared to those cultured on tissue culture plastic. However, by day 7 this difference was not statistically significant.

The cells cultured on the aligned PCL fibres had increased metabolic activity compared to the tissue culture plastic by day 3, and by day 7 this difference was statistically significant relative to the activity observed on tissue culture plastic.

The metabolic activity of the fibroblasts cultured on the 250 µm microgrooved fibres was higher than the tissue culture plastic, non-aligned fibres and aligned fibres. At day 7 the difference in metabolic activity between the 250 µm group and the tissue culture plastic, as well as the non-aligned fibres was statistically different. However, no statistical difference was observed between the 250 µm group and aligned fibres.

The 50 µm and angled grooves showed very similar metabolic activity to each other. By day 7, fibroblasts cultured on both groups displayed significantly higher metabolic activity compared to those cultured on tissue culture plastic, non-aligned fibres and aligned fibres. This suggests that the 50 µm and angled grooves had a greater impact on cell metabolism than the 250 µm grooves.

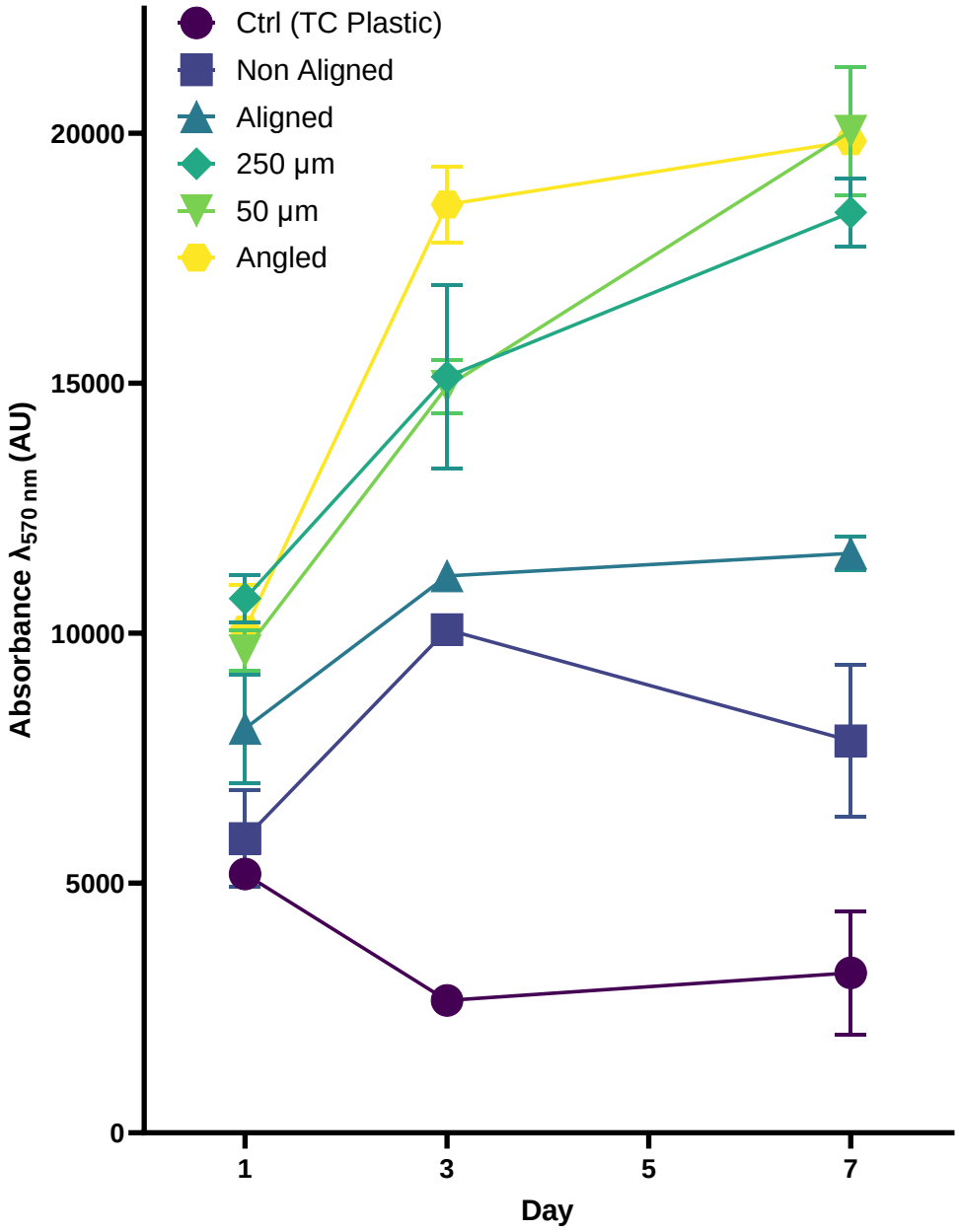

Figure 6.4 Metabolic rate of fibroblasts cultured on imprinted PCL fibre sheets. Graph comparing the metabolism of human oesophageal fibroblasts cultured on tissue culture plastic, non-aligned PCL fibres, aligned PCL fibres, and PCL fibres imprinted with microgrooves after 1, 3 and 7 days. Metabolic rate was determined by absorbance of cell culture media at 570 nm after cells were incubated with AlamarBlue. Data are presented as mean ± SEM (n=6).

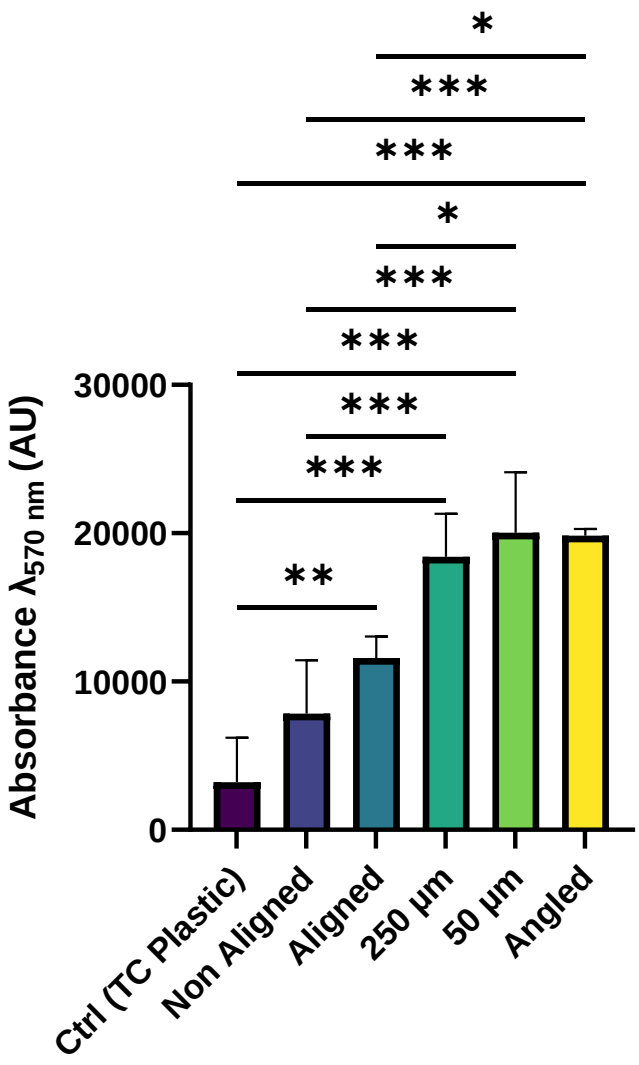

Figure 6.5 The effect of microgrooves on fibroblast metabolism after 7 days. Graph comparing the metabolic activity of fibroblasts cultured on microgrooved electrospun PCL fibre sheets to fibroblasts cultured on tissue culture plastic and non-aligned fibres. Data is presented as mean ± SD (n=6) with one-way ANOVA statistical test (* $p < 0.033$, ** $p < 0.002$, *** $p < 0.001$, ** $p < 0.002$).

6.3.4 Morphology of Fibroblasts Cultured on PCL Fibre Sheets with Microgrooves Parallel to Fibre Alignment

To investigate the effects of electrospun PCL fibre alignment and microgrooves, human oesophageal fibroblasts were cultured on various surfaces, including tissue culture (TC) plastic, as well as fibronectin-functionalised electrospun PCL fibres of several categories; non-aligned fibres, aligned fibres, and aligned fibres with 250 µm, 50 µm and angled microgrooves imprinted parallel to the fibre direction.

Following a 5-day incubation period, cells were stained with TRITC-conjugated phalloidin to stain the F-actin cytoskeleton red, and a vinculin antibody followed by FITC-conjugated immunoglobin G (IgG), which stained focal adhesions green. Nuclei were counterstained blue with DAPI as shown in **Figure 6.6**.

Cells cultured on TC plastic were randomly aligned with various levels of elongation. Cells cultured on the non-aligned fibres were clustered but showed no clear alignment or change in elongation compared to the TC plastic. Meanwhile, fibroblasts cultured on aligned fibres displayed slightly elongated morphologies but lacked significant alignment. Notably, fibroblasts cultured on the 250 µm, 50 µm and angled microgrooved fibre sheets exhibited alignment along the fibres and microgrooves, and displayed clear elongation.

Using ImageJ, the width and length of each fibroblast was measured, allowing the aspect ratio (width:length) to be calculated for each cell (see **Figure 6.7**). A perfectly round cell would have an aspect ratio of 1, with increasing elongation resulting in a decreased aspect ratio.

Analysis revealed that the aspect ratio of fibroblasts cultured on non-aligned fibres did not significantly differ from those cultured on TC plastic. However, cells cultured on

aligned fibres exhibited significantly greater elongation than both the TC plastic and the non-aligned fibres. This demonstrates the elongating effect of electrospun fibre alignment on fibroblasts.

Interestingly, fibroblasts cultured on angled microgrooves exhibited significantly greater elongation than those on TC plastic and non-aligned fibres, but did not display increased elongation compared to samples cultured on aligned fibres.

Fibroblasts cultured on the 250 µm and 50 µm microgrooved fibres exhibited significantly greater elongation than those on the TC plastic and non-aligned fibres, as well as compared to the aligned fibres, with the 50 µm microgrooves inducing the highest degree of cell elongation among all groups.

The pronounced elongation observed on the microgrooved fibres compared to the aligned fibres underscores the combined effect of the microgrooves and fibre alignment. Interestingly, the angled microgrooves had a less significant elongation effect compared to the 50 µm and 250 µm grooves, despite having a groove diameter between the other two. This discrepancy can likely be attributed to the less defined topography of these grooves, as observed in SEM imaging (**Figure 6.2**).

To investigate the effect of electrospun fibre alignment and microgrooves on fibroblast focal adhesions, cells were stained with an anti-vinculin monoclonal antibody and a FITC conjugated IgG (see **Figure 6.8**). While fluorescent microscopy of fibroblasts cultured on TC plastic showed well-defined focal adhesions, images obtained of fibroblasts cultured on PCL fibres were not clear enough to draw any conclusions about the focal adhesions. This is due to the autofluorescence of PCL, which is most significant when using green fluorescence[313]. Additionally, PCL autofluorescence can affect image contrast when using red fluorescence, as evidenced in **Figure 6.6**.

Because of this autofluorescence, the image contrast was lowered, making it difficult to distinguish subcellular structures.

In future, this could be addressed by using a different fluorescent conjugated secondary antibody, or treating the PCL to reduce autofluorescence, which could improve image quality and increase the image contrast, allowing for more detailed analysis of focal adhesions when cultured on PCL[313].

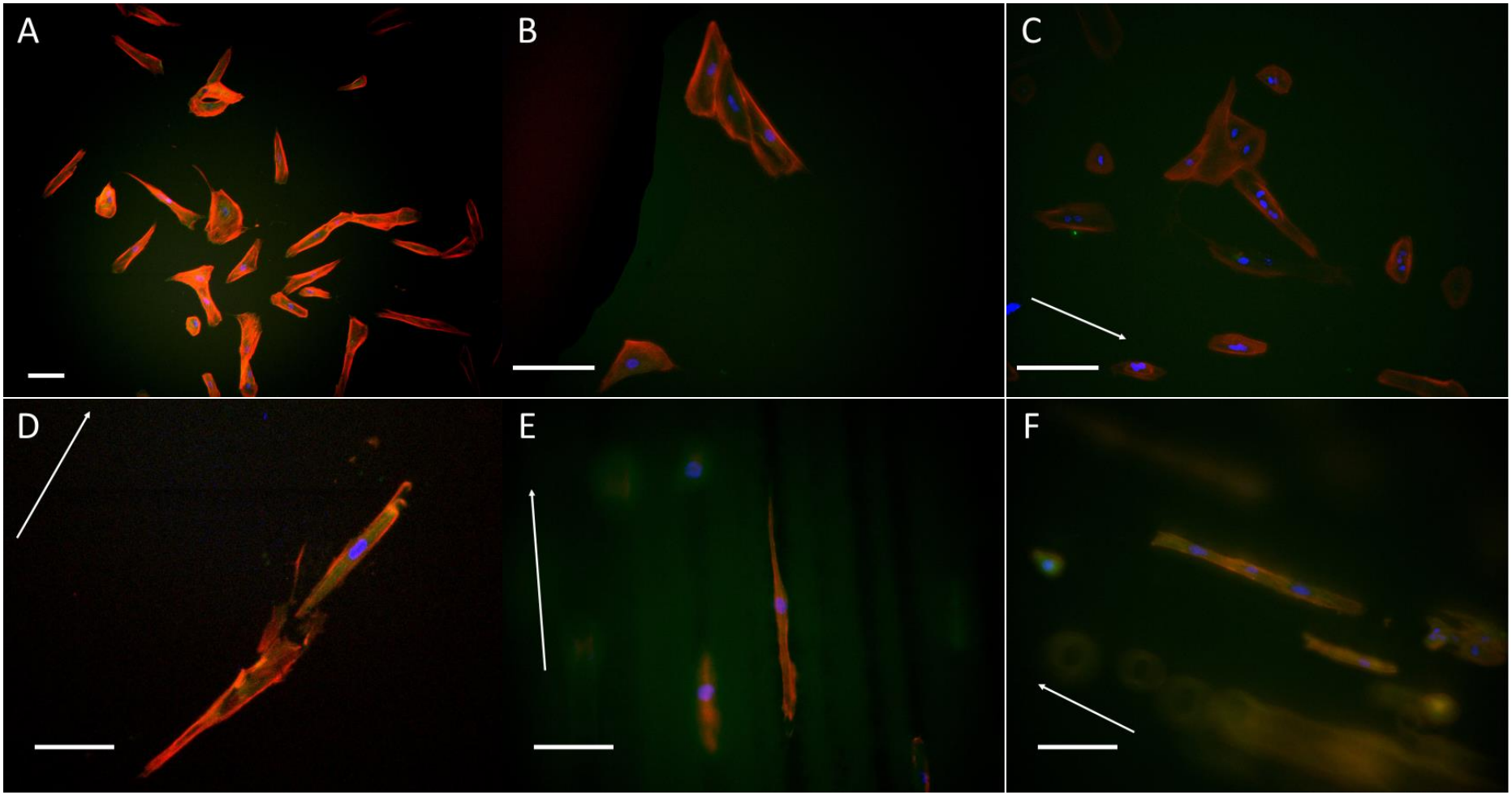

Figure 6.6 Representative fluorescent microscopy images of human oesophageal fibroblasts with phalloidin, DAPI and anti-vinculin after culture on microgrooves parallel to PCL fibre alignment. Cells were stained for F-actin (red), vinculin (green) and cell nuclei (blue) after culture for 5 days on **A** tissue culture plastic, **B** non-aligned PCL fibres, **C** aligned PCL fibres and fibres stamped with microgrooves parallel to the fibre alignment **D** 250µm grooves **E** 50µm grooves and **F** angled grooves. Arrows show dominant fibre direction; imprinted grooves are aligned with the dominant fibre direction. Scale bars: 100µm.

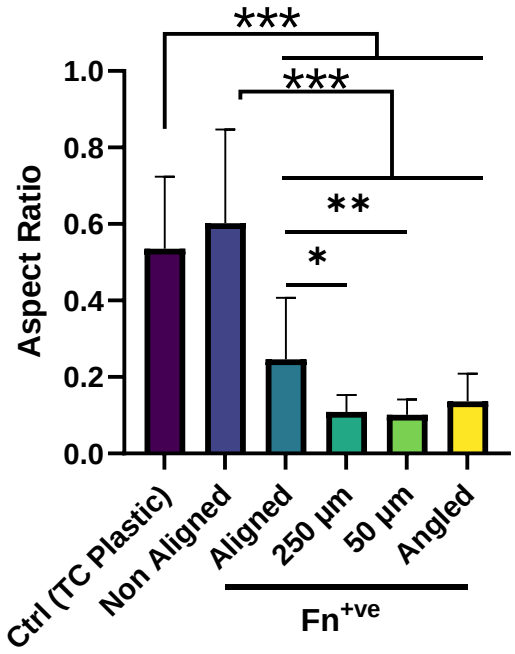

Figure 6.7 Effect of parallel microgrooves on fibroblast elongation. Graph comparing the aspect ratio (width/length) of human oesophageal fibroblasts cultured on microgrooved electrospun PCL fibre sheets to fibroblasts cultured on tissue culture plastic and non-aligned fibres. Data is presented as mean ± SD (n=6) with one-way ANOVA statistical test (* $p < 0.033$, ** $p < 0.002$, *** $p < 0.001$).

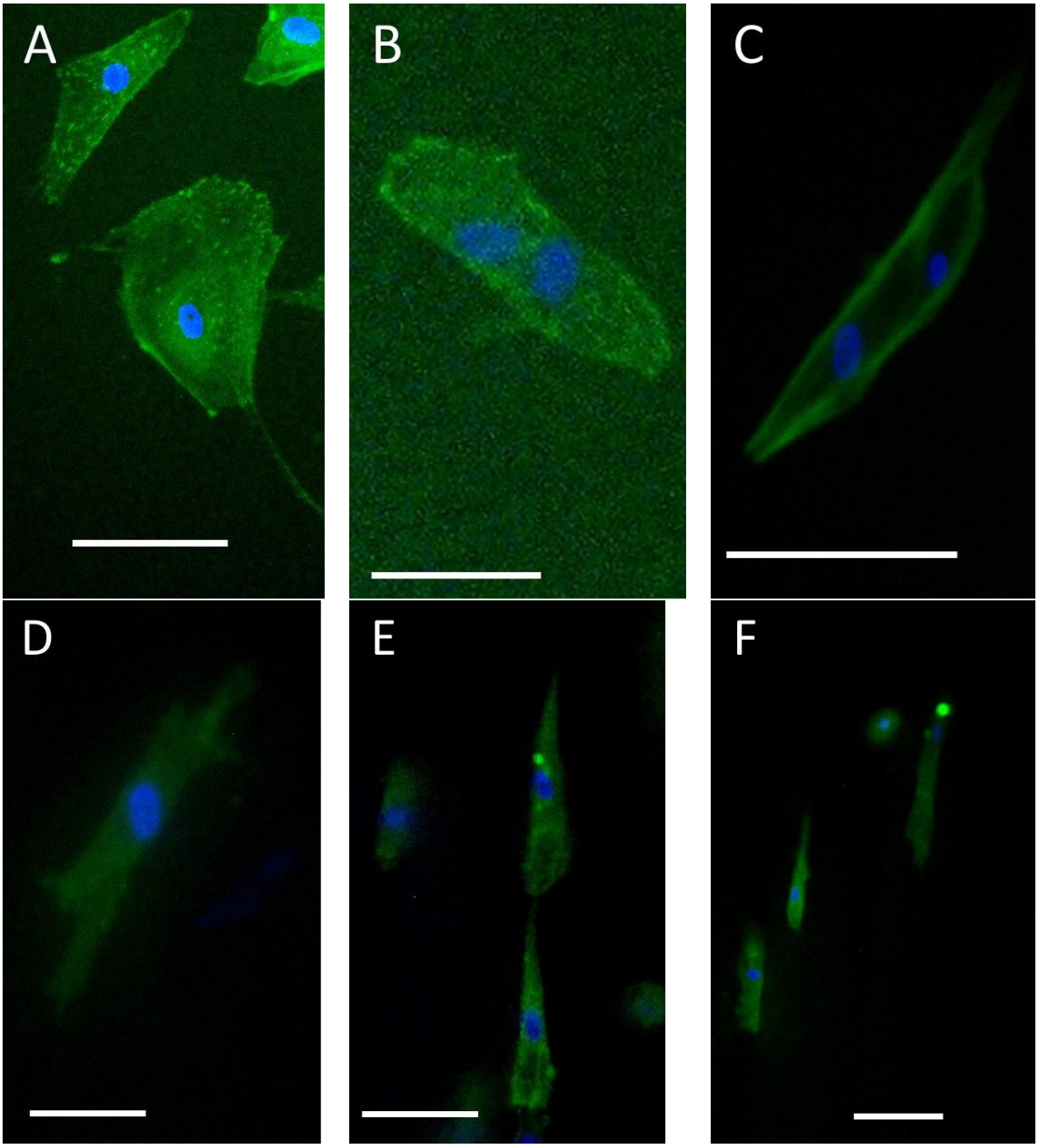

Figure 6.8 Vinculin staining of fibroblasts cultured on electrospun PCL fibres for 5 days. Representative fluorescent microscopy images of fibroblasts stained with an anti-vinculin antibody (green), after culture for 5 days on **A** tissue culture plastic, **B** non-aligned electrospun PCL fibres, **C** aligned PCL fibres, and fibres stamped with microgrooves parallel to the fibre alignment; **D** 250µm grooves **E** 50µm grooves and **F** angled grooves. Scale bars: 100µm.

6.3.5 Morphology of Fibroblasts Cultured on PCL Fibre Sheets with Microgrooves Perpendicular to Fibre Alignment

To further explore the impact of combining aligned electrospun PCL fibres with microgrooves on fibroblast elongation, 250 µm, 50 µm and angled microgrooves were added to fibre sheets perpendicular to the fibre direction.

Following a 5-day incubation period, cells were stained with TRITC-conjugated phalloidin and a vinculin antibody followed by FITC-conjugated IgG and DAPI, and fluorescent microscopy was used to obtain images of the cells cultured on each material, as shown in **Figure 6.9**.

In contrast to what was observed with the parallel microgrooves, where fibroblasts displayed more alignment on the microgrooved surfaces, placing the grooves perpendicularly to the fibre alignment did not result in noticeable alignment of the fibroblasts. This suggests that the organisational effect of the grooves was not as pronounced.

While the fibroblasts appeared to be more elongated on the microgrooved surface than the aligned fibres, the effect was not as distinct as that observed with parallel microgrooves. In addition, the observed elongation was aligned with the direction of the fibre alignment, rather than the microgrooves.

Analysis of fibroblast aspect ratio using ImageJ revealed some interesting effects

(see **Figure 6.10**).

Cells cultured on 250 µm and angled microgrooves had similar levels of elongation compared to those on aligned fibres, but remained significantly more elongated than those on non-aligned fibres.

However, fibroblasts cultured on 50 µm microgrooved fibres displayed significantly less elongation than those on aligned fibres and did not significantly differ from those on non-aligned fibres.

These results suggest that while microgrooves in combination with aligned fibres promote greater fibroblast elongation than aligned fibres alone, fibre alignment remains the primary factor influencing elongation. Additionally, these findings confirm that the smallest microgrooves (50 µm) exert the most significant effect on fibroblast elongation and orientation, and when they are positioned perpendicular to the fibre alignment, they nearly counteract the elongation effects of the fibres.

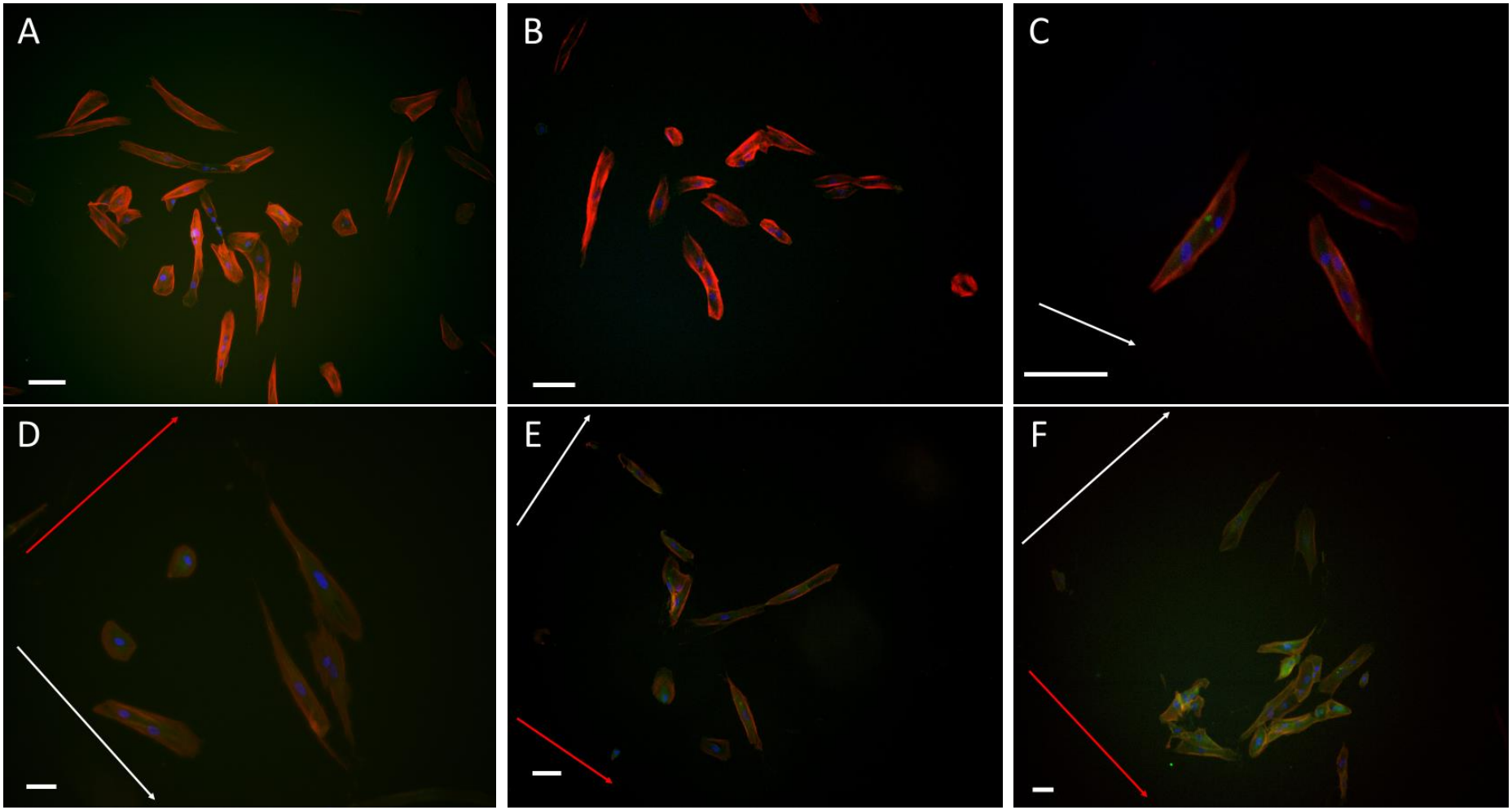

Figure 6.9 Representative fluorescent microscopy images of human oesophageal fibroblasts with phalloidin, DAPI and anti-vinculin after culture on microgrooves perpendicular to PCL fibre alignment. Cells were stained for F-actin (red), vinculin (green) and cell nuclei (blue) on **A** tissue culture plastic, **B** non-aligned PCL fibres, **C** aligned PCL fibres and fibres stamped with microgrooves perpendicular to the fibre alignment **D** 250µm grooves **E** 50µm grooves and **F** angled grooves. White arrow shows dominant fibre direction; red arrow shows microgroove direction. Scale bars: 100µm.

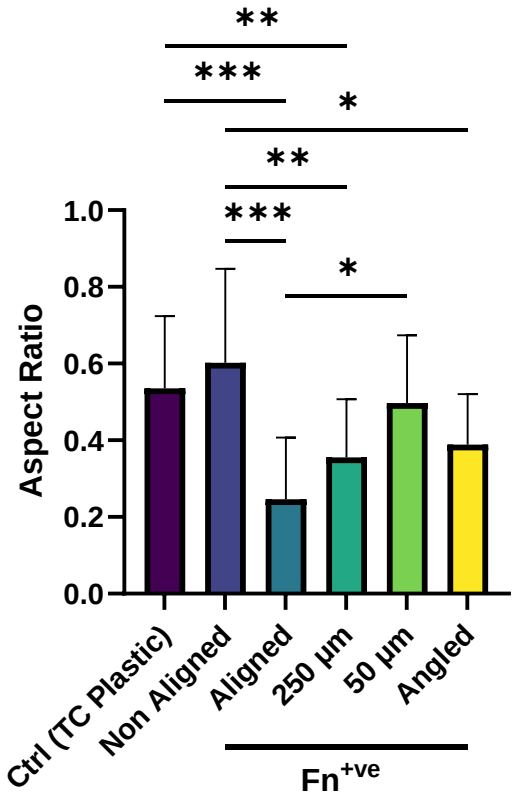

Figure 6.10 Effect of perpendicular microgrooves on fibroblast elongation. Graph comparing the aspect ratio (width/length) of human oesophageal fibroblasts cultured on electrospun PCL fibre sheets with microgrooves perpendicular to fibre direction, to fibroblasts cultured on tissue culture plastic and non-aligned fibres. Data is presented as mean ± SD (n=6) with one-way ANOVA statistical test (* $p < 0.033$, ** $p < 0.002$, *** $p < 0.001$).

To further illustrate these findings, the fibroblast elongation on each microgroove type when parallel and perpendicular to the fibre alignment was directly compared (**Figure 6.11**).

In each instance, fibroblasts cultured on perpendicular grooves exhibited significantly less elongation compared to those on parallel grooves. However, fibroblasts on 250 µm and angled perpendicular grooves remained significantly more elongated than those on randomly aligned fibres and TC plastic, showing that the elongating effect of the fibres remained significant.

However, fibroblasts on the 50 µm perpendicular grooves showed significantly less elongation compared to those on aligned fibres without microgrooves. Additionally, they were not significantly more elongated than fibroblasts on TC plastic or non-aligned fibres. This underscores the impact of the smallest microgrooves on fibroblast elongation, to the extent of counteracting the effect of electrospun fibre alignment.

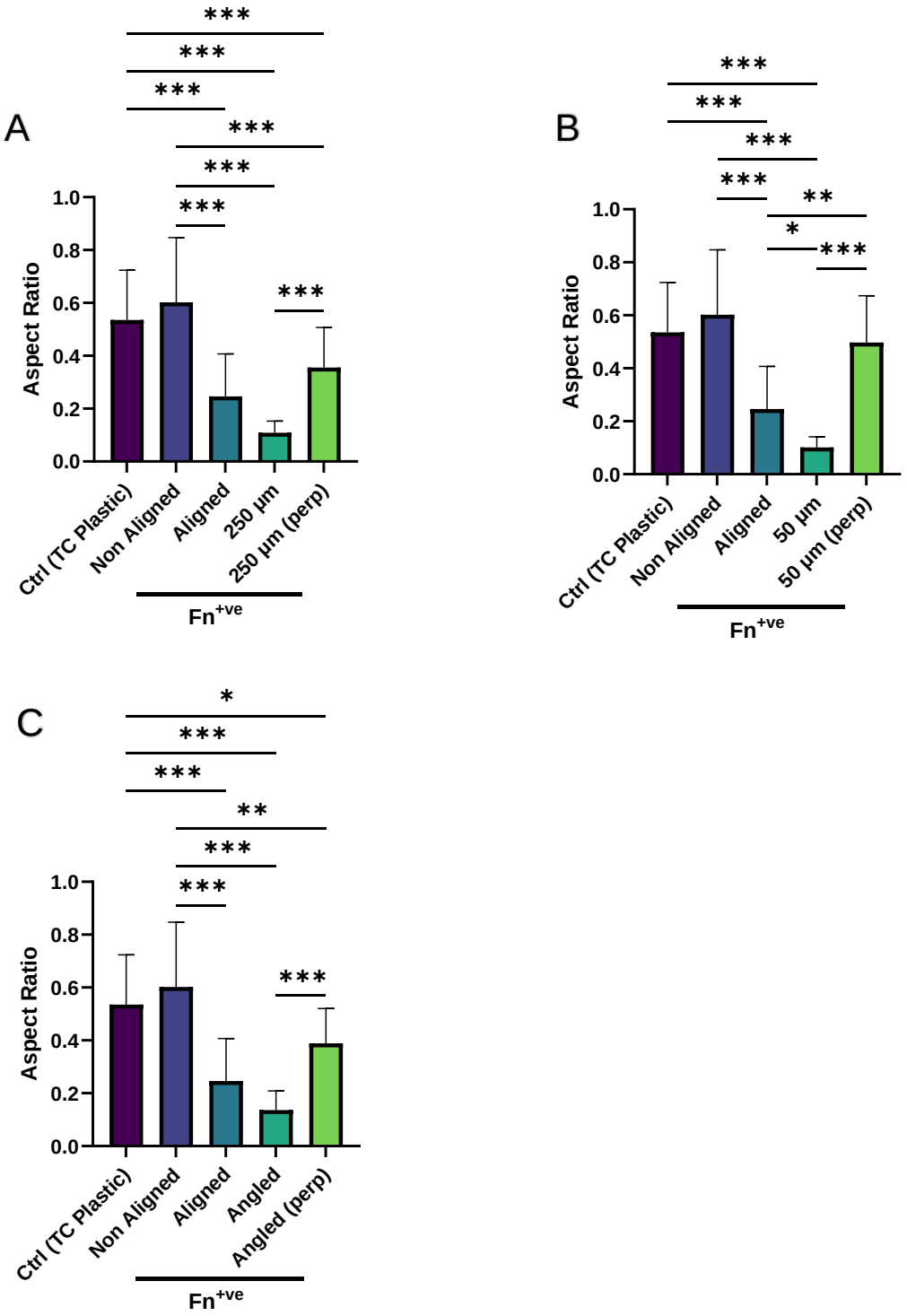

Figure 6.11 The effect of parallel and perpendicular microgrooves on fibroblast elongation. Graphs comparing the elongation of fibroblasts cultured on electrospun PCL fibre sheets with microgrooves imprinted parallel and perpendicular to the fibre alignment. **A** 250 µm, **B** 50 µm and **C** angled grooves. Data presented as mean ± SD (n=6), with one-way ANOVA statistical test (* $p < 0.033$, ** $p < 0.002$, *** $p < 0.001$).

6.4 Discussion

This chapter described the addition of microgrooves with diameters between 50 µm and 250 µm to sheets of aligned electrospun PCL fibres, and investigation of their effect on primary human oesophageal fibroblast elongation. SEM images of fibre sheets imprinted with microgrooves (250 µm, 50 µm and angled) provided insights into the introduced topographical features. Despite slight deviations from the intended groove dimensions, likely due to post-imprinting relaxation, the resulting microgrooves fell within the range that has been shown to illicit cellular responses[30,307], as evidenced by the clear fibroblast elongation observed along the microgrooves.

The results of the AlamarBlue assay indicate that human oesophageal fibroblasts exhibit a higher metabolic rate when cultured on electrospun PCL fibres compared to traditional tissue culture plastic. This suggests that the fibres may provide a more favourable environment for cellular activity and metabolism. Moreover, the fibroblast metabolic rate was further increased when cultured on electrospun fibre sheets imprinted with microgrooves, suggesting that microgrooves provide topographical cues that positively influence cell metabolism. These differences in metabolic activity became more pronounced over time, suggesting that the effects of substrate topography on cell metabolism may be cumulative, with longer incubation periods leading to more significant differences in metabolic rate. Actively proliferating cells have much higher metabolic requirements, in order to replicate the cell contents, and ECM protein deposition requires high metabolic activity[314]. The ability of the fibres to support and enhance cellular metabolism may promote cell proliferation, migration and ultimately tissue regeneration[315].

Aligned fibres play a significant role in influencing fibroblast elongation, a crucial aspect of cellular behaviour relevant to tissue engineering and regenerative medicine,

as it can indicate their migration capacity[316]. Cell migration is an important indicator in biomaterial scaffold success, as it increases the speed at which a scaffold becomes populated and granular tissue formation can begin[317,318]. In this study it was observed that fibroblasts cultured on aligned electrospun PCL fibres displayed a significantly higher degree of elongation compared to those on both TC plastic and non-aligned fibres. This underscores the importance of fibre alignment in modulating fibroblast behaviours.

The alignment of fibres provides physical cues that guide fibroblast morphology and behaviour[33,41,207]. Fibroblasts can sense and respond to the surrounding microenvironment, including substrate topography[201,207,231]. When cultured on aligned fibres, fibroblasts align themselves along the direction of fibre orientation, leading to elongated morphologies, characterised by pronounced dendritic extensions. This alignment is reminiscent of the orientation observed in native tissues, where fibroblasts align themselves along the predominant axis of mechanical stress[316,319,320].

The enhanced elongation of fibroblasts on aligned fibres can be attributed to several factors. The topographical cues provided by the fibres promote cell-substrate interactions, facilitating cell adhesion and spreading. Additionally, the physical guidance provided by the fibre alignment directs cytoskeletal organisation, leading to the alignment of cellular components along the fibre axis[207,311]. This cytoskeletal alignment contributes to the elongated morphology observed in fibroblasts cultured on aligned fibres.

Furthermore, the elongation of fibroblasts on aligned fibres may also be influenced by biochemical cues present in the microenvironment[271]. The fibronectin-functionalised

PCL fibres used in this study provided bioactivity that promoted cell adhesion and migration, further enhancing the elongation response of the cells.

Comparisons of the cell aspect ratio on non-aligned fibres, aligned fibres and fibres with imprinted grooves provide valuable insights into the influence of groove dimensions on fibroblast elongation. While aligned fibres alone resulted in significant fibroblast elongation, the addition of microgrooves parallel to the fibre direction significantly amplified this effect, particularly with the smallest groove dimensions (50 µm). Notably, the smallest grooves demonstrated the greatest effect on fibroblast elongation, underscoring the importance of groove dimensions in modulating fibroblast behaviour.

Previous studies have reported that aligned and elongated grooves on grooved topographies secrete higher levels of ECM components, potentially accelerating tissue repair[39,41]. This finding suggests that the observed increase in fibroblast elongation on microgrooved fibres could translate into enhanced tissue regeneration outcomes. By promoting the elongation and alignment of fibroblasts, microgrooves and aligned fibres may facilitate the deposition and organisation of ECM components, which are crucial steps in the tissue regeneration process.

The impact of topographical cues on fibroblast behaviour extends beyond elongation and alignment. These cues have been shown to influence fibroblast migration, proliferation, and overall functionality[41,200,312,321]. In the context of tissue engineering and regenerative medicine, understanding and leveraging these effects are essential for the design of biomimetic scaffolds that recapitulate the native tissue microenvironment and support tissue regeneration.

This study demonstrates that combining nanoscale and microscale topographies can have a synergistic effect on fibroblast behaviour. While the nanoscale topographies provided by aligned fibres promote cell alignment and elongation to some extent, the incorporation of microgrooves further enhances these effects. The interaction between nanoscale and microscale features creates a multiscale topographical substrate that more closely mimics the complexity of the native tissue microenvironment, potentially leading to more favourable tissue regeneration outcomes[304].

To further explore the influence of combining aligned electrospun PCL fibres with microgrooves on fibroblast elongation, the grooves were introduced perpendicular to the fibre orientation. Unlike the alignment observed with parallel microgrooves perpendicular grooves did not induce noticeable alignment of fibroblasts. This suggests that the organisational effect of the grooves was not present when positioned perpendicular to the fibre alignment.

In addition, the fibroblasts were not any more elongated on perpendicular 250 µm and angled microgrooves than aligned fibres alone, but remained more elongated than the non-aligned fibres. This indicates that the aligned fibres are the main driving force in the fibroblast elongation. However, there appears to be a cumulative effect when the grooves and fibres are orientated in the same direction.

However, fibroblasts cultured on the perpendicular 50 µm were significantly less elongated than aligned fibres, and were not any more elongated than the non-aligned fibres. This suggests that the 50 µm grooves exert a similarly strong effect on the fibroblast elongation. When the elongating effects of the 50 µm grooves and the aligned fibres act in perpendicular directions, they effectively neutralise each other.

Comparing fibroblast elongation on electrospun fibre sheets with microgrooves parallel and perpendicular to the fibre alignment sheds light on the role of topographical cues. Fibroblasts on perpendicular microgrooves exhibited significantly less elongation and noticeably less alignment, suggesting that the orientation of the microgrooves relative to the fibre alignment plays a crucial role in modulating cellular responses. The disruption of guidance by perpendicular grooves, especially the 50 µm grooves, underscores the importance of groove orientation.

These findings have important implications for tissue engineering applications, particularly in scaffold design. Previous research investigating the role of microscale topographies on cell morphologies has shown that aligned grooves can increase elongation and alignment of several cell types[32,33,39,207,311]. These findings suggest that combining the effects of microscale topography with aligned electrospun fibres, which provide topography similar to that of the smallest grooves that have been previously explored, presents an opportunity to develop a multiscale topographical material, with highly tailorable effects for tissue engineering applications.

While much attention has been paid to smaller diameter grooves in the range of 1-10 µm[33,39,207,311], these are comparable to the diameter of the electrospun fibres, making it impractical to combine them for multiscale topography; to combine grooves with electrospun fibres, the grooves must have a diameter distinguishable from the fibre topography in order to have a noticeable effect. Grooves with diameters in the range of 25-100 µm have been explored in relation to their effects on cell adhesion and elongation, and been shown to have a favourable effect on cytoskeletal organisation[201,322].

Future work should concentrate on characterising changes in gene and protein expression in fibroblasts cultured on aligned electrospun fibres and microgrooves to further investigate the mechanism of their effect on call morphology. In addition, mechanical stretching has been shown to increase ECM deposition and viability in cardiac fibroblasts[321]. This effect could be harnessed for oesophageal tissue engineering by applying tension to cell seeded fibres pre-implantation, an effect which has also been shown to increase the speed and distance travelled by fibroblasts[316].

In conclusion, this study has shown that combining aligned electrospun fibres and microgrooves in the range of 50-100 μm has a greater effect on cell elongation than the aligned fibres alone. Aligned fibres with microgrooves offer a promising strategy for engineering biomimetic scaffolds that mimic the structural and mechanical properties of native tissue and the hierarchal structure of the native ECM, facilitating cell alignment and tissue organisation. However, careful consideration of microgroove dimensions and orientation relative to fibre alignment is necessary to optimise cellular responses and enhance tissue regeneration outcomes.

7.0 Conclusions and Future Work

7.1 Summary of Key Findings

The primary goal of this thesis was to produce an electrospun PCL material suitable for tissue engineering and regenerative medicine, with a specific focus on oesophageal applications. The optimisation of the electrospinning process concentrated on reducing the diameter of electrospun PCL fibres, and increasing their alignment, as these two factors are critical in increasing cell migration and organisation in tissue engineering and regenerative medicine.

Key optimisations included the use of a 10 % w/v PCL solution in a 50:50 chloroform: DMF solvent system, an applied voltage of 20 kV, and a needle tip-collector distance of 20 cm, with a grounded mandrel rotating at 2000 RPM. This optimised process produced highly aligned electrospun PCL fibres with an average diameter of 0.22 ± 0.6 µm which are among the thinnest and most aligned fibred reported in the literature. Mechanical characterisation of the fibre sheets showed that they were highly anisotropic, with a higher elastic modulus and UTS when tested parallel to the fibre direction. The thickness of one fibre sheet is 70 ± 10 µm when electrospun for 8 hours with dual syringes. Additionally, fibronectin functionalisation successfully increased the bioactivity of the fibres, as demonstrated by the increased cell viability when cultured on functionalised fibres compared to non-functionalised fibres.

The mechanical properties of the electrospun PCL fibres require careful consideration for oesophageal tissue engineering applications. Successful scaffolds must integrate seamlessly with surrounding tissues, and large discrepancies in mechanical properties can cause damage and malfunction. In addition, cells in soft tissues are influenced by mechanical forces that they are exposed to from the extracellular environment, and

ECM elasticity can illicit various cellular responses including cell spreading, differentiation and signal transduction[244,323–327]. Given that these cellular responses are critical to tissue regeneration, achieving an elasticity that closely mimics the natural ECM should be carefully considered in biomaterial design, while the tensile strength and maximum extension should be sufficient to withstand the physical forces that the tissue experiences naturally.

Given that the relaxed oesophagus has a diameter of approximately 2 cm, and 3.5 cm is the approximate bolus size swallowing can accommodate without discomfort occurring, the normal extension required of the human oesophagus is around 75 %[63,328,329]. The maximum extension of the oesophageal tissue tested was 153 ± 16 %, which is well in excess of what is required during normal tissue function. In addition, the maximum extension of the PCL fibres was found to be 100 ± 20 %, which was significantly less than that of the tissue, but still in excess of what would be required during normal swallowing. The UTS of the PCL fibres was higher than the tissue parallel to the fibre direction, but was significantly lower perpendicular to the fibres.

The PCL fibres were significantly stiffer than the tissue when tested in parallel to the fibre direction, which poses a potential issue in grafting the material to the oesophagus *in vivo*. Given the role of ECM elasticity in cell behaviours, obtaining the closest possible elasticity to that of the natural ECM is paramount. However, given that the tissue tested in this study was not ECM, but complete mucosal tissue, including cellular material, direct comparisons cannot truly be made.

The investigation into the *in vitro* degradation behaviour of electrospun PCL fibres under different pH conditions, mimicking the fluctuating pH levels of the oesophageal environment, influenced by proximity to the stomach and exposure to swallowed

foods, has provided valuable insights into their suitability for oesophageal tissue engineering. The study used various metrics, including mechanical properties, fibre diameter and molecular weight, to assess the degradation kinetics over a 12-week period. The findings revealed noticeable signs of degradation within the experimental timeframe, with a higher rate of degradation observed in weakly acidic conditions.

This thesis also introduced novel findings regarding the effects of sterilisation and disinfection methods on electrospun PCL fibres. Ethanol and ethylene oxide treatments adversely affected fibre morphology and alignment, whereas radiation treatments (UV and gamma radiation) had much less detrimental effects. This is likely due to the fact that ethanol and ethylene oxide treatments involve physical interactions with the fibres, causing mechanical disruption of fibre alignment and chemical reactions that result in a melted fibre morphology and beading. Conversely, the radiation sterilisation methods, UV and gamma radiation, exhibited much less detrimental effects on the fibre morphology. These methods appear to be more chemically inert and, since they do not involve the suspension of fibres (either in liquid or gas phases), they do not affect fibre alignment.

While UV treatment is not suitable for terminal sterilisation, it was selected for use in *in vitro* studies due to its cost-effectiveness, rapidity and widespread availability. Gamma radiation emerged as the most suitable terminal sterilisation method, potentially applicable for implantable biomaterials. Nonetheless, further investigation is warranted to confirm its effectiveness and asses its long-term impact on material properties.

Overall, this research highlights the significant influence of sterilisation and disinfection processes on electrospun PCL properties, emphasising the importance of considering

these effects early in the development process of implantable biomaterials, enabling their incorporation into design considerations and facilitating necessary concessions if required. By comprehensively evaluating the impact of sterilisation methods, research can advance the development of biomaterials to meet the strict safety requirements for clinical applications. In addition, this study did not examine the effect on each sterilisation method on cell response to the material. Given that these treatments can affect the bioactivity of polymeric biomaterials differently, this should be specifically investigated[194,330].

The investigation of fibroblast response to the electrospun PCL fibres revealed that the cells will significantly elongate along the direction of fibre alignment, indicating a clear morphological response to the material. One of the most innovative aspects of this research is the addition of microgrooves to electrospun PCL fibre sheets. While there has been significant work published previously describing the effects of aligned nanoscale fibres and microscale topographies individually, very little work has been published describing the effects of combining the two. This thesis has shown that the addition of microgrooves parallel to the aligned fibres further amplified the elongation effect that the fibres had on fibroblasts, while the fibres remained the primary driver of elongation. Additionally, microgrooves visually enhanced the cell alignment and organisation compared to aligned fibres alone, suggesting promising implications for tissue engineering and regeneration applications, where fibroblast alignment and elongation can enhance the functionality of formed tissues[331]. This finding could have significant implications for biomaterials research in the field of tissue engineering, as it suggests that the influence of aligned electrospun fibres on cell behaviour, which is already significant, could become more powerful with the addition of microscale topographies.

In conclusion, the electrospun PCL fibre material developed shows promising characteristics for oesophageal tissue engineering, and future work could develop the material further for clinical use in tissue engineering and regenerative medicine.

7.2 Future Work

While this thesis describes the development of an electrospun PCL fibre biomaterial that shows promising characteristics making it potentially applicable for oesophageal tissue engineering applications, significant further work is required to develop the material and further characterise cellular responses to it before clinical use is possible.

A potential solution to the discrepancy in PCL fibre elasticity, is to combine layers of aligned fibres in several directions to produce a modular material with customisable properties. Given the average thickness of the porcine oesophagus mucosal layer (1.2 ± 0.4 mm), and the thickness of the optimised electrospun sheet (70 ± 10 µm), at least 17 layers of electrospun fibres would be needed to match the tissue thickness. Optimising layer orientation to mimic oesophageal ECM elasticity, combining the superior strength of the parallel fibres with the more favourable elasticity of the perpendicular fibres, could significantly enhance the material's suitability for clinical applications. In addition, using several fibre orientations in the final material could allow for cell infiltration into the scaffold from several directions surrounding the implant.

To ensure the safety and efficacy of the material, further extensive research into the cellular responses is needed. Specifically, investigating the effect on gene expression and protein expression is essential to mitigate potential negative outcomes. For example, fibroblast overexpression of ECM proteins can lead to misfunctioning tissues, such as those found in fibrosis[74,332]. Further research is required to determine

the underlying mechanism driving the effects observed on fibroblast elongation, and it is essential to determine whether or not this elongation translates into enhanced migration capacity. Quantitative analysis of fibroblast migration speed using time-lapse microscopy or wound healing assays can provide valuable information on the functional implications of fibroblast elongation[333].

Additionally, exploring changes in gene expression and protein secretion of fibroblasts cultured on electrospun PCL fibres with and without microgrooves could elucidate the molecular pathways responsible for mediating the cellular responses to nano- and microscale topographies. Pathways involved in cell adhesion, cytoskeletal reorganisation and mechanotransduction are likely to play a pivotal role in this process[38,200,203]. Assessing expression levels of ECM-related genes and proteins such as collagen, fibronectin and elastin, will provide insights into how aligned fibres and microgrooves modulate ECM deposition and the tissue regeneration process[231,333,334].

Long-term assessments of tissue integration and host immune response are critical to evaluate the material suitability and safety for clinical use. Comprehensive studies focusing on these aspects are necessary to ensure the successful translation of PCL fibres with microgrooves into clinical applications in tissue engineering and regenerative medicine.

While the study sheds light on the degradation behaviour of PCL fibres in *in vitro* conditions, it is crucial to acknowledge the limitations regarding the accuracy of simulating the complexity of the oesophageal environment. One significant limitation is the absence of mechanical stresses experienced *in vivo*, such as those induced by peristaltic contractions and food bolus passage. These dynamic mechanical forces

play a vital role in influencing scaffold integrity and degradation rates, which were not fully replicated in the *in vitro* study.

Future work should aim to bridge the gap between the *in vitro* findings and *in vivo* conditions by incorporating more comprehensive simulation models that mimic the mechanical stresses and dynamic pH fluctuations of the oesophageal environment. Advanced bioreactor systems capable of replicating peristaltic movements and food bolus passage could provide a more accurate representation of these conditions, allowing for a thorough evaluation of scaffold performance.

References

1. Langer, R. & Vacanti, J. P. Tissue engineering. *Science* **260**, 920–926 (1993).
2. *Organ and Tissue Donation and Transplantation: Activity Report 2022/23*. https://nhsbtdbe.blob.core.windows.net/umbraco-assets-corp/30188/activity-report-2022-2023-final.pdf (2023).
3. Di Maira, T., Little, E. C. & Berenguer, M. Immunosuppression in liver transplant. *Best Pract. Res. Clin. Gastroenterol.* **46–47**, 101681 (2020).
4. Hecking, M., Sharif, A., Eller, K. & Jenssen, T. Management of post-transplant diabetes: immunosuppression, early prevention, and novel antidiabetics. *Transpl. Int.* **34**, 27–48 (2021).
5. Doede, T., Bondartschuk, M., Joerck, C., Schulze, E. & Goernig, M. Unsuccessful alloplastic esophageal replacement with porcine small intestinal submucosa. *Artif. Organs* **33**, 328–333 (2009).
6. Lopes, M. F. *et al.* Esophageal replacement in rat using porcine intestinal submucosa as a patch or a tube-shaped graft. *Dis. Esophagus* **19**, 254–259 (2006).
7. Tan, B. *et al.* Tissue engineered esophagus by copper--small intestinal submucosa graft for esophageal repair in a canine model. *Sci. China Life Sci.* **57**, 248–255 (2014).
8. Chevallay, M. *et al.* Esophageal cancer surgery: review of complications and their management. *Ann. N. Y. Acad. Sci.* **1482**, 146–162 (2020).
9. Jadcherla, A. V., Litzenberg, K. & Balasubramanian, G. Esophageal Dysfunction in Post-lung Transplant: An Enigma. *Dysphagia* **38**, 731–743 (2023).
10. Yap, S., Vara, R. & Morais, A. Post-transplantation Outcomes in Patients with PA or MMA: A Review of the Literature. *Adv. Ther.* **37**, 1866–1896 (2020).

11. Cohen-Bucay, A., Gordon, C. E. & Francis, J. M. Non-immunological complications following kidney transplantation. *F1000Res.* **8**, (2019).
12. Almouemen, N., Kelly, H. M. & O'Leary, C. Tissue Engineering: Understanding the Role of Biomaterials and Biophysical Forces on Cell Functionality Through Computational and Structural Biotechnology Analytical Methods. *Comput. Struct. Biotechnol. J.* **17**, 591–598 (2019).
13. Akter, F. Chapter 2 - Principles of Tissue Engineering. in *Tissue Engineering Made Easy* (ed. Akter, F.) 3–16 (Academic Press, 2016).
14. Williams, D. F. On the nature of biomaterials. *Biomaterials* **30**, 5897–5909 (2009).
15. Zhang, X. & Williams, D. *Definitions of Biomaterials for the Twenty-First Century*. (Elsevier, 2019).
16. Browne, S. *et al.* Modulation of inflammation and angiogenesis and changes in ECM GAG-activity via dual delivery of nucleic acids. *Biomaterials* **69**, 133–147 (2015).
17. Wang, Y., Fan, Y. & Liu, H. Macrophage Polarization in Response to Biomaterials for Vascularization. *Ann. Biomed. Eng.* **49**, 1992–2005 (2021).
18. Teixeira, A. I., Duckworth, J. K. & Hermanson, O. Getting the right stuff: controlling neural stem cell state and fate in vivo and in vitro with biomaterials. *Cell Res.* **17**, 56–61 (2007).
19. Zhu, M. *et al.* In vivo engineered extracellular matrix scaffolds with instructive niches for oriented tissue regeneration. *Nat. Commun.* **10**, 4620 (2019).
20. Wu, J. *et al.* Influence of immunogenicity of allogeneic bone marrow mesenchymal stem cells on bone tissue engineering. *Cell Transplant.* **25**, 229–242 (2016).

21. Kiernan, C. H., Wolvius, E. B., Brama, P. A. J. & Farrell, E. The immune response to allogeneic differentiated mesenchymal stem cells in the context of bone tissue engineering. *Tissue Eng. Part B Rev.* **24**, 75–83 (2018).
22. Li, Y.-C., Zhu, K. & Young, T.-H. Induced pluripotent stem cells, form in vitro tissue engineering to in vivo allogeneic transplantation. *Journal of thoracic disease* vol. 9 455–459 (2017).
23. Chen, L., Tredget, E. E., Wu, P. Y. G. & Wu, Y. Paracrine factors of mesenchymal stem cells recruit macrophages and endothelial lineage cells and enhance wound healing. *PLoS One* **3**, e1886 (2008).
24. Hass, R., Kasper, C., Böhm, S. & Jacobs, R. Different populations and sources of human mesenchymal stem cells (MSC): A comparison of adult and neonatal tissue-derived MSC. *Cell Commun. Signal.* **9**, 12 (2011).
25. Gao, Y. & Jin, S.-Z. Strategies for treating oesophageal diseases with stem cells. *World J. Stem Cells* **12**, 488–499 (2020).
26. Park, S. Y. *et al.* Tissue-engineered artificial oesophagus patch using three-dimensionally printed polycaprolactone with mesenchymal stem cells: a preliminary report. *Interact. Cardiovasc. Thorac. Surg.* **22**, 712–717 (2016).
27. Baker, M. Why hES cells make teratomas. *Nat. Rep. Stem Cells* 1–1 (2009).
28. Greenow, K. & Clarke, A. R. Controlling the stem cell compartment and regeneration in vivo: the role of pluripotency pathways. *Physiol. Rev.* **92**, 75–99 (2012).
29. González-García, C., Sousa, S. R., Moratal, D., Ricoa, P. & Salmerón-Sánchez, M. Effect of nanoscale topography on fibronectin adsorption, focal adhesion size and matrix organisation. *Colloids and Surfaces B: Biointerfaces* **77**, 180–190 (2010).

30. Yang, C.-Y. *et al.* Neural tissue engineering: the influence of scaffold surface topography and extracellular matrix microenvironment. *Journal of Materials Chemistry B* **9**, 567–584 (2020).
31. Vigliotti, A., McMeeking, R. M. & Deshpande, V. S. Simulation of the cytoskeletal response of cells on grooved or patterned substrates. *J. R. Soc. Interface* **12**, (2015).
32. Biggs, M. J. P., Geoff Richards, R. & Dalby, M. J. Nanotopographical modification: a regulator of cellular function through focal adhesions. *Nanomedicine: Nanotechnology, Biology and Medicine* **6**, 619–633 (2010).
33. Dalby, M. J., Riehle, M. O., Yarwood, S. J., Wilkinson, C. D. W. & Curtis, A. S. G. Nucleus alignment and cell signaling in fibroblasts: response to a micro-grooved topography. *Exp. Cell Res.* **284**, 274–282 (2003).
34. Nguyen, A. T., Sathe, S. R. & Yim, E. K. F. From nano to micro: topographical scale and its impact on cell adhesion, morphology and contact guidance. *J. Phys. Condens. Matter* **28**, 183001 (2016).
35. Kim, G. H. Electrospun PCL nanofibers with anisotropic mechanical properties as a biomedical scaffold. *Biomed. Mater.* **3**, 025010 (2008).
36. Thrivikraman, G. *et al.* Cell contact guidance via sensing anisotropy of network mechanical resistance. *Proc. Natl. Acad. Sci. U. S. A.* **118**, (2021).
37. Tonndorf, R., Aibibu, D. & Cherif, C. Isotropic and Anisotropic Scaffolds for Tissue Engineering: Collagen, Conventional, and Textile Fabrication Technologies and Properties. *Int. J. Mol. Sci.* **22**, (2021).
38. Huang, C. *et al.* The involvement of integrin β1 signaling in the migration and myofibroblastic differentiation of skin fibroblasts on anisotropic collagen-containing nanofibers. *Biomaterials* **33**, 1791–1800 (2012).

39. Guillemette, M. D. *et al.* Surface topography induces 3D self-orientation of cells and extracellular matrix resulting in improved tissue function. *Integr. Biol.* **1**, 196–204 (2009).
40. Xiong, S., Gao, H., Qin, L., Jia, Y.-G. & Ren, L. Engineering topography: Effects on corneal cell behavior and integration into corneal tissue engineering. *Bioact Mater* **4**, 293–302 (2019).
41. Chou, L., Firth, J. D., Uitto, V. J. & Brunette, D. M. Substratum surface topography alters cell shape and regulates fibronectin mRNA level, mRNA stability, secretion and assembly in human fibroblasts. *J. Cell Sci.* **108 (Pt 4)**, 1563–1573 (1995).
42. Fitton, J. H. *et al.* Surface topography can interfere with epithelial tissue migration. *J. Biomed. Mater. Res.* **42**, 245–257 (1998).
43. Campos, D. M., Gritsch, K., Salles, V., Attik, G. N. & Grosgogeat, B. Surface Entrapment of Fibronectin on Electrospun PLGA Scaffolds for Periodontal Tissue Engineering. *Biores. Open Access* **3**, 117–126 (2014).
44. Chen, Y. *et al.* Vascular Endothelial Growth Factor-Recruiting Nanofiber Bandages Promote Multifunctional Skin Regeneration via Improved Angiogenesis and Immunomodulation. *Advanced Fiber Materials* **5**, 327–348 (2023).
45. Ye, L. *et al.* Heparin-Conjugated PCL Scaffolds Fabricated by Electrospinning and Loaded with Fibroblast Growth Factor 2. *J. Biomater. Sci. Polym. Ed.* **22**, 389–406 (2011).
46. Li, J., Zhang, Y.-P. & Kirsner, R. S. Angiogenesis in wound repair: angiogenic growth factors and the extracellular matrix. *Microsc. Res. Tech.* **60**, 107–114 (2003).
47. Jacob, J., More, N., Kalia, K. & Kapusetti, G. Piezoelectric smart biomaterials for bone and cartilage tissue engineering. *Inflamm. Regen.* **38**, 2 (2018).

48. Gouveia, P. J. *et al.* Flexible nanofilms coated with aligned piezoelectric microfibers preserve the contractility of cardiomyocytes. *Biomaterials* **139**, 213–228 (2017).
49. Ciofani, G., Ricotti, L. & Mattoli, V. Preparation, characterization and in vitro testing of poly(lactic-co-glycolic) acid/barium titanate nanoparticle composites for enhanced cellular proliferation. *Biomed. Microdevices* **13**, 255–266 (2011).
50. Günay, K. A. *et al.* PEG-Anthracene Hydrogels as an On-Demand Stiffening Matrix To Study Mechanobiology. *Angew. Chem. Int. Ed Engl.* **58**, 9912–9916 (2019).
51. Jiang, F. X., Yurke, B., Schloss, R. S., Firestein, B. L. & Langrana, N. A. The relationship between fibroblast growth and the dynamic stiffnesses of a DNA crosslinked hydrogel. *Biomaterials* **31**, 1199–1212 (2010).
52. Fu, L., Haage, A., Kong, N., Tanentzapf, G. & Li, H. Dynamic protein hydrogels with reversibly tunable stiffness regulate human lung fibroblast spreading reversibly. *Chem. Commun.* **55**, 5235–5238 (2019).
53. Li, J. *et al.* Biophysical and biochemical cues of biomaterials guide mesenchymal stem cell behaviors. *Front. Cell Dev. Biol.* **9**, 640388 (2021).
54. Truong, K. *et al.* Interaction of micropatterned topographical and biochemical cues to direct neurite growth from spiral ganglion neurons. *Hear. Res.* **409**, 108315 (2021).
55. Jenkins, P. M. *et al.* A nerve guidance conduit with topographical and biochemical cues: potential application using human neural stem cells. *Nanoscale Res. Lett.* **10**, 972 (2015).

56. Li, N. & Folch, A. Integration of topographical and biochemical cues by axons during growth on microfabricated 3-D substrates. *Exp. Cell Res.* **311**, 307–316 (2005).
57. Lv, H. *et al.* Biomaterial stiffness determines stem cell fate. *Life Sci.* **178**, 42–48 (2017).
58. Hernandez, J. L. & Woodrow, K. A. Medical Applications of Porous Biomaterials: Features of Porosity and Tissue-Specific Implications for Biocompatibility. *Adv. Healthc. Mater.* **11**, e2102087 (2022).
59. Poh, P. S. P., Valainis, D., Bhattacharya, K., van Griensven, M. & Dondl, P. Optimization of Bone Scaffold Porosity Distributions. *Sci. Rep.* **9**, 9170 (2019).
60. Ameer, J. M., Pr, A. K. & Kasoju, N. Strategies to Tune Electrospun Scaffold Porosity for Effective Cell Response in Tissue Engineering. *J. Funct. Biomater.* **10**, (2019).
61. Yang, Y., Zhu, X., Cui, W., Li, X. & Jin, Y. Electrospun composite mats of poly[(D,L-lactide)-co-glycolide] and collagen with high porosity as potential scaffolds for skin tissue engineering. *Macromol. Mater. Eng.* **294**, 611–619 (2009).
62. Zhu, Y., Zhou, M. & Hou, R. Tissue Engineering of Esophagus. in *Esophageal Abnormalities* (ed. Chai, J.) (IntechOpen, Rijeka, 2017).
63. Ferhatoglu, M. F. & Kıvılcım, T. Anatomy of Esophagus. in *Esophageal Abnormalities* (ed. Chai, J.) (IntechOpen, Rijeka, 2017).
64. Sweis, R. Physiology and function of the oesophagus. in *Advanced Nutrition and Dietetics in Gastroenterology* 8–14 (John Wiley & Sons, Ltd., Oxford, 2014).
65. Brügger, M. D. & Basler, K. The diverse nature of intestinal fibroblasts in development, homeostasis, and disease. *Trends Cell Biol.* **33**, 834–849 (2023).

66. Powell, D. W., Pinchuk, I. V., Saada, J. I., Chen, X. & Mifflin, R. C. Mesenchymal cells of the intestinal lamina propria. *Annu. Rev. Physiol.* **73**, 213–237 (2011).
67. Roulis, M. & Flavell, R. A. Fibroblasts and myofibroblasts of the intestinal lamina propria in physiology and disease. *Differentiation* **92**, 116–131 (2016).
68. Kuo, B. & Urma, D. Esophagus - anatomy and development. *GI Motility online* (2006) doi:10.1038/gimo6.
69. Li, Y., Zhu, Y., Yu, H., Chen, L. & Liu, Y. Topographic characterization and protein quantification of esophageal basement membrane for scaffold design reference in tissue engineering. *J. Biomed. Mater. Res. B Appl. Biomater.* **100**, 265–273 (2012).
70. Long, J. Esophageal submucosal glands: structure and function. *Am. J. Gastroenterol.* **94**, 2818–2824 (1999).
71. Standring, S. *et al.* Gray's anatomy: the anatomical basis of clinical practice. *AJNR Am. J. Neuroradiol.* **26**, 2703 (2005).
72. Bainbridge, P. Wound healing and the role of fibroblasts. *J. Wound Care* **22**, 407–8, 410–12 (2013).
73. el-Ghalbzouri, A., Gibbs, S., Lamme, E., Van Blitterswijk, C. A. & Ponec, M. Effect of fibroblasts on epidermal regeneration. *Br. J. Dermatol.* **147**, 230–243 (2002).
74. Kendall, R. T. & Feghali-Bostwick, C. A. Fibroblasts in fibrosis: novel roles and mediators. *Front. Pharmacol.* **5**, 123 (2014).
75. Hayashi, K. *et al.* A neo-esophagus reconstructed by cultured human esophageal epithelial cells, smooth muscle cells, fibroblasts, and collagen. *ASAIO J.* **50**, 261–266 (2004).
76. Franklin, R. A. Fibroblasts and macrophages: Collaborators in tissue homeostasis. *Immunol. Rev.* **302**, 86–103 (2021).

77. Bloom, D. E. *et al. The Global Economic Burden of Noncommunicable Diseases*. https://ideas.repec.org/p/gdm/wpaper/8712.html (2012).
78. Kato, H. & Nakajima, M. Treatments for esophageal cancer: a review. *Gen. Thorac. Cardiovasc. Surg.* **61**, 330–335 (2013).
79. Malhotra, G. K. *et al.* Global trends in esophageal cancer. *J. Surg. Oncol.* **115**, 564–579 (2017).
80. Sun, L. P. *et al.* Dietary factors and risk of mortality among patients with esophageal cancer: a systematic review. *BMC Cancer* **20**, 287 (2020).
81. Watanabe, M. *et al.* Recent progress in multidisciplinary treatment for patients with esophageal cancer. *Surg. Today* **50**, 12–20 (2020).
82. Fan, J. *et al.* Global trends in the incidence and mortality of esophageal cancer from 1990 to 2017. *Cancer Med.* **9**, 6875–6887 (2020).
83. Zhang, Y. Epidemiology of esophageal cancer. *World J. Gastroenterol.* **19**, 5598–5606 (2013).
84. Reismann, M., Granholm, T. & Ehrén, H. Partial gastric pull-up in the treatment of patients with long-gap esophageal atresia. *World J. Pediatr.* **11**, 267–271 (2015).
85. Nayar, R., Varshney, V. K. & Goel, A. D. Outcomes of Gastric Conduit in Corrosive Esophageal Stricture: a Systematic Review and Meta-analysis. *J. Gastrointest. Surg.* **26**, 224–234 (2022).
86. Khorobrykh, T. *et al.* Gastric Conduit Cancer following Ivor-Lewis Esophagectomy for Esophageal Adenocarcinoma: A Case Report and Literature Review. *Case Rep. Oncol.* **16**, 1196–1202 (2023).
87. Yang, Y. & Ma, L. Oesophageal reconstruction with a reversed gastric conduit for a complex oesophageal cancer patient: a case report. *BMC Surg.* **22**, 225 (2022).

88. Brown, J. *et al.* Colonic Interposition After Adult Oesophagectomy: Systematic Review and Meta-analysis of Conduit Choice and Outcome. *J. Gastrointest. Surg.* **22**, 1104–1111 (2018).
89. Yoshida, N. *et al.* Omental Flap Wrapping Around the Esophagogastric Anastomosis and Association with Anastomotic Leak in Esophagectomy for Esophageal Cancer: A Propensity Score-Matching Analysis. *J. Am. Coll. Surg.* **236**, 189–197 (2023).
90. Bakshi, A., Sugarbaker, D. J. & Burt, B. M. Alternative conduits for esophageal replacement. *Ann Cardiothorac Surg* **6**, 137–143 (2017).
91. Dai, J. G., Zhang, Z. Y., Min, J. X., Huang, X. B. & Wang, J. S. Wrapping of the omental pedicle flap around esophagogastric anastomosis after esophagectomy for esophageal cancer. *Surgery* **149**, 404–410 (2011).
92. Matsumine, H., Kubo, K., Hamahata, A. & Sakurai, H. Deltopectoral and Pectoralis Musculocutaneous Flap Technique for Cervical Esophageal Reconstruction after Free-Jejunal-Flap Necrosis. *Plast Reconstr Surg Glob Open* **5**, e1444 (2017).
93. McCarthy, C. M., Kraus, D. H. & Cordeiro, P. G. Tracheostomal and cervical esophageal reconstruction with combined deltopectoral flap and microvascular free jejunal transfer after central neck exenteration. *Plast. Reconstr. Surg.* **115**, 1304–10; discussion 1311-3 (2005).
94. Badylak, S. F. *et al.* Esophageal preservation in five male patients after endoscopic inner-layer circumferential resection in the setting of superficial cancer: a regenerative medicine approach with a biologic scaffold. *Tissue Eng. Part A* **17**, 1643–1650 (2011).

95. Londono, R. & Badylak, S. F. Regenerative Medicine Strategies for Esophageal Repair. *Tissue Eng. Part B Rev.* **21**, 393–410 (2015).
96. Poghosyan, T., Gaujoux, S., Sfeir, R., Larghero, J. & Cattan, P. Bioartificial oesophagus in the era of tissue engineering. *J. Pediatr. Gastroenterol. Nutr.* **52 Suppl 1**, S16-7 (2011).
97. Rove, J. Y., Krupnick, A. S., Baciewicz, F. A. & Meyers, B. F. Gastric conduit revision postesophagectomy: Management for a rare complication. *J. Thorac. Cardiovasc. Surg.* **154**, 1450–1458 (2017).
98. Vijay, K., Godara, R. & Vijayvergia, V. Failed Gastric Pull up after Esophagectomy Managed by Colonic Interposition. *Indian J. Surg.* **75**, 347–349 (2013).
99. Abbasi, H. R. *et al.* Repair of Esophageal Full-Thickness Defects with Expanded Polytetraflouroethylene (PTFE) Patch: An Experimental Study on Dogs. *J. Appl. Anim. Res.* **28**, 89–92 (2005).
100. González Sáez, L. A., Arnal Monreal, F., Pita Fernández, S. & Machuca Santa Cruz, J. Experimental study using PTFE (Goretex) patches for replacement of the oesophageal wall. *Eur. Surg. Res.* **35**, 372–376 (2003).
101. Stemerman, D. H. *et al.* Nonexpandable silicone esophageal stents for treatment of malignant tracheoesophageal fistulas: complications and radiographic appearances. *Abdom. Imaging* **22**, 14–19 (1997).
102. Fryfogle, J. D., Cyrowski, G. A., Rothwell, D., Rheault, G. & Clark, T. Replacement of the middle third of the esophagus with a silicone rubber prosthesis. An experiment and clinical study. *Dis. Chest* **43**, 464–475 (1963).
103. Freud, E., Efrati, I., Kidron, D., Finally, R. & Mares, A. J. Comparative experimental study of esophageal wall regeneration after prosthetic replacement. *J. Biomed. Mater. Res.* **45**, 84–91 (1999).

104. Badylak, S. F., Freytes, D. O. & Gilbert, T. W. Extracellular matrix as a biological scaffold material: Structure and function. *Acta Biomater.* **5**, 1–13 (2009).

105. Badylak, S. F. *et al.* Esophageal reconstruction with ECM and muscle tissue in a dog model. *J. Surg. Res.* **128**, 87–97 (2005).

106. Orozco-Vega, A. *et al.* Decellularization of porcine esophageal tissue at three diameters and the bioscaffold modification with EETs-ECM gel. *J. Biomed. Mater. Res. A* **110**, 1669–1680 (2022).

107. Wei, R.-Q. *et al.* Grafts of porcine small intestinal submucosa with cultured autologous oral mucosal epithelial cells for esophageal repair in a canine model. *Exp. Biol. Med.* **234**, 453–461 (2009).

108. Basu, J. *et al.* Extension of bladder-based organ regeneration platform for tissue engineering of esophagus. *Med. Hypotheses* **78**, 231–234 (2012).

109. Kuppan, P., Sethuraman, S. & Krishnan, U. M. In vitro co-culture of epithelial cells and smooth muscle cells on aligned nanofibrous scaffolds. *Mater. Sci. Eng. C Mater. Biol. Appl.* **81**, 191–205 (2017).

110. Zhu, Y., Chian, K. S., Chan-Park, M. B., Mhaisalkar, P. S. & Ratner, B. D. Protein bonding on biodegradable poly(L-lactide-co-caprolactone) membrane for esophageal tissue engineering. *Biomaterials* **27**, 68–78 (2006).

111. Zhu, Y., Leong, M. F., Ong, W. F., Chan-Park, M. B. & Chian, K. S. Esophageal epithelium regeneration on fibronectin grafted poly(L-lactide-co-caprolactone) (PLLC) nanofiber scaffold. *Biomaterials* **28**, 861–868 (2007).

112. Syed, O., Walters, N. J., Day, R. M., Kim, H.-W. & Knowles, J. C. Evaluation of decellularization protocols for production of tubular small intestine submucosa scaffolds for use in oesophageal tissue engineering. *Acta Biomater.* **10**, 5043–5054 (2014).

113. Yeo, M. *et al.* Esophageal wound healing by aligned smooth muscle cell-laden nanofibrous patch. *Mater Today Bio* **19**, 100564 (2023).
114. Jian, S. *et al.* Nanofibers with diameter below one nanometer from electrospinning. *RSC Adv.* **8**, 4794–4802 (2018).
115. Bian, Y., Wang, S., Zhang, L. & Chen, C. Influence of fiber diameter, filter thickness, and packing density on PM2.5 removal efficiency of electrospun nanofiber air filters for indoor applications. *Build. Environ.* **170**, 106628 (2020).
116. Zhang, Q., Li, Q., Young, T. M., Harper, D. P. & Wang, S. A Novel Method for Fabricating an Electrospun Poly(Vinyl Alcohol)/Cellulose Nanocrystals Composite Nanofibrous Filter with Low Air Resistance for High-Efficiency Filtration of Particulate Matter. *ACS Sustainable Chem. Eng.* **7**, 8706–8714 (2019).
117. Karabulut, F. *Melt-Blown Fibres vs Electrospun Nanofibres as Filtration Media*. https://www.innovationintextiles.com/uploads/12280/MB-vs.-NF-White-Paper.pdf (2020).
118. Faccini, M., Vaquero, C. & Amantia, D. Development of Protective Clothing against Nanoparticle Based on Electrospun Nanofibers. *J. Nanomater.* **2012**, (2012).
119. Hussain, M. *et al.* Polyacrylonitrile Nanofibers Containing Viroblock as Promising Material for Protective Clothing. *NATO Adv. Sci. Inst. Ser. E Appl. Sci.* **11**, 11469 (2021).
120. Koozekonan, A. G. *et al.* Fabrication and characterization of TiO2 and MWCNT coated electrospinning nanofibers for UV protection properties. *MethodsX* **8**, 101354 (2021).
121. Escorihuela, J. *et al.* Proton Conductivity through Polybenzimidazole Composite Membranes Containing Silica Nanofiber Mats. *Polymers* **11**, (2019).

122. Li, Y.-F. *et al.* Light responsive hybrid nanofibres for on-demand therapeutic drug and cell delivery. *J. Tissue Eng. Regen. Med.* **11**, 2411–2420 (2017).
123. Liang, Y., Zhu, H., Wang, L., He, H. & Wang, S. Biocompatible smart cellulose nanofibres for sustained drug release via pH and temperature dual-responsive mechanism. *Carbohydr. Polym.* **249**, 116876 (2020).
124. Uhljar, L. É. & Ambrus, R. Electrospinning of Potential Medical Devices (Wound Dressings, Tissue Engineering Scaffolds, Face Masks) and Their Regulatory Approac. *Pharmaceutics* **15**, (2023).
125. Neal, R. A. *et al.* Laminin nanofiber meshes that mimic morphological properties and bioactivity of basement membranes. *Tissue Eng. Part C Methods* **15**, 11–21 (2009).
126. Buttafoco, L. *et al.* Electrospinning of collagen and elastin for tissue engineering applications. *Biomaterials* **27**, 724–734 (2006).
127. Boys, C. V. On the Production, Properties, and some suggested Uses of the Finest Threads. *Proceedings of the Physical Society of London* **9**, (1887).
128. Taylor, G. I. Disintegration of water drops in an electric field. *Proc. R. Soc. Lond. A Math. Phys. Sci.* **280**, 383–397 (1964).
129. Taylor, G. I. & Van Dyke, M. D. Electrically driven jets. *Proc. R. Soc. Lond. A Math. Phys. Sci.* **313**, 453–475 (1969).
130. Yarin, A. L., Koombhongse, S. & Reneker, D. H. Bending instability in electrospinning of nanofibers. *J. Appl. Phys.* **89**, 3018–3026 (2001).
131. Reneker, D. H., Yarin, A. L. & Fong, H. Bending instability of electrically charged liquid jets of polymer solutions in electrospinning. *Journal of Applied* (2000).

132. Asmatulu, R. & Khan, W. S. Chapter 2 - Historical background of the electrospinning process. in *Synthesis and Applications of Electrospun Nanofibers* 17–39 (Elsevier, 2019).

133. Haider, A., Haider, S. & Kang, I.-K. A comprehensive review summarizing the effect of electrospinning parameters and potential applications of nanofibers in biomedical and biotechnology. *Arabian Journal of Chemistry* **11**, 1165–1188 (2018).

134. Megelski, S., Stephens, J. S., Chase, D. B. & Rabolt, J. F. Micro- and Nanostructured Surface Morphology on Electrospun Polymer Fibers. *Macromolecules* **35**, 8456–8466 (2002).

135. Deitzel, J. M., Kleinmeyer, J., Harris, D. & Beck Tan, N. C. The effect of processing variables on the morphology of electrospun nanofibers and textiles. *Polymer* **42**, 261–272 (2001).

136. Bhattarai, R. S., Bachu, R. D., Boddu, S. H. S. & Bhaduri, S. Biomedical Applications of Electrospun Nanofibers: Drug and Nanoparticle Delivery. *Pharmaceutics* **11**, (2018).

137. Doshi, J. & Reneker, D. H. Electrospinning process and applications of electrospun fibers. *J. Electrostat.* **35**, 151–160 (1995).

138. Jaeger, R., Bergshoef, M. M., Batlle, C. M. I., Schönherr, H. & Julius Vancso, G. Electrospinning of ultra-thin polymer fibers. *Macromol. Symp.* **127**, 141–150 (1998).

139. Gupta, P., Elkins, C., Long, T. E. & Wilkes, G. L. Electrospinning of linear homopolymers of poly(methyl methacrylate): exploring relationships between fiber formation, viscosity, molecular weight and concentration in a good solvent. *Polymer* **46**, 4799–4810 (2005).

140. Angammana, C. J. & Jayaram, S. H. Analysis of the effects of solution conductivity on electro-spinning process and fiber morphology. in *2008 IEEE Industry Applications Society Annual Meeting* (IEEE, 2008). doi:10.1109/08ias.2008.96.

141. De Vrieze, S. *et al.* The effect of temperature and humidity on electrospinning. *J. Mater. Sci.* **44**, 1357–1362 (2009).

142. Pelipenko, J. *et al.* The topography of electrospun nanofibers and its impact on the growth and mobility of keratinocytes. *Eur. J. Pharm. Biopharm.* **84**, 401–411 (2013).

143. Mattoso, L. H. C., Offeman, R. D., Wood, D. F., Orts, W. J. & Medeiros, E. S. Effect of relative humidity on the morphology of electrospun polymer fibers. *Can. J. Chem.* **86**, 590–599 (2008).

144. Alfaro De Prá, M. A., Ribeiro-do-Valle, R. M., Maraschin, M. & Veleirinho, B. Effect of collector design on the morphological properties of polycaprolactone electrospun fibers. *Mater. Lett.* **193**, 154–157 (2017).

145. Fialho, S. L., Behar-Cohen, F. & Silva-Cunha, A. Dexamethasone-loaded poly(epsilon-caprolactone) intravitreal implants: a pilot study. *Eur. J. Pharm. Biopharm.* **68**, 637–646 (2008).

146. Kim, J. *et al.* Long-term intraocular pressure reduction with intracameral polycaprolactone glaucoma devices that deliver a novel anti-glaucoma agent. *J. Control. Release* **269**, 45–51 (2018).

147. Mondal, D., Griffith, M. & Venkatraman, S. S. Polycaprolactone-based biomaterials for tissue engineering and drug delivery: Current scenario and challenges. *International Journal of Polymeric Materials and Polymeric Biomaterials* **65**, 255–265 (2016).

148. Bhaskar, P. *et al.* Cell response to sterilized electrospun poly(ε-caprolactone) scaffolds to aid tendon regeneration in vivo. *J. Biomed. Mater. Res. A* **105**, 389–397 (2017).

149. Fu, W. *et al.* Electrospun gelatin/PCL and collagen/PLCL scaffolds for vascular tissue engineering. *Int. J. Nanomedicine* **9**, 2335–2344 (2014).

150. Ju, Y. M., Choi, J. S., Atala, A., Yoo, J. J. & Lee, S. J. Bilayered scaffold for engineering cellularized blood vessels. *Biomaterials* **31**, 4313–4321 (2010).

151. Zhu, Y., Cao, Y., Pan, J. & Liu, Y. Macro-alignment of electrospun fibers for vascular tissue engineering. *J. Biomed. Mater. Res. B Appl. Biomater.* **92**, 508–516 (2010).

152. Wu, H., Fan, J., Chu, C.-C. & Wu, J. Electrospinning of small diameter 3-D nanofibrous tubular scaffolds with controllable nanofiber orientations for vascular grafts. *J. Mater. Sci. Mater. Med.* **21**, 3207–3215 (2010).

153. Nottelet, B. *et al.* Factorial design optimization and in vivo feasibility of poly(epsilon-caprolactone)-micro- and nanofiber-based small diameter vascular grafts. *J. Biomed. Mater. Res. A* **89**, 865–875 (2009).

154. Heidari, M., Bahrami, S. H., Ranjbar-Mohammadi, M. & Milan, P. B. Smart electrospun nanofibers containing PCL/gelatin/graphene oxide for application in nerve tissue engineering. *Mater. Sci. Eng. C Mater. Biol. Appl.* **103**, 109768 (2019).

155. Sorkio, A. *et al.* Surface Modified Biodegradable Electrospun Membranes as a Carrier for Human Embryonic Stem Cell-Derived Retinal Pigment Epithelial Cells. *Tissue Eng. Part A* **21**, 2301–2314 (2015).

156. Zhang, D. *et al.* Electrospun SF/PLCL nanofibrous membrane: a potential scaffold for retinal progenitor cell proliferation and differentiation. *Sci. Rep.* **5**, 14326 (2015).

157. Chanda, A. *et al.* Electrospun chitosan/polycaprolactone-hyaluronic acid bilayered scaffold for potential wound healing applications. *Int. J. Biol. Macromol.* **116**, 774–785 (2018).

158. Gümüşderelioğlu, M., Dalkıranoğlu, S., Aydın, R. S. T. & Cakmak, S. A novel dermal substitute based on biofunctionalized electrospun PCL nanofibrous matrix. *J. Biomed. Mater. Res. A* **98**, 461–472 (2011).

159. Ottosson, M., Jakobsson, A. & Johansson, F. Accelerated Wound Closure - Differently Organized Nanofibers Affect Cell Migration and Hence the Closure of Artificial Wounds in a Cell Based In Vitro Model. *PLoS One* **12**, e0169419 (2017).

160. Ansari, Z., Kalantar, M., Kharaziha, M., Ambrosio, L. & Raucci, M. G. Polycaprolactone/fluoride substituted-hydroxyapatite (PCL/FHA) nanocomposite coatings prepared by in-situ sol-gel process for dental implant applications. *Prog. Org. Coat.* **147**, 105873 (2020).

161. Mohandesnezhad, S. *et al.* In vitro evaluation of Zeolite-nHA blended PCL/PLA nanofibers for dental tissue engineering. *Mater. Chem. Phys.* **252**, 123152 (2020).

162. Chen, X., Xu, C. & He, H. Electrospinning of silica nanoparticles-entrapped nanofibers for sustained gentamicin release. *Biochem. Biophys. Res. Commun.* **516**, 1085–1089 (2019).

163. Tokiwa, Y., Calabia, B. P., Ugwu, C. U. & Aiba, S. Biodegradability of plastics. *Int. J. Mol. Sci.* **10**, 3722–3742 (2009).

164. Vollrath, A. *et al.* Effect of Crystallinity on the Properties of Polycaprolactone Nanoparticles Containing the Dual FLAP/mPEGS-1 Inhibitor BRP-187. *Polymers* **13**, (2021).

165. Tokiwa, Y. & Suzuki, T. Hydrolysis of polyesters by lipases. *Nature* **270**, 76–78 (1977).

166. Pranamuda, H., Tokiwa, Y. & Tanaka, H. Physical properties and biodegradability of blends containing poly(ε-caprolactone) and tropical starches. *J. Environ. Polym. Degrad.* **4**, 1–7 (1996).

167. Xue, J., Wu, T., Dai, Y. & Xia, Y. Electrospinning and Electrospun Nanofibers: Methods, Materials, and Applications. *Chem. Rev.* **119**, 5298–5415 (2019).

168. Buchko, C. J., Chen, L. C., Shen, Y. & Martin, D. C. Processing and microstructural characterization of porous biocompatible protein polymer thin films. *Polymer* **40**, 7397–7407 (1999).

169. Sill, T. J. & von Recum, H. A. Electrospinning: applications in drug delivery and tissue engineering. *Biomaterials* **29**, 1989–2006 (2008).

170. Li, W.-J., Danielson, K. G., Alexander, P. G. & Tuan, R. S. Biological response of chondrocytes cultured in three-dimensional nanofibrous poly(epsilon-caprolactone) scaffolds. *J. Biomed. Mater. Res. A* **67**, 1105–1114 (2003).

171. Pişkin, E. *et al.* In vivo performance of simvastatin-loaded electrospun spiral-wound polycaprolactone scaffolds in reconstruction of cranial bone defects in the rat model. *J. Biomed. Mater. Res. A* **90**, 1137–1151 (2009).

172. Ma, Z., He, W., Yong, T. & Ramakrishna, S. Grafting of gelatin on electrospun poly(caprolactone) nanofibers to improve endothelial cell spreading and proliferation and to control cell Orientation. *Tissue Eng.* **11**, 1149–1158 (2005).

173. Liverani, L., Killian, M. S. & Boccaccini, A. R. Fibronectin Functionalized Electrospun Fibers by Using Benign Solvents: Best Way to Achieve Effective Functionalization. *Front Bioeng Biotechnol* **7**, (2019).

174. Wang, X., Zhao, H., Turng, L.-S. & Li, Q. Crystalline Morphology of Electrospun Poly(ε-caprolactone) (PCL) Nanofibers. *Ind. Eng. Chem. Res.* **52**, 4939–4949 (2013).

175. Metwally, S. *et al.* Surface potential and roughness controlled cell adhesion and collagen formation in electrospun PCL fibers for bone regeneration. *Mater. Des.* **194**, 108915 (2020).

176. Seddighian, A., Ganji, F., Baghaban-Eslaminejad, M. & Bagheri, F. Electrospun PCL scaffold modified with chitosan nanoparticles for enhanced bone regeneration. *Prog Biomater* **10**, 65–76 (2021).

177. Valerini, D., Tammaro, L., Vitali, R., Guillot, G. & Rinaldi, A. Sputter-Deposited Ag Nanoparticles on Electrospun PCL Scaffolds: Morphology, Wettability and Antibacterial Activity. *Coat. World* **11**, 345 (2021).

178. Karakucuk, A. & Tort, S. Preparation, characterization and antimicrobial activity evaluation of electrospun PCL nanofiber composites of resveratrol nanocrystals. *Pharm. Dev. Technol.* **25**, 1216–1225 (2020).

179. Augustine, R., Kalarikkal, N. & Thomas, S. Electrospun PCL membranes incorporated with biosynthesized silver nanoparticles as antibacterial wound dressings. *Applied Nanoscience* **6**, 337–344 (2016).

180. Rabionet, M., Yeste, M., Puig, T. & Ciurana, J. Electrospinning PCL Scaffolds Manufacture for Three-Dimensional Breast Cancer Cell Culture. *Polymers* **9**, (2017).

181. Yao, Q. *et al.* Three dimensional electrospun PCL/PLA blend nanofibrous scaffolds with significantly improved stem cells osteogenic differentiation and cranial bone formation. *Biomaterials* **115**, 115–127 (2017).
182. Hanas, T., Sampath Kumar, T. S., Perumal, G. & Doble, M. Tailoring degradation of AZ31 alloy by surface pre-treatment and electrospun PCL fibrous coating. *Mater. Sci. Eng. C Mater. Biol. Appl.* **65**, 43–50 (2016).
183. Basar, A. O., Sadhu, V. & Sasmazel, H. T. Preparation of electrospun PCL-based scaffolds by mono/multi-functionalized GO. *Biomed. Mater.* **14**, (2019).
184. Singh, R. *et al.* Optimization of cell seeding on electrospun PCL-silk fibroin scaffolds. *Eur. Polym. J.* **134**, 109838 (2020).
185. Stevens, J. S., de Luca, A. C., Downes, S., Terenghi, G. & Schroeder, S. L. M. Immobilisation of cell-binding peptides on poly-ε-caprolactone (PCL) films: A comparative XPS study of two chemical surface functionalisation methods. *Surf. Interface Anal.* **46**, 673–678 (2014).
186. Elnaggar, M. A., El-Fawal, H. A. N. & Allam, N. K. Biocompatible PCL-nanofibers scaffold with immobilized fibronectin and laminin for neuronal tissue regeneration. *Mater. Sci. Eng. C Mater. Biol. Appl.* **119**, 111550 (2021).
187. Ezhilarasu, H. *et al.* Functionalized core/shell nanofibers for the differentiation of mesenchymal stem cells for vascular tissue engineering. *Nanomedicine* **14**, 201–214 (2019).
188. Amores de Sousa, M. C. *et al.* Functionalization of Electrospun Nanofibers and Fiber Alignment Enhance Neural Stem Cell Proliferation and Neuronal Differentiation. *Front Bioeng Biotechnol* **8**, 580135 (2020).

189. Dziemidowicz, K., Brocchini, S. & Williams, G. R. A simple route to functionalising electrospun polymer scaffolds with surface biomolecules. *Int. J. Pharm.* **597**, 120231 (2021).

190. Banimohamad-Shotorbani, B., Rahmani Del Bakhshayesh, A., Mehdipour, A., Jarolmasjed, S. & Shafaei, H. The efficiency of PCL/HAp electrospun nanofibers in bone regeneration: a review. *J. Med. Eng. Technol.* **45**, 511–531 (2021).

191. Moradipour, P., Limoee, M., Janfaza, S. & Behbood, L. Core-Shell Nanofibers Based on Polycaprolactone/Polyvinyl Alcohol and Polycaprolactone/Collagen for Biomedical Applications. *J. Pharm. Innov.* **17**, 911–920 (2022).

192. Anaya Mancipe, J. M., Boldrini Pereira, L. C., de Miranda Borchio, P. G., Dias, M. L. & da Silva Moreira Thiré, R. M. Novel polycaprolactone (PCL)-type I collagen core-shell electrospun nanofibers for wound healing applications. *J. Biomed. Mater. Res. B Appl. Biomater.* **111**, 366–381 (2023).

193. Kulkarni, D. *et al.* Surface Functionalization of Nanofibers: The Multifaceted Approach for Advanced Biomedical Applications. *Nanomaterials (Basel)* **12**, (2022).

194. Ghobeira, R. *et al.* Effects of different sterilization methods on the physico-chemical and bioresponsive properties of plasma-treated polycaprolactone films. *Biomed. Mater.* **12**, 015017 (2017).

195. Martins, A. *et al.* Surface modification of electrospun polycaprolactone nanofiber meshes by plasma treatment to enhance biological performance. *Small* **5**, 1195–1206 (2009).

196. Rogers, C. M. *et al.* A novel technique for the production of electrospun scaffolds with tailored three-dimensional micro-patterns employing additive manufacturing. *Biofabrication* **6**, 035003 (2014).

197. Newman, A. C., Nakatsu, M. N., Chou, W., Gershon, P. D. & Hughes, C. C. W. The requirement for fibroblasts in angiogenesis: fibroblast-derived matrix proteins are essential for endothelial cell lumen formation. *Mol. Biol. Cell* **22**, 3791–3800 (2011).

198. Wong, T., McGrath, J. A. & Navsaria, H. The role of fibroblasts in tissue engineering and regeneration. *Br. J. Dermatol.* **156**, 1149–1155 (2007).

199. Aoki, S., Toda, S., Ando, T. & Sugihara, H. Bone marrow stromal cells, preadipocytes, and dermal fibroblasts promote epidermal regeneration in their distinctive fashions. *Mol. Biol. Cell* **15**, 4647–4657 (2004).

200. Emon, B. *et al.* Mechanosensitive changes in the expression of genes in colorectal cancer-associated fibroblasts. *Sci Data* **10**, 350 (2023).

201. Sutherland, J., Denyer, M. & Britland, S. Contact guidance in human dermal fibroblasts is modulated by population pressure. *J. Anat.* **206**, 581–587 (2005).

202. Makogonenko, E., Tsurupa, G., Ingham, K. & Medved, L. Interaction of fibrin(ogen) with fibronectin: further characterization and localization of the fibronectin-binding site. *Biochemistry* **41**, 7907–7913 (2002).

203. Shams, F. *et al.* Overexpression of VEGF in dermal fibroblast cells accelerates the angiogenesis and wound healing function: in vitro and in vivo studies. *Sci. Rep.* **12**, 18529 (2022).

204. Kamkin, A. *et al. The Role of Mechanosensitive Fibroblasts in the Heart*. (Academia, 2005).

205. D'Urso, M. & Kurniawan, N. A. Mechanical and Physical Regulation of Fibroblast-Myofibroblast Transition: From Cellular Mechanoresponse to Tissue Pathology. *Front Bioeng Biotechnol* **8**, 609653 (2020).

206. Hinz, B. Matrix mechanics and regulation of the fibroblast phenotype. *Periodontol. 2000* **63**, 14–28 (2013).

207. Kim, D.-H. *et al.* Mechanosensitivity of fibroblast cell shape and movement to anisotropic substratum topography gradients. *Biomaterials* **30**, 5433–5444 (2009).

208. Kuppan, P., Sethuraman, S. & Krishnan, U. M. PCL and PCL-gelatin nanofibers as esophageal tissue scaffolds: optimization, characterization and cell-matrix interactions. *J. Biomed. Nanotechnol.* **9**, 1540–1555 (2013).

209. Eshraghi, S. & Das, S. Mechanical and microstructural properties of polycaprolactone scaffolds with one-dimensional, two-dimensional, and three-dimensional orthogonally oriented porous architectures produced by selective laser sintering. *Acta Biomater.* **6**, 2467–2476 (2010).

210. Yaseri, R., Fadaie, M., Mirzaei, E., Samadian, H. & Ebrahiminezhad, A. Surface modification of polycaprolactone nanofibers through hydrolysis and aminolysis: a comparative study on structural characteristics, mechanical properties, and cellular performance. *Sci. Rep.* **13**, 9434 (2023).

211. Mei, N. *et al.* Biocompatibility of Poly(epsilon-caprolactone) scaffold modified by chitosan--the fibroblasts proliferation in vitro. *J. Biomater. Appl.* **19**, 323–339 (2005).

212. Chutipakdeevong, J., Ruktanonchai, U. & Supaphol, P. Hybrid biomimetic electrospun fibrous mats derived from poly(ε-caprolactone) and silk fibroin protein for wound dressing application. *Journal of Applied Polymer Science* **132**, (2014).

213. Baranowska-Korczyc, A. *et al.* Antimicrobial electrospun poly ε-caprolactone scaffolds for gingival fibroblast growth. *RSC Adv.* **6**, (2016).

214. Hartman, O. *et al.* Biofunctionalization of electrospun PCL-based scaffolds with perlecan domain IV peptide to create a 3-D pharmacokinetic cancer model. *Biomaterials* **31**, 5700–5718 (2010).

215. Bazgir, M. *et al.* Degradation and Characterisation of Electrospun Polycaprolactone (PCL) and Poly(lactic-co-glycolic acid) (PLGA) Scaffolds for Vascular Tissue Engineering. *Materials* **14**, (2021).

216. Meng, Z. X., Zheng, W., Li, L. & Zheng, Y. F. Fabrication and characterization of three-dimensional nanofiber membrance of PCL–MWCNTs by electrospinning. *Materials Science and Engineering: C* **30**, 1014–1021 (2010).

217. Putti, M., Simonet, M., Solberg, R. & Peters, G. W. M. Electrospinning poly(ε-caprolactone) under controlled environmental conditions: Influence on fiber morphology and orientation. *Polymer* **63**, 189–195 (2015).

218. Telford, J. K. A brief introduction to design of experiments. *Johns Hopkins APL Tech. Dig.* **27**, 224–232 (2007).

219. Park, K. & Ahn, J.-H. Design of experiment considering two-way interactions and its application to injection molding processes with numerical analysis. *J. Mater. Process. Technol.* **146**, 221–227 (2004).

220. Coles, S. R. *et al.* A design of experiments (DoE) approach to material properties optimization of electrospun nanofibers. *J. Appl. Polym. Sci.* **117**, 2251–2257 (2010).

221. Sorkhabi, T. S. *et al.* Electrospinning of Poly (Acrylamide), Poly (Acrylic Acid) and Poly (Vinyl Alcohol) Nanofibers: Characterization and Optimization Study on the Effect of Different Parameters on Mean Diameter Using Taguchi Design of Experiment Method. *Materials* **15**, 5876 (2022).

222. Cui, W., Li, X., Zhou, S. & Weng, J. Investigation on process parameters of electrospinning system through orthogonal experimental design. *J. Appl. Polym. Sci.* **103**, 3105–3112 (2007).
223. Jankovic, A., Chaudhary, G. & Goia, F. Designing the design of experiments (DOE) – An investigation on the influence of different factorial designs on the characterization of complex systems. *Energy Build.* **250**, 111298 (2021).
224. Chloroform Solvent Properties. https://macro.lsu.edu/howto/solvents/chloroform.htm.
225. Viscosity of Chloroform. *Anton Paar* https://wiki.anton-paar.com/en/chloroform/.
226. Dimethylformamide. *Mitsubishi Gas Chemical Company, Inc.* https://www.mgc.co.jp/eng/products/nc/dimethylformamide.html.
227. Uliniuc, A. *et al.* Toward tunable amphiphilic copolymers via CuAAC click chemistry of oligocaprolactones onto starch backbone. *Carbohydr. Polym.* (2013).
228. Hansen Solubility Parameters. https://www.hansen-solubility.com/.
229. Díaz de los Ríos, M. & Hernández Ramos, E. Determination of the Hansen solubility parameters and the Hansen sphere radius with the aid of the solver add-in of Microsoft Excel. *SN Applied Sciences* **2**, 676 (2020).
230. Morad, M. R., Rajabi, A., Razavi, M. & Sereshkeh, S. R. P. A Very Stable High Throughput Taylor Cone-jet in Electrohydrodynamics. *Sci. Rep.* **6**, 38509 (2016).
231. Karamichos, D. *et al.* A role for topographic cues in the organization of collagenous matrix by corneal fibroblasts and stem cells. *PLoS One* **9**, e86260 (2014).
232. Rose, J. C. *et al.* Biofunctionalized aligned microgels provide 3D cell guidance to mimic complex tissue matrices. *Biomaterials* **163**, 128–141 (2018).

233. Wesełucha-Birczyńska, A. *et al.* Does 2D correlation Raman spectroscopy distinguish polymer nanomaterials due to the nanoaddition? *J. Mol. Struct.* **1217**, 128342 (2020).

234. Kołodziej, A. *et al.* A Raman Spectroscopic Analysis of Polymer Membranes with Graphene Oxide and Reduced Graphene Oxide. *Journal of Composites Science* **5**, 20 (2021).

235. Kołodziej, A., Wesełucha-Birczyńska, A., Świętek, M., Skalniak, Ł. & Błażewicz, M. Raman microspectroscopic investigations of polymer nanocomposites: evaluation of physical and biophysical properties. *International Journal of Polymeric Materials and Polymeric Biomaterials* **68**, 44–52 (2019).

236. Krüger, L. *et al.* Ductular and proliferative response of esophageal submucosal glands in a porcine model of esophageal injury and repair. *Am. J. Physiol. Gastrointest. Liver Physiol.* **313**, G180–G191 (2017).

237. Kapoor, H., Lohani, K. R., Lee, T. H., Agrawal, D. K. & Mittal, S. K. Animal Models of Barrett's Esophagus and Esophageal Adenocarcinoma-Past, Present, and Future. *Clin. Transl. Sci.* **8**, 841–847 (2015).

238. Durcan, C. *et al.* Experimental investigations of the human oesophagus: anisotropic properties of the embalmed mucosa-submucosa layer under large deformation. *Biomech. Model. Mechanobiol.* **21**, 1685–1702 (2022).

239. Ngwangwa, H. *et al.* Biomechanical analysis of sheep oesophagus subjected to biaxial testing including hyperelastic constitutive model fitting. *Heliyon* **8**, e09312 (2022).

240. Xing, J., Liu, N., Xu, N., Chen, W. & Xing, D. Engineering complex anisotropic scaffolds beyond simply uniaxial alignment for tissue engineering. *Adv. Funct. Mater.* **32**, 2110676 (2022).

241. Mitchell, G. R. & Tojeira, A. Role of anisotropy in tissue engineering. *Procedia Eng.* **59**, 117–125 (2013).

242. Fong, H., Chun, I. & Reneker, D. H. Beaded nanofibers formed during electrospinning. *Polymer* **40**, 4585–4592 (1999).

243. Horuz, T. İ. & Bülent Belibağlı, K. Production of electrospun gelatin nanofibers: an optimization study by using Taguchi's methodology. *Materials Research Express* **4**, (2017).

244. Wang, L., Wang, C., Wu, S., Fan, Y. & Li, X. Influence of the mechanical properties of biomaterials on degradability, cell behaviors and signaling pathways: current progress and challenges. *Biomater Sci* **8**, 2714–2733 (2020).

245. Wang, L. *et al.* Biomechanical study on implantable and interventional medical devices. *Acta Mech. Sin.* **37**, 875–894 (2021).

246. Merrilees, M. *et al.* Use of stacked layers of electrospun L-lactide/glycolide co-polymer fibers for rapid construction of skin sheets. *Bioengineering (Basel)* **8**, 7 (2021).

247. Lam, C. X. F., Hutmacher, D. W., Schantz, J.-T., Woodruff, M. A. & Teoh, S. H. Evaluation of polycaprolactone scaffold degradation for 6 months in vitro and in vivo. *J. Biomed. Mater. Res. A* **90**, 906–919 (2009).

248. Dias, J. R., Sousa, A., Augusto, A., Bártolo, P. J. & Granja, P. L. Electrospun polycaprolactone (PCL) degradation: An in vitro and in vivo study. *Polymers (Basel)* **14**, 3397 (2022).

249. Griffith, L. G. Polymeric biomaterials. *Acta Mater.* **48**, 263–277 (2000).

250. Li, S., Garreau, H. & Vert, M. Structure-property relationships in the case of the degradation of massive poly(α-hydroxy acids) in aqueous media. *J. Mater. Sci. Mater. Med.* **1**, 198–206 (1990).

251. Grizzi, I., Garreau, H., Li, S. & Vert, M. Hydrolytic degradation of devices based on poly(DL-lactic acid) size-dependence. *Biomaterials* **16**, 305–311 (1995).

252. Harrison, K. L. & Jenkins, M. J. The effect of crystallinity and water absorption on the dynamic mechanical relaxation behaviour of polycaprolactone. *Polym. Int.* **53**, 1298–1304 (2004).

253. Lin, W. J. Comparison of thermal characteristics and degradation properties of epsilon-caprolactone copolymers. *J. Biomed. Mater. Res.* **47**, 420–423 (1999).

254. Sun, H., Mei, L., Song, C., Cui, X. & Wang, P. The in vivo degradation, absorption and excretion of PCL-based implant. *Biomaterials* **27**, 1735–1740 (2006).

255. Karjalainen, T., Hiljanen-Vainio, M., Malin, M. & Seppälä, J. Biodegradable lactone copolymers. III. Mechanical properties of epsilon-caprolactone and lactide copolymers after hydrolysisin vitro. *J. Appl. Polym. Sci.* **59**, 1299–1304 (1996).

256. Woodward, S. C., Brewer, P. S., Moatamed, F., Schindler, A. & Pitt, C. G. The intracellular degradation of poly(epsilon-caprolactone). *J. Biomed. Mater. Res.* **19**, 437–444 (1985).

257. Pitt, C. G., Chasalow, F. I., Hibionada, Y. M., Klimas, D. M. & Schindler, A. Aliphatic polyesters. I. The degradation of poly(ϵ-caprolactone) *in vivo*. *J. Appl. Polym. Sci.* **26**, 3779–3787 (1981).

258. Sailema-Palate, G. P., Vidaurre, A., Campillo-Fernández, A. J. & Castilla-Cortázar, I. A comparative study on Poly(ε-caprolactone) film degradation at extreme pH values. *Polym. Degrad. Stab.* **130**, 118–125 (2016).

259. Lee, S.-H., Lee, J. H. & Cho, Y.-S. Analysis of degradation rate for dimensionless surface area of well-interconnected PCL scaffold via in-vitro accelerated degradation experiment. *Tissue Engineering and Regenerative Medicine* **11**, 446–452 (2014).

260. Bartnikowski, M., Dargaville, T. R., Ivanovski, S. & Hutmacher, D. W. Degradation mechanisms of polycaprolactone in the context of chemistry, geometry and environment. *Prog. Polym. Sci.* **96**, 1–20 (2019).

261. Tutuian, R. & Castell, D. O. Gastroesophageal reflux monitoring: pH and impedance. *GI Motility online* (2006) doi:10.1038/gimo31.

262. NMR Chemical Shifts of Impurities Charts. https://www.sigmaaldrich.com/GB/en/technical-documents/technical-article/analytical-chemistry/nuclear-magnetic-resonance/1h-nmr-and-13c-nmr-chemical-shifts-of-impurities-chart.

263. Arima, Y. & Iwata, H. Effect of wettability and surface functional groups on protein adsorption and cell adhesion using well-defined mixed self-assembled monolayers. *Biomaterials* **28**, 3074–3082 (2007).

264. Xing, Z. *et al.* Altered Surface Hydrophilicity on Copolymer Scaffolds Stimulate the Osteogenic Differentiation of Human Mesenchymal Stem Cells. *Polymers* **12**, (2020).

265. Steele, J. G., Johnson, G., McLean, K. M., Beumer, G. J. & Griesser, H. J. Effect of porosity and surface hydrophilicity on migration of epithelial tissue over synthetic polymer. *J. Biomed. Mater. Res.* **50**, 475–482 (2000).

266. Sundaram, S. *et al.* Esophageal regeneration following surgical implantation of a tissue engineered esophageal implant in a pediatric model. *NPJ Regen Med* **7**, 1 (2022).

267. Hassan, M. I., Sultana, N. & Hamdan, S. Bioactivity Assessment of Poly(***ε***-caprolactone)/Hydroxyapatite Electrospun Fibers for Bone Tissue Engineering Application. *J. Nanomater.* **2014**, (2014).

268. Salaris, V., López, D., Kenny, J. M. & Peponi, L. Hydrolytic Degradation and Bioactivity of Electrospun PCL-Mg-NPs Fibrous Mats. *Molecules* **28**, (2023).

269. Boccaccini, A. R. & Blaker, J. J. Bioactive composite materials for tissue engineering scaffolds. *Expert Rev. Med. Devices* **2**, 303–317 (2005).

270. Abdal-hay, A. *et al.* A review of protein adsorption and bioactivity characteristics of poly ε-caprolactone scaffolds in regenerative medicine. *Eur. Polym. J.* **162**, 110892 (2022).

271. Parisi, L. *et al.* A glance on the role of fibronectin in controlling cell response at biomaterial interface. *Jpn. Dent. Sci. Rev.* **56**, 50–55 (2020).

272. He, T. *et al.* Enhanced endothelialization guided by fibronectin functionalized plasma polymerized acrylic acid film. *Materials Science and Engineering: C* **32**, 1025–1031 (2012).

273. Missirlis, D., Haraszti, T., Kessler, H. & Spatz, J. P. Fibronectin promotes directional persistence in fibroblast migration through interactions with both its cell-binding and heparin-binding domains. *Sci. Rep.* **7**, 3711 (2017).

274. Miron-Mendoza, M., Lin, X., Ma, L., Ririe, P. & Petroll, W. M. Individual versus collective fibroblast spreading and migration: regulation by matrix composition in 3D culture. *Exp. Eye Res.* **99**, 36–44 (2012).

275. Richardson, S. A. *et al.* Covalent Attachment of Fibronectin onto Emulsion-Templated Porous Polymer Scaffolds Enhances Human Endometrial Stromal Cell Adhesion, Infiltration, and Function. *Macromolecular Bioscience* **19**, e1800351 (2018).

276. Mohapatra, S. Sterilization and Disinfection. *Essentials of Neuroanesthesia* 929 (2017).

277. Łopianiak, I. & Butruk-Raszeja, B. A. Evaluation of Sterilization/Disinfection Methods of Fibrous Polyurethane Scaffolds Designed for Tissue Engineering Applications. *Int. J. Mol. Sci.* **21**, (2020).
278. Kothekar, A. T. & Kulkarni, A. P. Basic Principles of Disinfection and Sterilization in Intensive Care and Anesthesia and Their Applications during COVID-19 Pandemic. *Indian J. Crit. Care Med.* **24**, 1114–1124 (2020).
279. Horakova, J. *et al.* Impact of Various Sterilization and Disinfection Techniques on Electrospun Poly-ε-caprolactone. *ACS Omega* **5**, 8885–8892 (2020).
280. Ziębowicz, A., Ziębowicz, B. & Dziekońska, M. The influence of sterilization on the properties of the polyethylene used in biomedical applications. (2018).
281. Ahmed, M., Punshon, G., Darbyshire, A. & Seifalian, A. M. Effects of sterilization treatments on bulk and surface properties of nanocomposite biomaterials: Effects of Sterilization on the Properties of Nanocomposite Biomaterials. *J. Biomed. Mater. Res. B Appl. Biomater.* **101**, 1182–1190 (2013).
282. Holy, C. E., Cheng, C., Davies, J. E. & Shoichet, M. S. Optimizing the sterilization of PLGA scaffolds for use in tissue engineering. *Biomaterials* **22**, 25–31 (2001).
283. Dai, Z., Ronholm, J., Tian, Y., Sethi, B. & Cao, X. Sterilization techniques for biodegradable scaffolds in tissue engineering applications. *J. Tissue Eng.* **7**, 2041731416648810 (2016).
284. Tao, M. *et al.* Sterilization and disinfection methods for decellularized matrix materials: Review, consideration and proposal. *Bioact. Mater.* **6**, 2927–2945 (2021).
285. Griffin, M. *et al.* Evaluation of Sterilisation Techniques for Regenerative Medicine Scaffolds Fabricated with Polyurethane Nonbiodegradable and Bioabsorbable Nanocomposite Materials. *Int. J. Biomater.* **2018**, 6565783 (2018).

286. Prajapati, S. *et al.* Effect of gamma irradiation on shape memory, thermal and mechanical properties of polycaprolactone. *Radiat. Phys. Chem.* **204**, 110671 (2023).

287. Spoto, M. H. F. *et al.* Gamma irradiation in the control of pathogenic bacteria in refrigerated ground chicken meat. *Sci. Agric.* **57**, 389–394 (2000).

288. Plikk, P., Odelius, K., Hakkarainen, M. & Albertsson, A. C. Finalizing the properties of porous scaffolds of aliphatic polyesters through radiation sterilization. *Biomaterials* **27**, 5335–5347 (2006).

289. Cottam, E., Hukins, D. W. L., Lee, K., Hewitt, C. & Jenkins, M. J. Effect of sterilisation by gamma irradiation on the ability of polycaprolactone (PCL) to act as a scaffold material. *Med. Eng. Phys.* **31**, 221–226 (2009).

290. Preem, L. *et al.* Effects and efficacy of different sterilization and disinfection methods on electrospun drug delivery systems. *Int. J. Pharm.* **567**, 118450 (2019).

291. ISO 11137-2:2013. *Iso.org* https://www.iso.org/obp/ui/.

292. Cohn, C. *et al.* Lipid-mediated protein functionalization of electrospun polycaprolactone fibers. *Express Polym Lett* **10**, 430–437 (2016).

293. Kotula, A. P., Snyder, C. R. & Migler, K. B. Determining conformational order and crystallinity in polycaprolactone via Raman spectroscopy. *Polymer* **117**, 1–10 (2017).

294. Jirofti, N., Mohebbi-Kalhori, D. & Masoumi, R. Enhancing biocompatibility of PCL/PU nano-structures to control the water wettability by NaOH hydrolysis treatment for tissue engineering applications. *J. Ind. Text.* **51**, 3278S-3296S (2022).

295. Sarkar, S. *et al.* Roles of Nanofiber Scaffold Structure and Chemistry in Directing Human Bone Marrow Stromal Cell Response. *Advances in Tissue Engineering and Regenerative Medicine* **1**, (2016).

296. Al-Azzam, N. & Alazzam, A. Micropatterning of cells via adjusting surface wettability using plasma treatment and graphene oxide deposition. *PLoS One* **17**, e0269914 (2022).

297. Phillip, E., Jr *et al.* Ethylene oxide's role as a reactive agent during sterilization: effects of polymer composition and device architecture. *J. Biomed. Mater. Res. B Appl. Biomater.* **101**, 532–540 (2013).

298. Valente, T. A. M. *et al.* Effect of Sterilization Methods on Electrospun Poly(lactic acid) (PLA) Fiber Alignment for Biomedical Applications. *ACS Appl. Mater. Interfaces* **8**, 3241–3249 (2016).

299. Cabrera, J. N. *et al.* Increased Surface Roughness in Polydimethylsiloxane Films by Physical and Chemical Methods. *Polymers* **9**, (2017).

300. Morent, R., De Geyter, N., Desmet, T., Dubruel, P. & Leys, C. Plasma surface modification of biodegradable polymers: A review. *Plasma Process. Polym.* **8**, 171–190 (2011).

301. Morris, G. E. *et al.* Human airway smooth muscle maintain in situ cell orientation and phenotype when cultured on aligned electrospun scaffolds. *Am. J. Physiol. Lung Cell. Mol. Physiol.* **307**, L38-47 (2014).

302. Pu, J., Yuan, F., Li, S. & Komvopoulos, K. Electrospun bilayer fibrous scaffolds for enhanced cell infiltration and vascularization in vivo. *Acta Biomater.* **13**, 131–141 (2015).

303. Chou, C.-L. *et al.* Micrometer scale guidance of mesenchymal stem cells to form structurally oriented cartilage extracellular matrix. *Tissue Eng. Part A* **19**, 1081–1090 (2013).

304. Gilchrist, C. L., Ruch, D. S., Little, D. & Guilak, F. Micro-scale and meso-scale architectural cues cooperate and compete to direct aligned tissue formation. *Biomaterials* **35**, 10015–10024 (2014).

305. Wilkinson, C. D. W., Riehle, M., Wood, M., Gallagher, J. & Curtis, A. S. G. The use of materials patterned on a nano- and micro-metric scale in cellular engineering. *Materials Science and Engineering: C* **19**, 263–269 (2002).

306. Abadi, P. P. S. S. *et al.* Engineering of mature human induced pluripotent stem cell-derived cardiomyocytes using substrates with multiscale topography. *Adv. Funct. Mater.* **28**, 1707378 (2018).

307. Juignet, L. *et al.* Macrotopographic closure promotes tissue growth and osteogenesis in vitro. *Acta Biomater.* **53**, 536–548 (2017).

308. Aoki, H., Miyoshi, H. & Yamagata, Y. Electrospinning of gelatin nanofiber scaffolds with mild neutral cosolvents for use in tissue engineering. *Polym. J.* **47**, 267–277 (2014).

309. McDevitt, T. C., Woodhouse, K. A., Hauschka, S. D., Murry, C. E. & Stayton, P. S. Spatially organized layers of cardiomyocytes on biodegradable polyurethane films for myocardial repair. *J. Biomed. Mater. Res. A* **66**, 586–595 (2003).

310. Nara, S. *et al.* Strategies for faster detachment of corneal cell sheet using micropatterned thermoresponsive matrices. *J. Mater. Chem. B Mater. Biol. Med.* **3**, 4155–4169 (2015).

311. Karuri, N. W., Nealey, P. F., Murphy, C. J. & Albrecht, R. M. Structural organization of the cytoskeleton in SV40 human corneal epithelial cells cultured on nano- and microscale grooves. *Scanning* **30**, 405–413 (2008).

312. Parrag, I. C., Zandstra, P. W. & Woodhouse, K. A. Fiber alignment and coculture with fibroblasts improves the differentiated phenotype of murine embryonic stem cell-derived cardiomyocytes for cardiac tissue engineering. *Biotechnol. Bioeng.* **109**, 813–822 (2012).

313. Qi, L. *et al.* Pre-culture Sudan Black B treatment suppresses autofluorescence signals emitted from polymer tissue scaffolds. *Sci. Rep.* **7**, (2017).

314. Lemons, J. M. S. *et al.* Quiescent fibroblasts exhibit high metabolic activity. *PLoS Biol.* **8**, e1000514 (2010).

315. Ma, C., Kuzma, M. L., Bai, X. & Yang, J. Biomaterial-Based Metabolic Regulation in Regenerative Engineering. *Adv. Sci.* **6**, 1900819 (2019).

316. Ao, M. *et al.* Stretching fibroblasts remodels fibronectin and alters cancer cell migration. *Sci. Rep.* **5**, 8334 (2015).

317. Yang, D. *et al.* Promoting Cell Migration in Tissue Engineering Scaffolds with Graded Channels. *Adv. Healthc. Mater.* **6**, (2017).

318. Wu, J. *et al.* Gradient biomaterials and their influences on cell migration. *Interface Focus* **2**, 337–355 (2012).

319. Neidlinger-Wilke, C., Grood, E. S., Wang JH-C, Brand, R. A. & Claes, L. Cell alignment is induced by cyclic changes in cell length: studies of cells grown in cyclically stretched substrates. *J. Orthop. Res.* **19**, 286–293 (2001).

320. Buck, R. C. Reorientation response of cells to repeated stretch and recoil of the substratum. *Exp. Cell Res.* **127**, 470–474 (1980).

321. Guo, Y. *et al.* Extracellular matrix of mechanically stretched cardiac fibroblasts improves viability and metabolic activity of ventricular cells. *Int. J. Med. Sci.* **10**, 1837–1845 (2013).

322. Biggs, M. J. P. *et al.* Adhesion formation of primary human osteoblasts and the functional response of mesenchymal stem cells to 330 nm deep microgrooves. *J. R. Soc. Interface* **5**, 1231–1242 (2008).

323. Oliver-De La Cruz, J. *et al.* Substrate mechanics controls adipogenesis through YAP phosphorylation by dictating cell spreading. *Biomaterials* **205**, 64–80 (2019).

324. Li, X. *et al.* Effect of substrate stiffness on the functions of rat bone marrow and adipose tissue derived mesenchymal stem cells in vitro. *J. Biomed. Mater. Res. A* **102**, 1092–1101 (2014).

325. Engler, A. J., Sen, S., Sweeney, H. L. & Discher, D. E. Matrix elasticity directs stem cell lineage specification. *Cell* **126**, 677–689 (2006).

326. Xie, J. *et al.* Substrate elasticity regulates adipose-derived stromal cell differentiation towards osteogenesis and adipogenesis through β-catenin transduction. *Acta Biomater.* **79**, 83–95 (2018).

327. Allen, J. L., Cooke, M. E. & Alliston, T. ECM stiffness primes the TGFβ pathway to promote chondrocyte differentiation. *Mol. Biol. Cell* **23**, 3731–3742 (2012).

328. Adnerhill, I., Ekberg, O. & Groher, M. E. Determining normal bolus size for thin liquids. *Dysphagia* **4**, 1–3 (1989).

329. Takeda, T., Nabae, T., Kassab, G., Liu, J. & Mittal, R. K. Oesophageal wall stretch: the stimulus for distension induced oesophageal sensation. *Neurogastroenterol. Motil.* **16**, 721–728 (2004).

330. Guedes, F. *et al.* Gamma Irradiation Processing on 3D PCL Devices-A Preliminary Biocompatibility Assessment. *Int. J. Mol. Sci.* **23**, (2022).

331. Aubin, H. *et al.* Directed 3D cell alignment and elongation in microengineered hydrogels. *Biomaterials* **31**, 6941–6951 (2010).
332. Gomes, R. N., Manuel, F. & Nascimento, D. S. The bright side of fibroblasts: molecular signature and regenerative cues in major organs. *NPJ Regen Med* **6**, 43 (2021).
333. Hashimoto, T., Kojima, K. & Tamada, Y. Higher Gene Expression Related to Wound Healing by Fibroblasts on Silk Fibroin Biomaterial than on Collagen. *Molecules* **25**, (2020).
334. Carver, W., Nagpal, M. L., Nachtigal, M., Borg, T. K. & Terracio, L. Collagen expression in mechanically stimulated cardiac fibroblasts. *Circ. Res.* **69**, 116–122 (1991).

Appendix A

Input Excel template for creating polar plots

After generating an orientation distribution table using the OrientationJ plugin in ImageJ, the “distribution of orientation” was used to populate column B of the following excel sheet:

	A	B	C	D	E	F
1	**Orientation_in_Degrees**	**Distribution_of_orientation**	**sum per 5deg**	**ratio to total orientation per 5deg**	**Range5deg**	**Fraction5deg**
2	-89.5				-85	=OFFSET($D$6,ROW(D6)-6)*5,0)
3	-88.5				-80	=OFFSET($D$6,ROW(D7)-6)*5,0)
4	-87.5				-75	=OFFSET($D$6,ROW(D8)-6)*5,0)
5	-86.5				-70	=OFFSET($D$6,ROW(D9)-6)*5,0)
6	-85.5		=SUM(B2:B6)	=C6/$B$183	-65	=OFFSET($D$6,ROW(D10)-6)*5,0)
7					-60	=OFFSET($D$6,ROW(D11)-6)*5,0)
8	-83.5				-55	=OFFSET($D$6,ROW(D12)-6)*5,0)
9	-82.5				-50	=OFFSET($D$6,ROW(D13)-6)*5,0)

10	-81.5				-45	=OFFSET($D$6,ROW(D14)-6)*5,0)
11	-80.5		=SUM(B7:B11)	=C11/$B$183	-40	=OFFSET($D$6,ROW(D15)-6)*5,0)
…	…		…	….	..	…
181	89.5		=SUM(B177:B181)	=C181/$B$183		
182						
183		=SUM(B2:B181)				

Appendix B

Python code used to produce polar plots

The following python code was opened in Visual Studio. When the code was run, the excel file populated with the orientation distribution data generated using OrientationJ (see **Appendix A**) was selected. A polar histogram was then generated by the software, which could be saved as an image file.

```
from cycler import cycler
import numpy as np
import matplotlib.pyplot as plt
import pandas as pd
from tkinter import *
from tkinter.filedialog import askopenfilename
import matplotlib.colors as mcolors
import matplotlib as mpl
def truncate_colormap(cmap, minval=0.0, maxval=1.0, n=-1):
    if n == -1:
        n = cmap.N
    new_cmap = mcolors.LinearSegmentedColormap.from_list(
         'trunc({name},{a:.2f},{b:.2f})'.format(name=cmap.name, a=minval,
b=maxval),
         cmap(np.linspace(minval, maxval, n)))
    return new_cmap
root = Tk()
root.withdraw()
```

```
root.update()
file_path = askopenfilename(initialdir="c:/")
refdata = pd.read_excel(file_path)
data = refdata
fig = plt.figure(figsize=(10, 4))
font = {'size': 13, 'weight': 'bold'}
plt.rc('font', **font)
# Adjust the gridspec to move the polar plot and colorbar closer together
gs = fig.add_gridspec(1, 6, width_ratios=[1, 1, 0.1, 5, 1, 1], wspace=0.001)
fc = data['Range5deg'].tolist()
fw = data['Fraction5deg'].tolist()
fc = [i for i in fc if str(i) != 'nan']
fw = [i for i in fw if str(i) != 'nan']
fw2 = [float(x) * float(100) for x in fw]
fc_corrected = [float(x) - float(2.5) for x in fc]
fc_corrected_radian = [float(x) * float((np.pi / 2) / 90) for x in fc_corrected]
theta = fc_corrected_radian
radii = fw2
min_length = min(len(theta), len(radii))
theta = theta[:min_length]
radii = radii[:min_length]
width = 5 * (np.pi / 2) / 90
# Create the first subplot on the left side for colorbar
ax_colorbar = fig.add_subplot(gs[0])
ax_colorbar.axis('off')
# Create the second subplot on the right side for the custom polar-like plot
```

```
ax_polar = fig.add_subplot(gs[3], projection='polar')

# Update theta values to show from -90 to 90 degrees

theta = np.flip(theta)

radii = np.flip(radii)

# Manually adjust the plot to resemble a polar plot

ax_polar.set_theta_zero_location('E')  # Rotate the plot by setting the zero location to East

ax_polar.set_theta_direction(-1)

# Set the start and end angle for the polar plot

start_angle = np.deg2rad(90)  # Start at 90 degrees (East)

end_angle = np.deg2rad(-90)  # End at -90 degrees (West)

ax_polar.set_thetamin(np.rad2deg(start_angle))

ax_polar.set_thetamax(np.rad2deg(end_angle))

bars = ax_polar.bar(theta, radii, edgecolor='black', linewidth=0.25, width=0.95 * width, bottom=0.0, zorder=2)  # Set higher zorder

minColor = 0.00

maxColor = 0.90

viridis = truncate_colormap(plt.get_cmap("viridis_r"), minColor, maxColor)

norm = mpl.colors.Normalize(vmin=0, vmax=15)

for r, bar in zip(radii, bars):

    bar.set_facecolor(viridis(norm(r)))

bar.set_alpha(0.5)

# Create a separate axis for the custom-sized colorbar

cb_axes = fig.add_subplot(gs[2])  # [left, bottom, width, height]

cb = fig.colorbar(mpl.cm.ScalarMappable(norm=norm, cmap=viridis), cax=cb_axes, label='% Alignment, 5° slices', aspect=50)

cb.set_label('% Alignment, 5° slices', size=12, color='black', fontweight='bold')
```

```
# Remove the frame around the colorbar
cb_axes.spines['top'].set_visible(False)
cb_axes.spines['bottom'].set_visible(False)
cb_axes.spines['left'].set_visible(False)
cb_axes.spines['right'].set_visible(False)
# Adjust the tick parameters
ax_polar.tick_params(axis='y', labelsize=10)
plt.tight_layout()  # Ensures that the plots don't overlap
plt.gca().set_facecolor('none')
plt.show()
plt.savefig('#insert directory/#insert file name.png', dpi=1200, transparent=True)
plt.close()
```
